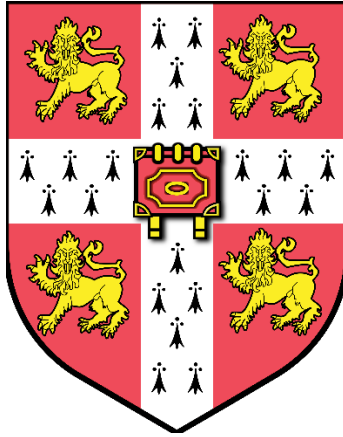


# Descending premotor target tracking systems in flying insects



**Jack Alexander Supple**

Department of Physiology, Development, and Neuroscience  
University of Cambridge

This dissertation is submitted for the degree of  
*Doctor of Philosophy*

Darwin College

September 2019



# Declaration

This dissertation is the result of my own work and includes nothing which is the outcome of work done in collaboration except as declared in the preface and specified in the text. It is not substantially the same as any that I have submitted, or, is being concurrently submitted for a degree or diploma or other qualification at the University of Cambridge or any other University or similar institution. I further state that no substantial part of my dissertation has already been submitted, or, is being concurrently submitted for any such degree, diploma or other qualification at the University of Cambridge or any other University or similar institution. This dissertation contains fewer than 60,000 words, exclusive of tables, footnotes, bibliography, and appendices.

# Descending premotor target tracking systems in flying insects

By Jack Alexander Supple

## Abstract

The control of behaviour in all animals requires efficient transformation of sensory signals into the task-specific activation of muscles. Predation offers an advantageous model behaviour to study the computational organisation underlying sensorimotor control. Predators are optimised through diverse evolutionary arms races to outperform their prey in terms of sensorimotor coordination, leading to highly specialised anatomical adaptations and hunting behaviours, which are often innate and highly stereotyped. Predatory flying insects present an extreme example, performing complex visually-guided pursuits of small, often fast flying prey over extremely small timescales (Olberg et al., 2007; Wardill et al., 2015, 2017). Furthermore, this behaviour is controlled by a tiny nervous system, leading to pressure on neuronal organisation to be optimised for coding efficiency (Gonzalez-Bellido et al., 2011).

In Dragonflies, a population of eight pairs of bilaterally symmetric Target Selective Descending Neurons (TSDNs) relay visual information about small moving objects from the brain to the thoracic motor centres. These neurons encode the movement of small moving objects across the dorsal fovea region of the eye which is fixated on prey during predatory pursuit, and are thought to constitute the commands necessary for actuating an interception flight path (Gonzalez-Bellido et al., 2013; Olberg, 1986; Olberg et al., 2007). TSDNs are characterised by their receptive fields, with responses of each TSDN type spatially confined to a specific portion of the dorsal fovea visual field and tuned to a specific direction of object motion (Gonzalez-Bellido et al., 2013). To date, little is known about the descending representations mediating target tracking in other insects. This dissertation presents a comparative report of descending neurons in a variety of flying insects. The results are organised into three chapters:

**Chapter 3** identifies TSDNs in demoiselle damselflies and compares their response properties to those previously described in dragonflies. Demoiselle TSDNs are also found to integrate binocular information, which is further elaborated with prism and eyepatch experiments.

**Chapter 4** describes TSDNs in two dipteran species, the robberfly *Holcocephala fusca* and the killerfly *Coenosia attenuata*.

**Chapter 5** describes an interaction between small- and wide-field visual features in TSDNs of both predatory and nonpredatory dipterans, finding functional similarity of these neurons for prey capture and conspecific pursuit. Dipteran TSDN responses are repressed by background motion in a direction dependent manner, suggesting a control architecture in which target tracking and optomotor stabilization pathways operate in parallel during pursuit.

# Acknowledgements

I am thankful to Dr Paloma Gonzalez-Bellido for welcoming me into her lab and all the help over the years. Thanks also to Dr Trevor Wardill for helping to get me up and running with experiments, and to all other members of the Fly Systems lab, especially Mary Sumner, Dr Kate Feller, Sergio Rossoni, and Sam Fabian. Special thanks to Daniel Pinto-Benito for being an excellent student and friend. It was a pleasure to collaborate with Dr Karin Nordström, and I am extremely grateful for her extensive and imaginative efforts. Thanks also to Professor Rob Olberg for his intracellular efforts in *demoiselles*, and for being such a pleasure to work with. Thanks to Professor Tom Daniel for hosting me in his lab and for lending inspiration throughout the years. Special thanks to Dr Kristian Franze for helping throughout the transition from Cambridge to Minnesota.

# Contributions

A large part of this work results from the efforts of members of the Fly Systems lab and external collaborators. Chapters 3 and 4 include data collected in part by Paloma Gonzalez-Bellido, my supervisor; Daniel Pinto-Benito, a summer student under my mentorship; and more recently Siddhant Pusdekar, Molly Liu, and Daniel Geleano who collected 2019 *Calopteryx maculata* behavioural data. In each case I was responsible for experimental design and data analysis, in addition to collecting a large portion of the dataset myself. Chapter 3 also includes data collected and analysed by Professor Rob Olberg; I was responsible for processing anatomical data and synthesising the data. Chapter 5 is based on a paper published in collaboration with Dr Karin Nordström's laboratory at Flinder's University, Australia. Dr Nordström's group was responsible for the experimental design, acquisition and analysis of all hoverfly data in the study. I was responsible for the experimental design, collection and analysis of all robberfly data, and contributed to the interpretation of the combined datasets. Other specific contributions throughout this thesis are documented in an 'Acknowledgements and contributions' section at the beginning of each results chapter.

Jack Supple

September 2019

# Table of Contents

Declaration	i
Abstract	ii
Acknowledgements	iv
Contributions	iv
Table of Contents	v
List of Figures	x
<b>Chapter 1: Introduction</b>	<b>1</b>
1.1 Target tracking and chasing	1
1.1.1 Definitions of biological sameness: homology and analogy	2
1.1.2 Diversity of chasing behaviours	4
1.2 The organisation of the insect visual system	7
1.2.1 Compound eyes	7
1.2.2 Ocelli	13
1.2.3 Brain organisation and nomenclature	13
1.2.4 The optic lobes	15
1.2.5 The central brain	17
1.2.6 Descending neurons and the ventral nerve cord	19
1.3 Neuronal mechanisms underlying motion vision	19
1.3.1 Elementary motion detection	19
1.3.2 Wide-field motion processing	23
1.3.2.1 Lobula Plate Tangential Cells (LPTCs)	23
1.3.2.2 Wide-field sensitive descending neurons	26
1.3.3 Target motion processing	28
1.3.3.1 Target selective lobula complex neurons	28
1.3.3.2 Target Selective Descending Neurons (TSDNs)	37
1.4 Models for visual control of target chasing	39
1.4.1 Land and Collett model	39
1.4.2 Inner- and outer-loop control	41

1.5	Aims and structure of the thesis	46
<b>Chapter 2: Methods and Materials</b>		<b>49</b>
2.1	Animals	50
2.1.1	Odonata	50
2.1.2	Diptera	50
2.2	Dissections	51
2.2.1	Ventral nerve cord	51
2.3	Visual stimuli	53
2.3.1	Using the DepthQ 360 DLP projector	53
2.3.2	StimGL	56
2.3.3	Tracking stimulus presentation	56
2.4	Electrophysiology	57
2.4.1	Extracellular recordings and spike sorting	57
2.4.2	Eyepatches and prisms	59
2.4.3	Data analysis	61
2.4.3.1	Visual receptive field mapping	61
2.5	Anatomy	67
2.5.1	2-Photon whole brain imaging	67
2.5.2	Macrophotography and pseudopupil measurements	68
2.6	Highspeed videography	71
2.6.1	Visual stimuli	71
2.6.2	Data acquisition	71
2.6.3	Calibration	73
2.6.4	Digitisation and 3D reconstruction	73
2.6.5	Behavioural analysis	75
<b>Chapter 3: Binocular encoding in the premotor target tracking system of damselflies</b>		<b>77</b>
3.1	Introduction	77
3.2	Methods and materials	79

3.2.1	Animals	79
3.2.2	High-speed videography of predation	79
3.2.3	Electrophysiology	81
3.2.4	Visual stimuli	82
3.2.5	Pseudopupil measurements	82
3.3	Results	82
3.3.1	Odonate ocular morphology	82
3.3.2	Attack trajectory in damselflies	86
3.3.3	TSDNs serving the demoiselle frontal fovea	86
3.3.4	Demoiselle TSDNs are binocular, exhibiting binocular-only, ocular-balanced, or ocular-dominant responses	93
3.3.5	Differences in global light intensity do not underlie the binocular input requirements of TSDNs	96
3.3.6	Demoiselle TSDN receptive fields resulting from reduced binocularity are consistent with binocular summation	96
3.4	Discussion	101
3.4.1	Eye morphology, hunting strategy, and TSDN homology within Odonata	101
3.4.2	Neuronal encoding of holoptic versus dichoptic visual space	102
3.4.3	Binocular properties of demoiselle TSDNs	103
3.5	Supplementary information	106

## **Chapter 4: Target Selective Descending Neurons in convergent predatory dipterans 133**

4.1	Introduction	113
4.2	Methods and materials	115
4.2.1	Animals and electrophysiology	115
4.2.2	2-Photon brain imaging	116
4.2.3	Data analysis	116
4.3	Results	116
4.3.1	Neuroanatomy and descending neuron organisation	116

4.3.2	Dipteran Target Selective Descending Neurons (dTSDNs) in robberflies and killer flies	119
4.3.3	<i>Holcocephala</i> dTSDN receptive fields	124
4.3.4	<i>Coenosia</i> dTSDN receptive fields	126
4.4	Discussion	127
	dTSDN response latencies	127
4.4.1	dTSDN receptive fields	128
4.4.2	Diversity of dipteran TSDNs	129

**Chapter 5: Integration of small- and wide-field visual features in Target Selective Descending Neurons of both predatory and non-predatory Dipterans**

		<b>133</b>
5.1	Introduction	133
5.2	Methods and materials	135
5.2.1	Animals and electrophysiology	135
5.2.2	Visual stimuli	135
5.2.3	Data analysis	136
5.3	Results	138
5.3.1	Descending neuron identification in hoverflies and robberflies	138
5.3.2	Dipteran TSDNs do not respond to targets moving in the same direction as background clutter	139
5.3.3	Dipteran TSDNs respond stronger to target motion when the background moves in the opposite direction	139
5.3.4	Local mechanisms do not explain dTSDN response from background motion	141
5.3.5	dTSDN response suppression is strongest when the background is most naturalistic	143
5.3.6	dTSDN habituation is facilitated by background movement	146
5.4	Discussion	147
5.4.1	TSDNs in predatory and non-predatory dipterans	147

5.4.2	Integration of small- and wide-field visual features in dTSDNs	147
5.4.3	Function of background suppression in premotor target tracking	148
<b>Chapter 6: Discussion</b>		<b>153</b>
5.4.4	TSDN implementation of the Land and Collett circuitry	155
5.4.5	TSDN The role of TSDN binocularity	158
5.4.6	Inner- and outer-loop control	159
5.4.7	Drawbacks and limitations to functional interpretation	162
5.4.8	TSDN evolution	163
5.4.9	Summary	165
<b>Bibliography</b>		<b>166</b>

# List of Figures

<b>Chapter 1</b>		<b>Page</b>
Figure 1.1	Predatory chasing strategies	3
Figure 1.2	Subjects of study	5
Figure 1.3	Compound eye design	8
Figure 1.4	Visual acuity in apposition eyes	10
Figure 1.5	Compound eye specializations for target tracking	12
Figure 1.6	Insect brain organization	14
Figure 1.7	Organization of the insect optic lobe	16
Figure 1.8	Visual output in the central brain	17
Figure 1.9	Descending neurons	18
Figure 1.10	Elementary motion detection	21
Figure 1.11	Cellular implementation of the Hassenstein-Reichardt detector in the optic lobe of <i>Drosophila</i>	22
Figure 1.12	Lobula Plate Tangential Cells	24
Figure 1.13	DNOVS descending neurons in <i>Calliphora</i>	27
Figure 1.14	Target sensitive MLG neurons in <i>Sarcophaga</i>	30
Figure 1.15	STMDs in the hoverfly	31
Figure 1.16	A subset of STMDs respond to target motion irrespective of background motion	32
Figure 1.17	Centrifugal STMD1 in the dragonfly	33
Figure 1.18	Object motion sensitive lobula columnar neurons in <i>Drosophila</i>	34
Figure 1.19	Target sensitive DNDC3-6b in <i>Sarcophaga</i>	36
Figure 1.20	Dragonfly Target Selective Descending Neurons (TSDNs)	38
Figure 1.21	Land and Collett circuitry for target tracking	40
Figure 1.22	Inner-loop stabilization reflexes and outer-loop goal-directed behaviours	42
Figure 1.23	Interactions between wide-field and target tracking systems	44

## **Chapter 2**

Figure 2.1	Dissections	52
Figure 2.2	Projector set-up for visual stimuli	54
Figure 2.3	Extracellular recordings and spike sorting	58
Figure 2.4	Eyepatches and Prisms	60
Figure 2.5	Visual receptive field mapping	62
Figure 2.6	Latency calculations	64
Figure 2.7	Analysis of rasterized visual stimuli	65
Figure 2.8	Multiphoton whole brain imaging	69
Figure 2.9	Macrophotography and pseudopupil measurements	70
Figure 2.10	Highspeed videography calibration	72
Figure 2.11	Image contrast adjustment in MATLAB and Fiji	73
Figure 2.12	Digitisation comparison between MATLAB and Fiji	74

## **Chapter 3**

Figure 3.1	Odonata phylogeny and ocular morphology	80
Figure 3.2	Pseudopupil measurements across Odonata	83
Figure 3.3	Comparison of external eye anatomy and hunting strategies of dragonflies and demoiselle damselflies	84
Figure 3.4	TSDNs sample the frontal visual field in demoiselles	85
Figure 3.5	TSDNs serving the demoiselle frontal foveae	88
Figure 3.6	Widefield responses of demoiselle TSDNs	89
Figure 3.7	Descending neuron anatomy in dragonflies and demoiselles	90
Figure 3.8	Neuroanatomy of intracellularly identified demoiselle TSDNs	91
Figure 3.9	Spike number and degree of binocular overlap, within the same type of TSDNs, shows high variability between damselfly individuals	92
Figure 3.10	Demoiselle TSDNs are binocular, with differing thresholds and input weights	94
Figure 3.11	Demoiselle TSDN receptive fields under opaque vs translucent eyepatches	98

Figure 3.12	Demoiselle TSDN receptive fields under prisms of varying deviation power	100
Figure 3.SI1	Path of prey through the visual field during predatory flights	106
Figure 3.SI2	Receptive field data	108
Figure 3.SI3	Eyepatch data	110
Figure 3.SI4	Prism data	112
<b>Chapter 4</b>		
Figure 4.1	Comparative neuroanatomy of <i>Holcocephala</i> and <i>Coenosia</i>	117
Figure 4.2	Target selectivity in dTSDNs	120
Figure 4.3	dTSDN response latency	121
Figure 4.4	dTSDN receptive fields in <i>Holcocephala</i> and <i>Coenosia</i>	122
Figure 4.5	<i>Holcocephala</i> dTSDN receptive fields are dependent on target size	123
Figure 4.6	Spike sorting <i>Holcocephala</i> dTSDNs	125
<b>Chapter 5</b>		
Figure 5.1	Fourier transforms and image spatial frequencies	137
Figure 5.2	dTSDNs in <i>Eristalis</i> and <i>Holcocephala</i>	140
Figure 5.3	Syn-directional background pattern motion strongly suppresses the dTSDN response to target motion	142
Figure 5.4	dTSDN response suppression is not explained by local mechanisms and is strongest when the background is most naturalistic	144
Figure 5.5	dTSDN habituation is facilitated by background movement	146
Figure 5.6	Model for the integration of small- and wide-field descending channels during pursuit	150
Figure 5.7	Output properties of the proposed controller	151
<b>Chapter 6</b>		
Figure 6.1	TSDN implementation of the Land and Collett minimal target tracking circuitry	156
Figure 6.2	Relationship of TSDNs with matched filter representations in the optomotor Pathway	160

# Chapter 1

## Introduction

### 1.1 Target tracking and chasing

Visual detection, tracking, and interaction with moving objects is a task faced by many animals wishing to feed, mate, and avoid predation. At the core of this task is an information processing challenge requiring an animal to acquire, represent, and transform complex visual information into motor commands that actuate the body musculature. Since neurons are energetically costly to build and maintain, neuronal circuits are specialised to represent only the most pertinent visual information for a given behavioural task and to minimise the transformational steps leading from sensor to musculature (Sterling and Laughlin, 2015). Arguably nowhere are these constraints more conspicuous than among flying insects, who are limited by a small neuronal population size, yet perform elaborate aerial altercations at high speeds (Gonzalez-Bellido et al., 2016; Olberg, 2012). Ultimately, an analysis of the neuronal computations involved in such behaviours aims to inform our understanding of the design principles and limitations underlying biological information processing.

Many flying insects chase targets with the intention of mating or catching prey. Dragonflies, for example, perform complex chases of small, often fast flying prey (Olberg et al., 2000), whilst males of many species chase their females prior to copulation (Collett and Land, 1975; Land and Collett, 1974). In contrast to escape behaviours, where success is generally achieved by manoeuvring to any of a range of locations distant from the threat, successful chasing is constrained to reaching a relatively smaller location in space, namely that of the target. Consequently, chasing demands precise sensorimotor control, and insects have evolved diverse and highly specialised behavioural, anatomical, and neuronal adaptations to maximise their chances of capture success within their specific ecological niche (Gonzalez-Bellido et al., 2016; Nordström, 2012).

### 1.1.1 Definitions of biological sameness: homology and analogy

Comparative analysis within an evolutionary context offers a framework to form and test hypotheses correlating neuronal function to behaviour (Buschbeck and Strausfeld, 1996; Keeley, 2000; Peek and Card, 2016). By correlating anatomical and neurophysiological adaptations to behaviour, and comparing these across different species, the underlying design principles for neuronal control of the behaviour may become apparent. Frequently, different species have converged to similar behavioural, anatomical, and neuronal adaptations that fulfil the demands of chasing, suggesting there may be globally efficient strategies robust to variation in ecological niche. In other cases, species have diverged from a common ancestral chasing strategy. In both instances, in addition to energetic constraints, the organisation of neuronal circuits implementing these behaviours is dependent on the local evolutionary history of the animal, such as the arrangement of pre-existing ancestral neural cell types and body plan. To what extent the representations and transformational processes within neuronal circuits vary across different species is an overarching interest of this thesis.

Essential to this approach is the analysis of ‘sameness’ between biological traits at the level of behaviour, anatomy, and neuronal computation. Broadly, sameness of traits in different species can either derive from common descent of an ancestral state, a condition termed *homology*, or arise independently without phyletic continuity, a condition termed *analogy* or *homoplasy* (Butler and Hodos, 2005; Butler and Sidel, 2000). Historically, homoplasy is a term used in systematics referring independent evolution of similar structures that perform similar functions, but for the purpose of this thesis the term analogy will be used as this encompasses homoplastic traits in addition to traits with similar functions that do not necessarily share the same anatomical structure, as could be the case for neuronal circuits calculating visual parameters (Borst and Helmstaedter, 2015).

Importantly, assertions of homology or analogy must be specified with reference to the specific characteristic being compared (Butler and Hodos, 2005). As pointed out by Butler and Hodos, the wings of birds and bats are analogous as wings, but not homologous as wings, as their last common ancestor did not possess wings; however, the wings of birds and bats are homologous as forelimb derivatives, as each lineage derived their wings from a shared ancestral forelimb (Butler and Hodos, 2005). Similarly, identified neurons in the brains of different species may be found to be analogous with respect to a target tracking computation, and homologous as ‘arising from the same population of neural progenitor cells’, but may not necessarily have derived from a shared ancestral state where these neurons implemented target tracking functionality.

Related to this problem, analogous traits can arise through multiple evolutionary mechanisms. Traditionally, analogous traits are strictly considered convergent when arising from vastly different precursor states with different genetic and developmental pathways, and are defined as parallel when arising in closely related lineages that are constrained to use similar genetic and developmental

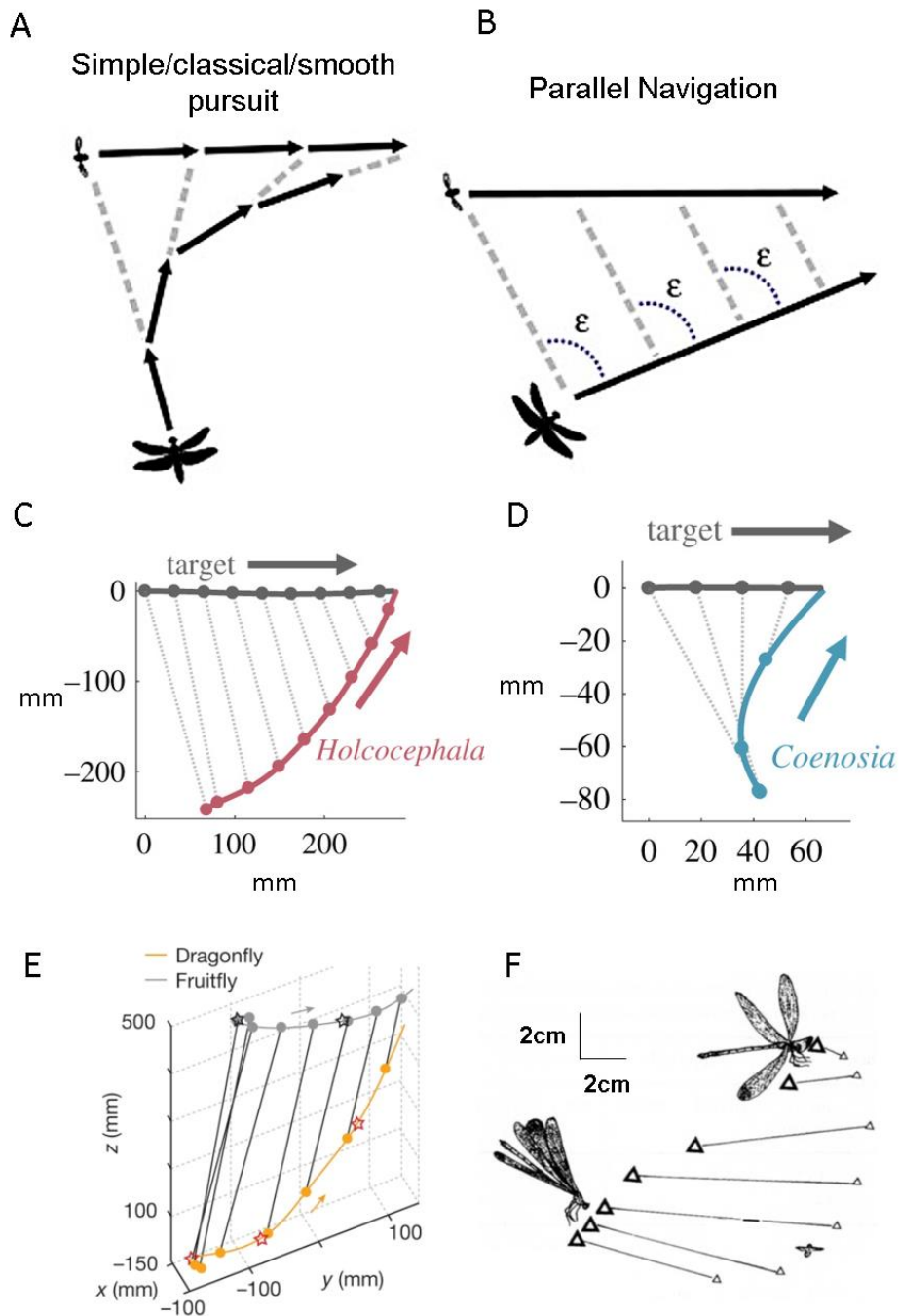


**Figure 1.1 Predatory chasing strategies (A-B)** General strategies for chasing moving targets. The chaser can either head towards the current position of the target, a strategy known as simple/classical/smooth pursuit (A), or the anticipated future location, a strategy known as parallel navigation (B). *Holcocephala* (C) and *Coenosia* (D) both implement parallel navigation, albeit over different spatial ranges with different levels of precision. Dragonflies approach their prey from below, and predatory flights resemble parallel navigation (E), although the implementation is thought to be based in largely on predictive rather than reactive mechanisms. Demoiselle damselflies (F) attack flying prey head on. It is currently unknown what chasing strategy is implemented by demoiselles. (A-B) adapted from (Gonzalez-Bellido et al., 2016); (C-D) adapted from (Fabian et al., 2018); (E) adapted from (Mischiati et al., 2015); (F) adapted from (Rüppell, 1999).

processes (Butler and Saidel, 2000). Analogy may also arise through reversal, where one lineage loses and subsequently regains a trait shared with phylogenetically adjacent lineages (Butler and Hodos, 2005). This situation is closely related to parallelism, and the distinction between homology and analogy becomes less clear. These distinctions are relevant as they reflect important constraints on the possible states that neuronal circuits can take throughout evolution. However, as these distinctions represent a continuum (Arendt and Reznick, 2008), for the purposes of this thesis the word ‘convergence’ shall broadly be used to mean ‘the evolution of an analogous trait without phyletic continuity, regardless of genetic and developmental mechanisms’. Whether such convergence is likely to arise under the constraints of parallel or reversal mechanisms shall be elaborated where this is relevant to the discussion of the structure of underlying neuronal circuitry.

### **1.1.2 Diversity of chasing behaviours**

Diptera is a large and diverse order of winged insects (Wiegmann et al., 2011), with adults of many species highly specialised for tracking and chasing other fast flying insects suited as mates or prey (Collett and Land, 1975; Land, 1993; Land and Collett, 1974; Perry and Desplan, 2016; Wardill et al., 2015, 2017). Male dipterans have long been the focus of behavioural and neurophysiological investigations into target tracking during conspecific chasing, and have been found to employ various chasing strategies (Boeddeker and Egelhaaf, 2005; Collett and Land, 1975, 1978; Land and Collett, 1974).

One simple method is to head towards the instantaneous position of the target (Figure 1.1A). This strategy, known as simple, classical, or smooth pursuit, relies on the chaser being faster than the target, and is utilised by male houseflies (Boeddeker et al., 2003; Land and Collett, 1974; Wehrhahn et al., 1982). An alternative method is to head towards the future location of the target, which can be achieved by maintaining a constant angle between the heading of the chaser and the retinal position of the target (Figure 1.1B). This intercepting strategy, known as parallel navigation, results in shorter flight paths relative to classical pursuit, and is implemented by male hoverflies (Collett and Land, 1978). In each case, the retinal position of the target is used as continuous input to a feedback controller to correct for any deviation of the target (Boeddeker and Egelhaaf, 2005; Collett and Land, 1978). Consequently, these chasing strategies suffer a delay between retinal slip of the target and corrective movements, measured as ~30ms in houseflies (Wehrhahn et al., 1982), and ~20ms in hoverflies (Wijngaard, 2010).

Interestingly, adults of several dipteran lineages have converged independently to predatory livelihoods from non-predatory ancestors, offering a unique opportunity to investigate the evolution of specialised target tracking circuits from available ancestral circuitry. The robberfly *Holcocephala fusca* (family *Asilidae*), and the killerfly *Coenosia attenuata* (aka hunterflies, family *Muscidae*) are two such examples (Figure 1.2). *Holcocephala* and *Coenosia* are generalist predators, detecting their prey from a perched position before initiating intercepting flights (Fabian et al., 2018; Wardill et al., 2015, 2017),

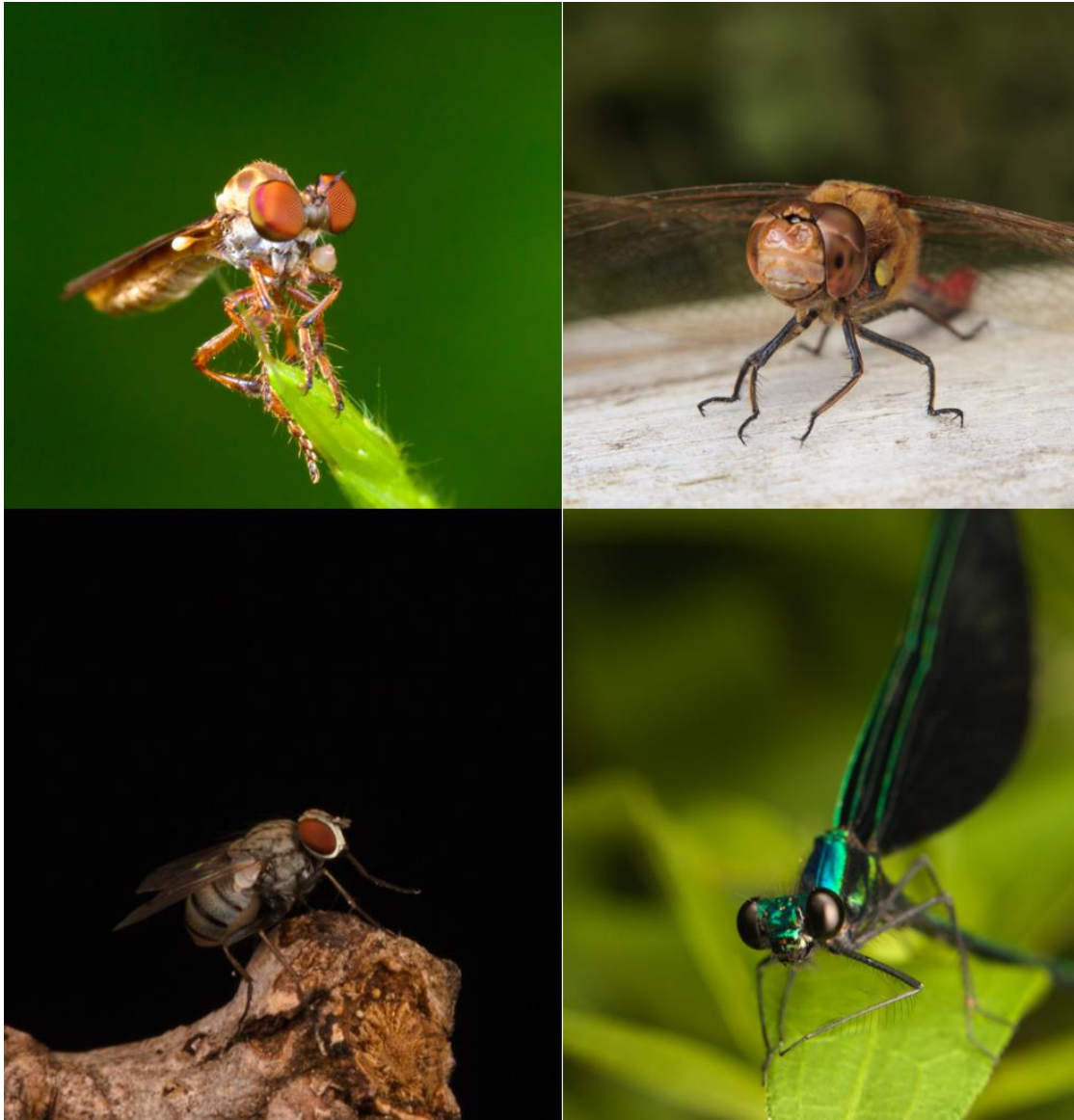


**Figure 1.2 Subjects of study** (Top left) The robberfly *Holocephala fusca* found feeding on a small gnat while perched in York, Pennsylvania, USA, August 2017. (Bottom left) The killerfly *Coenosia attenuata* in the laboratory in Minnesota, USA, August 2019. (Top right) The common darter dragonfly *Sympetrum striolatum* (family Libellulidae), found in Grantchester Meadows in Cambridge, UK, September 2017. (Bottom right) The demoiselle damselfly *Calopteryx maculata*, found at a creek in Nixon Park, York, Pennsylvania, USA, July 2019.

and each possess neuronal adaptations for target detection in the early visual system (Gonzalez-Bellido et al., 2011; Wardill et al., 2017). However, whilst *Holocephala* and *Coenosia* both utilise parallel navigation as a chasing strategy (Figure 1.1C-D), *Holocephala* hunt at much greater distances from their targets, with flight trajectories of ~80cm for *Holocephala* compared with ~20cm for *Coenosia* (Fabian et al., 2018). Furthermore, their visual ecologies vary, with *Holocephala* contrasting prey against the bright sky (Wardill et al., 2017), whilst *Coenosia* hunt among foliage (Bautista-Martínez et

al., 2017; Wardill et al., 2015). Currently little is known about the neuronal adaptations within motion processing circuitry that underlies target chasing in these two predators.

Odonata is an ancient predatory lineage comprising two distinct extant sister groups, the damselflies and dragonflies (Figure 1.2) (Grimaldi and Engel, 2005). Damselflies and dragonflies share a last common ancestor ~270 Million Years Ago and have subsequently diverged in behaviour, anatomy, and flight kinematics (Bomphrey et al., 2016; Corbet, 1999). Adult dragonflies are diurnal aerial predators, hunting flying prey around ponds and rivers (Grimaldi and Engel, 2005; Olberg et al., 2000). During chasing, dragonflies hunt from below, fixating their prey within the dorsal region of the visual field (Figure 1.1E) (Lin and Leonardo, 2017; Olberg et al., 2000, 2007). This strategy serves to enhance the visual contrast of the prey against the backdrop of a bright sky, in addition to camouflaging the dragonfly within the visual blind spot of the prey (Olberg, 2012). Fixation of the target within the dorsal visual field throughout flight is maintained by compensatory head movements, known as foveation, as the dragonfly aligns its body with the flight path of the prey (Mischiati et al., 2015). Interestingly, the latency between head and body movements is ~4 ms, too short to be under direct visual feedback control which has a measured latency on the order of 30 ms (Gonzalez-Bellido et al., 2013). This suggests that foveation may be driven by predictive internal models of body movement (Mischiati et al., 2015). Furthermore, retinal slip of the prey is largely nullified throughout flight due to the efficiency of foveation, suggesting that whilst dragonfly prey-capture flights resemble parallel navigation interception (Mischiati et al., 2015; Olberg et al., 2000), this is largely implemented by predictive components rather than closed-loop feedback from the visual system (Mischiati et al., 2015).

In contrast, damselflies forage for prey amongst foliage surrounding ponds and rivers (Corbet, 1999), and hunt their prey head on (Ingley et al., 2012; von Reyn et al., 2014; Ruppell, 1999). All damselflies possess conspicuously separated and binocularly overlapping compound eyes (Figure 1.2) (Horridge, 1977a, 1978). Most damselflies typically hunt with a stealthy approach followed by a darting snatch of stationary prey from a substrate, a behaviour known as gleaning (Ingley et al., 2012; von Reyn et al., 2014). However, many damselflies will also attack flying prey, with the demoiselle damselfly lineage (family *Calopteryx*) exclusively attacking flying prey from perched positions (Figure 1.1F) (Corbet, 1999; Ruppell, 1999). Currently little is known about the dynamics of predation in any damselfly, nor the neuronal circuitry driving this behaviour. Damselflies and dragonflies thus present a unique opportunity to investigate the divergent evolution of target tracking and chasing within an historically predatory lineage.

The following section describes the general organisation of the insect visual system, highlighting relevant examples where different species have evolved specialisations to facilitate target tracking. The subsequent section will then focus specifically on the known neuronal mechanisms underlying motion vision.

## 1.2 The organisation of the insect visual system

### 1.2.1 Compound eyes

Insects primarily sample the visual world through compound eyes, convex structures comprised of a hexagonal lattice of discrete optical units called ommatidia (Figure 1.3A) (Land and Nilsson, 2007). Within each ommatidium a distal corneal facet lens sits atop a crystalline cone, which together refract incoming light from a narrow region of space onto a cluster of retinular photoreceptor cells which project axons to the optic lobes (Land and Nilsson, 2007). Each photoreceptor cell captures light within an elongated photosensitive structure called the rhabdomere, which is formed from membranous microvilli containing rhodopsin visual pigments (Figure 1.3A) (Hardie and Juusola, 2015). In most species, each ommatidia contains eight photoreceptor cells (R1-R8) that express differing visual pigments and are arranged in variable configurations depending on the species (Wernet et al., 2015).

Compound eyes broadly fall into two optical types, apposition and optical superposition eyes (Land and Nilsson, 2007). In both types, each ommatidial facet samples a narrow region of visual space. However, in apposition eyes, rhabdomeres are restricted to a single facet field of view by a sheath of insulating pigment cells (Figure 1.3C-D), whilst optical superposition rhabdomeres sample light from multiple adjacent facets to enhance visual sensitivity (Figure 1.3B). Superposition eyes are common among nocturnal species, whilst apposition eyes are more common among diurnal insects, such as the odonate and dipteran subjects of this thesis (Greiner, 2006; Land and Nilsson, 2007; Warrant, 2017).

Apposition eyes assume one of two architectures according to the configuration of the rhabdom (i.e. the collective term for the rhabdomeres within the ommatidium; Figure 1.3C-D) (Agi et al., 2014; Land and Nilsson, 2007). In fused rhabdom eyes, rhabdomeres from each photoreceptor cell are in direct contact with each other forming a single photo-detecting structure functioning as a waveguide that measures the average brightness of the facet field of view (Figure 1.3C). Fused rhabdom eyes represent the ancestral form (Agi et al., 2014) and are present in many insects including dragonflies (Figure 1.3F) (Laughlin and McGinness, 1978) and damselflies (Meyer and Labhart, 1993). In neural superposition apposition eyes, rhabdomeres are fully or partially separated and thus sample separate optical axes within a single ommatidium facet field of view (Figure 1.3D) (Agi et al., 2014; Osorio, 2007). Axons from photoreceptors sampling aligned optical axes in adjacent ommatidia are pooled at the first synaptic layer, functioning to enhance visual sensitivity whilst minimising losses in visual resolution (Land and Nilsson, 2007). Neural superposition eyes are found in various species including throughout the dipteran suborder *Brachycera* (encompassing robberflies, hoverflies, killerflies (Figure 1.3G), and blowflies) (Mahato et al., 2018; Osorio, 2007; Seifert and Smola, 1990).

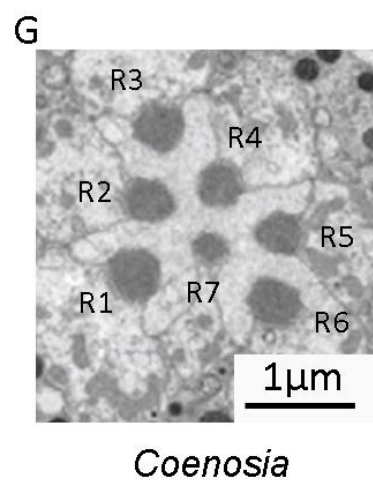
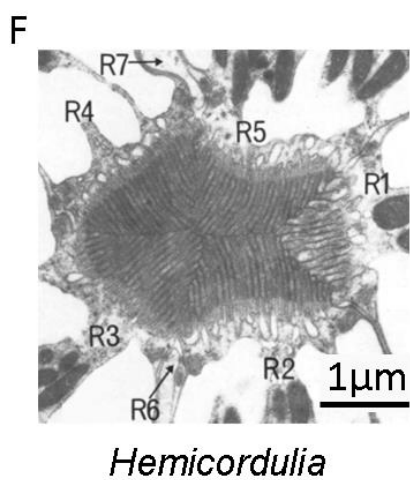
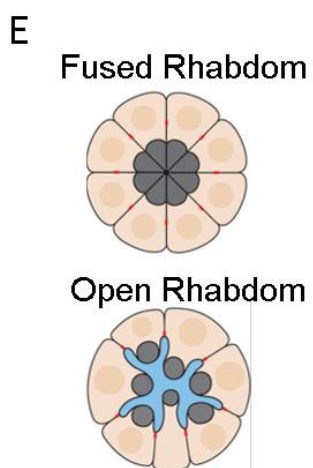
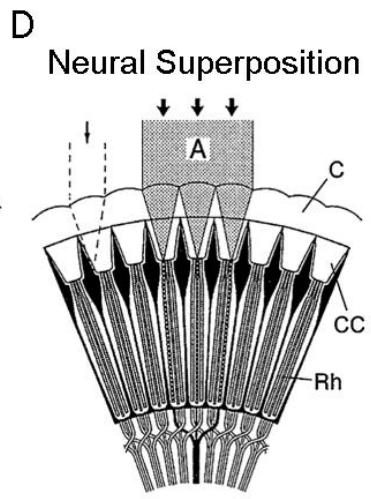
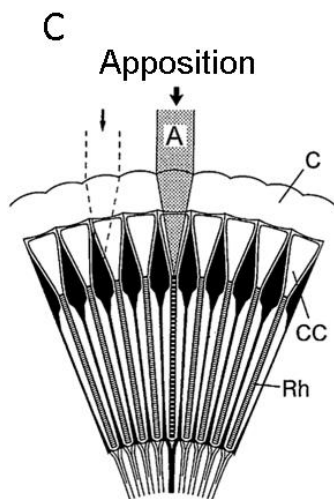
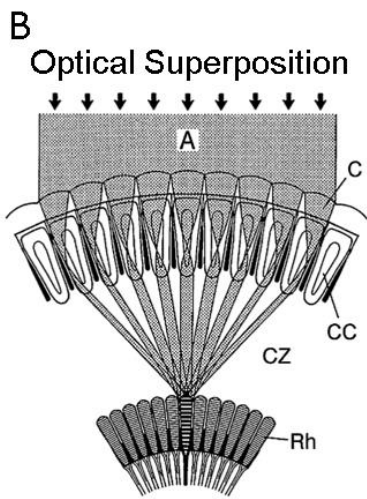
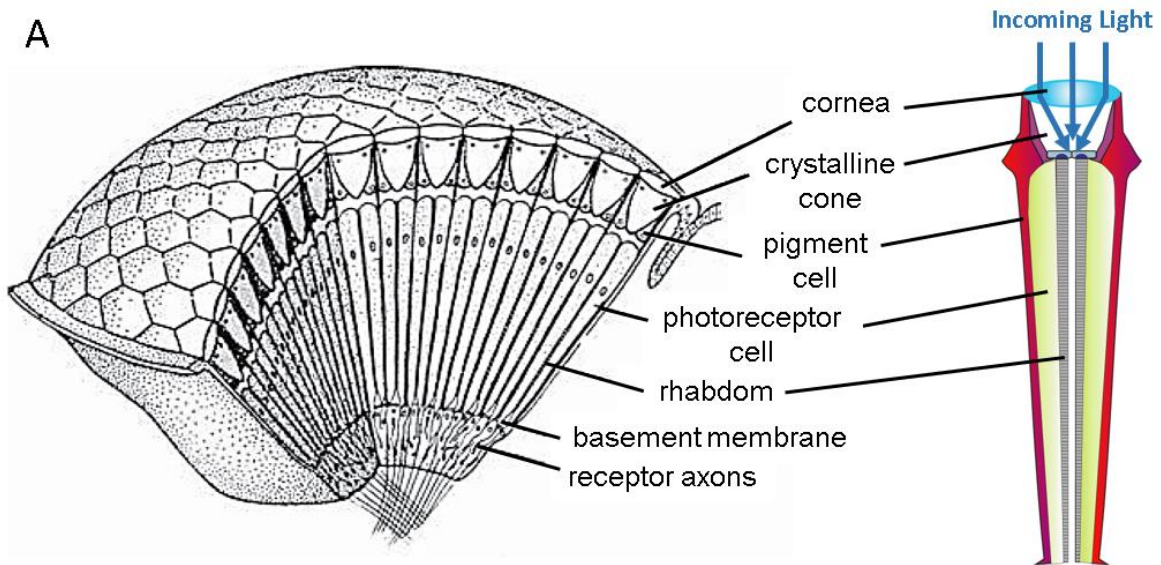


**Figure 1.3 (left) Compound eye design** (A) Illustration of a compound eye and a longitudinal cross section of a single ommatidium highlighting the main cellular elements. Incoming light is refracted by the corneal lens and crystalline cone onto the photoreceptor rhabdomeres. Adapted from (Hardie, 2012; Land and Nilsson, 2007). (B-D) Compound eyes are configured with different architectures depending on the species. (B) Optical superposition eyes focus light from multiple corneal facets onto each rhabdom, Rh, increasing the effective aperture, A, and are common amongst nocturnal insects. (C-D) Optical apposition eyes insulate each facet with screening pigments such that any given photoreceptor rhabdomere receives input from a small field of view restricted to one facet, and light from other axes are absorbed by the screening pigment (dashed lines). Apposition eyes have two architectures: (C) Apposition eyes in which the rhabdomeres from each photoreceptor cell are fused and thus sample the same visual field, and (D) Neural superposition eyes in which photoreceptor rhabdomeres remain separated and sample slightly different axes within the facet field of view. The axons of photoreceptors sampling the same visual axis in adjacent ommatidia are pooled (shaded black), increasing the effective aperture, A, leading to increased visual sensitivity. (B-D) adapted from (Greiner, 2006). (E) Cross section illustration of the rhabdomere configuration in fused and open rhabdom ommatidia, adapted from (Mahato et al., 2018). (F) The fused rhabdom of the dragonfly *Hemicordulia tau* indicating the position of each photoreceptor cell, adapted from (Laughlin and McGinness, 1978). (G) The open rhabdom of the killerfly *Coenosia attenuata*, adapted from (Gonzalez-Bellido et al., 2011). Abbreviations: A, aperture; c, corneal lens; cc, crystalline cone; cz, clear zone; Rh, rhabdom.

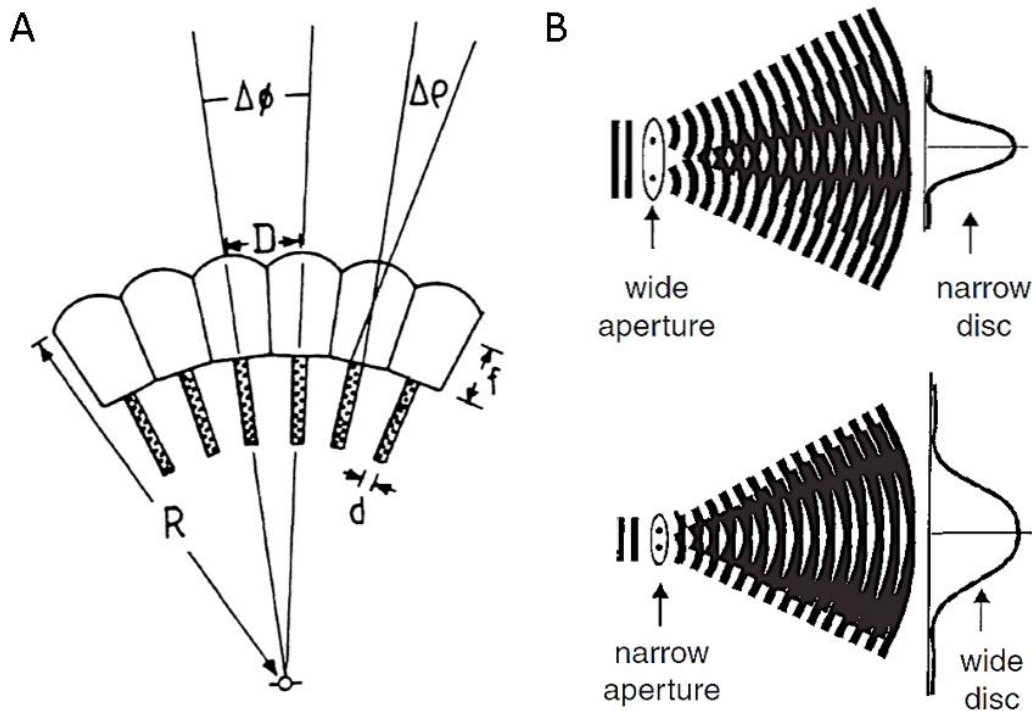


**Figure 1.4 Visual acuity in apposition eyes (A)** The angular separation between the optical axes of adjacent ommatidia, i.e. the interommatidial angle ( $\Delta\Phi$ ), limits the maximum spatial frequency that an apposition eye can sample.  $\Delta\Phi$  is determined by the arc distance between the optical axes of adjacent facets (related to facet aperture diameter,  $D$ ), and the radius of curvature of the eye,  $R$ , according to the equation  $\Delta\Phi = D/R$ . Acuity is also limited by the rhabdom acceptance angle,  $\Delta\rho$ , which relates to the diameter,  $d$ , of the rhabdom tip and the focal length,  $f$ , of the lens by  $\Delta\rho = d/f$ . Abbreviations:  $\Delta\Phi$ , interommatidial angle;  $D$ , facet lens diameter;  $R$ , local radius of curvature of the eye;  $\Delta\rho$ , rhabdom acceptance angle;  $d$ , rhabdom diameter;  $f$ , lens focal length. Adapted from (Land, 1989). **(B)** Furthermore, the maximum spatial frequency that is transmissible through the lens is limited by diffraction effects which increase as the lens aperture size decreases. A point source passing through a narrow aperture generates a wider point spread function than through a wide aperture due to the wave nature of light. This limits the extent to which facet diameters can be decreased; consequently, the radius of curvature should be increased to attain smaller interommatidial angles. Adapted from (Land and Nilsson, 2007).

The visual acuity of an apposition eye is determined by several factors including the angular separation between optical axes of adjacent ommatidia (interommatidial angles), diffraction through the facet lens, and rhabdom acceptance angles (i.e. the visual field width of an individual rhabdom) (Horridge, 1977b; Land, 1997; Land and Nilsson, 2007). Whilst interommatidial angles can be increased by either decreasing the facet diameter or increasing the radius of curvature of the eye (Figure 1.4A), as the size of the facet lens decreases the maximum spatial frequency that can be transmitted through the lens falls due to diffraction (Figure 1.4B). Consequently, high resolution is best achieved by (1) increasing facet diameter size to minimize diffraction artefacts, and (2) flattening the curvature of the eye to reduce interommatidial angles. Moreover, the rhabdom acceptance angles, determined by their diameter and the focal distance of the lens, must be kept small so as not to exceed the interommatidial angle (Figure 1.4A). Such steric constraints on rhabdom diameter necessarily constrains sensitivity, which is proportional to the photosensitive area.

Adaptations to enhance visual resolution under these optical constraints are found in many insects specialised for target tracking and are generally regionalised to a restricted portion of the visual field termed acute zones, or foveae (Land, 1997; Land and Eckert, 1985). In dragonflies, a dorsal fovea is specialised for detecting and fixating upon prey throughout chasing (Figure 1.5A) (Lin and Leonardo, 2017; Mischiati et al., 2015; Olberg et al., 2007). The dorsal fovea is characterised by enlarged facet diameters and small interommatidial angles (Figure 1.5B) which is facilitated by the flattening and fusion of the dorsal aspect of the eyes known as a holoptic configuration (Figure 1.5A) (Horridge, 1978; Labhart and Nilsson, 1995; Laughlin and McGinness, 1978). Furthermore, rhabdomeres in the dorsal fovea are elongated to enhance visual sensitivity without increasing the rhabdom diameter and acceptance angle (Labhart and Nilsson, 1995). Similar foveae have been found in robberflies (Figure 1.5C) and killerflies (Figure 1.5D) as indicated by enlarged facet diameters, reduced interommatidial angles, and small rhabdom acceptance angles (Gonzalez-Bellido et al., 2011; Wardill et al., 2017). In dipterans, regional specialisations are often sexually dimorphic, with males featuring enhanced visual acuity in the frontodorsal region with which they detect females, and is thus occasionally termed a ‘love spot’ (Land, 1997; Perry and Desplan, 2016).

Whilst interommatidial angles and rhabdomere acceptance angles are best measured histologically, a useful non-invasive method to measure how visual acuity varies across the eye derives from the pseudopupil (Horridge, 1978; Land and Nilsson, 2007). The pseudopupil is an observer-dependent anatomical feature of the compound eye, appearing as a dark spot which moves across the eye as the animal is rotated (Figure 1.5A). The pseudopupil arises because light entering ommatidia that sample along the line-of-sight axis with the observer is absorbed by photoreceptors, whilst light hitting off-axis ommatidia is reflected. The pseudopupil thus corresponds to the set of ommatidia sampling along the axis to the observer and offers a useful readout to measure relative changes in visual acuity across the compound eye.

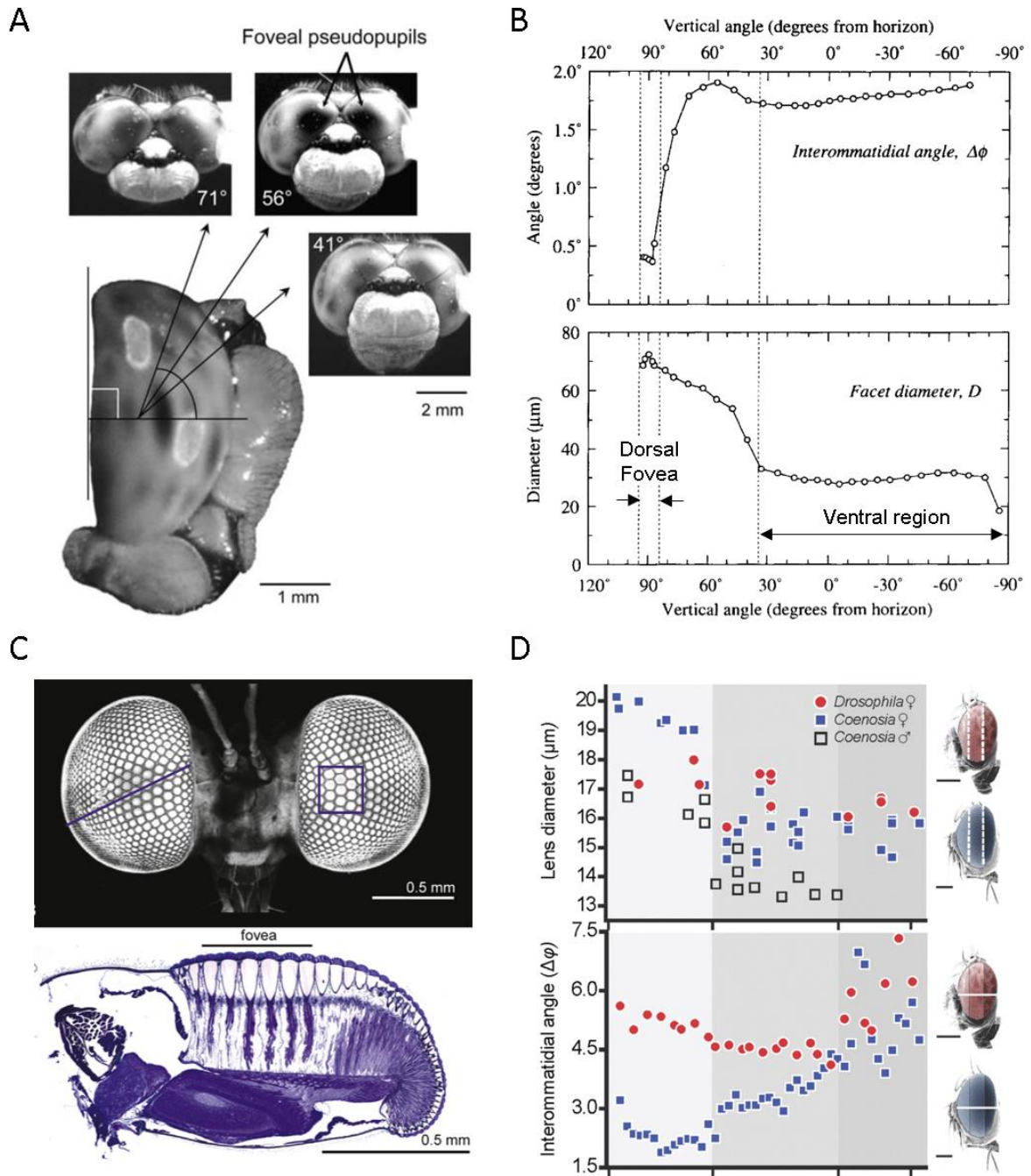


Figure 1.5 (legend right)

**Figure 1.5 (left) Compound eye specializations for target tracking** (A) Dragonflies possess an acute zone, or fovea, in the dorsal region of the visual field, as indicated by an enlarged pseudopupil at  $56^\circ$  in elevation from the horizontal axis in this female *Erythemis simplicicollis*. The pseudopupil size is proportional to the number of ommatidia sampling along the axis to the observer, thus offering a non-invasive readout of visual acuity. (B) Measurements of the interommatidial angles (top) and facet diameter (bottom) along the vertical axis of the eye of the dragonfly *Sympetrum striolatum*. Interommatidial angles decrease and facet diameters increase in the dorsal fovea region. Adapted from (Labhart and Nilsson, 1995). (C) Enlarged facet diameters (top) and flattened curvature (bottom, cross section) in the frontal visual field of the robberfly *Holcocephala fusca*. Adapted from (Wardill et al., 2017). (D) Enlarged facet diameters (top) and reduced interommatidial angles (bottom) in the female killerfly *Coenosia attenuata* (blue) relative to *Drosophila* (red).

## 1.2.2 Ocelli

In addition to visual input from the compound eyes, most flying insects possess three simple eyes called ocelli on the dorsal surface of the head (Berry et al., 2007b, 2007a). Each ocellus samples a defocused image with a wide field of view, and collectively are thought to function as horizon detectors, measuring changes in brightness resulting from self-motion (Stange et al., 2002). This crude representation has the advantage of relaying information about self-motion much faster than the compound eyes, with a latency of  $\sim 6$  ms compared with  $\sim 20$ - $30$  ms, respectively (Hardcastle and Krapp, 2016; Parsons et al., 2010). Whilst this thesis primarily considers image-forming visual input from the compound eyes, the ocelli are an important system for detecting and responding to unexpected changes in self-motion, which is crucial for any motor task (see section 1.3.2.2).

## 1.2.3 Brain organisation and nomenclature

The insect central nervous system consists of a series of segmented bilaterally symmetric neuromeres linked together by pairs of connectives (Smarandache-Wellmann et al., 2016). Each neuromere gives rise to the neurons involved in sensory processing and motor actuation of each segment. The neuronal circuits in each neuromere organise into synapse rich regions called neuropils interconnected by fibrous tracts, whilst the neuronal cell bodies are located within a surrounding outer rind. Adjacent neuromeres are fused together in various arrangements depending on the species, but broadly divide into a cephalised brain (referring to all neuromeres within the head capsule) and the ventral nerve cord (Niven et al., 2008; Smarandache-Wellmann et al., 2016; Strausfeld, 2009a). Due to the approximately  $90^\circ$  tilt of the brain axis within the head capsule, brain regions can be described both with respect to the neuraxis (n-) and the body (b-) axis (Figure 1.6A) (Ito et al., 2014); thus, n-anterior (i.e. anterior with respect to the neuraxis) corresponds to b-dorsal (i.e. dorsal with respect to the body axis).

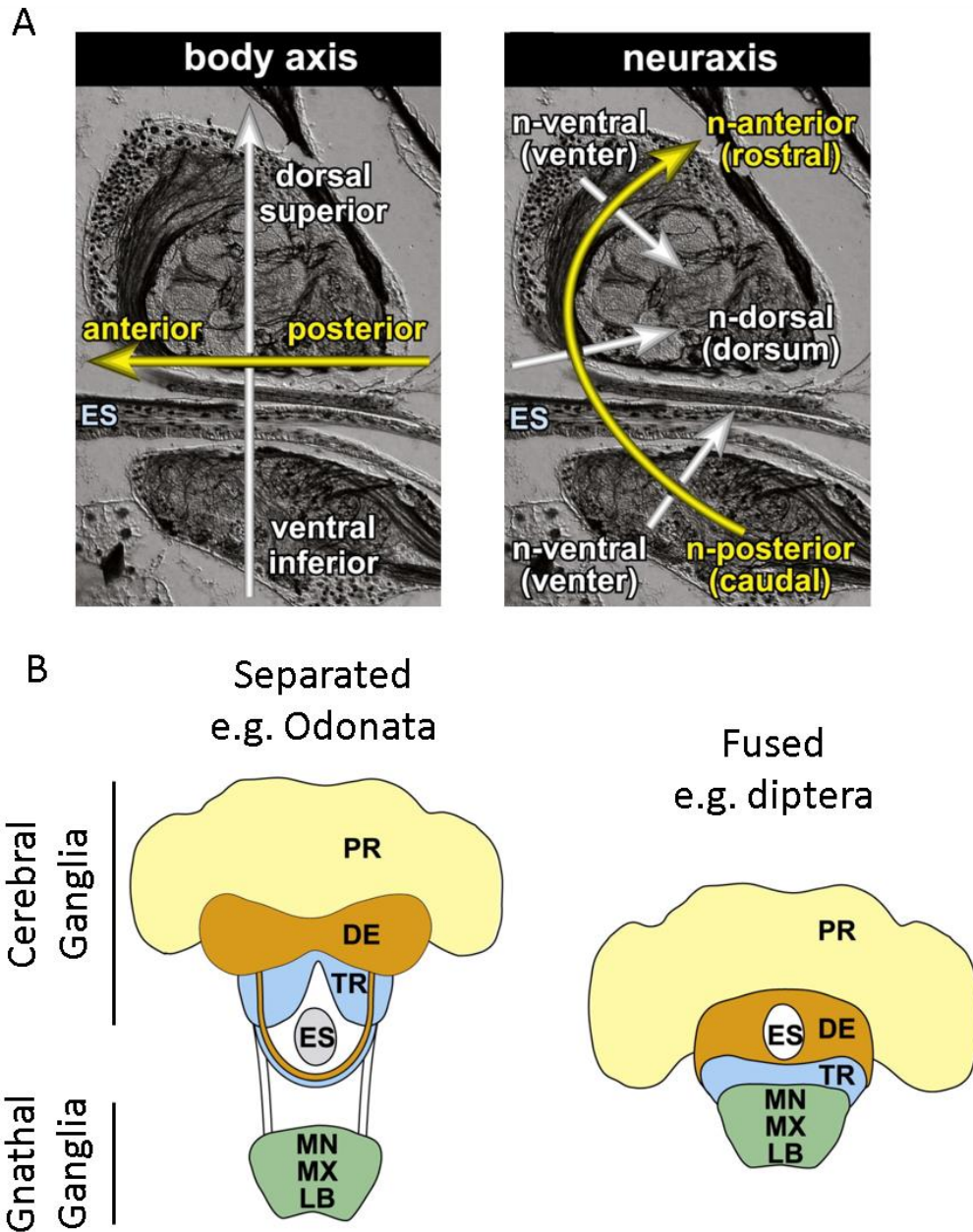


**Figure 1.6 Insect brain organization** (A) Sagittal section of a *Drosophila* brain showing how the esophagus (ES) passes through the neuraxis. Brain regions can be described with reference to the body axis (left) or the neuraxis (right). (B) The central brain derives from six neuromeres. The three most n-anterior neuromeres form the cerebral ganglia: protocerebrum (PR), deutocerebrum (DE), and tritocerebrum (TR). The gnathal ganglia are formed by the mandibular (MN), maxillary (MX), and labial (LB) neuromeres. In hemimetabolous insects (i.e. undergoing intermediate metamorphosis, e.g. Odonata) the gnathal ganglia are clearly separated from the cerebral ganglia by two circumesophageal connectives, whilst in holometabolous (i.e. undergoing full metamorphosis, e.g. Diptera) the cerebral and gnathal ganglia are fused. ES, esophagus. Adapted from (Ito et al., 2014).

The brain broadly divides into two regions, the n-anterior cerebral ganglia followed by the gnathal ganglia (Figure 1.6B) (Ito et al., 2014). The cerebral ganglia arise from a fusion of three neuromeres: the protocerebrum, deutocerebrum, and tritocerebrum, from n-anterior to n-posterior, respectively. The protocerebrum encompasses neuropils involved in visual processing and is a major site for higher level integration of sensory information with internal state (Strausfeld, 2009a). The deutocerebrum is largely involved in chemo- and mechano-sensation, and is the site at which the esophagus penetrates through the neuraxis (Boyan et al., 2003), whilst the tritocerebrum innervates the labrum (Strausfeld, 2009b). The gnathal ganglia comprise the mandibular, maxillary, and labial neuromeres, and give rise to a subset of motor neurons controlling the neck (Ito et al., 2014; Namiki et al., 2018; Strausfeld et al., 1987).

#### **1.2.4 The optic lobes**

All visual information detected by the compound eyes is initially processed in the optic lobes. These large structures derive from the protocerebrum, lie directly beneath the ommatidial lattice, and comprise anatomically distinct, layered neuropils of variable number depending on the species (Strausfeld, 2005). Each of these neuropils repeat the columnar geometry of the compound eye, with adjacent columns of interneurons arranged to process input from adjacent ommatidia (Hausen, 1984; Strausfeld, 1984). Collectively these columns are retinotopic, i.e. adjacent columns along the plane of each neuropil process information corresponding to adjacent regions of visual space, although optic chiasmata connecting neighbouring neuropils invert the relative orientation in some cases (Figure 1.6A).

In all insects, the outermost optic neuropil proximal to the ommatidial lattice is the lamina, which is connected via the external optic chiasm to the medulla. These two neuropils are the targets for photoreceptor innervation. Photoreceptors R1-6 project to the lamina, whilst R7-8 bypass the lamina projecting to the medulla (Hardie, 1985). R1-6 express broad-band opsin with peak sensitivity for green and synapse with lamina monopolar cells, which project to the medulla and contribute to the achromatic motion vision pathway (Yamaguchi et al., 2008). R7-8 express one of four opsins with narrower and variable spectral sensitivities, and contribute primarily to the chromatic visual pathway (Schnaitmann et al., 2018, 2020), although there is some cross-talk with the motion pathway (Wardill et al., 2012).

Proximal to the medulla lies the lobula complex, which differs in structure across species (Strausfeld, 2005). In many insects, including dipterans, the lobula complex comprises two distinct neuropils: the lobula and the lobula plate (Figure 1.6A), whilst in odonates there are multiple subdivisions (Figure 1.6B) (Fabian et al., 2020). The lobula complex is a major site of visual feature extraction, correlating visual information from ommatidia across the compound eye (Hausen, 1984; Keleş and Frye, 2017a; Taylor and Krapp, 2007; Wu et al., 2016a). The dipteran lobula plate is a major site for detecting wide-field optic flow (See section 1.3.2) (Borst and Haag, 2002), whilst numerous cell types in the lobula detect visual features such as edges and objects (see section 1.3.3) (Wu et al., 2016a). Furthermore, heterolateral lobula complex neurons connect the two optic lobes, enabling integration of binocular

information to facilitate self-motion estimation (Krapp et al., 2001; Wertz et al., 2008), stereopsis (Rosner et al., 2019), and higher level processes such as selective attention (Wiederman and O'Carroll, 2013). A large subset of lobula complex visual projection neurons send axons to the central brain where they relay the extracted visual feature space to control behaviour (Keleş and Frye, 2017a).

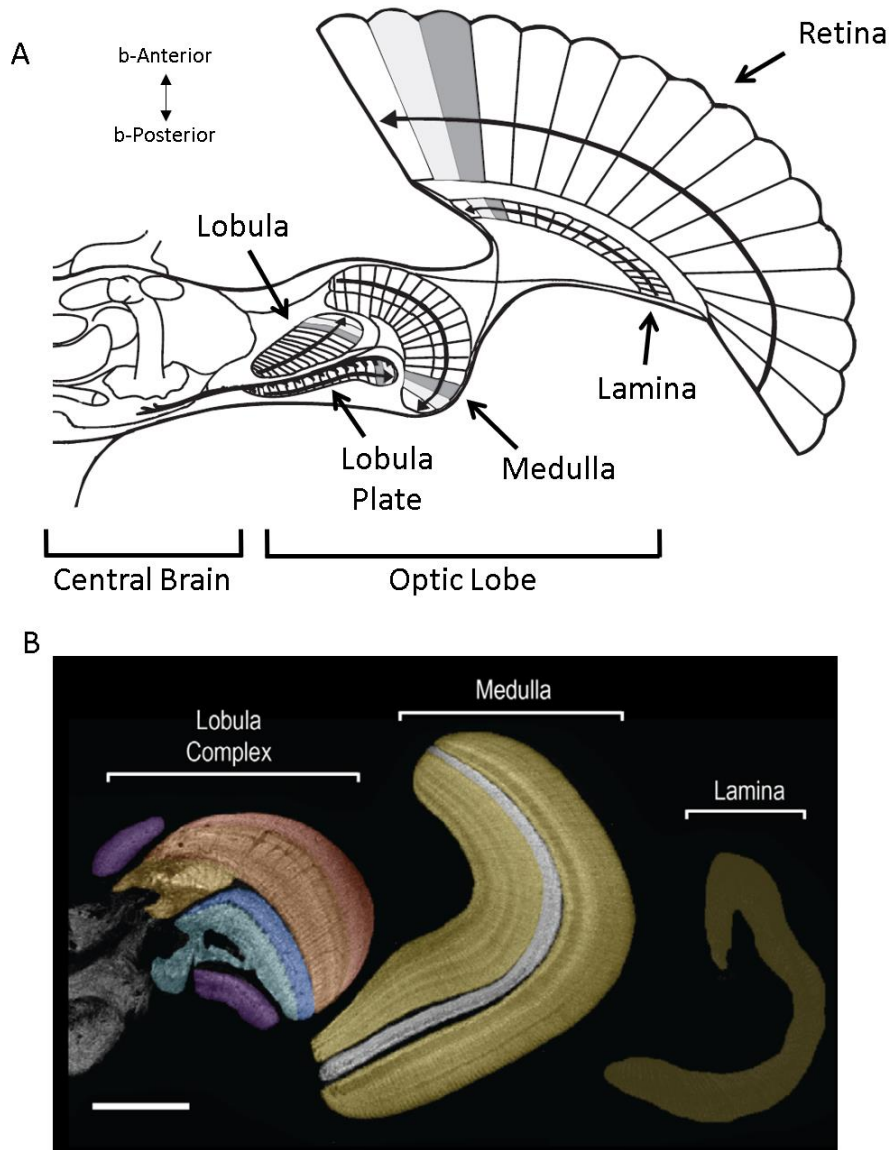


**Figure 1.7 Organization of the insect optic lobe (A)** Cross section schematic of the dipteran optic lobe indicating the main neuropils, with arrows representing the retinotopic relationships between each stage. Neurons from the lobula complex output to the central brain. Adapted from (Taylor and Krapp, 2007). **(B)** Optic lobe cross section from the dragonfly, *Hemicordulia tau*. The lobula complex is comprised of multiple distinct subunits in contrast to the bipartite organization seen in diptera. Adapted from (Fabian et al., 2020).

### 1.2.5 The central brain

Output neurons from the lobula complex project to multiple regions across the protocerebrum, predominantly the posterior slope and the lateral protocerebrum (Boergens et al., 2018; Strausfeld and Bassemir, 1985a; Wu et al., 2016a). In flies, the posterior slope is innervated by lobula plate projections, whilst a major site targeted by the lobula includes a collection of discrete glomerular neuropils in the lateral protocerebrum called optic glomeruli (Figure 1.7) (Mu et al., 2012; Strausfeld and Okamura, 2007). Each optic glomerulus receives input from one type of visual projection neuron, with different types of visual projection neuron projecting to different optic glomeruli (Wu et al., 2016a). Optic glomeruli contain local interneurons, some of which interconnect both ipsi- and contralateral optic glomeruli, suggesting further high-level visual processing (Morimoto et al., 2020; Strausfeld and Okamura, 2007). The retinotopic organisation of the lobula complex representation generally appears to be lost upon projection to optic glomeruli (Mu et al., 2012; Wu et al., 2016a). Instead, glomeruli are thought to encode salient features of the visual image, with spatial location of secondary importance (Mu et al., 2012). Nonetheless, recent evidence suggests that retinotopy may still be available to optic glomeruli interneurons through specific synaptic connections (Morimoto et al., 2020).

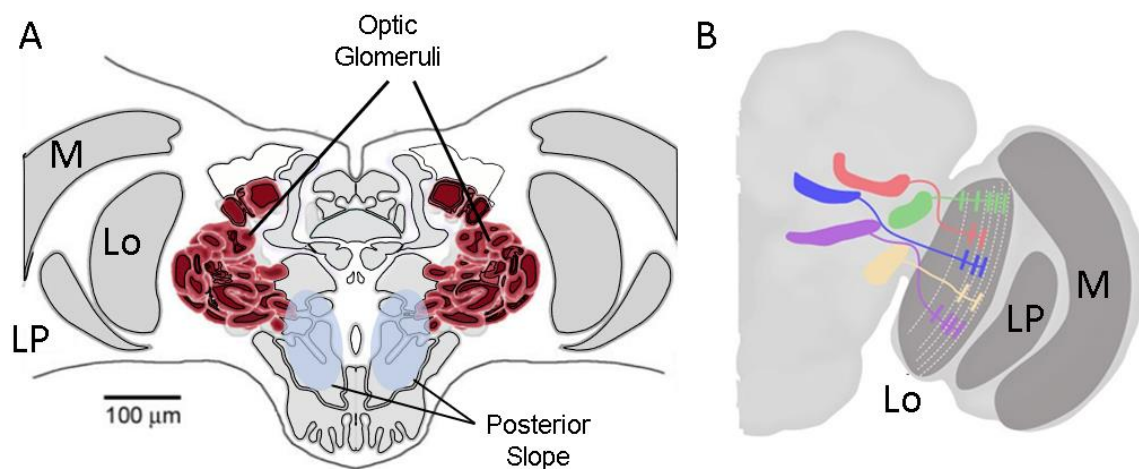


**Figure 1.8 Visual output in the central brain (A)** The primary output sites for lobula complex visual projection neurons in flies are the posterior slope (shaded blue) and the optic glomeruli (red). Adapted from (Strausfeld and Okamura, 2007). **(B)** In flies, distinct subtypes of lobula visual projection neurons innervate separate optic glomeruli. Different neuron subtypes are thought to encode qualitatively distinct visual features. Here only a single neuron of each type is shown, but multiple neurons of the same type project to each optic glomerulus. Adapted from (Keleş and Frye, 2017b). Abbreviations: M, medulla; Lo, lobula; LP, lobula plate.

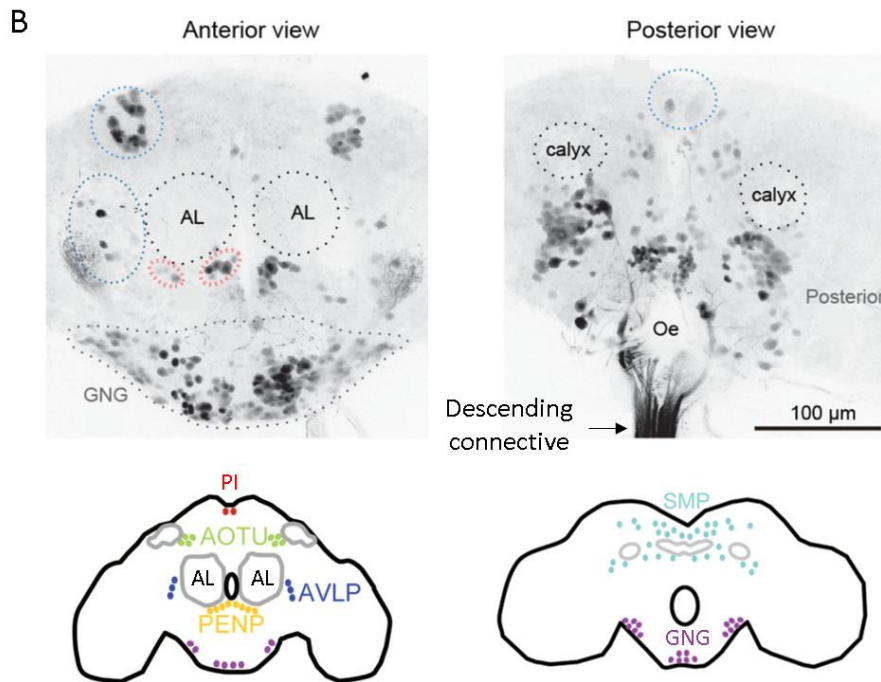
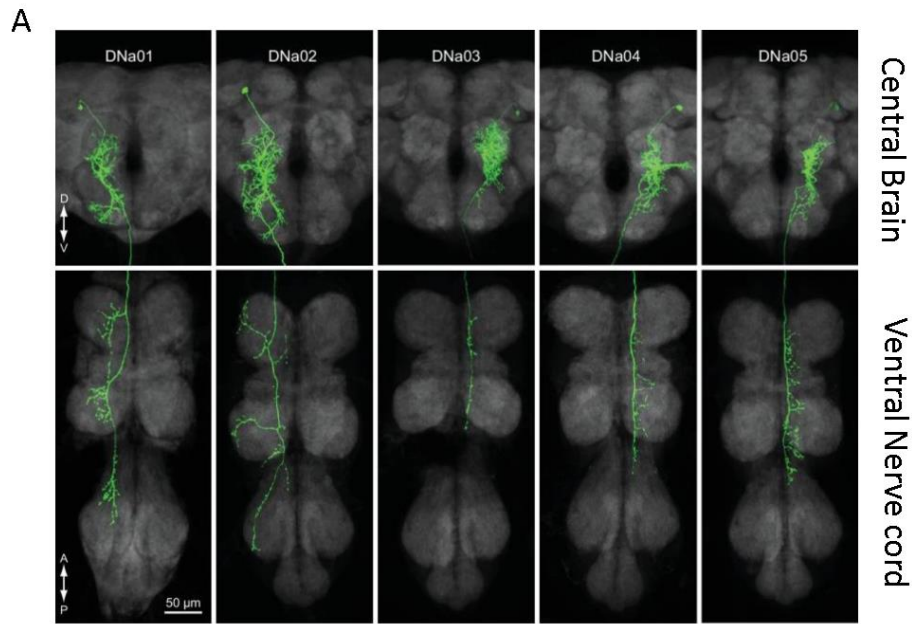


**Figure 1.9 Descending neurons** (A) A subset of fluorescently labelled descending neurons in *Drosophila* indicating their cell body location and dendritic arborization in the central brain (top panels) and projection into the ventral nerve cord (bottom panels). Different descending neurons have different dendritic and axonal projection patterns. D, b-dorsal; V, b-ventral; A, anterior; P, posterior. Adapted from (Namiki et al., 2018). (B) Ventral nerve cord dye stains showing the location of descending neuron cell bodies in *Drosophila*. b-Anterior (left) and b-posterior view (right) of the brain. Cell bodies reside in distinct locations in the outer rind. AL, antennal lobe; GNG, gnathal ganglia; Oe, oesophagus; Pi, Pars Intercerebralis; AOTU, anterior optic tubercle; AVLP, anterior ventrolateral protocerebrum; PENP, periesophageal; SMP, superior medial protocerebrum. Backfills adapted from (Namiki et al., 2018), schematic adapted from (Hsu and Bhandawat, 2016).

## **1.2.6 Descending neurons and the ventral nerve cord**

Ultimately, any visual information that influences behaviour must be relayed from the brain to motor centres in the body ganglia. This is mediated by a population of descending neurons that project axons from the central brain to motor centres in the ventral nerve cord (Figure 1.8) (Heinrich, 2002; Hsu and Bhandawat, 2016; Namiki et al., 2018; Okada et al., 2003; Staudacher, 1998; Strausfeld and Gronenberg, 1990). Descending neurons derive from the central brain cerebral and gnathal ganglia, and their cell bodies occupy distinct locations within the cell body ring (Figure 1.8B) (Hsu and Bhandawat, 2016; Namiki et al., 2018). Visually sensitive descending neurons receive their input from throughout the posterior slope and lateral protocerebrum, in proximity to the arborisations of lobula complex visual projection neurons (Gronenberg and Strausfeld, 1990; Namiki et al., 2018; Strausfeld and Bassemir, 1985a). In general, descending neurons receive input from local interneurons rather than directly from visual projection neurons (Mu et al., 2012; Strausfeld and Okamura, 2007). However, in some cases descending neurons form direct chemical and electrical synapses with visual projection neurons to decrease the latency of visuomotor transformation (Haag et al., 2007; von Reyn et al., 2017; Strausfeld and Bassemir, 1985a; Suver et al., 2016; Wertz et al., 2008).

The ventral nerve cord comprises all neuromeres posterior to the central brain. Each neuromere is clearly organised into ventral sensory and dorsal motor regions that process the respective information for each segment. The thoracic ganglia consists of the pro-, meso-, and metathoracic neuromeres, from anterior to posterior respectively, which innervate the neck (prothoracic), legs (pro/meso/metathoracic), and wings (meso/metathoracic) (Namiki et al., 2018). Visual descending neurons target dorsal neuropils with various innervation patterns throughout the thoracic ganglia (Namiki et al., 2018), where they synapse with motor neurons (Gronenberg and Strausfeld, 1991; Strausfeld and Bassemir, 1985a; Strausfeld and Seyan, 1985). Descending neurons are consequently referred to as ‘premotor’ to reflect their intermediate position in the sensorimotor pathway.

## **1.3 Neuronal mechanisms underlying motion vision**

### **1.3.1 Elementary motion detection**

Individual photoreceptors detect changes in luminance within their field of view. This one-dimensional, temporal luminance signal is unable to distinguish the direction of a moving contrast, nor even whether the luminance change results from image motion or a dimming/brightening of a static light source. Thus, in the first instance, the detection of motion requires a comparison of luminance values over time from at least two locations in visual space (Borst and Egelhaaf, 1989).

One such mechanism, known as the Hassenstein-Reichardt detector, or the Elementary Motion Detector (EMD), involves the spatiotemporal cross-correlation of luminance signals from photoreceptors sampling adjacent points in space using a delay-and-compare algorithm (Borst and Helmstaedter, 2015). In its simplest form, an EMD comprises a motion-sensitive subunit in which the luminance value output from one photoreceptor is delayed and multiplied with that obtained in an adjacent photoreceptor at a distance  $\Delta x$  (Figure 1.10). Motion along the preferred direction results in the two photoreceptor signals coinciding in time leading to a positive EMD output response (Figure 1.10, middle column), while motion along the anti-preferred direction results in negligible response (Figure 1.10, right column). A fully directionally-opponent EMD can be established by subtracting the outputs of two mirror symmetric EMDs, resulting in responses with identical time-courses but opposite amplitude sign for motion along the preferred and anti-preferred axis (Figure 1.10, bottom row) (Borst and Helmstaedter, 2015). To detect motion of luminance increments and decrements, the directionally-opponent EMD system is further elaborated to include two classes of EMD connected to ON and OFF input signals, respectively (Borst and Helmstaedter, 2015).

In insects, the delay-and-compare input arms to the EMD multiplier are thought to be implemented by columnar interneurons in the medulla (Borst and Helmstaedter, 2015). The multiplicative correlator of the EMD resides at their downstream targets, the columnar T4 cells in the proximal medulla and T5 cells in the posterior lobula (Borst and Helmstaedter, 2015) (Figure 1.11A). T4 and T5 each have four subtypes directionally selective to one of the four cardinal directions (front-to-back, back-to-front, upward, and downward) (Maisak et al., 2013). The complete circuitry underlying the EMD delay-and-correlate implementation remains tentative (Takemura et al., 2017). T4 cells represent the ON EMD (Borst and Helmstaedter, 2015), with dendrites synapsing extensively with Medulla intrinsic-1 (Mi1) and Transmedulla-3 (Tm3) neurons, which in turn receive input from ON lamina monopolar L1 cells (Takemura et al., 2013) (Figure 1.11A). Electrophysiological responses to visual white noise stimuli indicates that Mi1 is delayed  $\sim 18$  ms relative to Tm3 (Figure 1.11B) (Behnia et al., 2014), as would be expected for the two inputs to an EMD (Borst and Helmstaedter, 2015). Electron microscopy indicates that the input Mi1 and Tm3 receptive fields to T4 are spatially displaced and consistent with T4 direction selectivity (Takemura et al., 2013), however the magnitude of this offset was found to be smaller in later studies (Takemura et al., 2017). It is likely that several other medulla interneurons contribute to the input arms of the T4 EMD in addition to Mi1 and Tm3, which may explain these discrepancies (Shinomiya et al., 2019). T5 cells represent the OFF EMD pathway and receive input from Tm1-2, and Tm4, which are postsynaptic to OFF lamina monopolar L2 cells (Figure 1.11A) (Shinomiya et al., 2014). Further input arises from Tm9, which is postsynaptic to OFF lamina monopolar L3 cells (Shinomiya et al., 2014), and is temporally delayed relative to other inputs (Arenz et al., 2017). This suggests that, like T4, T5 cells receive differentially delayed medullary input, however the full circuitry is likely comprised of several additional cell types (Shinomiya et al., 2019).

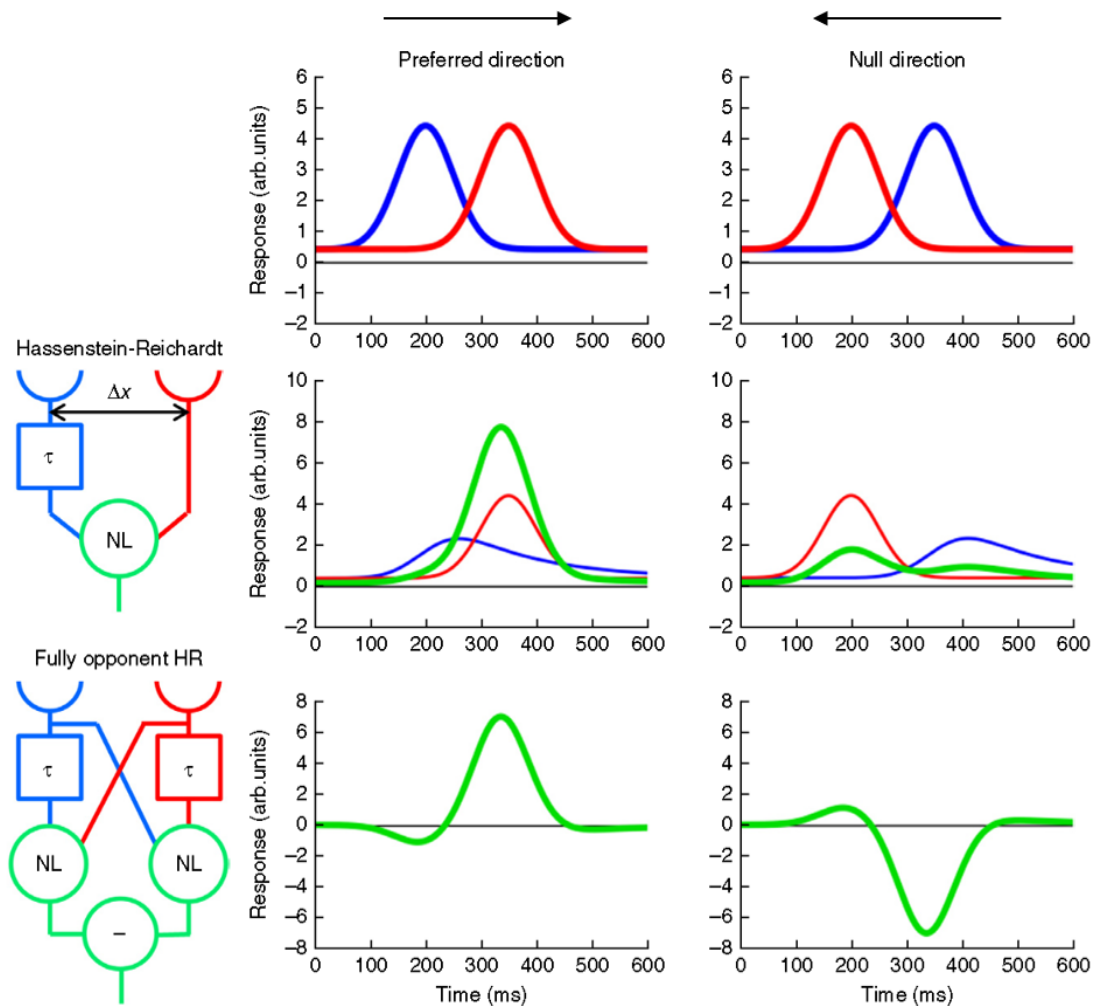


**Figure 1.10 Elementary motion detection** A simple algorithm to detect motion is to correlate luminance signals from adjacent photoreceptors. Known as the Hassenstein-Reichardt detector, this algorithm delays input from one photoreceptor (blue) with a time constant  $\tau$ , which then undergoes a multiplicative non-linearity (NL, green) with an adjacent photoreceptor (red). **(Top row)** A luminance contrast moving from left to right results in two identical signals in the blue receptor followed by the red receptor. A luminance contrast moving from right to left results in the red receptor being activated before blue. **(Middle row)** Response of a Hassenstein-Reichardt half detector. For motion in the preferred direction from left to right, the blue receptor is delayed by a constant  $\tau$ , causing it to coincide with the subsequent activation of the red receptor. Multiplication of blue and red results in an amplified resultant response (green). For motion in the anti-preferred direction, the delay of the blue receptor reduces the temporal overlap with the red receptor leading to a negligible response. **(Bottom row)** A fully opponent Hassenstein-Reichardt detector (HR) subtracts the responses of two mirror-symmetric half detectors. This results in a positive response along the preferred direction (in this case left to right) and a negative response of equal amplitude for motion along the anti-preferred direction (in this case right to left). Figure reproduced from (Borst and Helmstaedter, 2015).

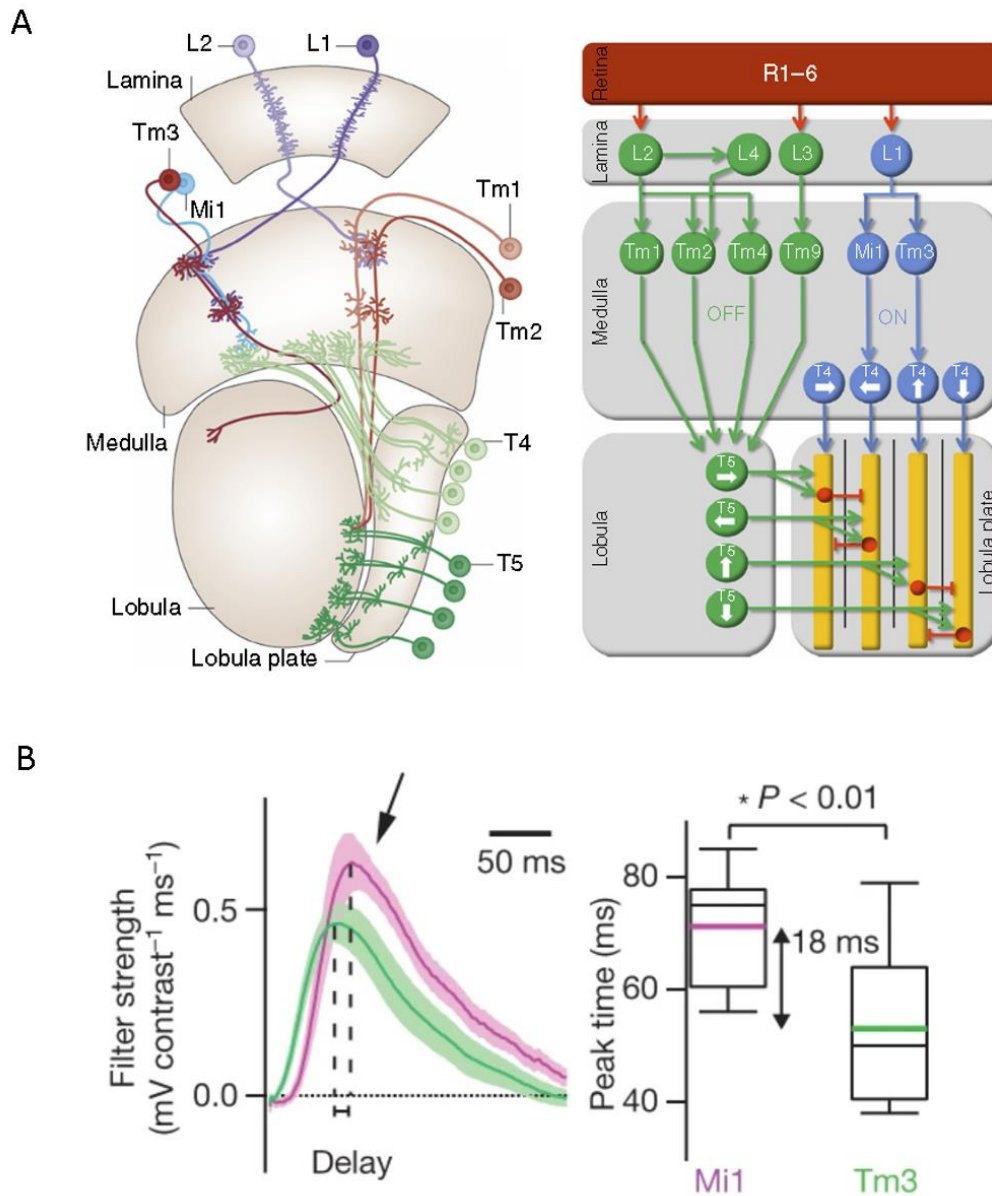


**Figure 1.11 Cellular implementation of the Hassenstein-Reichardt detector in the optic lobe of *Drosophila*** (A) In *Drosophila*, luminance changes detected by photoreceptors R1-6 are relayed by lamina monopolar neurons, splitting into an ON channel (L1) and an OFF channel (L2). Medulla interneurons Mi1 and Tm3 receive ON input from L1, and Tm1 and Tm2 receive OFF input from L2. Medulla interneurons project to T4 and T5 cells, which innervate neurons in the lobula plate. Figure reproduced from (Borst and Helmstaedter, 2015). (B) Evidence of a temporal delay between ON sensitive Mi1 and Tm3 medulla interneurons in *Drosophila*, as predicted by the Hassenstein-Reichardt model. Linear filters extracted from intracellular membrane voltage fluctuations in response to white noise stimuli suggest that the response of Mi1 is delayed ~18 ms relative to Tm3. Adapted from (Behnia et al., 2014).

The EMD, as implemented by T4 and T5 cells, encodes motion information at a local scale, sampling in a columnar arrangement across the visual field. However, detection of local motion at the level of the EMD omits information about higher-order correlated patterns of motion subtending multiple EMD units across the visual field (Krapp, 2014). To extract this information, the visual system must pool EMD outputs from across the visual field. Such integration can broadly be categorised into two perceptual systems: a wide-field system for the estimation and stabilisation of self-motion, and an object-detecting system guiding goal directed behaviours such as chasing. Each system is likely to be crucial for a target chasing system, as a moving pursuer must be able to distinguish independent movement of the target's heading versus motion of the target on the retina resulting from self-motion (see section 1.4). Furthermore, several computational concepts have been extensively studied within the widefield motion processing system which may have parallels within target tracking systems. The following sections describe the known circuitry underlying these two systems in insects.

### **1.3.2 Wide-field motion processing**

In an otherwise stationary environment, self-motion results in panoramic shifts of the visual scene across the retina, known as wide-field optic flow. The instantaneous pattern of optic flow is determined by the combination of translational and rotational components of self-motion; consequently, optic flow patterns can be decoded to estimate self-motion (Taylor and Krapp, 2007). This measurement can then be compared with expected levels of self-motion, and any difference used as input for reflexes stabilising posture and steady-state locomotion in response to unexpected external perturbations (Krapp and Wicklein, 2008). Whilst stabilisation reflexes also receive mechanosensory input, which has shorter transduction latencies relative to visual processing (Hardcastle and Krapp, 2016; Hengstenberg, 1993), only visual information can ultimately confirm whether stabilisation has been successfully implemented (Taylor and Krapp, 2007). Consequently, visually guided stabilisation reflexes, also known as optomotor responses, form an indispensable component for feedback control across much of the animal kingdom (Taylor and Krapp, 2007).

#### **1.3.2.1 Lobula Plate Tangential Cells (LPTCs)**

In insects, wide-field motion is detected within specialised subregions of the lobula complex by interneurons with large dendritic fields spanning across multiple retinal columns (Hausen, 1984). These tangential cells integrate local motion information from subsets of upstream T4 and T5 cells, resulting in receptive fields selective for specific patterns of optic flow across large regions of visual space (Figure 1.12) (Borst et al., 2010). Response selectivity is further fine-tuned by interconnectivity among tangential cell types (Haag and Borst, 2001, 2004, 2008; Wang et al., 2017). A fundamental feature of the representation used by tangential cells to encode widefield motion is the tuning of receptive fields to specific optic flow patterns, known as 'matched filtering' (although this is more accurately described

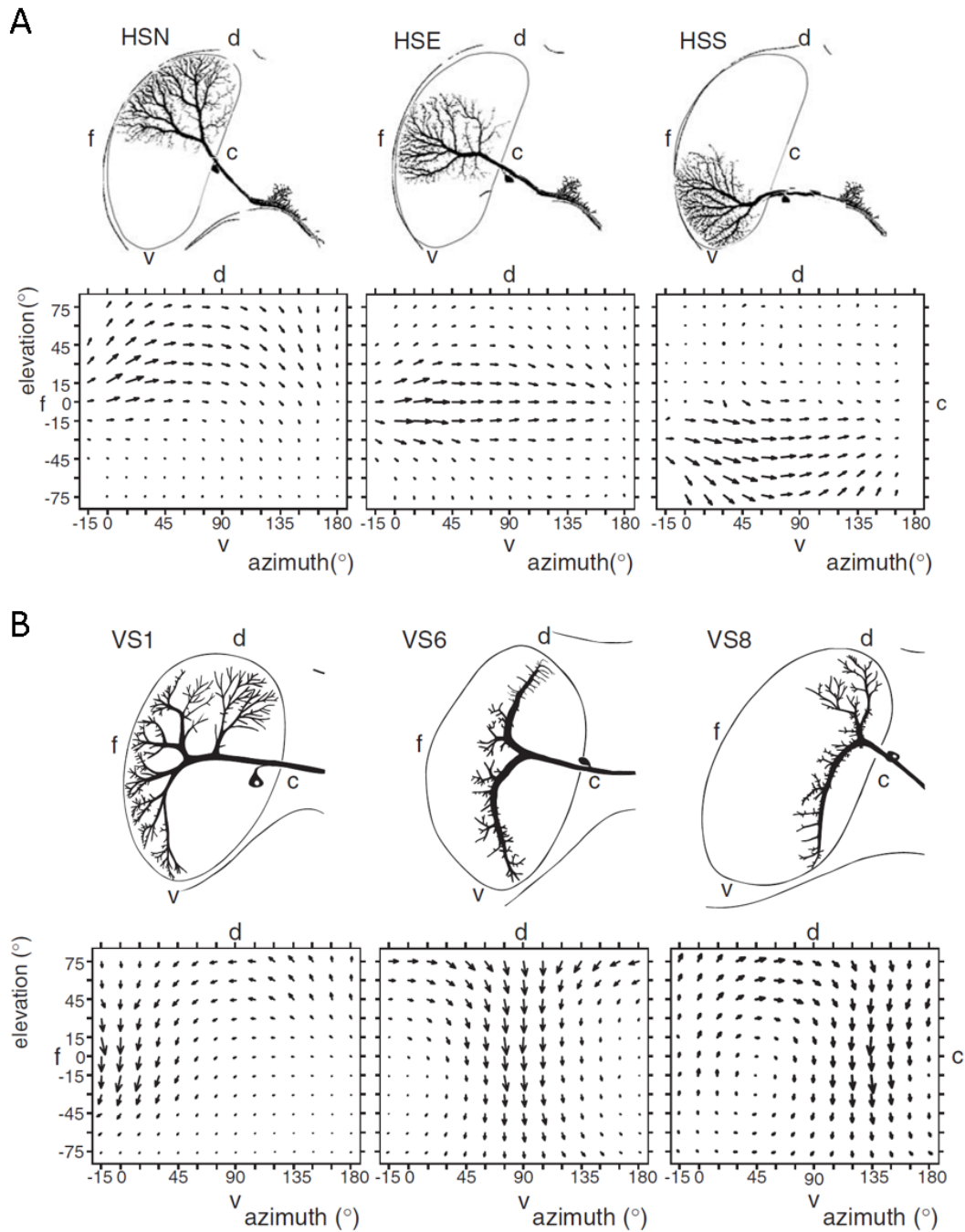


**Figure 1.12 Lobula Plate Tangential Cells** (A) Three horizontal system (HS) cells, shown here from *Calliphora*, have broad dendritic arborizations across displaced but overlapping regions in the lobula plate (top row). These cells respond to roughly horizontal motion across large portions of the visual field (bottom row). Each receptive field plot shows the local directional preference of movement across the visual field for each neuron. The visual field is represented by elevation and azimuth with (0,0) being frontal. Arrow directions indicate the directional preference and arrow length represents the relative sensitivity to local motion at each point in the visual field. (B) In contrast, vertical system cells are tuned to wide-field motion patterns with axes of rotation arranged at sequential positions in the visual field. Shown here are VS1, VS6, and VS8 from *Calliphora*. Receptive field plots as in (A). Abbreviations: c, caudal; d, dorsal; f, frontal; v, ventral. Adapted from (Taylor and Krapp, 2007).

as a ‘tuned filter’, for historical reasons the term ‘matched filter’ is used in biological literature) (Franz and Krapp, 2000; Taylor and Krapp, 2007).

In dipterans, the lobula plate is a major centre for widefield motion processing by tangential cells (Borst and Haag, 2002; Hausen, 1984). Among these lobula plate tangential cells (LPTCs), the most prominent are cells of the horizontal and vertical system (Borst and Haag, 2002; Taylor and Krapp, 2007). The horizontal system (HS) is comprised of three HS cells that preferentially respond to anterior-to-posterior horizontal motion with displaced but slightly overlapping receptive fields, from dorsal to ventral respectively: HS-North (HSN), HS-Equatorial (HSE), and HS-South (HSS) (Figure 1.12A) (Hausen, 1982a, 1982b). In addition to input from T4 and T5 cells (Borst and Helmstaedter, 2015), HS cells also receive input from heterolateral tangential cells which project from the contralateral lobula plate to enhance the rotational component of the HS cell response (Haag and Borst, 2001; Horstmann et al., 2000; Krapp et al., 2001).

The vertical system (VS) is comprised of a variable number of VS cells depending on species (Buschbeck and Strausfeld, 1997). In *Calliphora*, 10 VS cells respond maximally to rotational optic flow fields with axes of rotation positioned approximately along the eye equator in adjacent regions of the visual field from frontal to caudal for VS1-VS10 respectively (Figure 1.12B) (Hengstenberg et al., 1982; Krapp and Hengstenberg, 1996). VS cells receive input from T4 and T5 (Borst and Helmstaedter, 2015); however, their receptive fields are broadened by electrical coupling between adjacent VS cells, and selectivity for rotatory motion is enhanced by input from HSN (Haag and Borst, 2004). In *Drosophila*, only 6-9 VS cells have been detected (Boergens et al., 2018; Rajashekhar and Shamprasad, 2004); horseflies (*Tabanidae*) were found to have up to 25 VS cells (Buschbeck and Strausfeld, 1997), while in robberflies (*Asilidae*) none could be identified (Buschbeck and Strausfeld, 1997). This raises the interesting possibility that the axes of rotation encoded by the population of VS cells may be tuned to account for variations in body plan and/or flight dynamics, although this awaits verification (Taylor and Krapp, 2007).

Together, HS and VS cells function as matched filters for specific optic flow patterns rotating around different axes, with HS cells responding to rotation in yaw, and the VS responding to combinations of roll and pitch (Taylor and Krapp, 2007). HS and VS cells project axons to the ventrolateral protocerebrum where they provide input to descending neurons (Gronenberg and Strausfeld, 1990; Suver et al., 2016). After laser or genetic ablation of HS and VS cells, flies remain able to walk and fly but optomotor reflexes are severely attenuated, outlining the importance of these neurons in the stabilisation control system (Geiger and Nässel, 1981; Heisenberg et al., 1978).

Wide-field sensitive tangential cells have also been anatomically and physiologically described in the lobula plate of moths (Wicklein and Varjú, 1999), and butterflies (Ichikawa, 1994), and the sublobula of bees (DeVoe et al., 1982; Ibbotson, 1991a), locusts (Rind, 1990), and dragonflies (Evans et al., 2019).

In each case, these neurons respond to wide-field motion along specific directions, and project to the ventrolateral midbrain, where they are thought to connect with descending neurons, as do dipteran LPTCs (Rind, 1990). Interestingly, tangential cells in species that often hover in-flight are tuned to detect slower image velocities as would be experienced whilst hovering, suggesting that the neuronal representation of wide-field motion is fine-tuned to match visual ecology (Evans et al., 2019; O’Carroll et al., 1996, 1997).

### 1.3.2.2 Wide-field sensitive descending neurons

Descending neurons responsive to wide-field optic flow have been described in several insect lineages including dragonflies (Olberg, 1981a, 1981b), locusts (Griss and Rowell, 1986; Kien, 1974; Rowell and Reichert, 1986), mantids (Yamawaki and Toh, 2009), butterflies (Singarajah, 1988), moths (Kern, 1998; Olberg and Willis, 1990), honeybees (Goodman et al., 1987; Ibbotson, 1991b, 1991a; Ibbotson and Goodman, 1990; Ibbotson et al., 2017), and dipteran flies (Gronenberg and Strausfeld, 1990; Gronenberg et al., 1995; Haag et al., 2007; Nicholas et al., 2020; Strausfeld and Gronenberg, 1990; Suver et al., 2016; Wertz et al., 2008, 2009b, 2009a). In each case, these descending neurons project from the protocerebrum to the thoracic ganglia and respond selectively to a preferred direction of widefield motion subtending large regions of the visual field.

In dipterans, a population of descending neurons receive input from widefield motion sensitive ocelli interneurons and/or LPTCs (Gronenberg and Strausfeld, 1990; Strausfeld and Bassemir, 1985a; Suver et al., 2016). One class comprising four descending neurons of the ocellar and vertical system (DNOVS1-4; also called DNDC 1-1 to 1-4 in (Gronenberg and Strausfeld, 1990)), receive input from VS cells and ocelli interneurons (Figure 1.13) (Gronenberg and Strausfeld, 1990; Strausfeld and Bassemir, 1985a). In *Calliphora*, DNOVS1-2 have been characterized in detail (Haag et al., 2007; Wertz et al., 2008, 2009b, 2009a). Both neurons receive input from different subsets of VS cells via electrical synapses, with DNOVS1 maximally coupled to VS6-7 (Figure 1.13B) (Haag et al., 2007), and DNOVS2 maximally coupled to VS5-6 (Figure 1.13C) (Wertz et al., 2008). DNOVS1-2 respond maximally to image motion corresponding to rotation of the fly approximately  $\pm 30^\circ$  along the azimuth from the roll axis, respectively (Figure 1.13D-F) (Haag et al., 2007; Wertz et al., 2009a). Sensitivity to rotation is thought to be enhanced by ocellar input (Haag et al., 2007; Wertz et al., 2008), and, in the case of DNOVS2, contralateral input from the heterolateral tangential cell V1 tunes DNOVS2 to rotation by providing sensitivity to upwards motion in the contralateral visual field (Wertz et al., 2008). Putative homologs of DNOVS1-2 have also been identified in *Drosophila*, and respond to rotation around axes roughly equivalent to those encoded in *Calliphora* (Suver et al., 2016), despite the variation in the number of input VS cells between the two species (Boergens et al., 2018).

Another class of wide-field motion sensitive descending neurons receive input from the horizontal system (DNHS) (Strausfeld and Bassemir, 1985b; Suver et al., 2016). In *Drosophila*, DNHS1 forms

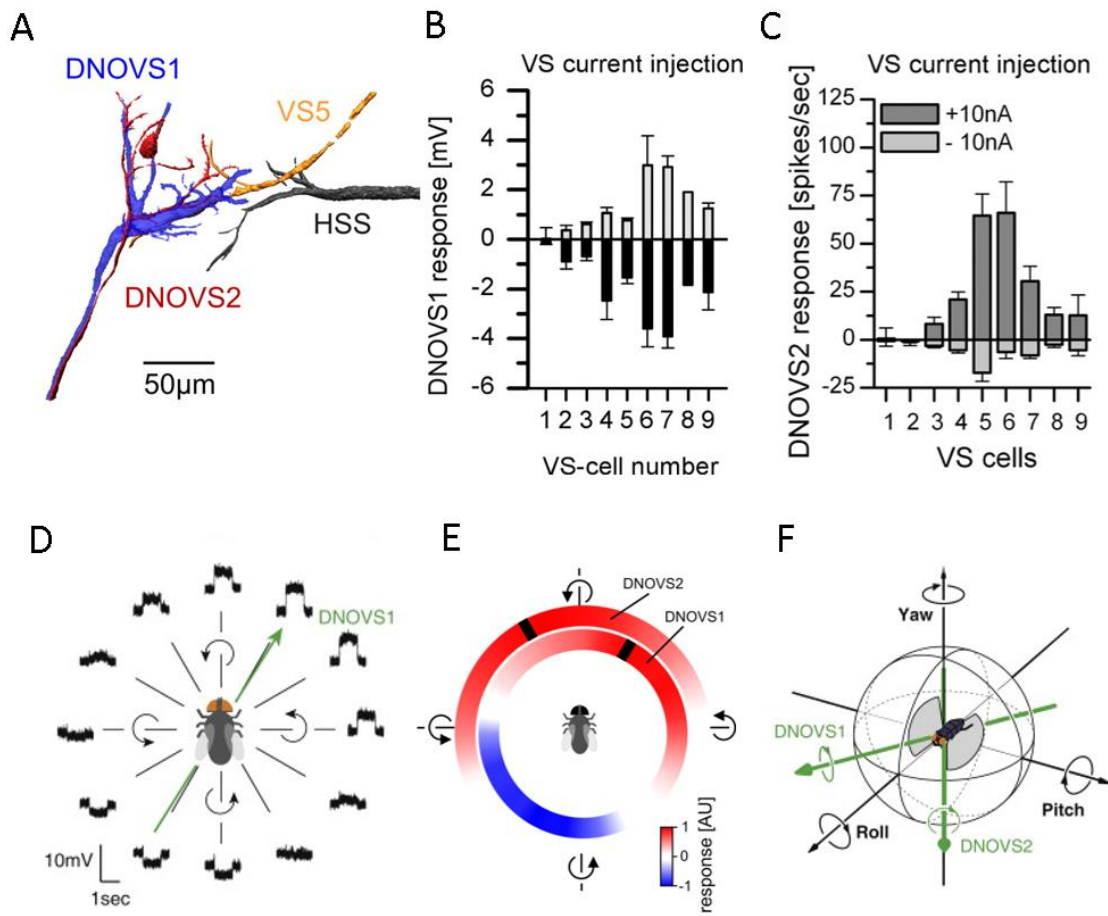


**Figure 1.13 DNOVS descending neurons in *Calliphora*** (A) Intracellular dye fills reveal the proximity of DNOVS1 and DNOVS2 dendrites to the output arborization of VS cell (shown here VS5). Whilst HS neurons terminate in a similar region, their terminals do not contact DNOVS dendrites (shown here HSS). (B) Injection of positive (white bars) and negative current (black bars) into different VS cells result in depolarization and hyperpolarization of DNOVS1, respectively. This indicates electrical continuity between DNOVS1 and VS cells, with the greatest coupling to VS6 and VS7. Adapted from (Haag et al., 2007). (C) As with DNOVS1, positive and negative current injection into VS cells results in an increase and decrease of membrane potential in DNOVS2, respectively. DNOVS2 is maximally coupled to VS5 and VS6. Adapted from (Wertz et al., 2008). (D) Traces show DNOVS1 membrane potential in response to image rotation along indicated axes. DNOVS1 is maximally depolarized by counter clockwise rotation along an axis positioned  $\sim 30^\circ$  in azimuth from the body axis. (E) DNOVS1 and DNOVS2 respond to rotation axes offset  $\pm 30^\circ$  along the azimuth from the roll axis. Red indicates membrane depolarization, and action potential firing rates for DNOVS1 and DNOVS2, respectively. Black bars indicate maximum responses. Blue indicates membrane hyperpolarization for DNOVS1. (D-E) adapted from (Wertz et al., 2009a). (F) Schematic illustrating the offset of rotation axis preference by DNOVS1-2. Adapted from (Krapp, 2010).

electrical synapses with HSN and HSE, and responds to pure roll rotation (Suver et al., 2016). Together, DNOVS1-2 and DNHS1 encode rotation along three roughly orthogonal axes, suggesting a progressive dimensionality reduction between visual motion representations in the lobula and premotor descending neurons (Suver et al., 2016). Furthermore, under identical visual stimulation conditions, the response of DNOVS1 is less variable compared with VS cells, suggesting refinement in the precision of the neuronal representation of motion at sequential stages of the visuomotor pathway (Wertz et al., 2009a). Ultimately, DNOVS and DNHS cells terminate onto motor neurons in the thoracic ganglia controlling the neck and wings (Strausfeld and Bassemir, 1985a).

### **1.3.3 Target motion processing**

#### **1.3.3.1 Target selective lobula complex neurons**

Akin to wide-field motion processing, the lobula complex is a major site for encoding the motion of objects by pooling and correlating local motion information from EMDs. In the lobula, a large and diverse population of visual projection neurons respond to various visual features, such as moving edges or bars, or small moving targets (Wu et al., 2016b). Many of these neurons are arranged in a columnar array with individual dendritic fields spanning only a few columns of retinotopic space in the lobula, whilst other tangential neurons have wider dendritic fields and respond across a larger region of visual space (Figure 1.14A) (Strausfeld, 1991). Together these neurons are thought to decompose retinal images into a set of primitive features which is then projected to the central brain (Keleş and Frye, 2017b). Historically, lobula complex neurons responsive to moving targets have primarily been described in species specialised for chasing, including flesh flies (Gilbert and Strausfeld, 1991, 1992; Gronenberg and Strausfeld, 1991; Strausfeld and Gilbert, 1992), dragonflies (Bolzon et al., 2009; Geurten et al., 2007a; Lancer et al., 2019; Nordström et al., 2011; O'Carroll, 1993; Wiederman and O'Carroll, 2011, 2013), and hoverflies (Barnett et al., 2007; Nordström and O'Carroll, 2006; Nordström et al., 2006).

In male *Sarcophaga* flesh flies, a system of male-specific lobula giant (MLG) visual projection neurons respond to moving targets within the frontodorsal acute zone of the visual field (Figure 1.14B-E) (Gilbert and Strausfeld, 1991; Gronenberg and Strausfeld, 1991; Strausfeld, 1991). MLG neurons project to either the ipsi- or contra-lateral central brain, where they provide input to descending neurons (Figure 1.14B). MLGs are not present in female flies, suggesting a role in the sex-specific chasing behaviours of males (Strausfeld, 1991). Whilst MLGs have been described anatomically (Gilbert and Strausfeld, 1991; Gronenberg and Strausfeld, 1991; Strausfeld, 1991; Strausfeld and Gilbert, 1992), only limited information is available about their physiological response properties. MLGs were initially tested with moving gratings, to which MLGs appeared to phase-lock with the moving bars (Gilbert and Strausfeld, 1991, 1992). Subsequent experiments suggested a preference for targets across the visual

acute zone (Figure 1.14C) (Gronenberg and Strausfeld, 1991); however, their receptive field shape and preferred stimulus parameters remain unknown.

In hoverflies, a population of small target motion detector (STMD) neurons are arranged throughout the lobula that respond selectively to small moving targets (Barnett et al., 2007; Nordström and O'Carroll, 2006; Nordström et al., 2006). Columnar STMDs have restricted dendritic fields and are arranged in a retinotopic fashion throughout the lobula, but appear to over-sample the frontodorsal visual field corresponding to the specialised region of high acuity in males (Barnett et al., 2007; Nordström et al., 2006). Columnar STMDs include both directionally selective and nondirectional neurons, both of which project to central brain regions likely corresponding to the lateral protocerebrum and posterior slope (Figure 1.15B) (Barnett et al., 2007; Nordström and O'Carroll, 2006; Nordström et al., 2006). Interestingly, different STMDs respond differently to the presence of a moving background. Some STMDs respond to moving targets irrespective of background motion, even when there is no relative motion between the target and background (Figure 1.16A) (Barnett et al., 2007; Nordström et al., 2006). In other STMD types, responses are attenuated when the background moves in the same direction as the target (Figure 1.16B) (Barnett et al., 2007).

In dragonflies, in addition to lobula neurons with responses comparable to hoverfly STMDs (Geurten et al., 2007a), a specialised centrifugal STMD (CSTMD1) responds to small targets moving across a large portion of the visual field (Dunbier et al., 2012; Geurten et al., 2007a; Wiederman and O'Carroll, 2013). CSTMD1 dendrites reside in the ventrolateral protocerebrum ipsilateral to the cell body, with an axon projecting to the contralateral hemisphere where it arborizes in both the adjacent ventrolateral protocerebrum and throughout the lobula (Figure 1.17A) (Geurten et al., 2007a; Wiederman and O'Carroll, 2013). CSTMD1 responses are excited and inhibited by target movement within the ipsilateral and contralateral visual field, respectively, forming a pronounced midline boundary in the receptive field (Figure 1.17B) (Geurten et al., 2007a; Wiederman and O'Carroll, 2013). Each bilateral CSTMD1 pair is thought to feed forward to inhibit its contralateral partner in a winner-takes-all mechanism, forming the basis for the selective attention to a single target amongst distractors (Wiederman and O'Carroll, 2013).

It is currently unclear to what extent *Sarcophaga* MLGs and STMDs represent a specialised target tracking system in species implementing chasing behaviours. More recently, split-GAL4 genetic intersection techniques in *Drosophila* have isolated a class of over 20 types of lobular columnar visual projection neuron, a subset of which respond selectively to moving targets and/or bars (Figure 1.18A) (Keleş et al., 2020; Staedele et al., 2020; Wu et al., 2016b). In contrast to hoverfly and dragonfly STMDs, moving object responses in *Drosophila* lobula columnar neurons were abolished upon simultaneous background motion (Figure 1.18B-C) (Keleş et al., 2020; Staedele et al., 2020). However, when tested in the presence of an octopamine agonist, a subset of neurons regained responses to moving

objects in the presence of a moving background, whilst others remain unresponsive (Figure 1.18BC) (Staedele et al., 2020). Octopamine is an insect analogue to norepinephrine, and is known to increase the gain and shift the temporal frequency tuning of visual processing neurons as is found during flight (Suver et al., 2012). This differential repression by background motion under octopamine agonism in *Drosophila* is reminiscent of the differential background antagonism found in hoverfly STMDs (Barnett et al., 2007; Nordström et al., 2006). It remains unknown whether hoverfly STMD responses vary under octopamine or free flight conditions.

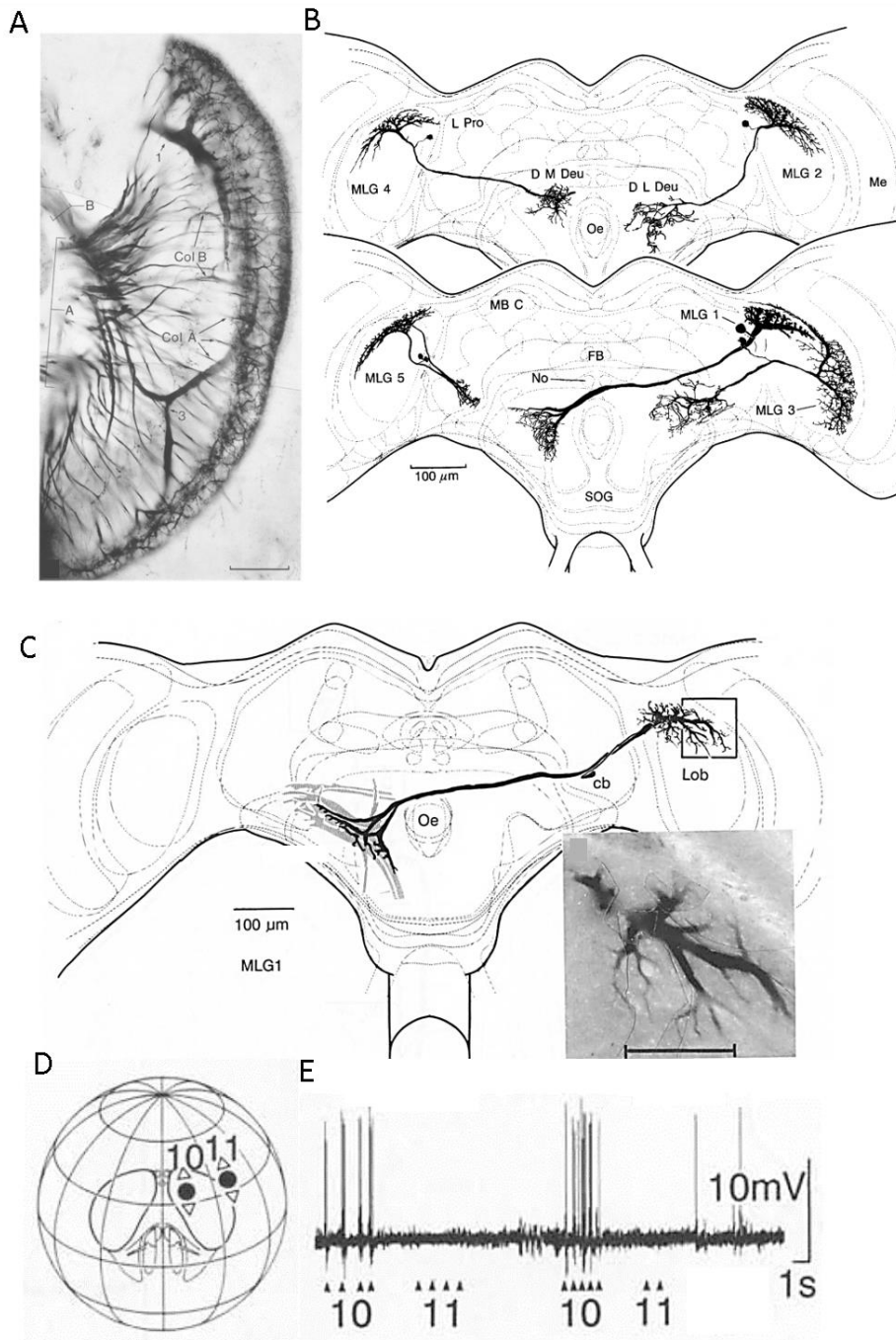
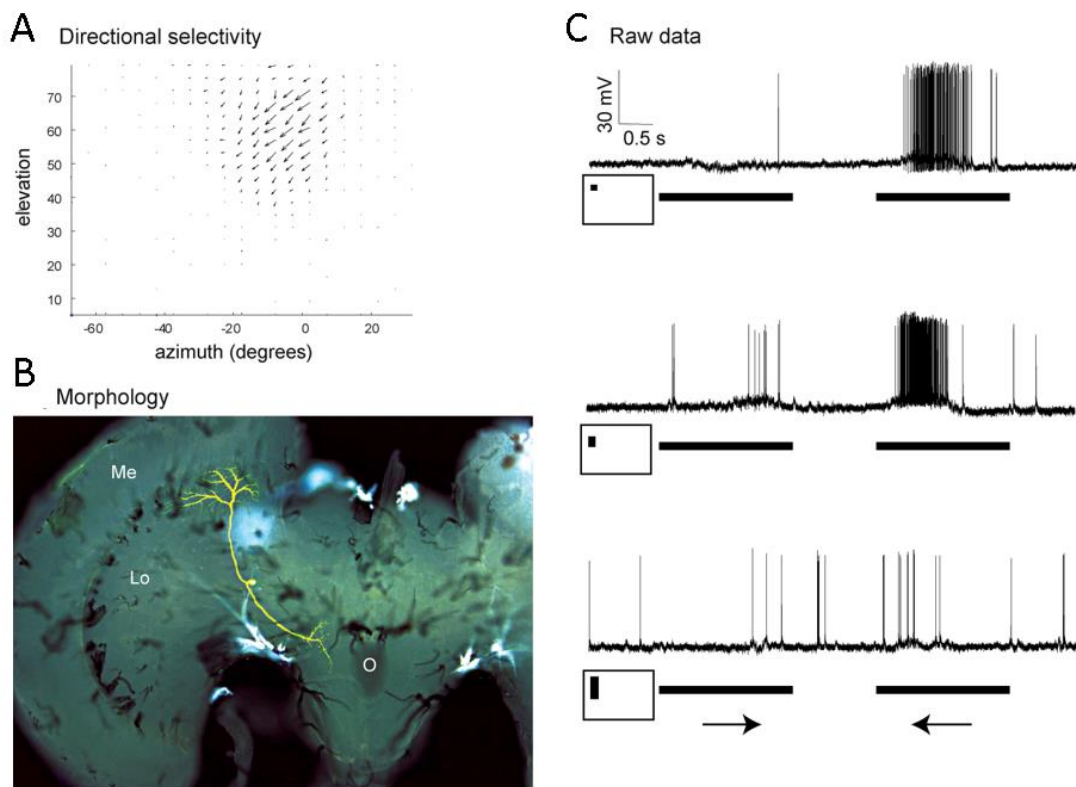
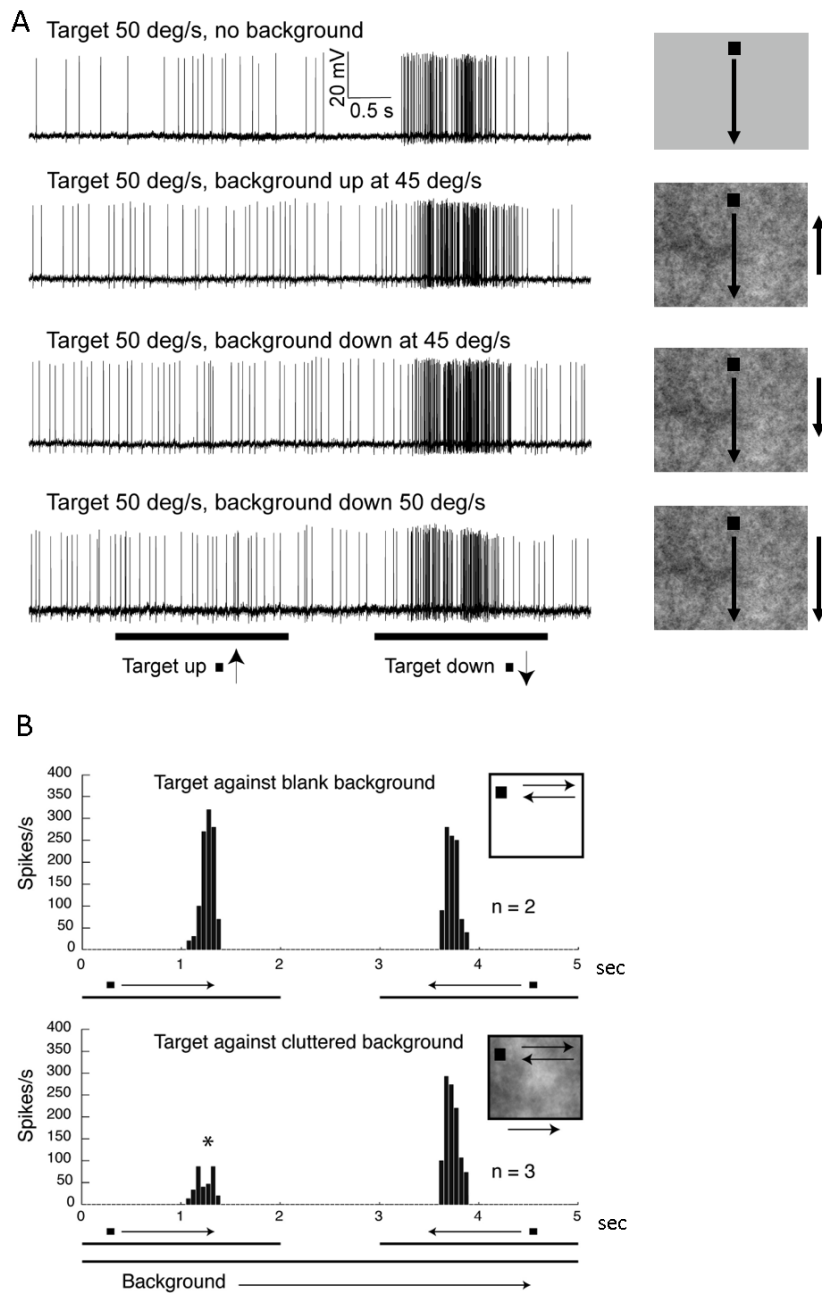


Figure 1.14 (legend right)

**Figure 1.14 (left) Target sensitive MLG neurons in *Sarcophaga*** (A) Arrangement of tangential and columnar neurons in the dipteran lobula. Columnar neurons (Col A and Col B) have dendritic fields spanning a few retinal columns, with neurons of the same type arranged side-by-side in a lattice across the lobula. Tangential neurons such as MLG1 (1) and MLG3 (3) have dendrites spanning several columns. Reproduced from (Strausfeld, 1991). (B) Output organization of male specific lobula giant (MLG) neurons in *male Sarcophaga*. Adapted from (Gronenberg and Strausfeld, 1991). (C) MLG1 has dendrites in the lobula (inset), and projects to the contralateral protocerebrum. (D-E) MLG1 responds to small moving objects in the ipsilateral visual field (bottom trace). Targets were moved across the frontal visual field (D, 10) and the peripheral visual field (D, 11). MLG responded selectively for target movement within the frontal visual field (indicated by the number 10) compared with movement in the periphery (indicated by the number 11). Abbreviations: cb, cell body; Lob, lobula; Oe, oesophagus. (C-E) adapted from (Strausfeld, 1991).



**Figure 1.15 STMDs in the hoverfly** (A) Receptive field of an *Eristalis* hoverfly STMD. Arrow directions represent the preferred direction of target motion at each location in the visual field. Arrow lengths represent the relative sensitivity of the STMD response to target motion at each location in the visual field. (B) Anatomy of the neuron in (A). The STMD receives input in the lobula and projects to the ipsilateral protocerebrum. Abbreviations Me, medulla; Lo, lobula; O, oesophagus. (C) A raw intracellular trace for the STMD in (A-B). Bars under the trace indicate when the target is moved. Arrows under the bottom trace indicate the direction of target motion. The size of the target is indicated by the illustrations on the left. The cell responds preferably to leftward motion, with a preference for smaller objects. Reproduced from (Nordström et al., 2006).



**Figure 1.16 A subset of STMDs respond to target motion irrespective of background motion (A)** Intracellular traces from a hoverfly STMD. The bars under the bottom trace indicate when the stimuli are presented. The schematics to the right indicate the combination of target and background motion. The cell responds preferably to downwards target motion. The cell responds to targets moving across a grey uniform background (top trace), a background moving in the opposite direction to the target (second from top trace), a background moving in the same direction and slower (third from top trace) or at the same speed (bottom trace) as the target. Reproduced from (Nordström et al., 2006). **(B)** Example of a hoverfly STMD that is repressed by background motion. Bars underneath the graphs represent the time when the stimuli are presented, with arrows representing the direction of motion. The neuron is non-directional, and the response is attenuated when the background moves in the same direction and at the same speed as the target. Adapted from (Barnett et al., 2007).

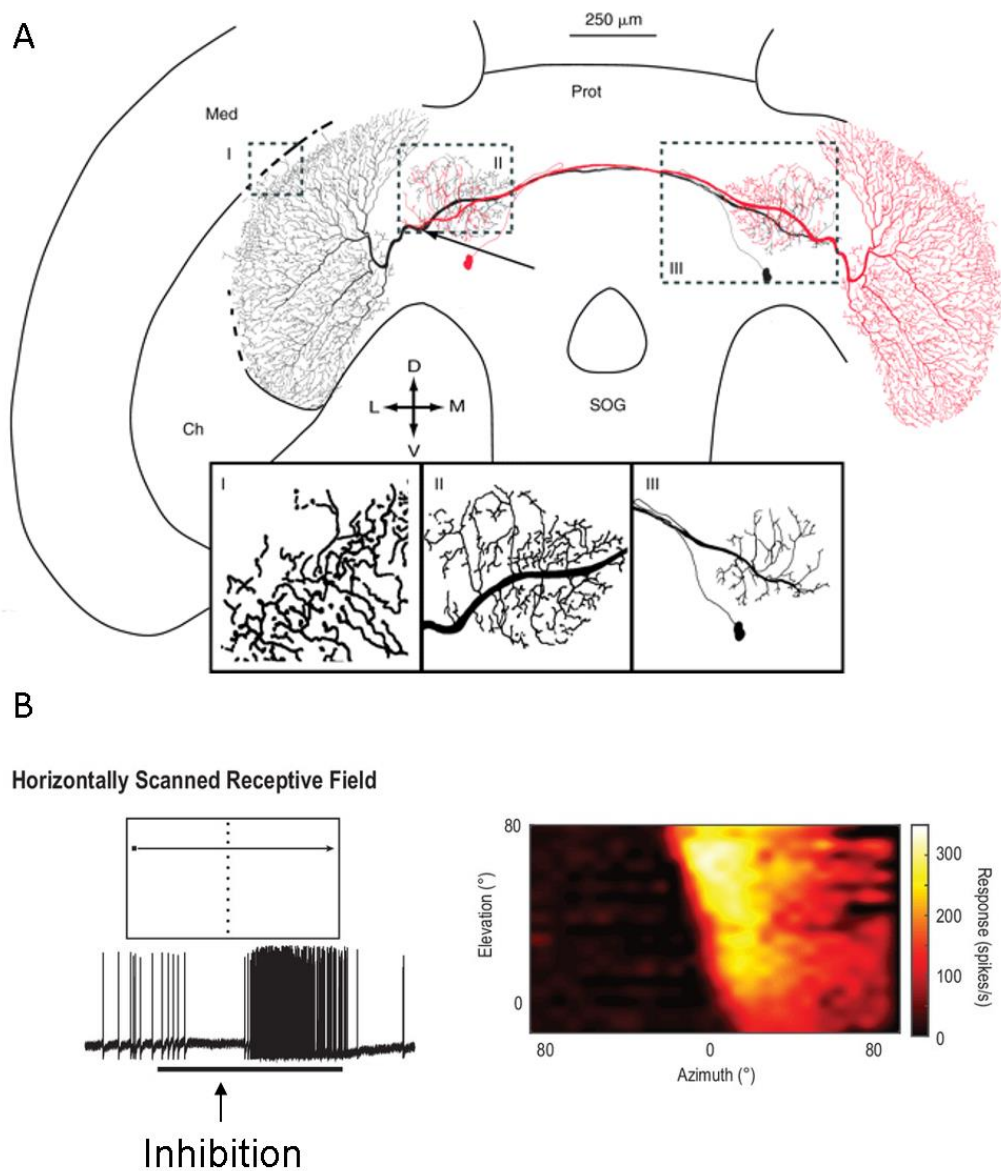


**Figure 1.17**

**Centrifugal STMD1 in the dragonfly *Hemicordulia tau*** (A) Reconstruction of a dye injected CSTMD1 (black). The neuron is flipped (red) to indicate the relative location of the bilaterally symmetric pair. CSTMD1 is thought to output in the lobula and protocerebrum contralateral to the cell body (insets I and II indicate beaded arborisations corresponding to axon terminals). Input is thought to arise from the protocerebrum ipsilateral to the cell body (inset III indicates smooth dendritic terminals). Reproduced from (Geurten et al., 2007b). (B) CSTMD1 responds to targets across the visual hemifield ipsilateral to the cell body. The schematic above the trace indicates the direction of target motion across the visual field. The bar below the trace represents when the target was in motion. The baseline firing rate is reduced when the target travels through the contralateral visual field (left, arrow indicates the inhibitory response of the neuron). Firing rate is increased above baseline when the target enters the ipsilateral visual field. (left) The full CSTMD1 receptive field measured by scanning a target horizontally across the visual field at different elevations. Reproduced from (Wiederman et al., 2017).

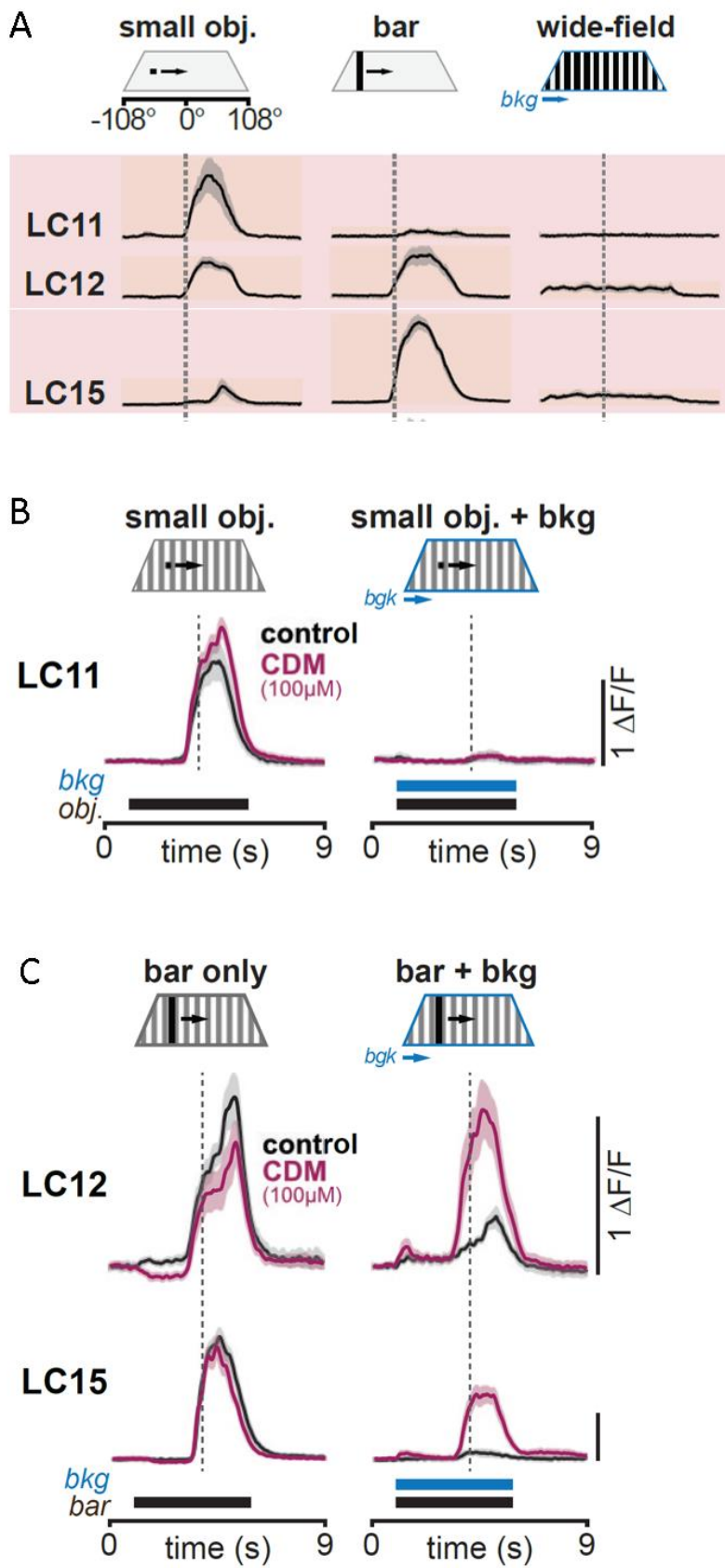
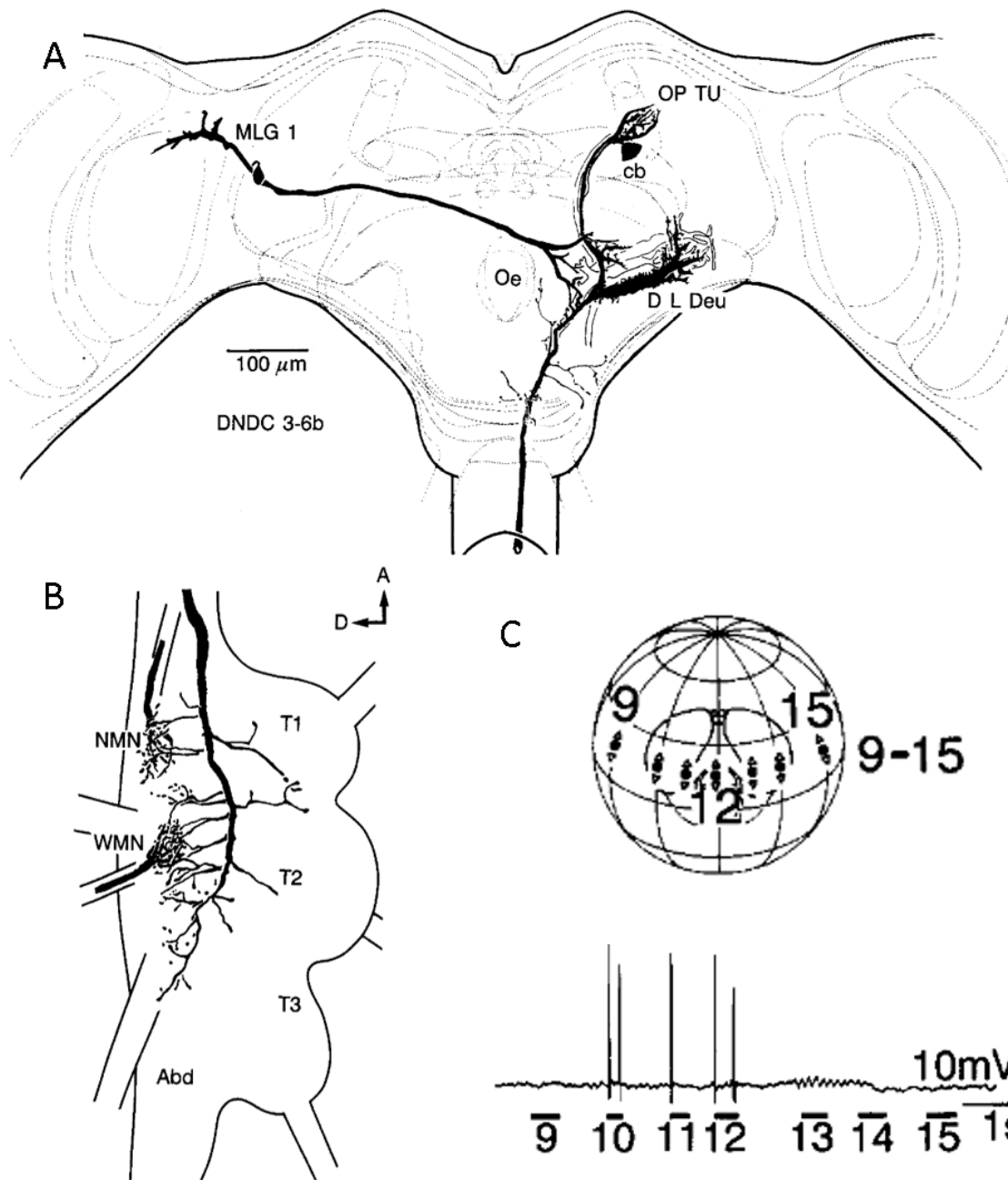


Figure 1.18 (legend right)

**Figure 1.18 (left) Object motion-sensitive lobula columnar neurons in *Drosophila*** (A) A subset of lobula columnar neurons (LC11, LC12, and LC15) in *Drosophila* respond to small moving objects or bars or both. Neither respond to widefield gratings. Traces represent relative changes in calcium indicator fluorescence as measured at the optic glomulus targeted by each fluorescently labelled LC subtype. The vertical dashed line corresponds to the moment when the object (or left-most bar of a grating) passes the visual midline. (B) LC11 calcium responses to moving targets are repressed by concurrent background motion in the same direction (black traces). Application of CDM, an octopamine agonist, has no effect (magenta traces). (C) LC12 and LC15 calcium responses to moving bars are repressed by concurrent background motion (black traces). Application of CDM results in sensitivity to the bar moving across a moving background (magenta traces). Abbreviations: Bkg, background. CDM, chlordimeform, obj., object. Adapted from (Staedele et al., 2020).



**Figure 1.19 Target sensitive *DNDC3-6b* in *Sarcophaga*** (A) Intracellular dye stain of DNDC3-6b dye coupled to MLG1. DNDC3-6b derives its cell body close to the anterior optic tubercle (OP TU) and has dendrites in the OP TU and the lateral protocerebrum. MLG1 projects to the contralateral protocerebrum where it is dye-coupled with DNDC3-6b. (B) DNDC3-6b descends to the thoracic ganglia where it is dye-coupled a neck motor neuron (NMN) and wing motor neurons (WMN). (C) Intracellular recording of DNDC3-6b. Up and down target motion at various azimuth positions is indicated by the numbers 9-15, with 9 corresponding to motion in the contralateral visual field, and 15 to motion in the ipsilateral visual field. DNDC3-6b responds to target motion in the contralateral and frontal visual field. Abbreviations: T1-3, pro-, meso-, meta-thoracic ganglion respectively; Abd, abdominal ganglia. D, dorsal; A, anterior.

### 1.3.3.2 Target Selective Descending Neurons (TSDNs)

In *Sarcophaga*, MLGs project to the lateral protocerebrum where they synapse with descending neurons that project to wing and neck motor neurons in the thoracic ganglia (Gronenberg and Strausfeld, 1991). One such descending neuron, DNDC3-6b, derives from a cell body cluster adjacent to the anterior optic tubercle, forms electrical connections with MLG1, and responds to small target motion in the contralateral visual field (Figure 1.19) (Gronenberg and Strausfeld, 1990, 1991). Beyond DNDC3-6b, little is known of the descending connections to target sensitive visual projection neurons in *Sarcophaga*. Similarly, the downstream targets of hoverfly STMDs remain uncharacterised.

In dragonflies, a population of eight bilaterally symmetric Target Selective Descending Neurons (TSDNs) respond selectively to movement of small objects within the visual field of the dorsal acute zone (Frye and Olberg, 1995; Gonzalez-Bellido et al., 2013; Olberg, 1981a, 1986). Each TSDN receives input from the lateral protocerebrum (Frye and Olberg, 1995; Olberg, 1986), and innervates neck and wing motor neuropil in the thoracic ganglia (Gonzalez-Bellido et al., 2013; Olberg, 1986). Whilst electrical stimulation of TSDNs changes the angle of attack and beating of the wings (Olberg, 1978, 1983), the downstream motor neuron targets of TSDNs within the thoracic ganglia remains unknown. TSDNs derive their cell bodies from different locations across the protocerebral rind, but are named according to whether the descending axon passes through the dorsal-intermediate or median-dorsal tract in the ventral nerve cord (DIT1-3 and MDT1-5, respectively; Figure 1.20) (Olberg, 1986). Whilst TSDNs are presumed to receive direct input from lobula complex STMDs (Nordström, 2012), this remains uncharacterised.

Responses of each TSDN type are spatially localised to a specific region in either the ipsi- or contralateral visual field of the dorsal fovea (Figure 1.20) (Frye and Olberg, 1995; Gonzalez-Bellido et al., 2013). Individual TSDN responses are selective to a specific direction of object motion within this receptive field (Figure 1.20) (Frye and Olberg, 1995; Gonzalez-Bellido et al., 2013; Olberg, 1986). The direction of object motion can be decoded with high accuracy from the combination of TSDN responses using a linear population vector decoder, and is robust to single cell ablation (Gonzalez-Bellido et al., 2013). However, whilst a population decoder optimised to represent target motion occurring with equal probability along any direction would have equally distributed directional tuning curves, the TSDN population appears to oversample lateral target motion (Figure 1.20) (Gonzalez-Bellido et al., 2013). Furthermore, the spatial geometry of TSDN receptive fields differs across TSDN types, with some TSDNs sampling restricted regions of visual space (e.g. DIT1, DIT2), and others sampling larger portions of the visual field (e.g. DIT3, MDT1, MDT3, MDT4). Together this suggests that the TSDN representation may be matched to some aspect of dragonfly biology, for instance, dynamics of prey capture may result in higher probabilities for lateral prey movement owing to range of factors including the long slender dragonfly body and tetraptera flight kinematics, and/or prey evasion tactics.

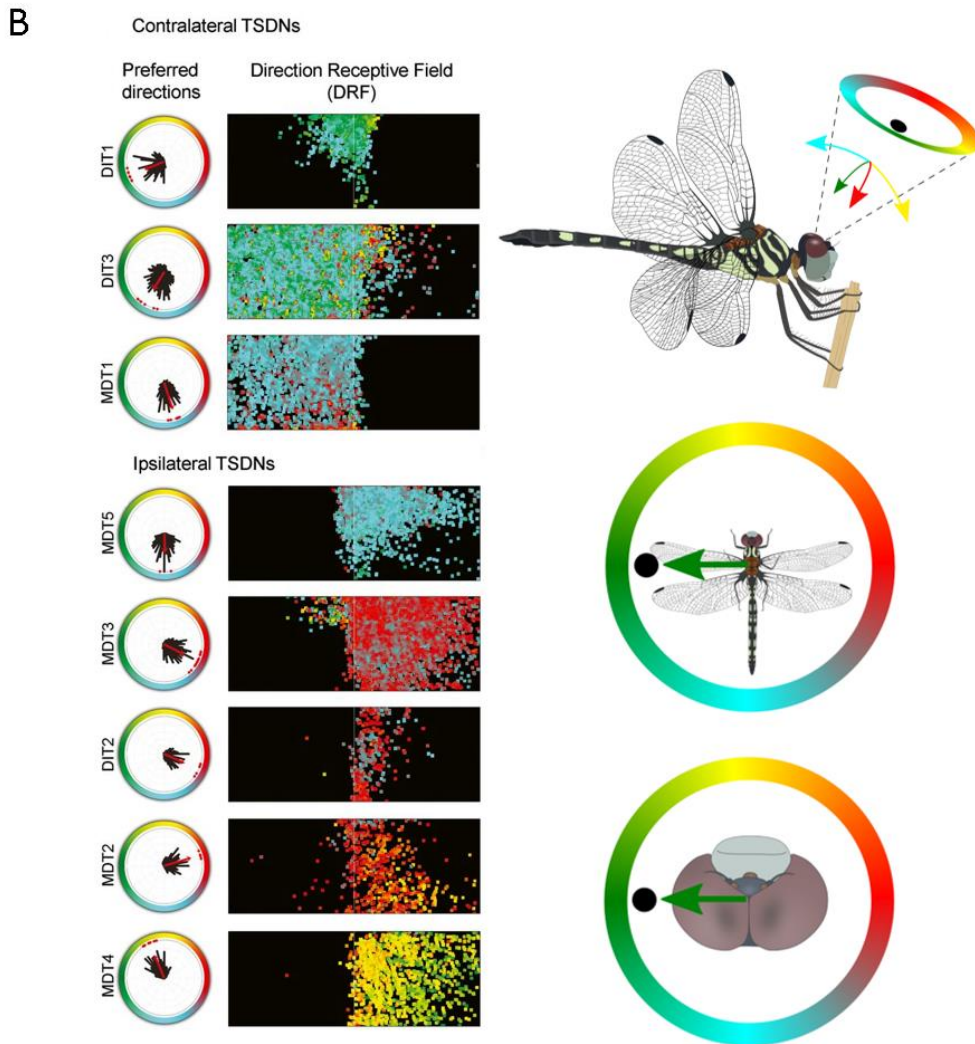
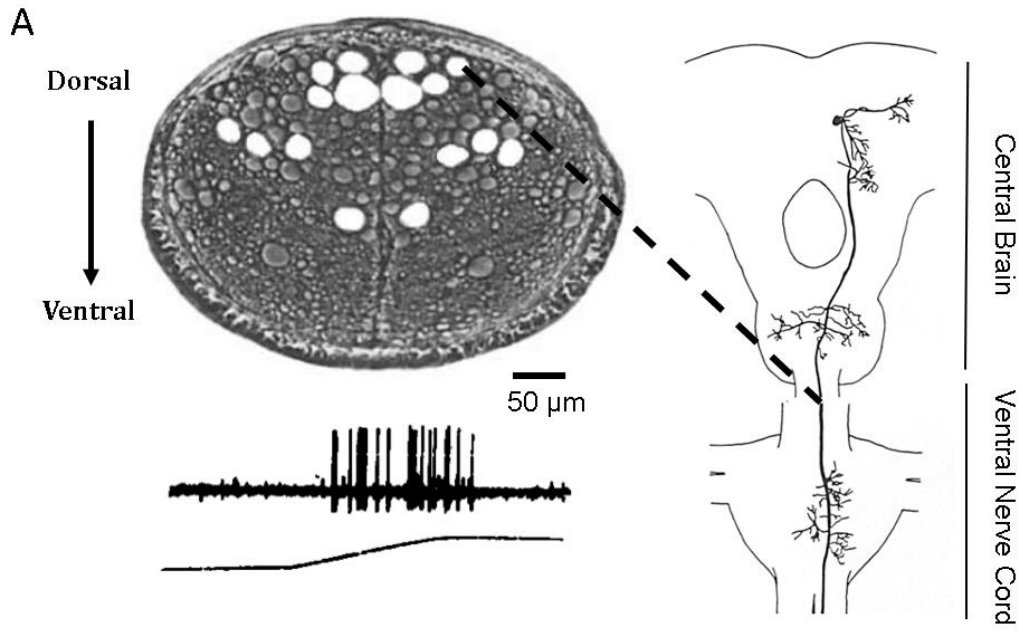


Figure 1.20 (legend right)

**Figure 1.20 (left) Dragonfly Target Selective Descending Neurons (TSDNs)** (A) Cross section of the dragonfly ventral nerve cord. TSDNs are highlighted in white. Adapted from (Adelman et al., 2003). Intracellular injection of lucifer yellow into a dragonfly TSDN (MDT4) shows arborization in the central brain and thoracic ganglia, adapted from (Olberg, 1986). Trace shows an example response of a TSDN when a small object is moved across the dorsal fovea (timing of target motion indicated beneath the trace). Adapted from (Olberg, 1981b). (B) TSDN receptive fields. Each direction receptive field represents the location and direction of target movement when a spike was recorded. Direction of object motion is relative to the dorsal fovea, with the color-coordinate system as indicated by the pictograms to the right. The coordinate system is God's eye view (Gonzalez-Bellido et al., 2013) where the experimenter looks down on the subject dorsally. The polar histograms represent the direction selectivity of the combined responses in the direction receptive field maps. Red arrows are the average directional preference for each map. Red dots show the preferred directions from multiple recordings of the same cell in different animals. Adapted from (Gonzalez-Bellido et al., 2013).

## 1.4 Models for visual control of target chasing

### 1.4.1 Land and Collett model

Visually-guided target chasing requires a transformation of the motion of a target across the retina into changes in the rotational and/or translational velocity of the pursuer (Boeddeker and Egelhaaf, 2005; Land, 1992; Land and Collett, 1974). Following observations of conspecific chasing among houseflies, Land and Collett determined a control system for smooth pursuit of targets based on (1) the relative rotational velocity of the target within the frontal visual field, and (2) abrupt larger saccadic turns proportional to the positional error angle when the target is located more peripherally (Land and Collett, 1974). They proposed a minimal circuitry comprised of two pairs of bilaterally symmetric frontal velocity sensors and a lattice of peripheral positional sensors feeding onto descending neurons to control the rotational velocity of the pursuer (Land and Collett, 1974). A pair of these descending neurons should be directionally selective and represent the magnitude of contralateral yaw torque in response to lateral target movement (Figure 1.21). For example, a left-hand-side descending neuron would receive input from ipsi- and contra-lateral tangential cells, both responding selectively to leftward motion of a target. Additionally, ipsilateral columnar cells responding to target position with increased weighting towards the periphery would facilitate additional responses to targets further from the midline. This descending neuron then projects to the contralateral right-hand-side wing motor to generate net leftward torque (Figure 1.21).

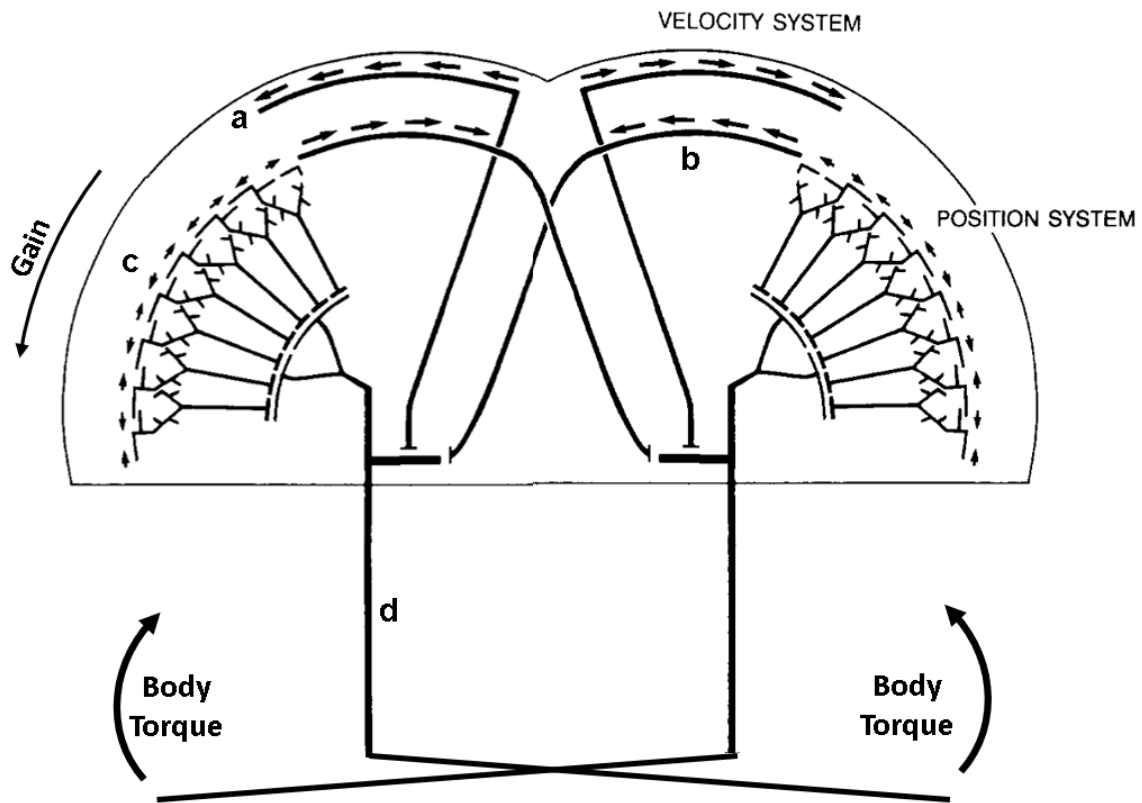


**Figure 1.21 Land and Collett circuitry for target tracking** Schematic of the minimal target tracking circuitry described by Land and Collett (Land and Collett, 1974), further elaborated by Strausfeld based on anatomical and physiological data (Strausfeld, 1991). Two bilaterally symmetric tangential cell types in the lobula (**a**, **b**) receive input from the frontal visual field of each eye and respond to opposite velocities of target motion (arrows). These neurons respond to either medial-to-lateral (**a**) or lateral-to-medial movement (**b**) in each eye. Subsets of these neurons are predicted to project to descending neurons (**d**) that control body torque. Ipsilateral medial-to-lateral input from (**a**) and contralateral lateral-to-medial input from (**b**) result in descending neurons responding to targets moving towards the side of each neuron. These descending neurons input to contralateral steering motors to generate a compensatory body torque in the direction of target movement. Land and Collett also suggested the presence of a separate positional detection system (**c**) to account for very high gain turns to peripheral targets in hoverflies (Land and Collett, 1974). These neurons provide ipsilateral input to the same descending neurons, with increased gain the more lateral the target is from the midline. Candidates for these neurons are the retinotopically organized columnar cells in the lobula. Adapted from (Strausfeld, 1991).

Based on the presence of tangential MLG neuron subtypes projecting to descending neurons in either the ipsi- or contralateral protocerebrum (Figures 1.14, 1.19), Gronenberg and Strausfeld proposed that the MLG system may represent an implementation of the Land and Collett circuitry (Gronenberg and Strausfeld, 1991; Strausfeld, 1991). MLGs were proposed to supply the velocity dependent component within the frontal visual field, and sexually isometric columnar neurons sampling the peripheral visual field were proposed to supply the position dependent component of the controller (Gronenberg and Strausfeld, 1991; Strausfeld, 1991). These inputs were proposed to converge onto descending neurons, including DNDC3-6b, which project lateral turning commands to thoracic motor neurons (Gronenberg and Strausfeld, 1991). However, the directional preferences of both MLG neurons and target selective descending neurons in flesh flies as predicted by the Land and Collett circuitry remain uncharacterised physiologically.

Whilst the input circuitry to dragonfly TSDNs is unknown, TSDNs are obvious neuronal candidates for the Land and Collett descending channels. Individual TSDNs such as DIT1, DIT2, MDT2, and MDT3 all match the lateral direction selectivity predicted by the Land and Collett model (Figure 1.20B). However, it is not clear whether this subset of TSDNs that are sensitive to lateral target displacement encode redundant parallel channels to fine-tune the accuracy of the resultant descending signal, or whether each TSDN serves specific functions, such as innervating different subsets of wing motor neurons. Furthermore, the Land and Collett model exclusively focuses on the generation of yaw torque, although half of the TSDN population (DIT3, MDT1, MDT4, MDT5) roughly encodes target motion along the anterior-posterior axis within the visual field (Figure 1.20B). It is currently unknown whether these TSDNs form part of a rotational or thrust controller.

## **1.4.2 Inner- and outer-loop control**

The Land and Collett model does not account for any interaction between the target tracking and wide-field optomotor systems. Motor control can broadly be conceptualised as two functional divisions: inner-loop stabilization reflexes, and outer-loop goal-directed behaviours (Krapp and Wicklein, 2008). Stabilization reflexes function to maintain postural equilibrium in response to external perturbation, and are continuously implemented by an inner-loop control system (Figure 1.22) (Krapp and Wicklein, 2008). However, in order to perform goal-directed behaviours, this inner-loop system must distinguish sensory inputs produced by external perturbations (so called ‘exafferent’ signals) from those resulting from self-movement (‘reafferent’ signals). A failure to distinguish these sensory origins would result in the activation of stabilization reflexes in response to any volitional outer-loop action, such as the chasing of targets (Krapp, 2015).

One mechanism to distinguish exafferent versus reafferent sensory information is to prepare the inner loop to anticipate the specific pattern of sensory input that would result from volitional movement. This is thought to be accomplished by sending signals corresponding to a copy of the outer-loop command

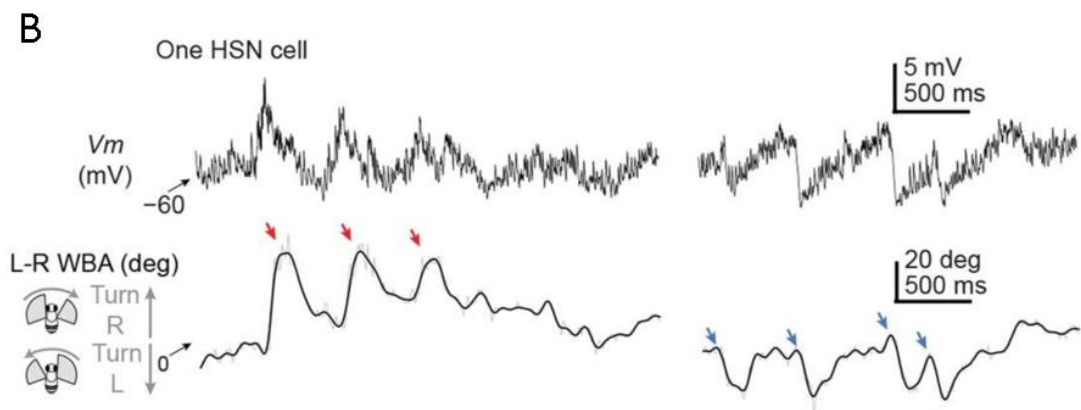
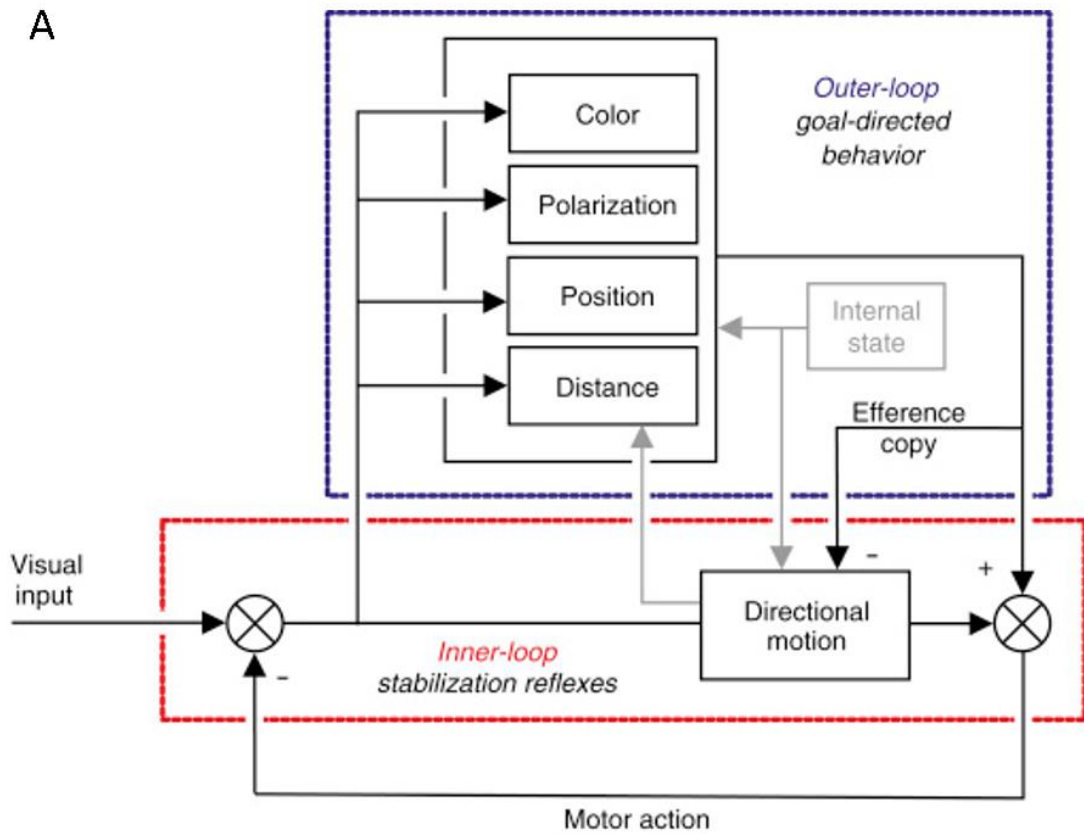


Figure 1.22 (legend right)

**Figure 1.22 (left) Inner-loop stabilization reflexes and outer-loop goal-directed behaviours.** (A) An inner-loop (red) comprised of autonomous stabilization reflexes continuously operate to maintain postural stability. Outer-loop goal-oriented behaviours (blue) are directed according to several salient classes of external visual features, such as color, polarised light, spatial position and distance of objects. These visual features are integrated into the motor controller. However, an efference copy of these commands must be forwarded to the inner-loop controller to prevent stabilization reflexes becoming activated in response to volitional motion. Figure adapted from (Krapp and Wicklein, 2008). (B) Cellular evidence for an efference copy in *Drosophila*. Top trace is the membrane voltage from an intracellular recording of the LPTC HSN on the right side of the brain, indicating the starting membrane potential of -60 mv. HSN depolarizes to medial to lateral motion, in the case of the right-hand side HSN, medial to the right of the animal. The bottom trace is a smoothed wing beat amplitude (WBA) difference measured in degrees. The right WBA is subtracted from the left WBA. A positive value corresponds to a turn to the right (R), because the left WBA is greater than the right WBA, causing rightward torque. A negative value corresponds to a turn to the left (L) because the right WBA is greater than the left WBA, causing a leftward torque. When the animal spontaneously turns to the right (indicated by red arrows), HSN membrane potential is depolarized to counter the hyperpolarizing effect that optic flow would have on HSN. Conversely, spontaneous turns to the left (blue arrows) results in hyperpolarization of HSN membrane potential to counter the depolarizing effect that optic flow would have on HSN. Adapted from (Kim et al., 2015).

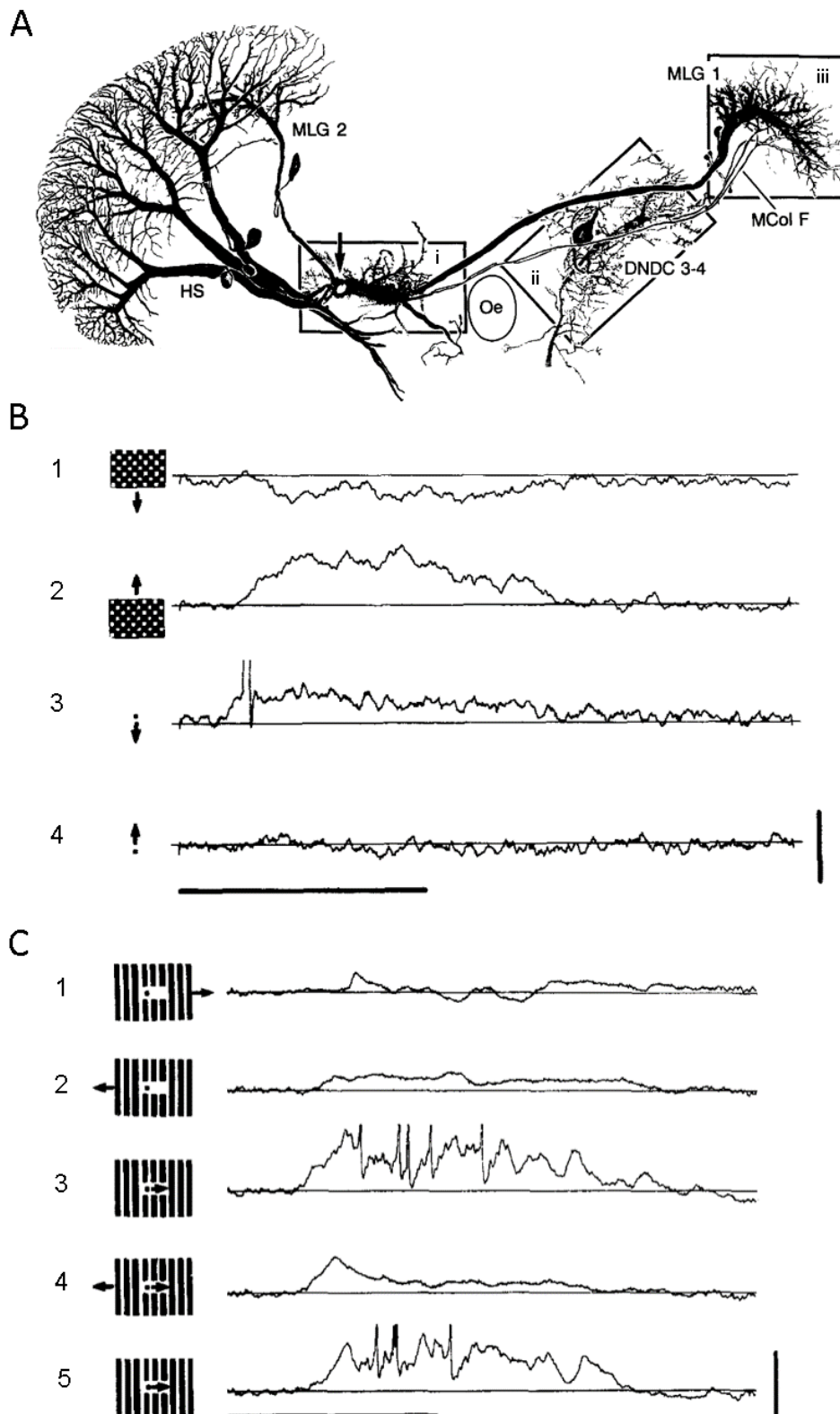


Figure 1.23 (legend right)

**Figure 1.23 (left) Interactions between wide-field and target tracking systems** (A) Cobalt injection into the protocerebrum (injection site indicated by arrow, inset i) stained several neurons including HS cells, MLG cells, lobula columnar cells (MCol F). Inset ii indicates the dendrites of a descending neuron DCDN3-4, inset iii indicates the dendritic field of MLG1 and MCol F in the lobula. Note that, whilst HS and MLG neurons were co-stained by cobalt, it is not clear from the original source whether DCDN3-4 was co-stained or is presented to indicate relative position in the protocerebrum. Adapted from (Gronenberg and Strausfeld, 1991). (B) Intracellular recordings of a dragonfly TSDN responding to moving gratings (traces 1-2) and moving targets (traces 3-4). The preferred direction for target movement in this cell is downwards (note action potential, trace 3). Downward movement of a wide-field checker pattern showed hyperpolarizing response (trace 1), and upward movement showed depolarizing response (trace 2). Movement speed 45°/200 ms; Scale bar 5mV. (C) Dragonfly TSDN responses to target movement with and without a moving background. Against a stationary background, this TSDN (DIT1) produced spikes in response to rightward movement of a 4° target (trace 3) and was depolarized by leftward movement of a wide-field grating pattern (trace 2). However, leftward movement of the grating in unison with rightward movement of the target inhibited responses to the target (trace 4). Bottom trace 5 shows recovery of target response in the absence of grating movement. The five traces are shown in the sequence they were obtained. Movement speed 45°/200 ms; Scale bar 5mV. Figure and legend text reproduced and adapted from Figure 7-8 in Olberg 1986.

to the inner-loop (Crapse and Sommer, 2008; Krapp, 2015; Krapp and Wicklein, 2008; Wolpert et al., 1995). This ‘efference copy’ is subtracted from the inner-loop sensor measurement to cancel reafferent input (Figure 1.22). Conceptually, this corresponds to changing the set-point of the inner-loop and has the effect of preventing stabilization reflexes from counteracting volitional movement, whilst enabling the inner-loop to respond to unanticipated perturbations of the volitional movement from external sources. Evidence for efference copies feeding into the inner-loop controller has been identified in LPTCs in *Drosophila* (Figure 1.22B) (Kim et al., 2015). HS cells receive inhibitory or excitatory input in response to contralateral and ipsilateral yaw saccades, respectively (Figure 1.22B) (Kim et al., 2015). This represents a cancelling of reafferent stimulation that would be experienced by HS cells during a yaw saccade in either direction. In consequence, the inner-loop stabilisation pathway is prevented from responding to a voluntary turn. Whether and how the proposed Land and Collett tracking circuitry forms part of an efference copy system to repress optomotor pathways remains unanswered. Cobalt injections in *Sarcophaga* suggest that lobula MLG and lobula plate HS neurons converge together onto descending neuron dendrites (Figure 1.23A) (Gronenberg and Strausfeld, 1991). This raises the possibility that reafferent signals could be cancelled in LPTCs by feedforward connections from MLG and/or descending neurons.

Furthermore, aside from the problem of sensing reafferent signals following volitional movements, unintended self-motion during chasing will result in simultaneous wide-field optic flow and target

motion across the retina. If both the descending outer-loop target tracking system (implemented by TSDNs) and the descending inner-loop stabilisation system (implemented by DNOVS and DNHS) are activated this may result in over-compensation of the turning response. In dragonfly TSDNs, wide-field motion results in subthreshold hyperpolarisation when moving in the preferred target direction, and depolarisation when moving in the anti-preferred target direction (Figure 1.23B-C) (Olberg, 1986). This inverse relationship between responses to target and background motion suggests that the inner-loop stabilisation system may feed forward onto the target tracking system, potentially functioning to repress the target tracking system whilst correcting for unintended self-motion. The convergence of HS terminals onto descending neuron dendrites in *Sarcophaga* (Figure 1.23A) (Gronenberg and Strausfeld, 1991) could reflect a similar interaction between inner- and outer-loop control in Diptera, however this has not been demonstrated physiologically. Interestingly, synchronous motion of the target in the preferred direction and background in the anti-preferred target direction results in a reduction of dragonfly TSDN responses rather than an increased response as would be expected from the summation of the individual target and background responses (Figure 1.23C). The significance of this interaction remains unknown.

## 1.5 Aims and structure of the thesis

Descending neurons in insects present a unique opportunity to explore encoding strategies in neural circuits as these neurons (1) pass through the ventral nerve cord, an information bottleneck between the central brain and thoracic ganglia which is presumably under selective pressure for efficient encoding (Namiki et al., 2018); (2) necessarily encode the entire subset of visual information that directly guides behaviour; and (3) are conveniently organised into an experimentally tractable bundle of axon fibres. Nonetheless, the function of TSDNs within a control architecture for chasing is poorly understood. Furthermore, aside from dragonfly TSDNs, the descending representations used to guide chasing in other species remain largely uncharacterised. It is currently unexplored whether dragonfly TSDNs represent a globally efficient solution robust to contextual differences in visual ecology, behavioural strategy, flight kinematics, and/or body plan, or whether other species employ vastly differing descending representations to guide chasing.

This thesis takes a comparative approach to understand the design principles underlying TSDN function, using a range of experimental techniques at the level of behaviour, physiology, and anatomy. The experimental methodology shall be outlined in Chapter 2.

The first results section (Chapter 3) investigates the hunting strategy and TSDN properties in *Calopteryx* damselflies. As dragonflies and damselflies are both predators having diverged from a predatory last common ancestor, damselflies offer a unique opportunity to explore whether and how the TSDN encoding strategy varies in species with divergent predatory behaviours.

The second results section (Chapter 4) investigates TSDNs in the robberfly *Holcocephala fusca*, and the killerfly *Coenosia attenuata*. Each species has converged upon a predatory livelihood, offering the opportunity to investigate whether evolution shapes similar descending representations for chasing, even among distantly related species.

The third and final results section (Chapter 5) investigates the integration of wide-field and small-field motion in target selective descending neurons in the robberfly *Holcocephala fusca* and the hoverfly *Eristalis tenax*. This study aims to understand the role of TSDNs within an inner- and outer-loop control architecture for chasing, and whether TSDNs perform analogous roles in both predatory and non-predatory species.



# Chapter 2

## Methods and materials

### 2.0 Acknowledgements and contributions

Visual parameters (e.g. target size, position, velocity) for each frame of the stimuli were calculated using custom MATLAB code written by Jack Supple. These parameters were then rendered by StimulateOpenGL visual projection software developed by C. Culianu for the Anthony Leonardo lab at Janelia Farm Research Campus [https://github.com/cculianu/StimulateOpenGL\\_II](https://github.com/cculianu/StimulateOpenGL_II). DepthQ 360 projector settings were determined by Jack Supple. Extracellular electrophysiology protocols were developed by Jack Supple. 3D printed equipment was designed and built by Jack Supple. Electrophysiology data was processed in Spike2 software (Cambridge Electronic Design, CED) by Jack Supple to yield spike-sorted spike times and waveform shapes. Code for all further electrophysiology analysis was written in MATLAB by Jack Supple. Ventral nerve cord backfill protocol was developed by Jack Supple. Multiphoton brain scans were acquired with equipment built and developed by Trevor Wardill using protocols developed by Paloma Gonzalez-Bellido and Trevor Wardill. Multiphoton image data was analysed by Jack Supple using Fiji and Vaa3D software based on protocols developed by Trevor Wardill and Paloma Gonzalez-Bellido. Macrophotographs were acquired by Jack Supple. Highspeed videography acquisition, camera calibration, and 3D reconstruction was based on protocols developed by Paloma Gonzalez-Bellido and Trevor Wardill. Fiji image sequence digitisation protocol and all further behavioral analysis code was written in MATLAB by Jack Supple.

## 2.1 Animals

### 2.1.1 Odonata

Odonates used in this study were either caught in the wild or reared from nymphs in the lab. All odonates caught in the wild were captured using sweep nets and transported in petri dishes humidified by a small piece of damp tissue. On hotter days (>25°C), petri dishes were stored in a cooler box to prevent death from overheating.

#### *Damselflies*

*Calopteryx splendens* demoiselles were wild caught between April-August along the river Cam in Grantchester Meadows, Cambridge, UK. *Calopteryx maculata* demoiselles were wild caught between July-August at Nixon Park in York, Pennsylvania, USA. Demoiselle were stored alive at 4°C and typically used within 4 days after capture. *Enallagma civile* damselflies used for pseudopupil measurements were reared to adults from nymphs caught at Cedar Bog in Minnesota, USA. Adults were stored in hunting cages feeding on a diet of *Drosophila melanogaster*.

#### *Dragonflies*

The dragonflies used in this study were either reared from nymphs in the laboratory or caught wild. *Sympetrum vulgatum* were reared from nymphs in the lab at Cambridge, UK, on a diet of bloodworms. *Pachydiplax longipennis* were reared from nymphs (Carolina Biological Supply Company) in the lab at University of Minnesota on a diet of bloodworms. Adults of each species were stored in hunting cages for 1-2 weeks feeding on a diet of *Drosophila melanogaster*. *Gomphus spicatus* and *Cordulia shurtleffi* dragonflies were wild caught at Itasca research station, Minnesota, USA and used on day of capture.

### 2.1.2 Diptera

#### *Robberflies*

*Holcocephala fusca* robberflies (family *Asilidae*) were wild caught between July-August (inclusive) in York, Pennsylvania, USA. Robberflies including *Holcocephala fusca* are relatively abundant during this period and can be found perching on tall grasses in areas close to creeks and rivers with substantial vegetation clearings that permit hunting against the sky backdrop. *Holcocephala fusca* were caught in small (8 x 3 cm) vials capped with sponge. Longevity of *Holcocephala fusca* in the lab is extremely sensitive to ambient humidity - animals will die within 1-3 days if allowed to desiccate or survive in good health up to 7 days when fully humidified. Humidification is best performed by mounting the vials sponge down into a shallow basin of water: the water saturates the sponge with water vapour continually

drawn up into the vial. Simply placing a small piece of damp tissue in the vial and topping up throughout the day is typically not enough to prevent decussation, especially overnight.

### ***Killerflies***

The killerfly (aka ‘hunterfly’) *Coenosia attenuata* (family *Muscidae*) (Bautista-Martínez et al., 2017; Sorokina, 2014; Wardill et al., 2015) was reared in the lab from an established breeding colony in Cambridge, UK. Typically, only females were used for electrophysiological and anatomical experiments due to the sexual dimorphism in size with females (4-5 mm) being substantially larger than the males (2-3 mm) (Bautista-Martínez et al., 2017).

## **2.2 Dissections**

### **2.2.1 Ventral nerve cord**

Ventral nerve cord dissections for all animals in this thesis follow the same basic protocol. The following protocol outlines the process for *Holcocephala fusca* dissections, relating to Figure 2.1:

(i) Align double-sided tape with the edge of a platform. (ii) Anaesthetize fly for 3 min in a -20C freezer. Place the fly onto the sticky tape aligning the neck joint with the edge. Wax the tip of the wings (blue arrow), and either side of the thorax (white arrow). (iii) Wax the meso- and meta-thoracic legs. (iv) wax the tip of the abdomen (as minimally as possible to avoid occluding spiracles). (v-vi) Rotate the animal, and complete waxing of the thorax to secure the animal as much as possible. At this point, rotate the animal and amputate the prothoracic legs as close to the thorax as possible (see panel ix). This will be necessary to access the ventral cord. It is best to amputate the legs before the next step to avoid the animal pulling its head out of position. (vii-viii) Rotate to the anterior view and wax the head in a tilted position. Tilting the head ensures the ventral cord is taught, which helps stabilize the axons during electrophysiology. (ix-x) Wax over the legs and lateral thorax to stabilize the preparation and provide a foundation to secure the head. (xi) Secure the posterior aspect of the head. Use as little wax as possible to avoid heat damage to the optic lobes. (xii) Hydrate the ventral cavity with a small drop of saline applied to the amputated legs. Dry excess saline with paper towel. (xiii) Pull a glass micropipette and manually break the tip with fine forceps to create the hydration (blue arrow) and reference electrode (white arrow). The hydration electrode should be slightly larger than the reference. Try to break each pipette without any jagged edges (jagged edges accumulate more dried saline making clogging more likely). Clean breaks of the pipettes are usually achieved by grasping the tip with forceps then pulling along the axis of the tip. Before proceeding with the dissection, fill the two micropipettes with saline and secure them to micromanipulators on the electrophysiology rig to minimize the time between ventral cord exposure and insertion of the hydration electrode on the rig. (xiv) Using a hypodermic needle, cut the ventral thoracic cuticle at the posterior (blue arrow) and the lateral aspect (white arrow) using the cavities of the amputated legs as a start point. This results in a flap of cuticle connected at the

anterior aspect. (xv) Remove this flap using fine forceps. Remove any superficial tracheae. The ventral cord (white arrow) and the thoracic ganglion (blue arrow) should be visible. (xvi) Insert the hydration pipette (blue arrow), and reference pipette (white arrow) into the ventral cavity. Place a small hook fashioned from a hypodermic needle (purple arrow) under the ventral cord (green arrow) to stabilize it for recording.

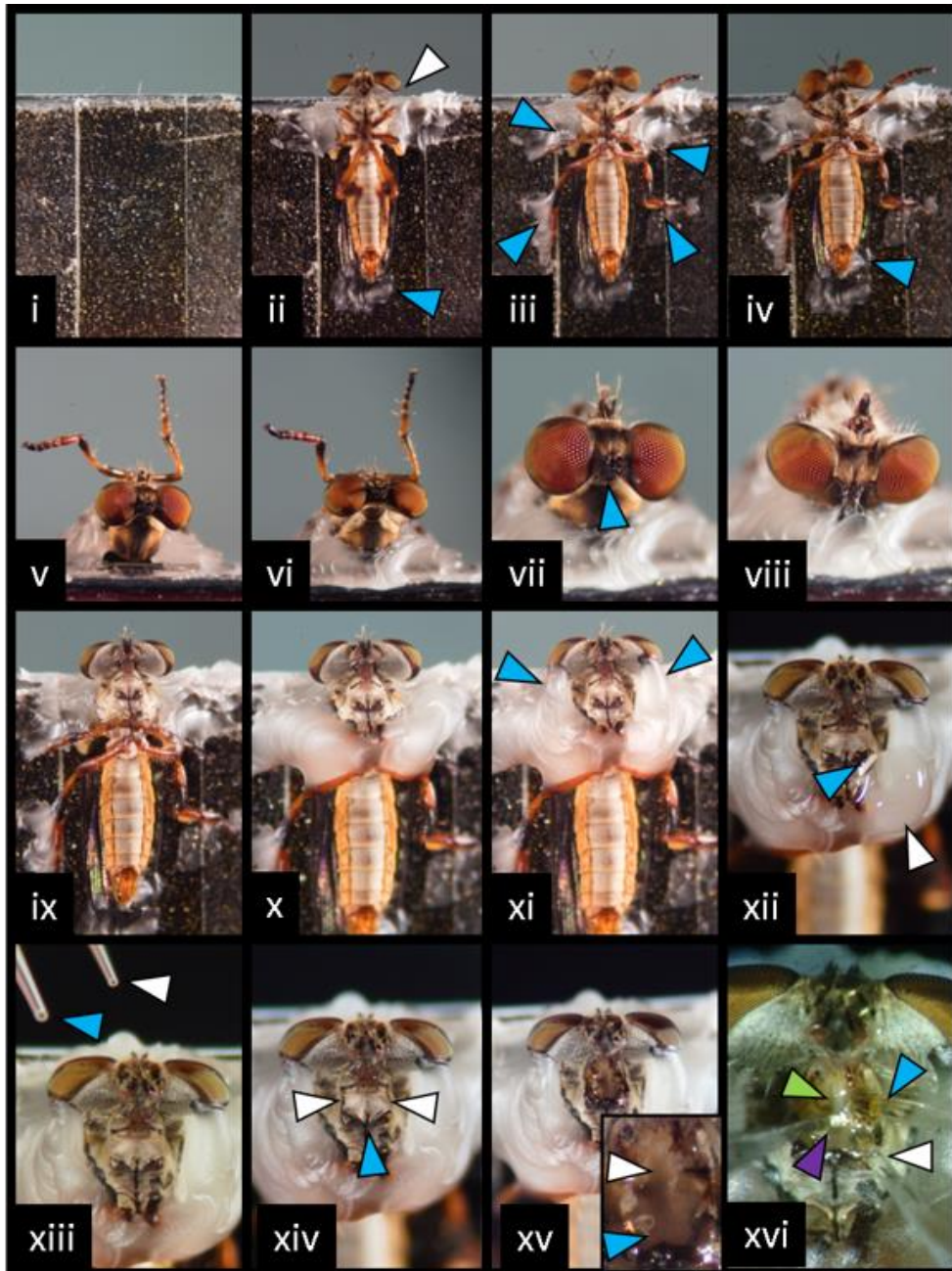


**Figure 2.1 Dissections** (A) Ventral nerve cord dissections were performed following a series of steps as outlines in the main text. In brief the animal is positioned on the platform (steps i-vi), the head secured in place (steps vii-xi), the ventral nerve cord exposed (steps xii-xv), and electrodes placed into the cavity for recording (xvi).

## 2.3 Visual Stimuli

### 2.3.1 Using the DepthQ 360 DLP projector

Visual stimuli were presented to the animal using a DepthQ360Hz DLP (Digital Light Processing) projector with a spatial resolution of 1280 x 720 pixels (Cambridge Research Systems). The projector was oriented to project light onto a screen made from rear-projection material (Dual Vision DA-LITE fabric, gain = 0.9, half-angle = 65°, viewing cone = 130°, Milestone AV Technologies LLC) mounted on customized laser-cut acrylic. Under this configuration the screen is positioned intermediate between the animal and the projector such that the projector is functioning as a ‘rear projector’ (Figure 2.2A). The projector lens was fitted to the projector chassis atop of 1.5 mm spacers. This lengthens the distance of the lens from the DLP mirror (i.e. focal length) resulting in a smaller angular projection, with a resulting dimension of 17.3 x 9.6 cm when in-focus. The intensity of projected images in this configuration is ~20 kLux (measured at 7cm from the screen).

#### *Subframe rendering*

Computer monitors display images using a trichromatic bit plane where a variety of colors can be generated using a combination of three spatially separated monochromatic subpixels surrounded by a black mask (e.g. Red, Green, and Blue subpixels for ‘RGB’ displays; Figure 2.2B). Because the size of these subpixels is smaller than the human spatial resolution for color, each subpixel becomes perceptually fused. By varying the relative intensity of each subpixel, a continuous spectrum of color can be generated. Most display projectors generate color images in a slightly different way. Whilst colors remain encoded in a trichromatic bit plane, instead of using spatially separated subpixels like computer monitors, projectors display each monochromatic bit plane in temporal sequence (i.e. subframes) using a rotating color wheel (Figure 2.2C). This mechanism has the advantage that spatial resolution can be greater because each pixel no longer needs to be subdivided into subpixels. Furthermore, for any given color projector tricolor framerate, monochromatic images can be displayed at a three times higher framerate than color images by removing the color wheel, treating each subframe as an individual frame.

The DepthQ 360 DLP display is a commonly used projector in the visual neurosciences. This projector is a 120Hz color projector with the color wheel removed so that each subframe is rendered monochromatically, yielding a resultant monochromatic frame rate of 360Hz. This is desirable for invertebrate visual experiments in particular as insects have high flicker fusion rates on the order of 200-300Hz. By using a 360Hz frame rate insects should perceive the visual stimuli as continuous objects. The DepthQ 360 happens to display each bit plane in the order BRG rather than RGB. This means the blue bit plane is projected before the red, which is displayed before the green. This is important when designing stimuli because assigning the position of the object for each subframe to the

correct bit plane is necessary to generate smooth continuous motion - mismatching the subframe bit plane results in jittery motion. For example, an object moving downwards needs to be encoded so that for each frame (composed of three 360 Hz subframes) the first subframe should include the top-most position of the object and needs to be in the blue bit plane, the second subframe should contain the next position (middle) of the object and should be in the red bit plane, and the third subframe should contain the bottom-most position of the object needs to be encoded in the green bit plane (Figure 2.2D).

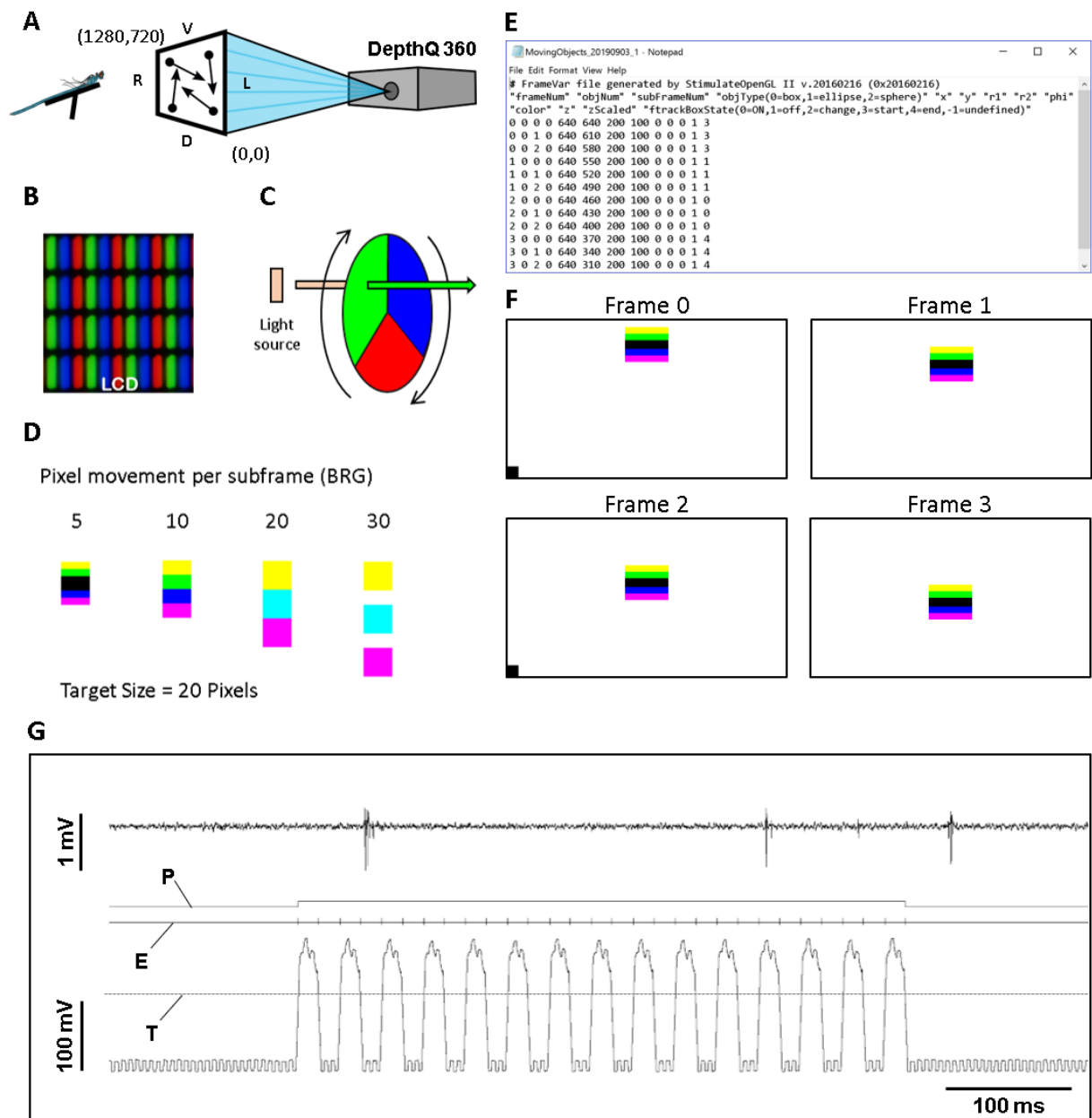


Figure 2.2 (legend right)

**Figure 2.2 (left) Projector set-up for visual stimuli** (A) The animal is oriented facing a projection screen behind which a DepthQ 360 projector projects a greyscale image with dimensions of 1280 x 720 pixels. (B) Close up of an RGB computer monitor display. Each pixel is composed of three subpixels of different color (red, green, and blue). Arbitrary colors are generated by varying the relative intensities of each subpixel. (C) Projectors generate display color using a spinning trichromatic color wheel rotating in front of a light source. This produces arbitrary colors as each temporally separated monochromatic subframe becomes perceptually fused by the viewer. By removing the color wheel, a 120 Hz color projector is converted into a 360 Hz monochromatic projector, as each subframe can be treated as a single monochromatic frame. (D) Moving targets that are encoded at the subframe level can be confirmed by displaying targets on an RGB color monitor. The black target is seen as a combination of the two unused color channels at the target position. The direction of target movement can be confirmed by the position of each color combination. (E) An example text file used to present an object using the StimGL format. The names for each column of data are in the header lines. This stimulus runs for four frames (0 to 3, column 1, “frameNum”) with three subframes each (column 3, “subFrameNum”), and renders a square object 200x100 pixels in size (columns 7-8, “r1” and “r2”), starting at position (x,y) = (640,640) moving downwards at 30 pixels per subframe for the duration of the stimulus (columns 5-6, “x” and “y”). Column “phi” represents the rotation of the object, here zero. The object color (column 10) is zero corresponding to black. The trackbox is encoded in the final column of the text file. (F) The rendered output for the text file in (E). (G) An example electrophysiology trace of a stimulus used in experiments. The photodiode trace (bottom) is converted into a series of frames using a threshold (‘T’) to generate the events channel (‘E’). The events channel is then clustered into stimulus blocks (‘P’) which can be matched with the electrophysiology trace (top).

Testing whether each target position is assigned to the correct bit plane can be performed on a PC RGB monitor (Figure 2.2D). Displaying the three subframes on an RGB monitor renders the superimposed subframe data of the target trajectory for one 120Hz frame (i.e. each subframe becomes a subpixel on the display). Because the target is rendered black on a white background, this means that the target position for each subframe is rendered as a color. In Figure 2.2D, a 20-pixel black target is moving downwards at 5, 10, 20, and 30 pixels per subframe. The target starts at the top and moves to the bottom of the figure over the course of one 120 Hz frame (i.e. three BRG subframes). When the total distance moved by the target exceeds the target size, the three individual target positions are seen (e.g. 20 and 30 pixels per subframe, Figure 2.2D). The target appears yellow at the top position because the blue bit plane is zero (because the target is black, i.e. the target position is assigned an intensity value of 0 in the blue bit plane, with red and green equal to the maximum intensity), and the combination of the remaining pixels (red + green) produces a yellow percept. The target is cyan in the middle position because the red bit plane is zero (blue + green = cyan), and magenta in the bottom position because the green bit plane is zero (blue + red = magenta). From this sequence of colors, when rendered in BRG (as rendered in the DepthQ) the target will be moving from top to bottom.

When the total distance moved by the target does not exceed the size of the target (e.g. 5 and 10 pixels per subframe, Figure 2.2D), then the targets from subsequent subframes overlap and a single channel of the RGB colors is seen as two of the channels become set to zero. For example, when the top-most and middle positions of the target overlap, both the blue bit plane (top) and the red bit plane (middle) are set to zero, and the resulting color is green. When the middle and bottom most positions of the target overlap, then both red (middle) and green bit plane (bottom) are set to zero resulting in blue. In the condition when all three of the targets are overlapping (e.g. 5 pixels moved by the target per subframe, Figure 2.2D) then all color channels become set to zero and the target appears black.

### ***Projector settings***

In the projector settings, ‘Rear Project’ should be set to ‘off’. When rear project is off, the projector functions as though it is projecting onto an opaque screen to be reflected back to the viewer. Whilst the projector is in fact being used in a rear projection orientation, (i.e. the animal is viewing stimuli on the other side of the screen, looking directly into the projector bulb), turning off rear projector mode means that the coordinate system of the projected visual stimuli matches the standard anatomical coordinate system (‘God’s eye view’; Gonzalez-Bellido et al., 2013). This minimizes confusion during analysis. I.e.  $(x,y) = (0,0)$  at bottom left, and  $(x,y) = (1280,720)$  at the top right. For consistency, other important parameters in the projector settings are: ‘Brightness’ = 50; ‘Contrast’ = 50; Sharpness = ‘maximum’.

### **2.3.2 StimGL**

Visual stimuli were rendered to the DepthQ 360 projector using StimulateOpenGL (StimGL) II v.20160216 (developed by C. Culianu for the Anthony Leonardo lab at Janelia Farm Research Campus [https://github.com/cculianu/StimulateOpenGL\\_II](https://github.com/cculianu/StimulateOpenGL_II)). StimGL functions to render objects or gratings based on either vectorized parameter input (such as object shape, object size, initial coordinates, velocity, etc.) or a text file containing the instantaneous frame-by-frame parameters of the object (Figure 2.2E). Each method can be run through StimGL either directly through the StimGL console, or via MATLAB (32-bit, v.2009b). The text file version of the input is most useful as this text file can be edited freely to create any arbitrary trajectory desired. Figure 2.2F shows the output of the text file in 3E. There are 4 frames (0-3), with an 200x100 pixel object starting at the top of the screen  $(x,y) = 640,640$ , and moving down the y dimension in 30 pixel steps per subframe (colors are as described in section 2.3.1).

### **2.3.3 Tracking stimulus presentation**

Stimulus presentation timing was measured with respect to electrophysiological recordings by a photodiode recording of a small square (termed a ‘trackbox’) in the corner of the screen that switched on and off for each frame in the stimulus (Figure 2.2F-G). The trackbox is configured be black on the first frame and then switch off and on for each frame thereafter (Figure 2.2F-G). The use of a trackbox

rendered with the stimulus provides a direct measure of the frame rendering throughout the experiment, enabling the detection of dropped frames. In post-processing, each frame is extracted from the photodiode trace in Spike2 (CED) using a horizontal threshold (Figure 2.2G, label 'T') to generate an events channel (label 'E'). This events channel is then clustered into blocks of frames that correspond to each stimulus block (label 'P') which can then be used in combination with the events channel for further analysis.

## 2.4 Electrophysiology

### 2.4.1 Extracellular recordings and spike sorting

#### *Sample preparation*

For ventral nerve cord recordings, an extracellular recording electrode was inserted into the cervical connective, with mechanical support given to the cord by a small hook fashioned from a hypodermic needle (see Figure 2A-xvi). The animal was grounded using a saline-filled glass microelectrode inserted into the ventral cavity, which also served as the reference electrode. Fly saline for dipterans is as described in Gengs et al., 2002: 138 mM NaCl, 2 mM KCl, 1.8 mM CaCl<sub>2</sub>, 4 mM MgCl<sub>2</sub>, 5 mM TES, pH 7.15. Saline for Odonates is based on Duchateau et al., 1953: 134mM NaCl, 5.4mM KCl, 3.8mM CaCl<sub>2</sub>, 3.0mM MgCL<sub>2</sub>\*6H<sub>2</sub>O, 0.5mM NaHCO<sub>3</sub>, pH 7.4.

#### *Data acquisition*

Extracellular signals were amplified at 500x gain and filtered through a 300 – 3000 Hz analogue bandpass filter on an NPI BA-03x amplifier (NPI Electronic). The filtered signal was further filtered through a HumBug (Digitimer). Analogue signals were digitized on a micro1401-3 DAQ (CED) and acquired at 25kHz using Spike2 software (CED).

#### *Extracellular electrodes and spike sorting*

Several different extracellular recording electrode types were used (Figure 2.3). Extracellular spike sorting was performed in Spike2 software (Cambridge Electronic Design Ltd, UK) using principal component analysis (PCA) on waveform shapes (Figure 2.3,ii) (Rey et al., 2015) followed by manual clustering (Figure 2.3,iii). Spikes were detected using a voltage threshold manually adjusted to the trace thermal noise but pass through the action potential spike voltage. At the time point when the neural signal exceeds the voltage threshold, the voltage trace within a short window ( $\pm 0.5$  ms) is extracted, this is the spike waveform. The set of spike waveforms in a recording each consist of 25 data points, corresponding to the number of sampled voltage levels within the time window (1 ms multiplied by 25 kHz sampling rate equals 25 data points). The set of spike waveforms can be represented as points in multidimensional space, with each dimension corresponding to voltage value of each data point in the spike waveform. Thus, a spike waveform with 25 voltage values within the 1 ms window is represented

as a point in 25-dimensional space. PCA functions to identify the axes of maximum variation between points in this multidimensional space, termed principal components. By projecting the data onto the principal components (Figure 2.3,ii), the separation of clusters within the data is maximised. Throughout this thesis spike clusters are identified manually, such that the experimenter draws an arbitrary boundary between clusters. Whilst in some cases cluster separation is unambiguous (e.g. Figure 2.3Aii,iii), in other cases cluster assignment is less clear (e.g. Figure 2.3Cii,iii).

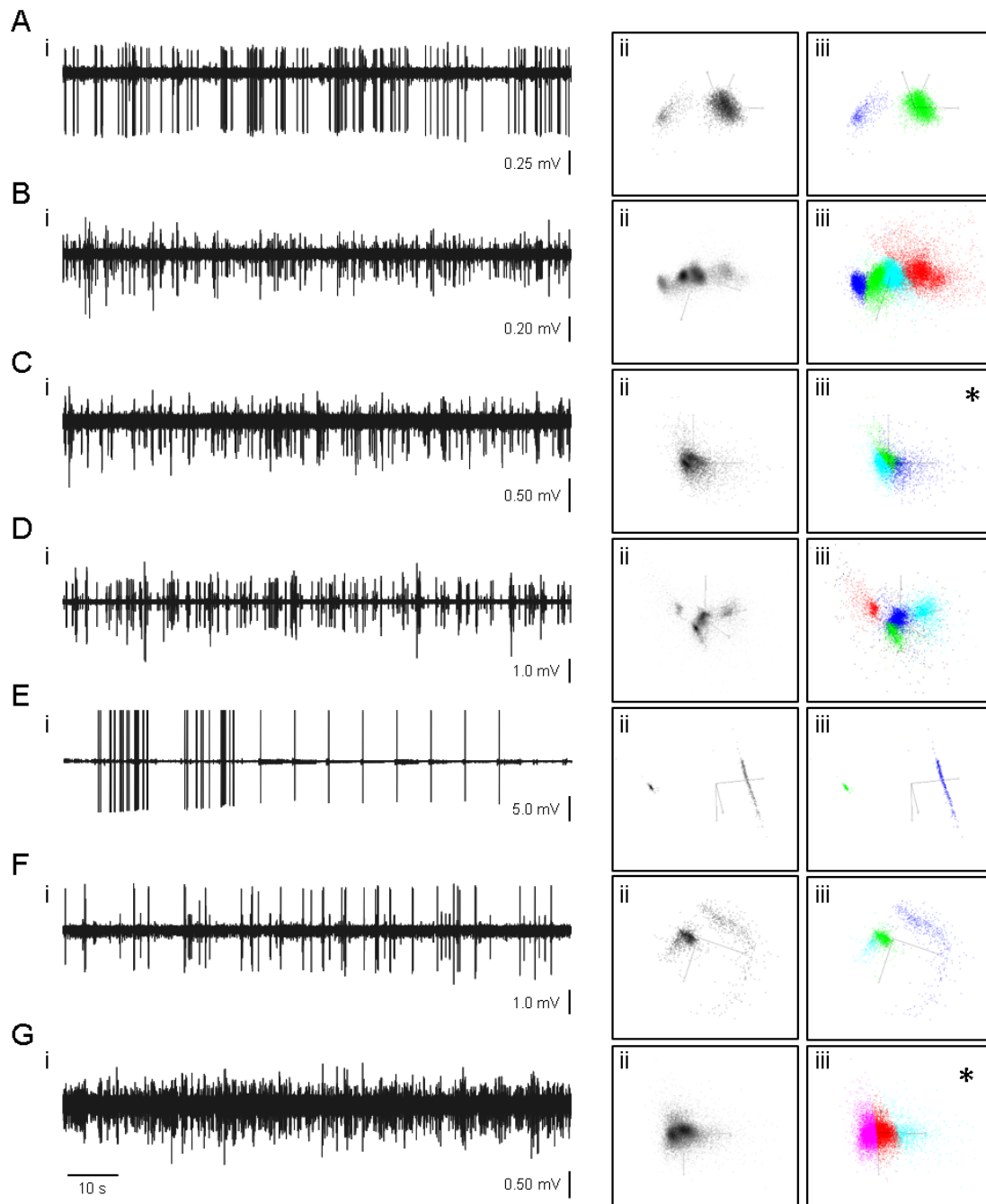


Figure 2.3 (legend right)

**Figure 2.3 (left) Extracellular recordings and spike sorting** Example traces (i) and spike sorting based on principle component analysis of spike waveforms (ii-iii) for several different extracellular electrode types used throughout the study. **(A)** High signal-to-noise and **(B)** low signal-to-noise recordings using 0.1 MOhm tungsten electrodes in *Holcocephala*; **(C)** low signal-to-noise 0.1 MOhm tungsten electrode recording in *Calopteryx*. Signal of this quality in which spike clusters are barely identifiable would not be used for analysis. **(D)** recording from a severed *Coenosia* cervical connective using a broken-tip glass suction micropipette to ‘clamp’ severed axons; **(E)** High signal-to-noise example trace from *Calopteryx* using a 5.1 MOhm glass-insulated tungsten electrode with 11  $\mu\text{m}$  tip; **(F)** Typical data quality when using high-resistance glass-insulated tungsten electrodes in *Calopteryx*, here using a 13  $\mu\text{m}$  tip 3.25 MOhm electrode. **(G)** Example low signal-to-noise trace from *Calopteryx* using a 14 $\mu\text{m}$  4.9 MOhm glass-insulated tungsten electrode. Signal of this quality in which spike clusters are barely identifiable would not be used for analysis. All traces are 100 sec, scale indicated at lower left in (G). Voltage scales indicated for each trace. Asterisks indicate example traces that would not be used for further analysis.

Commercial 0.1MOhm polyester-insulated tungsten electrode occasionally yield high signal-to-noise recordings with unambiguous spike separation (Figure 2.3A), however most recordings are composite signals from several neurons (Figure 2.3B-C). Whilst single units are often visible in PCA space (Figure 2.3B), there is usually extensive overlap between units. Other extracellular recording methods include breaking the tip of a glass micropipettes and using suction to clamp onto the end of a severed ventral cord just anterior to the prothoracic ganglion with the aim to suck up a small subset of axons. This method has a relatively lower success rate compared to tungsten electrodes, but signal-to-noise can be very high (Figure 2.3D), although these usually represent a composite signal from several axons (Figure 2.3Dii-iii).

The most reliable extracellular recording method to yield consistent high signal-to-noise single unit isolation were sharp glass-insulated tungsten electrodes with a tip length  $\sim 10\text{-}15\mu\text{m}$  and impedances between 2-5 MOhm (Figure 2.3E-G) (Microelectrodes Ltd., Cambridge, UK). In Odonata these electrodes often yield exceptionally high signal-to-noise recordings (Figure 2.3E) resembling intracellular data. In other cases, signal-to-noise is lower (Figure 2.3Fi) but nonetheless yields clear unit separation in PCA (Figure 2.3Fii-iii). Due to the small tips and high impedances, these electrodes often isolate only 1-2 neurons at a time, which simplifies the spike sorting process. However, for the same reasons, these electrodes are prone to missing neurons all together yielding exceptionally poor recordings (Figure 2.3G). The choice of high- versus low-resistance electrodes reflects a dichotomy between high success rate multi-unit recordings that yield ambiguous spike sorting, and relatively lower success rate recordings with 1-2 units yielding unambiguous spike sorting.

## 2.4.2 Eyepatches and prisms

A 3-D printed eyepatch machine was used to position eyepatches independently in front of each eye (Figure 2.4A). Eyepatches were made from either black card (160gsm, WHSmith’s) or translucent

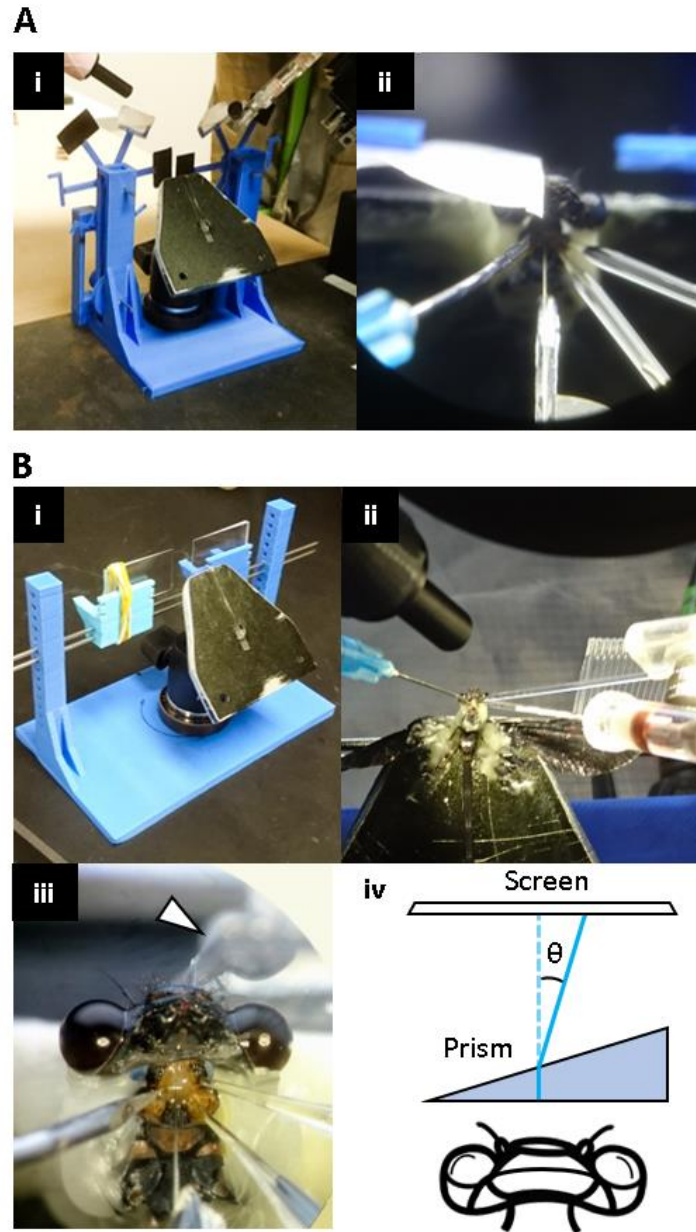


**Figure 2.4 Eye patches and Prisms (A) (i-ii)** A 3-D printed eyepatch machine was used to position eyepatches made from different materials independently in front of each eye. **(ii)** An eyepatch made from translucent electrical insulation paper is placed in front of the right eye of a demoiselle (animal's perspective). **(B) (i-ii)** Prisms were positioned in front of the eye using a linear sliding mechanism in order to keep the prisms at a constant horizontal angle. **(iii)** a prism (white arrow) is positioned in front of the left eye of a demoiselle during electrophysiological recording. **(iv)** Schematic illustrating the position of the prism in front of both eyes and the direction of refraction of the visual stimuli that the demoiselle would experience (demoiselle orientation same as in (iii)).

electrical insulation film (RS Components LTD, product 536-3980). By rotating the eyepatch holder for either eye, these eyepatches could be interchanged during electrophysiological recordings to test the effect of covering each eye independently with different types of materials.

Prisms were positioned in front of the eyes using a 3-D printed machine using a horizontal sliding mechanism (Figure 2.4B). This linear actuation mechanism was chosen to control the horizontal angle of the prisms, as any variation in this angle between prism types would alter the direction of refraction through the prism around the roll dimension of the animal. The prism machine was lubricated using silicon grease (Trident) to minimize the probability of jolting the preparation whilst moving the prisms during electrophysiological recordings.

### **2.4.3 Data Analysis**

All data analysis was performed in MATLAB (Mathworks) using custom written code.

#### **2.4.3.1 Visual receptive field mapping**

##### *Stimulus*

Visual receptive field mapping was based on a previously developed stimulus protocol (Gonzalez-Bellido et al., 2013). This stimulus consisted of a sequence of 3000 target trajectories, with each trajectory composed of three phases (Figure 2.5Ai-ii): (1) a small stationary target (standard size  $2^\circ \times 2^\circ$ ) appears at a random position on the screen for 150 ms (red phase), (2) the target moves in a random direction for 100 ms at constant speed (standard speed  $160^\circ/\text{s}$ ; green phase), (3) the object disappears followed by a 150 ms delay before the next trajectory is presented (grey phase). This method allows receptive fields to be mapped with high spatial resolution whilst also measuring latency and avoiding habituation of the cell responses (Gonzalez-Bellido et al., 2013).

##### *Receptive fields*

For each 3000-trajectory stimulus presentation, extracellular spikes were detected with a manually adjusted voltage threshold and single units isolated with spike sorting (Figure 2.5Aii-iv; see section 2.4.1). The receptive field of each code was calculated from spikes falling within the moving phase of the stimulus trajectories (Figure 2.5Av-vi) as previously described (Gonzalez-Bellido et al., 2013). The latency for each spike-sorted code was calculated to adjust for the time taken for visual responses to reach the recording site in the cervical connective (Figure 2.5Avii) (See next section, Latency). Adjusting spike times by subtracting this latency gives a more accurate timestamp to correlate exactly where the target stimulus was in the visual field when the response was initiated (Gonzalez-Bellido et al., 2013). Direction receptive field maps were calculated by noting the pixel locations of the target (including the full area of the target) and the direction of target movement that was associated with each latency-adjusted spike time (Figure 2.5Aviii). If a given (x,y) pixel coordinate on the screen was associated with more than one spike, the directions of target movement were averaged using the circular mean (CircStat toolbox) (Berens, 2009). As such, direction receptive field maps do not represent the

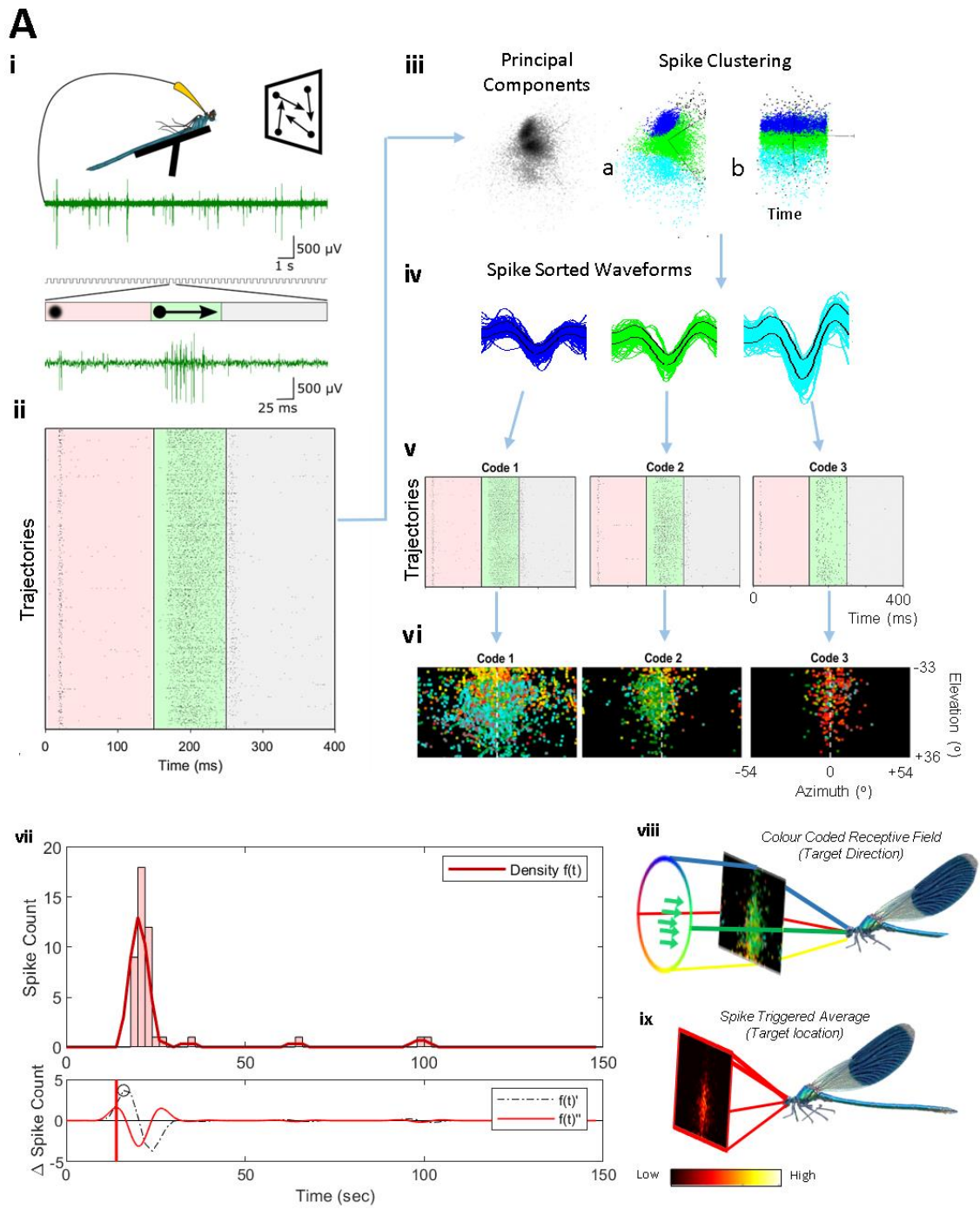


Figure 2.5 (legend right)

**Figure 2.5 (left) Visual receptive field mapping (A)** Workflow for extracellular receptive field analysis. **(i)** Damselflies were positioned for extracellular recordings on a platform with the anterior aspect of the head positioned to view a screen onto which was projected a series of small target trajectories. Each trajectory consisted of a small target appearing stationary at a random location on the screen for 100 ms (red phase), moving in a random direction at constant speed for 150 ms (green phase), then disappearing for 100ms before the start of the next trajectory (grey phase). **(ii)** Extracellular ventral nerve cord spikes to 3000 of these trajectories displayed as a raster plot. Damselfly TSDNs typically respond with an on transient to object appearance, followed by activity throughout movement of the object. **(iii-vi)** The population of recorded spikes are spike sorted (iii-iv), and the spikes within the moving phase for each spike-sorted code processed into receptive fields (v-vi). **(vii)** Latency was calculated from the stationary phase and subtracted from each spike time to more accurately correlate the stimulus location at time of spike initiation. **(viii-ix)** Receptive fields are displayed as a direction receptive field map to indicate directionality of responses, and spike triggered average (STA) maps to represent the relative spiking activity across the visual field.

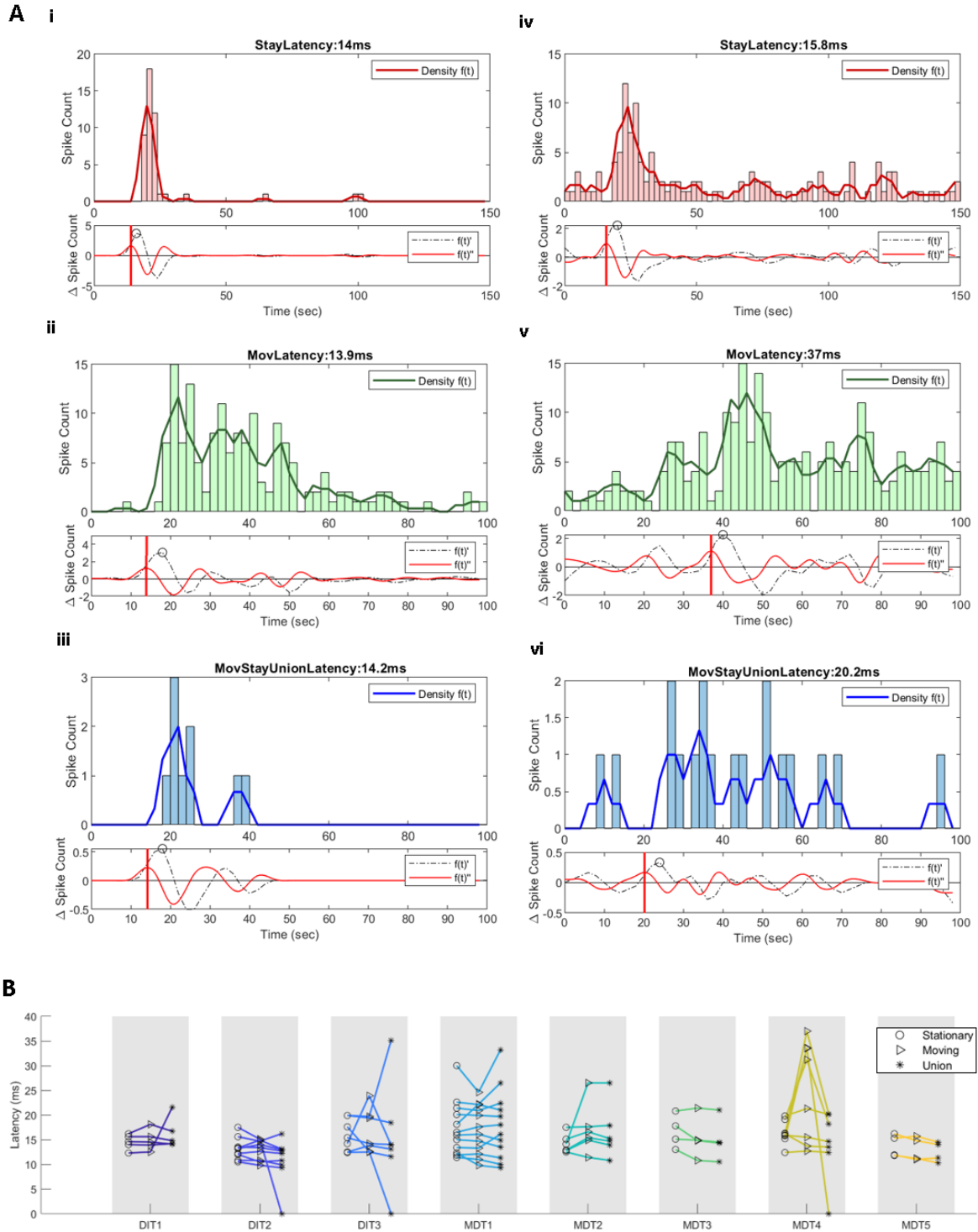
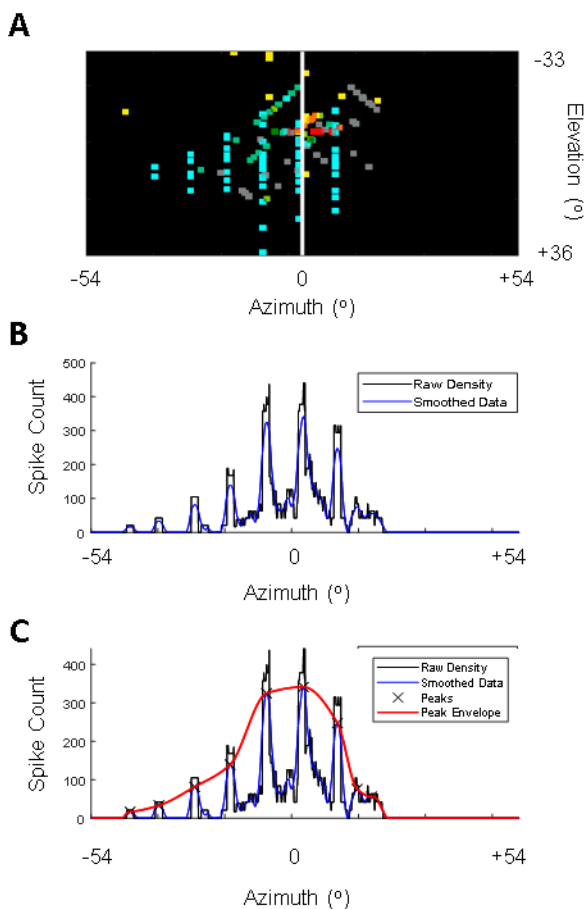


Figure 2.6 (legend right)

**Figure 2.6 (left) Latency calculations (A)** Top panels, peri-stimulus time histogram and density. Bottom panels, automated derivative latency calculation. The first derivative of the PSTH density (black line,  $f(t)'$ ) typically peaks within the main rising phase of spike onset from which latency is calculated. The peak of the second derivative (red line,  $f(t)''$ ) is taken as the spike latency and represents the initiation of spike onset (vertical red line). **(i-iii)** Example of a recording where stationary (i) and moving phase latencies (ii) are approximately the same. **(iv-vi)** Example of a recording where the stationary (iv) and moving phase latencies (v) differ. This often arises from objects originating outside the receptive field of the neuron, and latencies appear longer as the object needs to move into the receptive field before spikes are initiated. **(vi)** This can be mitigated by only including trajectories with responses within both the stationary and moving phase, although the number of spikes within this condition is often very low (compare y-axis range in iv-vi), which disrupts the automated latency calculation. **(C)** Comparison of latency measurements for stationary (circles), and moving phases (triangles), and trajectories that include both stationary and moving phase spikes (union, asterisks). Data of damselfly TSDN cell types from Chapter 3.



**Figure 2.7 Analysis of rasterized visual stimuli**

**(A)** Example receptive field measured with a rasterized stimulus. **(B)** The receptive field is projected onto the azimuth axis, resulting in a spike count density, which is smoothed using a Savitsky-Golay filter. **(C)** To estimate the full receptive field, spike count peaks are identified, and an interpolated enveloping curve is calculated between peaks.

relative activity across the visual field, with each pixel location given an equal binary weighting (spike or no spike). Spike triggered average (STA) maps were generated to represent the relative activity across the visual field, and were calculated by summing the number of spikes associated with each (x,y) pixel location on the screen (Figure 2.5Aix).

### ***Latency***

Spike latency was calculated from the peri-stimulus time histogram (PSTH) of the first spike time in the stationary phase of each trajectory (i.e. only one spike time per trajectory; 2.6A). Latency was defined as the moment when the PSTH density (Figure 2.6A) starts to rise (indicated by the vertical red line in bottom panels of Figure 2.6A). This was calculated as the time of the maximum peak in the second derivative (red curve,  $f(t)''$ ) that precedes the maximum peak in the first derivative (black curve,  $f(t)'$ ) of the PSTH.

The latency calculated from stationary objects was used in receptive field mapping (Figure 2.6Ai,iv). Latency could be calculated from either the stationary phase (red) or the moving phase of the trajectory (green) (Figure 2.6A-B). Latency calculated from the moving phase of each trajectory would in theory account for any additional processing time associated with object movement; however, some responses within the moving phase may result from a target trajectory where the object starts outside the receptive field. This leads to an artificially longer latency as the object needs to move into the receptive field before eliciting a spike (Figure 2.6Aii,v). Whilst only using trajectories that have responses in both stationary and moving phases would mitigate this bias, in practice this typically reduces the number of spikes in the dataset making the derivative latency calculation less reliable (Figure 2.6Aiii,vi). In practice, latencies calculated within the stationary phase were more reliable and amendable to the automated derivative calculation (Figure 2.6B).

### ***Rasterized stimulus analysis***

Receptive fields can be estimated faster but less accurately using a rasterized stimulus that scans across the full extent of the screen in a reduced number of directions (Figure 2.7A). The resulting receptive field has a sparse activity pattern reflecting the sparsity of the rasterized stimulus (Figure 2.7A). To estimate the full receptive field, the receptive field is projected onto the azimuth axis forming a spike count density (Figure 2.7B). The raw density is smoothed using a Savitsky-Golay filter and peaks are identified to create an interpolated enveloping curve (Figure 2.7C). This envelope over the sparse receptive field density provides an estimate of the full receptive field for further analysis (Figure 2.7C).

## 2.5 Anatomy

### 2.5.1 2-Photon whole brain imaging

#### *Ventral cord backfills*

For ventral cord backfills, animals were initially prepared as for electrophysiology (section 2.2.1). The ventral cord was cut posterior to the prothoracic ganglion with fine scissors and surrounded with Vaseline, taking care not to seal the severed end. A Vaseline seal is important to prevent dye leaking into the ventral cavity and the head capsule, which would otherwise increase non-specific background staining. Once the cord is fully surrounded the cord was carefully cut anterior to the prothoracic ganglion. A small ~1µl droplet of 10% lysine-fixable Texas Red 3000-dextran (Invitrogen) was applied to the tip of the severed ventral cord. The dye droplet was enclosed in Vaseline, and the animal stored at 4°C in a chamber humidified with wet paper towel overnight. The whole animal was fixed the next morning in 4% paraformaldehyde at room temperature for 24 hrs. The brain was dissected, de/rehydrated in ethanol, and incubated in 0.05% lucifer yellow (LY; Invitrogen) overnight at 4°C to stain neuropil (Kanzaki et al., 2003; Reborá et al., 2013). The brain was transferred to 4% paraformaldehyde for 1 hr at room temperature to fix LY to the tissue. The brain was then cleared following previous protocols (Gonzalez-Bellido and Wardill, 2012).

#### *Imaging*

Cleared brains were submerged in 97% TDE (2,2'-Thiodiethanol) and positioned into a small groove of Sylgard (Sigma-Aldrich) in a petri dish. The brains were strapped down into place using two laterally positioned strips of Sylgard (Figure 2.8A). Sylgard straps were carved out of the original Sylgard plate using a scalpel and should be shaped as a triangular prism. The straps should be in the reverse orientation to when they were carved such that the original Sylgard surfaces sandwich tightly together. The straps should be long and wide to create enough surface tension to adhere to the Sylgard plate, however if created too large surface tension will be lost due to the low frequency curvature of the Sylgard surface when poured into petri dishes. An additional posteriorly placed Sylgard strap is included if a substantial amount of ventral nerve cord is still present (as is usually the case with Odonates).

Brains were imaged using an Olympus XLSL Plan N 25x /1.00 Glyc MP ∞/0-0.23/FN18 multiphoton objective, a Newport Spectra-Physics InSight® DS+™ laser tuned to 920 nm, and a Bruker (Prairie Technologies) *in vivo* multiphoton microscope using GFP (500-550 nm) and RFP detection channels (610-650 nm) (Figure 2.8B). Images were acquired as an x,y-tiled Z-stack (Figure 2.8C) with isovoxel (x,y,z) resolution (Prairie View v5.4), and stitched in Fiji (Preibisch et al., 2009; Schindelin et al., 2012). Image brightness and contrast of the stitched hyperstacks was adjusted manually in Fiji. Hyperstacks were converted to 8-bit, transformed into an RGB-composite stack (color > make composite), and exported as a tiff image sequence to load into Vaa3D for further processing (Peng et al., 2010). Image

**Figure 2.8 (right) Multiphoton whole brain imaging** (A) A demoiselle brain mounted on Sylgard. The brain is positioned in a shallow groove carved out of the Sylgard plate and is secured into position by two laterally placed Sylgard straps for the optic lobes, and one posteriorly positioned Sylgard strap for the ventral nerve cord (white arrows). (B) 2-photon setup. Sample is mounted on an x,y linear platform beneath the Olympus 25x objective. The long 8 mm working distance of this objective necessitates an overflow dish for TDE. (C) Example multi-tile setup for z-stack imaging of a damselfly midbrain. This single (middle) slice of the z-stack includes sixty 512x512 pixel (204.8x204.8  $\mu\text{m}$ ) tiles. (D) Prairie View 5.4 GUI. (i) Image x,y resolution and scanning mode are selected in the top half of the GUI. Other imaging parameters can be found in the tabs in the lower half of the GUI. The ‘2-P laser’ tab sets the wavelength tuning of the 2-photon. (ii) The ‘Power/Gain’ tab sets the laser power (Pockels) and sensor (PMT) sensitivity. (iii) The ‘Z-Series’ tab sets the z stack bounds (start and stop position) and the z resolution (step size) which should be matched to the x,y pixel resolution. The table in the ‘Z-Series’ tab also allows variation of the laser power at different depths in the Z-stack. Since light becomes attenuated through tissue, the laser excitation power needs to be increased at deeper levels in the tissue to generate the same extent of fluorophore excitation. Pockels power can be manually adjusted in this tab.

sequences were loaded into Vaa3D using the ‘image geometry > crop3d\_image\_series > crop a 3D stack from image series’ plugin.

## 2.5.2 Macrophotography and pseudopupil measurements

Animals were photographed using a DSLR (Digital Single-Lens Reflex camera) macrophotography set-up (Figure 2.9Ai-ii). A manual-aperture Canon 50 mm FD-mount prime lens was reverse-mounted onto a Canon 7D Mark I DSLR camera. By using a reverse ring adapter to mount the lens in reverse orientation onto the DSLR body, the effective focusing distance of the lens is decreased, allowing the camera to focus onto objects closer to the lens. This results in magnification of small objects to fill the camera sensor (*see* <http://extreme-macro.co.uk/single-reverse-lens/>). Alternatively, the Canon 65mm MPE macro lens was used for focus-stacked macrophotographs of Odonate heads in Chapter 3. To reduce image blur due to camera wobble, the camera was stabilized on a tripod and image acquisition was controlled by a USB tether to a laptop running DigiCamControl (<http://digidigicamcontrol.com/>). Images were typically acquired at aperture f/8, with approximately 1/160 shutter speed and ISO 100-400, and additional flash lighting. The flash lighting was diffused through a DIY diffuser made from a plastic cup and a white pillow protector (Figure 2.9Ai-ii).

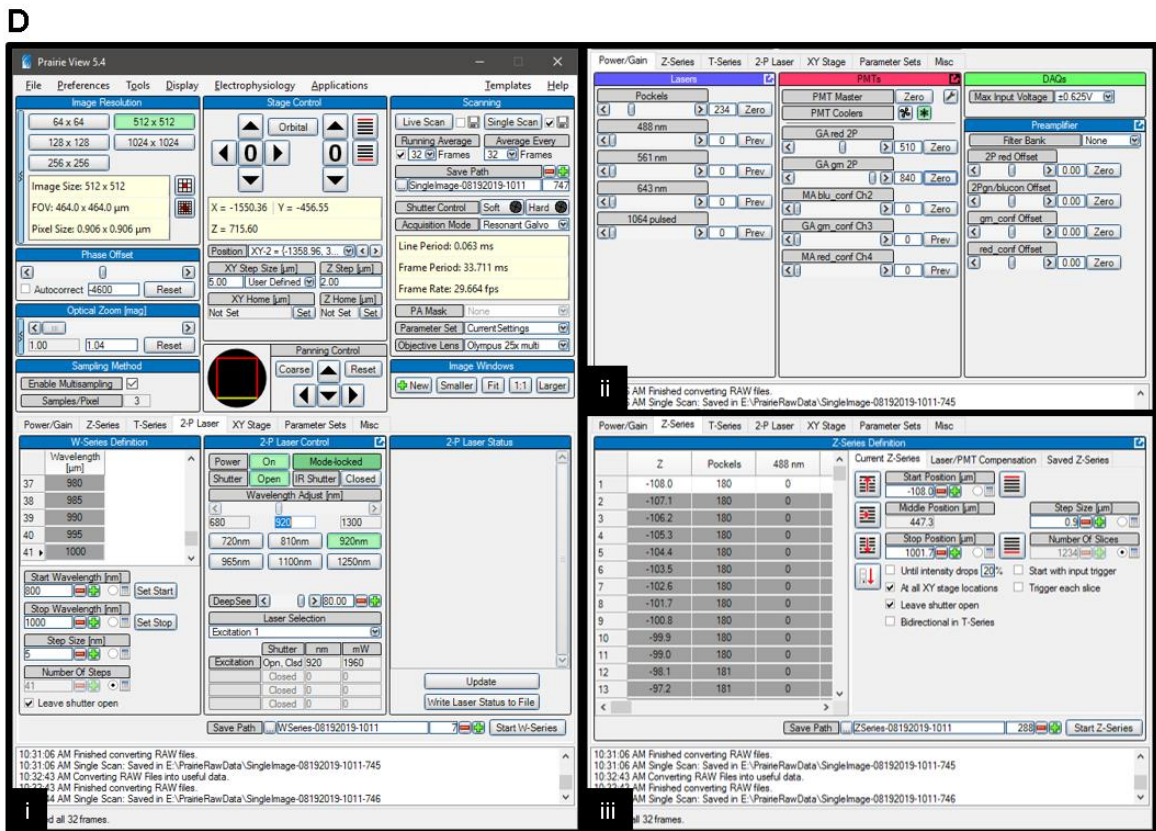
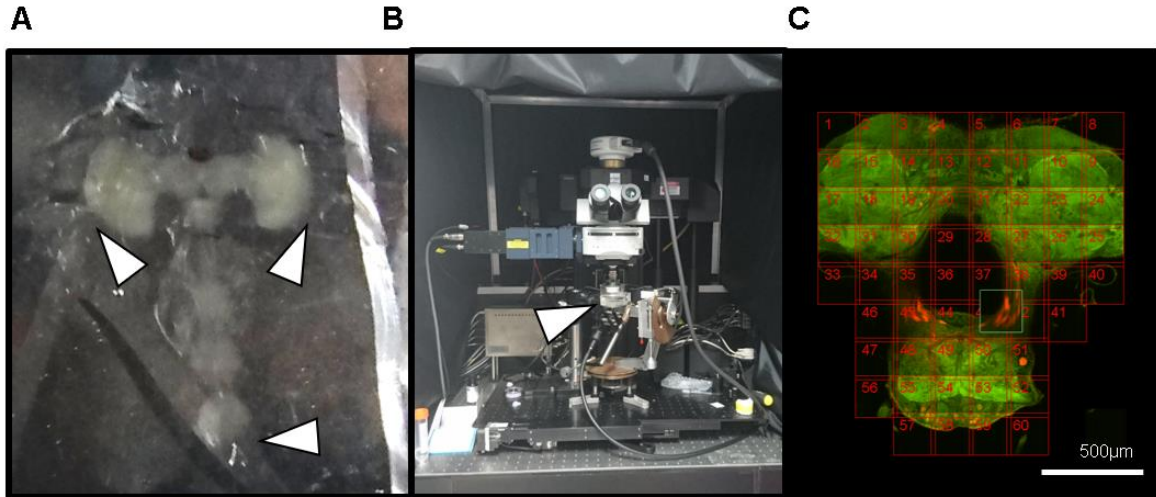
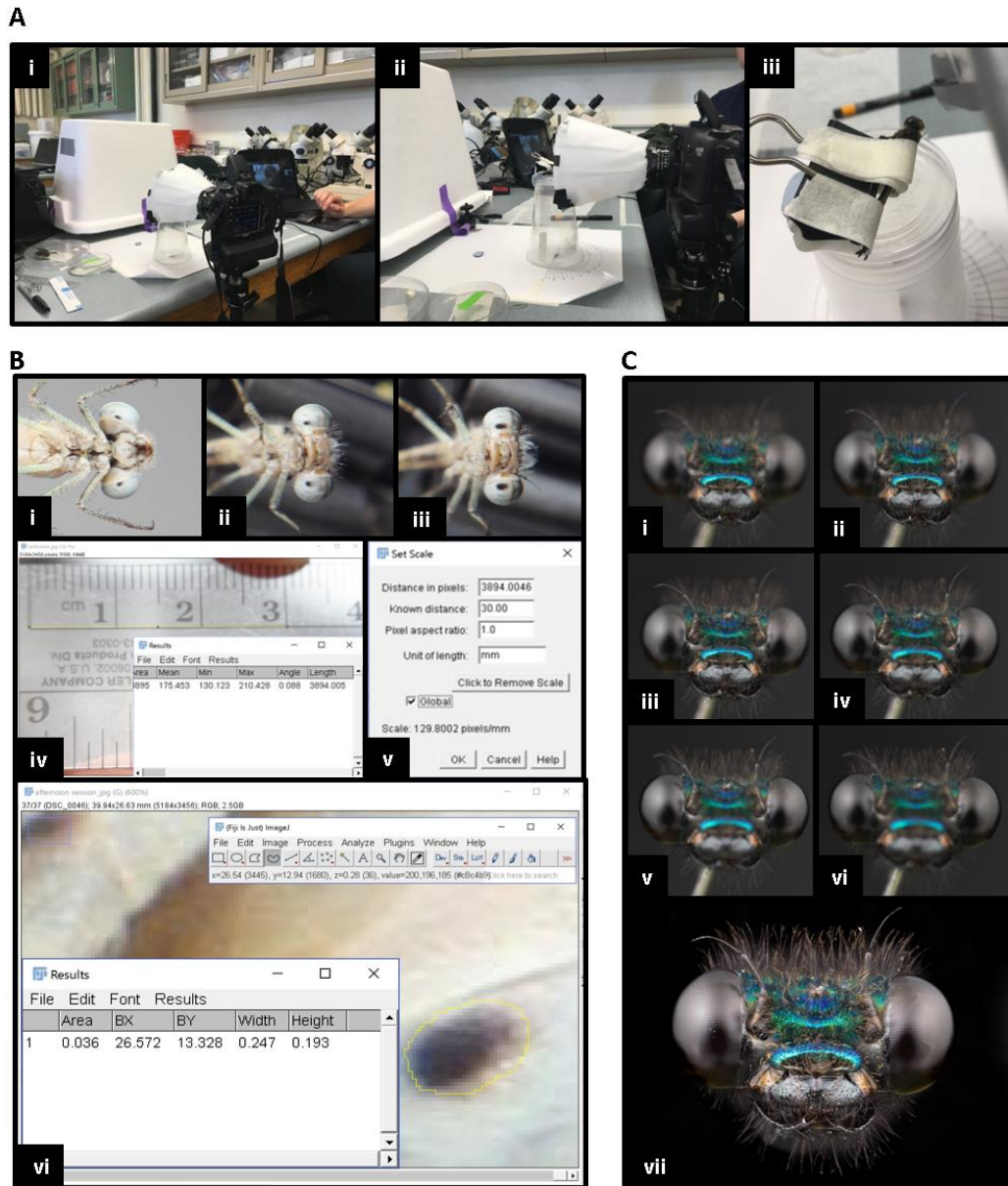


Figure 2.8 (legend left)



**Figure 2.9 Macrophotography and pseudopupil measurements** (A) Macrophotography setup for pseudopupil measurements. A DSLR mounted on a tripod acquires images via a USB tether (i-ii). The animal is secured in a Bulldog clip with tape and mounted to a rotation platform (iii). (B) (i-iii) Incremental rotation a damselfly. Images were calibrated in Fiji using a ruler (iv-v), and pseudopupils were measured using the freehand tool (vi). (C) Sequential macrophotographs moving the region of focus across the sample (i-vi) were stitched to create a fully in-focus demoiselle head (vii).

### *Pseudopupil measurements*

To sample the pseudopupil from different angles, the animal was positioned on a DIY turntable platform made from a plastic cup positioned on a sheet of paper with 5-degree angular increments marked using a protractor (Figure 2.9A-B). The animal was positioned on its side such that yaw rotation of the

platform rotated the animal along the ventral-dorsal axis (Figure 2.9Aiii). The animal was mounted onto the rotation platform using a bulldog clip which held the animal by the wings close to the wing hinge. The bulldog clip was secured to the plastic cup using Blu-Tac to enable fine alignment of the head. To keep the animal still throughout the experiment, the legs were sequestered using tape, and the back of the head was glued to the thorax with fast-curing UV glue (5 Second Fix™), taking care to fix the head in an aligned, natural pose (Figure 2.9Aiii).

Images were calibrated in FIJI using a photograph of a ruler (Figure 2.9Biv-v). The pseudopupil was selected using the freehand tool in each image (Figure 2.9Bv) and the resulting data was loaded into MATLAB. Data was smoothed using the `sgolayfilt()` function with a 3<sup>rd</sup> degree polynomial and a 7 point window.

### ***Focus stacking***

Due to the inherently shallow depth-of-field of high-magnification macrophotographs, only a small region of the image is in focus for any given photograph. By combining multiple images with slightly different parts of the subject in focus, a final fused image can be generated in software with the entire subject in focus. For photographs of Odonate heads in Chapter 3, the region of focus was scanned across the head using the linear axis of a 3D printer moving in 100µm steps (Figure 2.9C).

## **2.6 High speed videography**

### **2.6.1 Visual stimuli**

Artificial prey for *Pachydiplax longipennis* dragonflies and *Calopteryx maculata* damselflies were fashioned from either black or silver 3 mm beads dangling on fishing line, respectively.

### **2.6.2 Data acquisition**

Two synchronised Photron SA2 cameras were initially used to film *Calopteryx maculata* demoiselles attacking artificial prey within a temporary outdoor plastic tent at York College, Pennsylvania, 2017. Later experiments filming *Calopteryx maculata* demoiselles in the wild (York, Pennsylvania, 2019; Figure 2.10A), and *Pachydiplax longipennis* dragonflies in the lab (Minnesota, 2019) used a similar synchronised Photron Mini AX200 dual camera system. Nikon 24 mm AF-S NIKKOR f1/8G ED lenses were used to film dragonflies and demoiselles in flight arenas, and the more telescopic Nikon 85mm AF-S DX Micro NIKKOR f/3.5G ED VR lenses were used to film wild demoiselles at creeks. All highspeed recordings were acquired at 1000 frames/sec with apertures ~f/5.6-8.

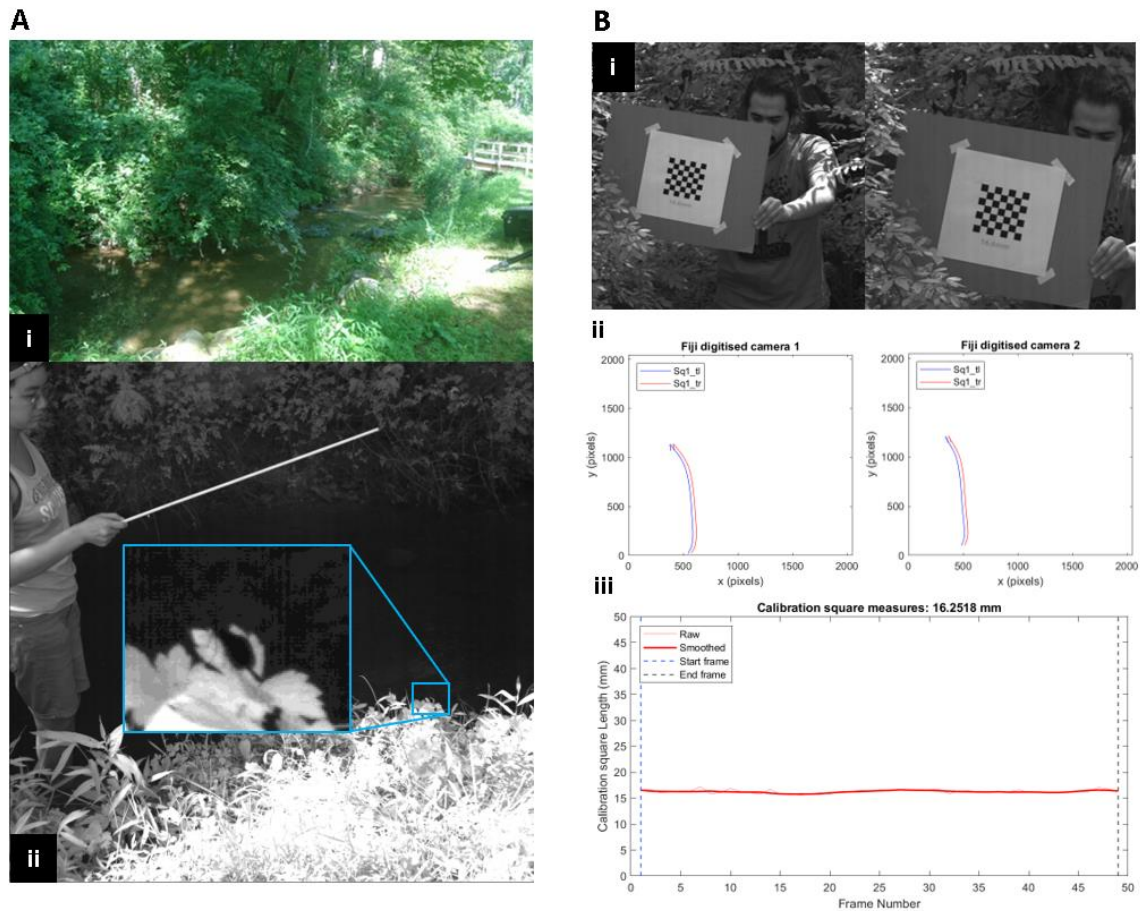


**Figure 2.10 Highspeed videography calibration (A)** (i) *Calopteryx maculata* habitat. Photographed at Nixon Park, York, Pennsylvania, USA, 2019. (ii) Typical raw image acquired with the highspeed setup. Inset: damselfly perched on a leaf. **(B)** (i) Calibration of the dual camera system using checkboard protocols described previously (Wardill et al., 2015, 2017). (ii-iii) Calibrations were validated by 3D reconstructing the corners of the calibration checker squares. (ii) The digitized position of the calibration checker corners in the two cameras during the calibration sequence. (iii) Measurement of the calibration checker side length after 3D reconstruction. In this case the 16 mm calibration square was reconstructed with an average length of 16.3 mm. Example images acquired by Siddhant Pusdekar, Molly Liu, and Daniel Galeano at Nixon Park, York, Pennsylvania, USA, 2019, and analysed by Jack Supple.

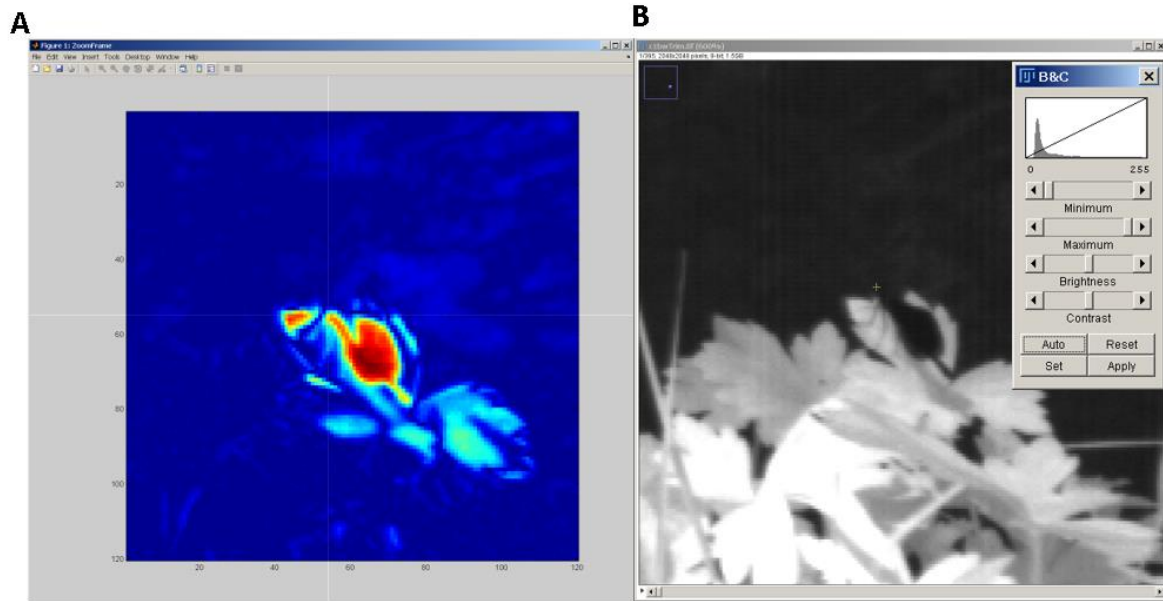


**Figure 2.11 Image contrast adjustment in MATLAB and Fiji** (A) Default image representation in MATLAB. (B) Image representation in FIJI. Fiji offers more accessible manipulation of the image histogram (B, inset) compared to MATLAB, which helps improve the contrast of the subject (here a demoiselle damselfly) from the cluttered background foliage.

### 2.6.3 Calibration

The two-camera system was calibrated for 3D reconstruction based on a checkerboard calibration sequence (Figure 2.10B) using scripts originally written by J.Y. Bouguet's laboratory (Caltech, [http://www.vision.caltech.edu/bouguetj/calib\\_doc/](http://www.vision.caltech.edu/bouguetj/calib_doc/)) as previously described (Wardill et al., 2015, 2017). Calibration validity was checked by 3D reconstructing the corners of the calibration squares which have known length (Figure 2.10Bii-iii).

### 2.6.4 Digitisation and 3D reconstruction

For each highspeed video, the two synchronised image sequences were digitized to yield two (x,y)-coordinate time series for the points of interest. These stereo (x,y)-coordinate timeseries pairs were then reconstructed into 3D cartesian space using the checkerboard calibration as described previously (Wardill et al., 2015, 2017).

Digitisation quality is dependent on the contrast of acquired images. Contrast can be enhanced by the positioning the subject in front of a white background and/or using small focusing distances to magnify the subject on the camera sensor. Demoiselles are relatively skittish animals and their hunting behaviour is not very robust to artificial habitat perturbations. Demoiselles do not predate reliably within controlled environments such as a mesh or plastic tent (either indoors or outside). Furthermore,

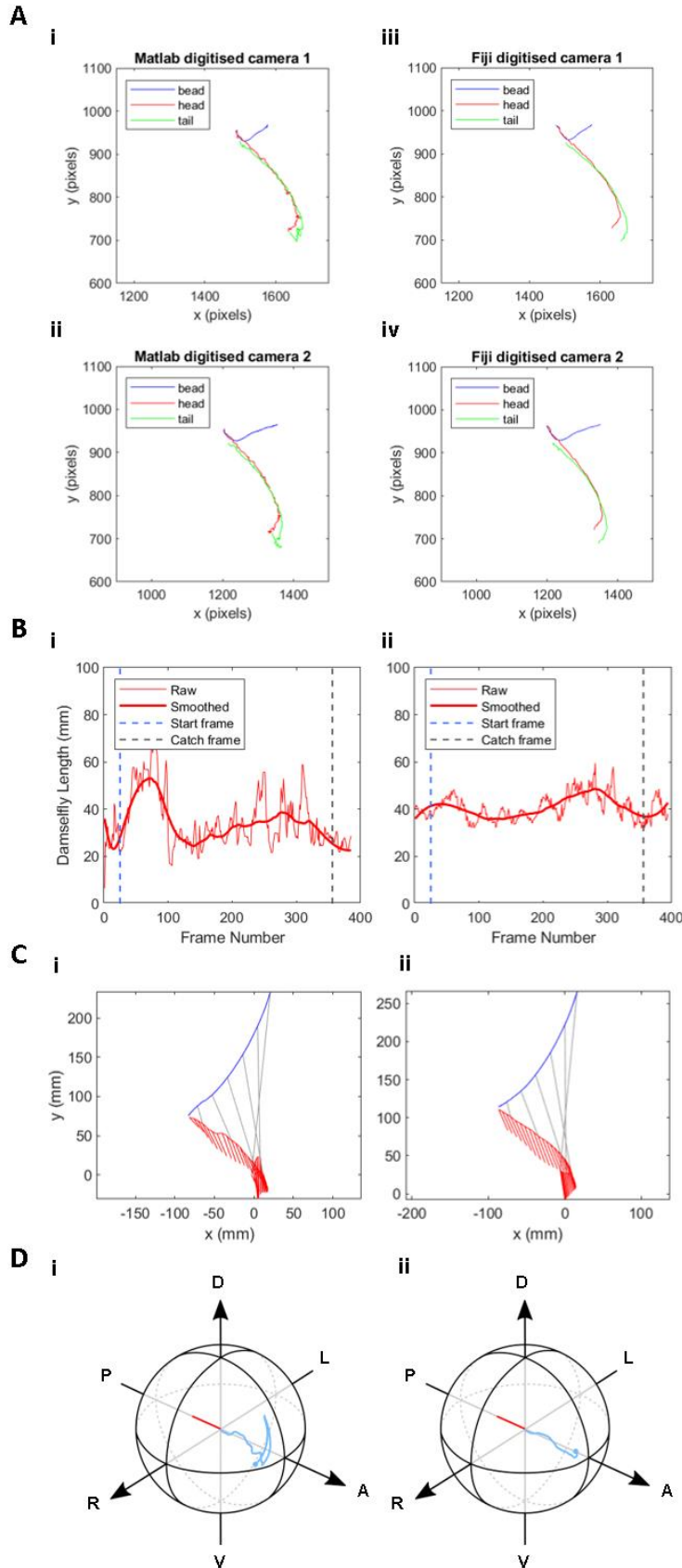


**Figure 2.12**

**Digitisation comparison between MATLAB and FIJI** (A) Digitisation output using either MATLAB (i-ii) or Fiji (iii-iv) protocols for each camera. (B) Measurements of 3D reconstructed demoiselle body lengths for MATLAB (i) and Fiji (ii) digitisations. (C) 3D reconstructed trajectories for MATLAB (i) and Fiji (ii) digitisations (following color coordination used in Chapter 3: bead is blue, head is continuous red line, body axis is represented as a straight red line in 100ms intervals). (D) Spherical plots tracing the path of the prey in the predator's visual field throughout a predatory flight. The predator body axis is in red, the start position of prey is represented by a blue circle on the surface of the sphere, and relative path of the prey through the predator's visual field is indicated as a blue line. The effect of digitisation quality in MATLAB (i) vs Fiji (ii) is reflected in the variation in 3D reconstructed trajectories.

their natural predatory habitat along riverbanks makes it difficult to position the animal against high-contrast backdrops or position the videography equipment close to the subject (Figure 2.10Ai). These factors lead to raw images of the form shown in Figure 2.10Aii. Raw data of this contrast was not amendable to digitisation using MATLAB protocols described previously (Wardill et al., 2015, 2017) (Figure 2.11-2.12). Digitisation was improved using the multipoint tool in Fiji (Figure 2.12), as the image histogram can be easily adjusted to generate the best possible image contrast (Figure 2.11B, inset).

### **2.6.5 Behavioural analysis**

Following 3D reconstruction, the position of the prey, predator body axis, and the line of sight between the prey and predator's head was plotted in cartesian space (Figure 2.12C). To trace the path of the prey within the predator's visual field during predatory flight, the body axis of the predator from each frame of the recording were superimposed (Figure 2.12C). Alignment assumed that the body axis did not rotate around the roll axis during flight. For clarity of comparison, all prey trajectories within the visual field were normalised to the maximum radial distance from the head (Figure 2.12C). A typical predatory flight is therefore represented as the prey starting at the surface of the sphere (start of predatory flight) and moving in towards the centre of the sphere (position of the predator's head) (Figure 2.12C).



# Chapter 3

## Binocular encoding in the premotor target tracking system of damselflies

### 3.0 Acknowledgements and contributions

Extracellular electrophysiology data were collected by Daniel Pinto-Benito and Jack Supple. 2017 *Calopteryx maculata* behavioural data were collected by Sam Fabian and Jack Supple. 2019 *Calopteryx maculata* behavioural data were collected by Siddhant Pusdekar, Molly Liu, and Daniel Geleano, digitised by Siddhant Pusdekar and Jack Supple, and analysed by Jack Supple. Pseudopupil measurements were organized by Jack Supple and collected during a group teaching laboratory session at Itasca state park by Ashley Lee, Brevin Bushlack, Christina Gilbert, Emilia Skogen, and Samuel Taylor. *Calopteryx maculata* intracellular data were collected by Rob Olberg and Paloma Gonzalez-Bellido in July 2019. Brains were imaged by Jack Supple and Paloma Gonzalez-Bellido. Neuron tracing was performed by Hanchuan Peng, Lijuan Liu, Shengdian Jiang, Yimin Wang, and Jintao Pan. All other data collection and analysis by Jack Supple. Full data sets are presented in a supplementary information (SI) section at the end of the Chapter. Much of this work is now published in the journal *Current Biology* (Supple et al., 2020).

### 3.1 Introduction

Despite sampling the visual world through two eyes, our brain fuses these images into a cyclopean percept with a single point of view (Barendregt et al., 2015). Binocular image fusion imparts several perceptual advantages including enhanced visual sensitivity (Campbell and Green, 1965; Elberger, 1989), decreased reaction times (Blake et al., 1980), and the potential to calculate depth from image disparity (Nityananda and Read, 2017). As such, binocularity is often found in visually guided predatory species (Lythgoe, 1979).

Odonata is an ancient predatory lineage comprising two distinctive extant sister groups, the damselflies (Zygoptera) and dragonflies (Eiprocta, comprising Anisoptera and Epiophlebioptera) (Figure 3.1). Damselflies and dragonflies share a last common ancestor ~270 Million Years Ago (MYA) and have subsequently diverged in behaviour and anatomy (Corbet, 1999; Grimaldi and Engel, 2005). Dragonflies are well known for their large round compound eyes and agile interception flights to catch flying prey (Olberg et al., 2007). To date, a large body of work describes the behavioural and neurophysiological mechanisms underlying target interception in dragonflies (Gonzalez-Bellido et al., 2013; Lin and Leonardo, 2017; Mischiati et al., 2015; Nordström et al., 2011; O'Carroll, 1993; Olberg, 1981b, 1986; Olberg et al., 2007; Wiederman and O'Carroll, 2013). Such studies have focused on abundant Anisopteran dragonflies (families *Aeshnoidea*, *Corduliidae*, and *Libellulidea*) that intercept prey from below, stabilising the prey image upon a cyclopean dorsal fovea (Gonzalez-Bellido et al., 2013; Lin and Leonardo, 2017; Mischiati et al., 2015; Nordström et al., 2011; O'Carroll, 1993; Olberg, 1981b, 1986; Olberg et al., 2007; Wiederman and O'Carroll, 2013). This fovea is formed by fusing the compound eyes at the dorsal surface into a continuous plane of ommatidia with reduced binocular overlap, known as a holoptic eye (Figure 3.1B) (Perry and Desplan, 2016).

Target movement across the dragonfly dorsal fovea is encoded at the pre-motor level by a small population of eight bilaterally symmetric Target Selective Descending Neurons (TSDNs) (Frye and Olberg, 1995; Gonzalez-Bellido et al., 2013; Olberg, 1986). TSDNs receive input from the lateral protocerebrum, and project to the gnathal and thoracic motor centres with a total latency of less than 30 ms (Frye and Olberg, 1995; Gonzalez-Bellido et al., 2013; Olberg, 1986). Each TSDN type possesses a characteristic receptive field that is directionally tuned and spatially localised to a specific region of the dorsal visual field (Gonzalez-Bellido et al., 2013). As a population, TSDNs primarily encode target movement away from or along the midline (Gonzalez-Bellido et al., 2013) and TSDN firing can change the angle of attack and beating of the wings (Olberg, 1978, 1983), presumably reflecting their role as part of a reactive steering mechanism keeping the dragonfly locked onto the prey during pursuit (Gonzalez-Bellido et al., 2013).

The holoptic eye morphology of extant dragonflies appears to be a secondarily derived trait, which has evolved repeatedly within the Odonatoptera superorder throughout the last 320 MYA (Grimaldi and Engel, 2005; Nel et al., 2018). Holoptic eyes are absent in all damselflies, several extant dragonfly lineages (families *Gomphoidea*, *Petaluroidea*, and the basal dragonfly lineage *Epiophlebiidae*) (Figure 3.1) and extinct archaic Odonatopterans (Bechly et al., 2001). Instead, all damselflies have two conspicuously separated (dichoptic) compound eyes (Figure 3.1B) (Corbet, 1999; Horridge, 1978). Hitherto, little is known about the anatomical and neuronal specializations facilitating predation in any damselfly (Horridge, 1978). While most damselflies are known to hunt by snatching stationary prey from a substrate, a behaviour termed gleaning (Corbet, 1999; von Reyn et al., 2014), the demoiselle damselflies (*Calopterygidae*) are thought only to attack flying prey (Corbet, 1999; Rüppell, 1999),

somewhat similar to dragonflies. Demoiselles are thus uniquely placed within Zygoptera to investigate how frontal facing foveae with large interocular distance may influence prey tracking circuits, especially in comparison to those described in dragonflies.

In this study we investigate how the divergences between damselflies and dragonflies at the level of visual anatomy are reflected in their predatory tactic and target tracking circuitry. In comparison to dragonflies, we found that damselflies attack when their prey is positioned more frontally, rather than dorsally, in the visual field. We also report that this frontal area of the visual field in damselflies is sampled by TSDNs homologous to those of dragonflies. Unlike the holoptic dragonflies studied to date, all TSDNs responses in damselflies integrate information from both eyes and they encode target direction in a binocular, fused reference frame. This is distinctly different from holoptic dragonflies, whose TSDNs encode direction of a moving target in a sagittal reference frame relative to the midline formed by their two merged eyes.

## **3.2 Methods and Materials**

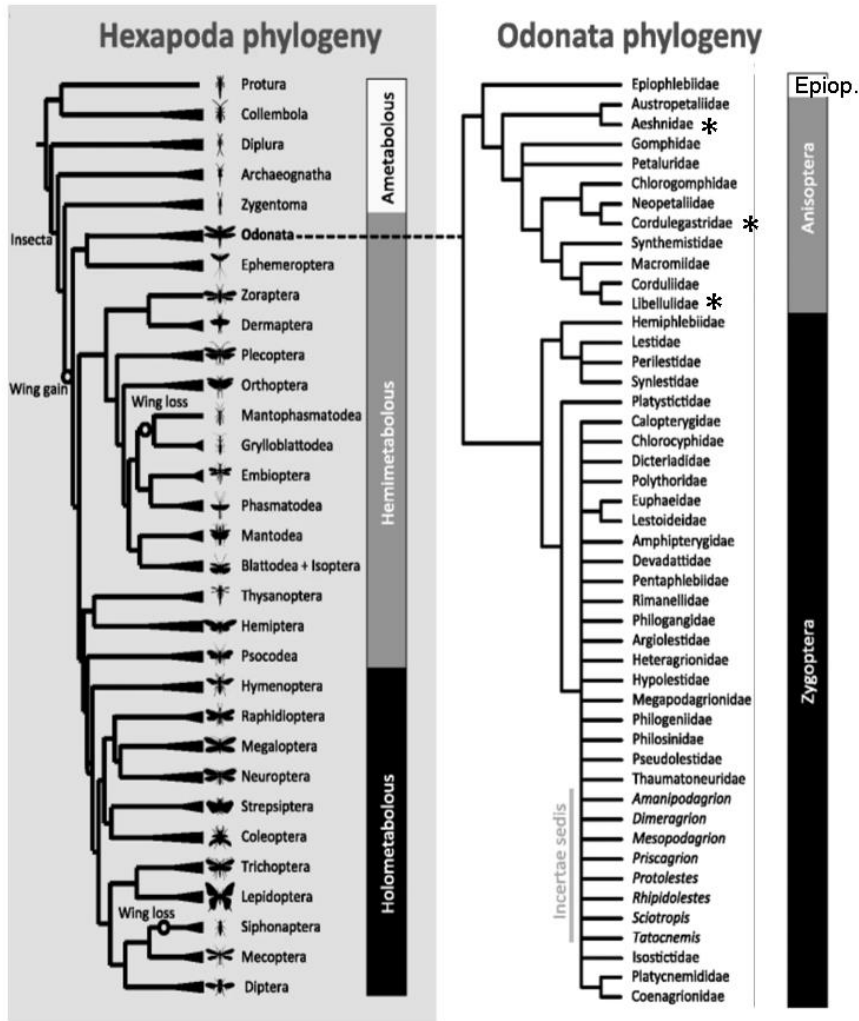
### **3.2.1 Animals**

Adult *Calopteryx splendens* demoiselle damselflies used for extracellular and anatomical experiments were caught wild along the River Cam in Grantchester Meadows, Cambridge (UK), between May and August of years 2016-2018. *Calopteryx maculata* demoiselles used for behavioural experiments were collected in York County, Pennsylvania (USA), during July of years 2017 and 2019 with collection permission from park rangers. *Enallagma civile* damselflies used for pseudopupil measurements were reared to adults from nymphs caught at Cedar Bog in Minnesota, USA, 2019. *Sympetrum vulgatum* dragonflies used for electrophysiology and anatomical experiments were reared from nymphs in the lab at Cambridge, UK in 2016. *Pachydiplax longipennis* dragonflies used for behavioural experiments were reared from nymphs (Carolina Biological Supply Company) in the lab at University of Minnesota in 2019, with adults maintained in an indoor flight arena feeding on *Drosophila melanogaster*. *Gomphus spicatus* and *Cordulia shurtleffii* dragonflies were wild caught in June 2019 at Itasca research station, Minnesota, USA. Mounted Odonata specimens were accessed at the University of Minnesota entomology collection in 2019.

### **3.2.2 High-speed videography of predation**

Two synchronised Photron SA2 cameras were used to film *Calopteryx maculata* demoiselles attacking artificial prey made from a silver 3 mm bead dangling on fishing line. The recordings were done either within a temporary outdoor plastic tent (York College) or unenclosed by a creek

A



B

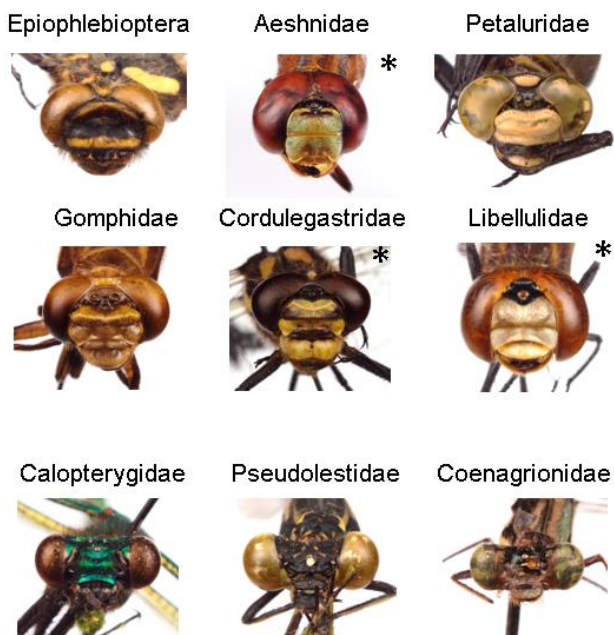


Figure 3.1 (legend right)

**Figure 3.1 (left) Odonata phylogeny and ocular morphology (A)** Odonatoptera phylogeny reproduced from (Bybee et al., 2016). Epiop. = Epiophlebioptera. **(B)** Several extant dragonflies with holoptic morphology are indicated with asterisk. All other extant dragonflies, damselflies, and basal Odonatopterans (Bechly et al., 2001) feature dichoptic eyes. Photographed Odonata species (left to right per row): *Epiophlebia superstes*, *Aeshna tuberculifera*, *Tachopteryx thoreyi*; *Progomphus obscurus*, *Cordulegaster obliqua*, *Pachydiplax longipennis*; *Calopteryx splendens*, *Pseudostigma accedens*, *Agria apicalis*.

at Nixon State Park. *Erythemis simplicicollis* dragonflies hunting a black 3 mm bead were filmed using a similar dual synchronised Photron Mini AX200 camera system within an internal laboratory flight arena. High-speed recordings were carried out at 1000 frames per second with either a 24 mm AF-S NIKKOR f/1.8G ED Nikon lens or a Nikon 85mm f/1.8D lens.

Acquired image sequences were digitised in Fiji and 3D reconstructed as detailed in Methods Chapter section 2.6. The average elevation of the prey just prior to the flight initiation was calculated as follows: the frame prior to the predator's first movement was identified for each flight, the elevation values were measured (from the 3D flight reconstruction at each frame), and a circular mean from all flights was then calculated. The confidence interval for this measure is shown as the shaded cones in Figure 3.3C. To estimate the elevation of the prey relative to the head axis before take-off, the tilt angle between the body axis and the head axis was measured from macrophotographs (Figure 3.SI1). The value of this offset was then applied to the elevation of the prey from body axis just prior to any movement of the predator.

The reported average and confidence intervals for the elevation of the prey, relative to the predator's body axis throughout flight, was calculated as follows: i. for each flight, an average elevation angle was calculated (i.e. circular mean of the values throughout a single trajectory) then, ii. the values obtained in (i) for each trajectory were averaged (i.e. circular mean of all the flights). The average trajectories shown as blue traces in Figure 3.3C were calculated as follows: i. normalising each trajectory to the maximum distance between the predator and prey throughout flight, ii. binning along 5% radial intervals (0% predator's head, 100% maximum distance of the prey), iii. averaging the elevation and azimuth values within each bin for each individual flight (circular mean within a bin), iv. averaging each bin across all flights (circular mean of bins across flights). Statistical tests reported in the main text were performed using the Watson-Williams test for equality of means.

### 3.2.3 Electrophysiology

Extracellular electrophysiology data was collected as described in Methods Chapter section 2.4 at a temperature of 23°C. *Calopteryx maculata* intracellular recordings were acquired using thin wall borosilicate glass electrodes (OD of 1 mm and ID of 0.75 mm; WPI Cat# TW100F – 4) which were pulled with a laser electrode puller (Sutter P-2000), by choosing the following settings: Heat 340; Fil

4; Vel 50; Del 210; Pul 150. Once the electrodes were filled with 1.5 or 3% Lucifer Yellow in 1M LiCl, or with 1M KCL, the resulting resistance was circa 80 or 20 M $\Omega$ , respectively. Dye was injected using negative current (total between -2 and -15 nA, depending on the preparation) with square pulses (6 seconds on, 1 second off), for as long as the cell was held. Measurements were taken at 23 °C. Injected animals were immediately fixed in 4% PFA and left at room temperature overnight. Brains were dissected and processed for imaging as previously described (Gonzalez-Bellido and Wardill, 2012). Brains were imaged as described in Methods Chapter section 2.5.1.

### **3.2.4 Visual Stimuli**

Visual stimuli were presented using a DepthQ 360 Hz projector as described in section 2.3.1. Demoiselles were positioned 7 cm from the screen, giving a subtended projected screen size of 102° x 69°, azimuth and elevation respectively. Visual stimuli consisted of widefield gratings (4° spatial frequency, 45°/sec), a high spatial resolution receptive field mapping stimulus consisting of a series of 3000 small (2° x 2°) moving targets as described previously (see Methods Chapter, section 2.4.3) (Gonzalez-Bellido et al., 2013), and a low resolution receptive field mapping stimulus consisting of rasterised trajectories of a small (2° x 2°) target moving across the screen in eight directions (see Methods Chapter, section 2.4.3.1).

### **3.2.5 Pseudopupil measurements**

To compare pseudopupil sizes across different Odonata specimens, the body axis was defined as zero degrees. For the Familiar Bluet damselfly, the body axis was defined by the sharp boundary between dorsal and ventral coloration which runs along the anterior-posterior axis. This coloration boundary likely functions as a countershading camouflage which by functional necessity will align with the body axis. For both dragonfly specimens (which do not display countershading), the body axis was defined as orthogonal to the posterior aspect of the head, which when viewed laterally has a distinct vertical edge aligning along the ventral-dorsal axis.

## **3.3 Results**

### **3.3.1 Odonate ocular morphology**

Damselflies have two distinctly separated (i.e. dichoptic) compound eyes with a binocular overlap of at least 20 degrees (Corbet, 1999; Horridge, 1978). Each eye possesses a frontal region of high visual acuity, i.e. a fovea, but lacks the holoptic dorsal fovea present in dragonflies (Horridge, 1977a, 1978). In *Enallagma civile* pond damselflies (family Coenagrionidae), we found an enlargement of the pseudopupil, indicative of increased visual acuity (see section 1.2.1), aligned at ~10° inclined from the body axis with a half-width of 30° (Familiar Bluet; Figure 3.2).

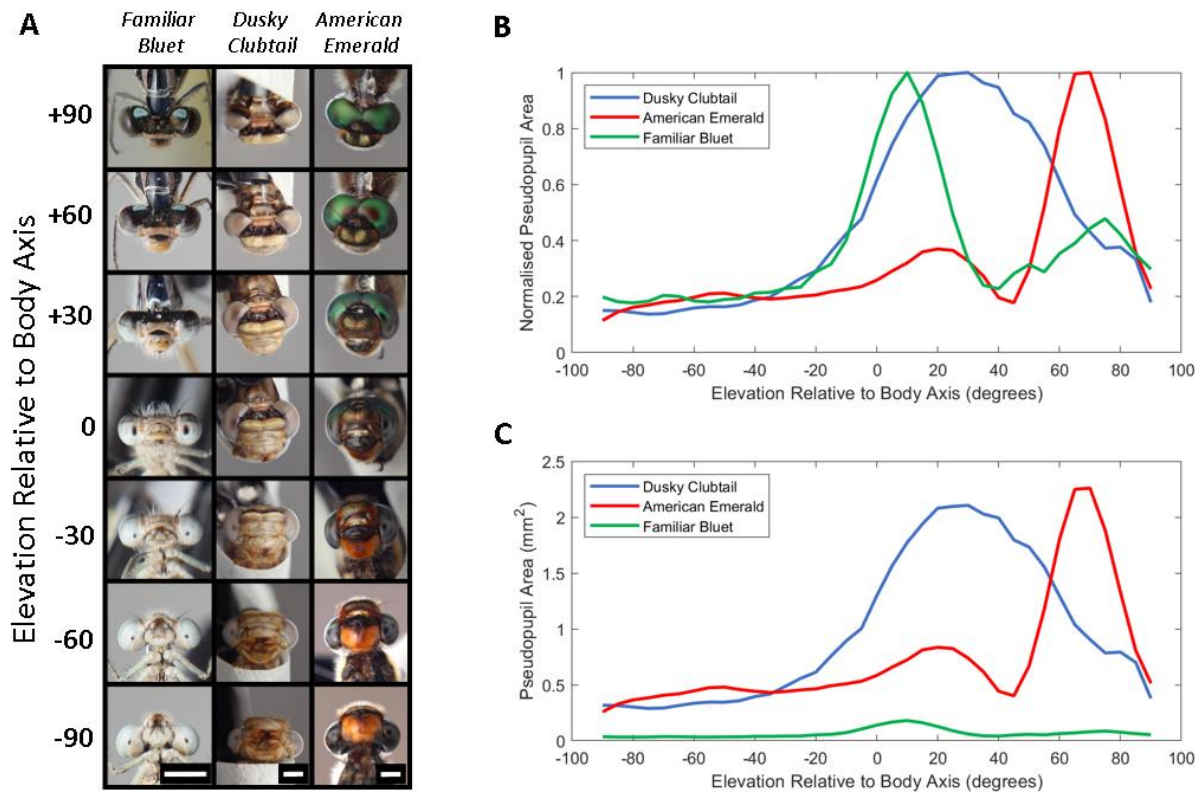


**Figure 3.2 Pseudopupil measurements across Odonata** (A) Macrophotograph montage for each species at 30° increments in elevation. Familiar Bluet (*Enallagma civile*, family *Coenagrionidae*, left), Dusky Clubtail (*Gomphus spicatus*, family *Gomphoidea*, middle), and American Emerald (*Cordulia shurtleffii*, family *Libellulidea*, right). Scale bars 2mm. (B) Pseudopupil area measurements at varying elevations along the ventral-dorsal axis. Measurements are normalized to the maximum pseudopupil area for each species. (C) Absolute measurements of pseudopupil area in mm<sup>2</sup> of the same data as (B).

Most dragonfly species have large round holoptic eyes that form a dorsal fovea; however, some dragonfly lineages (families Gomphoidea, Petaluroidea, Epiophlebiidae) have dichoptic eyes resembling those of damselflies (Figure 3.1B). In *Gomphus spicatus* dragonflies (aka Clubtails, family Gomphoidea), which feature dichoptic eyes, an enlarged pseudopupil area is positioned at ~30° inclined above the body axis with a half-width of 60° (Dusky Clubtail; Figure 3.2). This is intermediate between *Enallagma civile* pond damselflies and a holoptic dragonfly, *Cordulia shurtleffii* (common name: *American Emerald*, family *Libellulidea*), where the maximum pseudopupil area is aligned at ~70° inclined above the body axis with a half-width of 30° (American Emerald; Figure 3.2). *C. shurtleffii* also features a second, more ventrally positioned region of increased visual acuity aligned at ~20° inclined above the body axis with a half-width of ~20° (Figure 3.2). This smaller frontal fovea pseudopupil reaches a maximum area ~40% of that of the dorsal fovea (Figure 3.2B). This frontal fovea matches those previously described in other *Libellulidea* and *Aeshnoidea* dragonflies (Horridge, 1978).

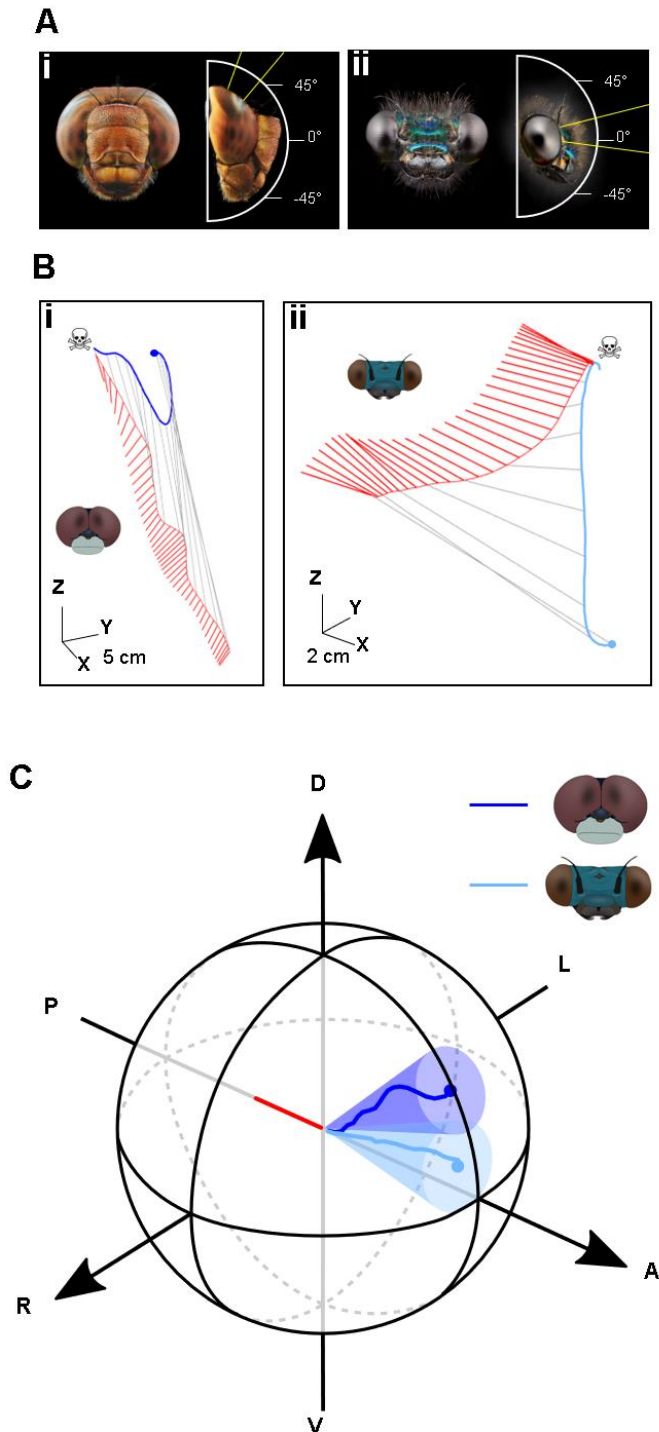


**Figure 3.3 Comparison of external eye anatomy and hunting strategies of dragonflies and damselflies**

**(A)** Frontal and lateral views of a dragonfly with holoptic eyes (*Sympetrum vulgatum*) and a damselfly with dichoptic eyes (*Calopteryx splendens*). Yellow lines indicate visual area sampled by the dorsal ( $\sim 60^\circ$  elevated in dragonflies (Olberg et al., 2007)) and frontal foveae, respectively.

**(B)** Predatory flights of a dragonfly (i, *Erythemis simplicicollis*) and damselfly (ii, *Calopteryx aequabilis*) whilst chasing an artificial prey (blue) reconstructed in 3D. Predator head positions are represented as a continuous red curve, with the body axis plotted at 10 ms intervals to indicate orientation of the predator throughout the attack (red lines). Line-of-sight between predator head position and artificial prey in grey.

**(C)** Spherical plots, tracing the average subtended position of the prey (blue) compared to the body axis of the predator throughout the flight (red). Cones depict the 95% confidence

interval of the prey just before the predator's first movement. In dragonfly attacks, the prey (dark blue) was on average aligned above the dragonfly body axis by  $32.6^\circ$  just prior to the first movement of the predator (95% CI =  $\pm 12.4^\circ$ , n=8) and by  $33.7^\circ$  throughout flight (95% CI =  $\pm 5.3^\circ$ , n=8). In damselfly attacks, the prey (light blue) was on average aligned above the body axis by  $13.9^\circ$  just prior the first movement of the predator (95% CI =  $\pm 13.0^\circ$ , n=10) and by  $11.4^\circ$  throughout flight (95% CI =  $\pm 6.5^\circ$ , n=10). D=Dorsal, V=Ventral, A=Anterior, P=Posterior, L=Left, R=Right.

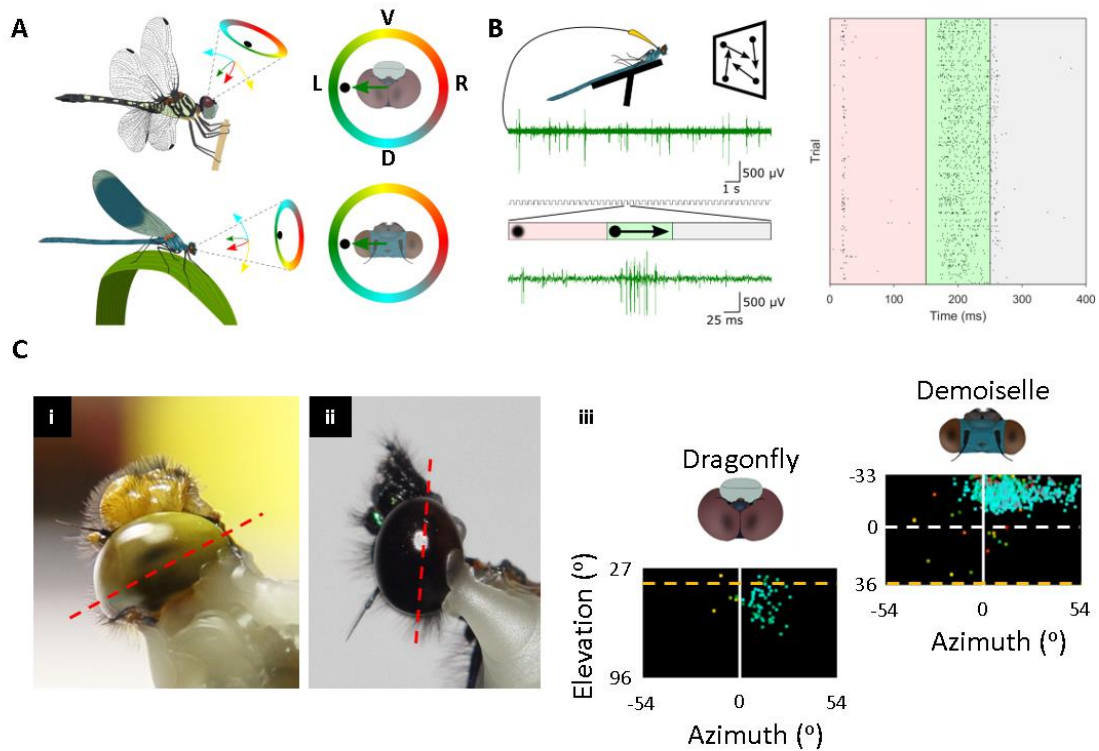


**Figure 3.4 TSDNs sample the frontal visual field in demoiselles** (A) Coordinate system used for direction receptive field maps. Receptive field maps are represented in a “God’s eye perspective” following previous work (Gonzalez-Bellido et al., 2013). D=Dorsal, V=Ventral, L=Left, R=Right. (B) Set-up and stimulus for recording from target responses in the demoiselle ventral nerve cord follow a series of 3000 target trajectories moving with fixed size and speeds in random directions and locations in the visual field as used previously in dragonflies (Gonzalez-Bellido et al., 2013). Top trace = raw responses to 44 trajectories indicated by stimuli steps. Bottom trace: responses to a single target trajectory. The trajectory begins when a target appears and remains stationary on the screen for 150 ms (red), moves in a random direction at constant speed for 100 ms (green), and disappears for 150ms (grey) before the start of the next trajectory. The raster plot shows the responses to a subset of trajectories used to map the cell. (Further details for the analysis workflow are found in Methods Chapter, section 2.4.3.1). (C) Example of relative position of dragonfly and demoiselle TSDN receptive fields within the visual field. (i-ii) The body axis was defined as perpendicular to the longest diameter axis of the eye (red line, note animals are prepared for electrophysiology with a dorsal tilt of the head to tighten the cord). (iii) Example comparison of an MDT5 neuron in a dragonfly (*Sympetrum vulgatum*) and demoiselle (*Calopteryx splendens*). The dragonfly receptive field is centered at approximately 50 degrees elevated from the body axis, and the demoiselle receptive field is centered at approximately -20 degrees below the body axis, yielding an elevation difference of ~70 degrees.

Whilst the dark pigmentation of demoiselle damselfly compound eyes does not permit pseudopupil measurement, demoiselle eyes have a distinct flattening of the ommatidia surface - which is indicative of increased visual resolution (see section 1.2.1) (Land, 1997)- at the frontal aspect of the eye approximately aligned with the body axis (Figure 3.3A).

### **3.3.2 Attack trajectory in demoiselle damselflies**

As previously reported (Lin and Leonardo, 2017; Mischiati et al., 2015; Olberg et al., 2007), we found that dragonflies approach their prey from below (Figure 3.3Bi), tracking targets within the dorsal fovea. Just prior to, and throughout the flight, the prey aligned above the dragonfly body azimuth on average  $32.6^\circ$  (95% confidence interval (CI) =  $\pm 12.4^\circ$ , n=8) and  $33.7^\circ$  (95% CI =  $\pm 5.3^\circ$ , n=8), respectively (Figures 3.3C).

In contrast, we found that damselflies fly to the elevation of the target (Figure 3.3Bii), keeping it in the frontal aspect of their visual field before lunging forwards to grasp it. We found that just prior to, and throughout the flight, the prey aligned above the demoiselle body azimuth on average  $13.9^\circ$  (95% CI =  $\pm 13.0^\circ$ , n=5) and  $11.4^\circ$  (95% CI =  $\pm 6.5^\circ$ , n=10), respectively (Figure 3.3C).

Both measures of prey location here reported, i.e., above the body axis prior to the initiation of flight, and throughout flight, were statistically significantly different between dragonflies and demoiselles ( $p = 0.0441$ , and  $p = 6.98e-05$ , respectively, Watson-Williams tests).

### **3.3.3 TSDNs serving the demoiselle frontal foveae**

We next investigated how the frontal predatory tactic and dichoptic ocular arrangement of demoiselles is reflected in the premotor target tracking system. In extracellular recordings from the demoiselle ventral nerve cord, responses to small moving objects were confined to the frontal visual field (Figure 3.4). Thus, we positioned the animals and visual stimuli accordingly. We first recorded target responses from the ventral nerve cord with extracellular tungsten electrodes, and after spike sorting (see Methods Chapter, section 2.4.1), we calculated the latency, spike triggered averages, and directional tuning maps (see Methods Chapter, section 2.4.3.1).

We discovered demoiselle descending neurons that shared distinguishing features with dragonfly TSDNs: (i) robust responses to small targets of fixed size that moved in cardinal directions, (ii) directional tuning, and (iii) no sustained responses to wide-field stimuli (Figure 3.5-3.6) (Gonzalez-Bellido et al., 2013; Olberg, 1986). We classified these cells as demoiselle TSDNs and assigned them to previously described dragonfly TSDN cell types (Gonzalez-Bellido et al., 2013) according to the position and direction tuning of their receptive fields (Figure 3.5, we putatively recorded the following number of cells for each TSDN type MDT1 = 12, MDT2 = 6, MDT3 = 4, MDT4 = 8, MDT5 = 4, DIT1 = 5, DIT2 = 9, DIT3 = 7). We found that the response properties of demoiselle TSDNs are qualitatively

very similar in directional selectivity to those previously described in dragonflies (Gonzalez-Bellido et al., 2013), and the overall tuning curves for moving targets appears to be remarkably conserved (Figure 3.5).

We hypothesized that demoiselle TSDNs would not only be functionally similar to dragonfly TSDNs, but also anatomically similar. Ventral nerve cord backfills of both demoiselles and dragonflies labelled three conspicuous bilaterally symmetric clusters of very large cell bodies (~50  $\mu\text{m}$ ) and their corresponding axons (Figure 3.7). These were located at the n-ventral, n-anterior, and n-dorsal surface of the brain (Figure 3.7), which in dragonflies corresponds to the position of TSDN cell bodies, with the majority (i.e. DIT1, DIT2, MDT2, MDT4, MDT5) residing within the n-ventral cluster (Frye and Olberg, 1995; Olberg, 1986). However, to link TSDN anatomy and function directly, we recorded the responses from the demoiselle TSDNs intracellularly (Figure 3.5, rows marked '\*') and loaded them with fluorescent dye at the end of the recording. The receptive field location and the directional tuning of these intracellularly identified neurons were consistent with those isolated extracellularly (Figure 3.5), validating our extracellularly recorded receptive fields. Our intracellular maps appear sparser due to a reduced mapping stimulus (1.3 vs 20 minutes), as we aimed to maximize time for dye loading. Lines of activity are observed due to the longer, rasterised target trajectories presented across the visual field with this reduced stimulus. The cell body position and arborisation pattern of all demoiselle TSDNs matched closely those of dragonflies (Figure 3.8) (Frye and Olberg, 1995; Olberg, 1986), with the majority of demoiselle TSDN cell bodies (i.e. DIT1, DIT2, MDT2, MDT4, MDT5) also arising from the n-ventral cell body cluster (Figure 3.8). Together, the anatomical and electrophysiological properties of demoiselle TSDNs strongly suggests that these neurons are homologous with dragonfly TSDNs as a descending target tracking system that guides prey capture.

Intracellular recordings highlight the variability in the number of spikes (Figures 3.5, 3.9), and the extensive bilateral location of the receptive fields. Given these properties, responses to moving targets alone are not sufficient to distinguish with absolute certainty between some TSDNs. This is the case for all three ipsilateral cells responsive to targets moving towards the right of the animal (MDT2/DIT2/MDT3). The same ambiguity exists between the two contralateral cells responsive to targets moving towards the left (DIT1/DIT3). The intracellular dataset also highlights that both the spike rate and overall binocular extent of a single TSDN type can differ substantially across animals (Figure 3.9).

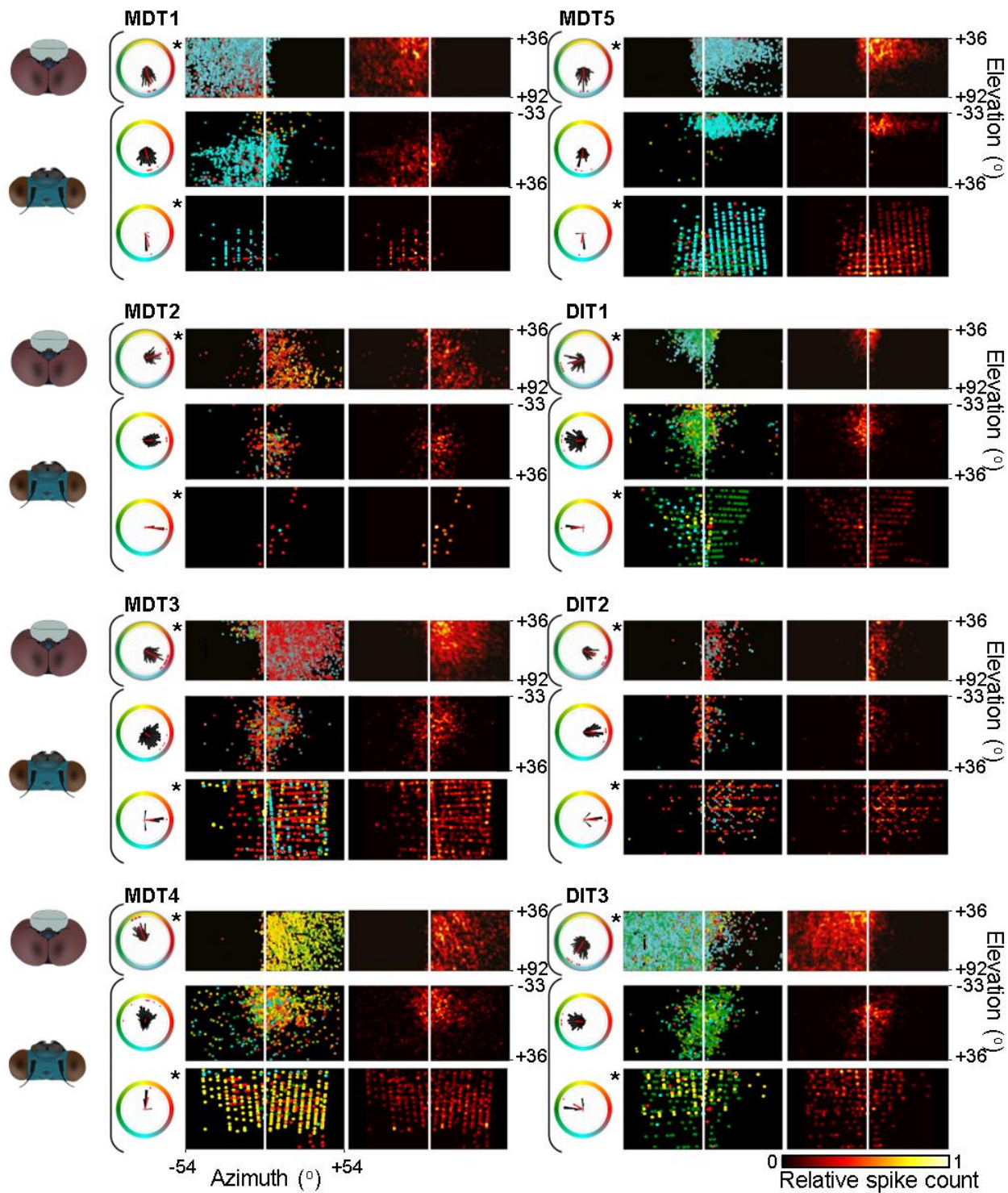
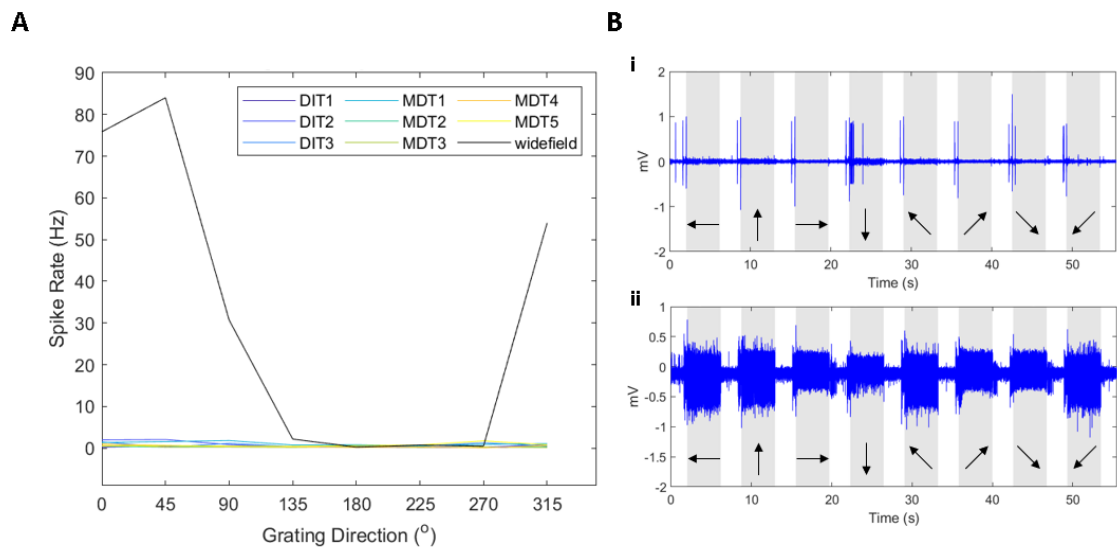
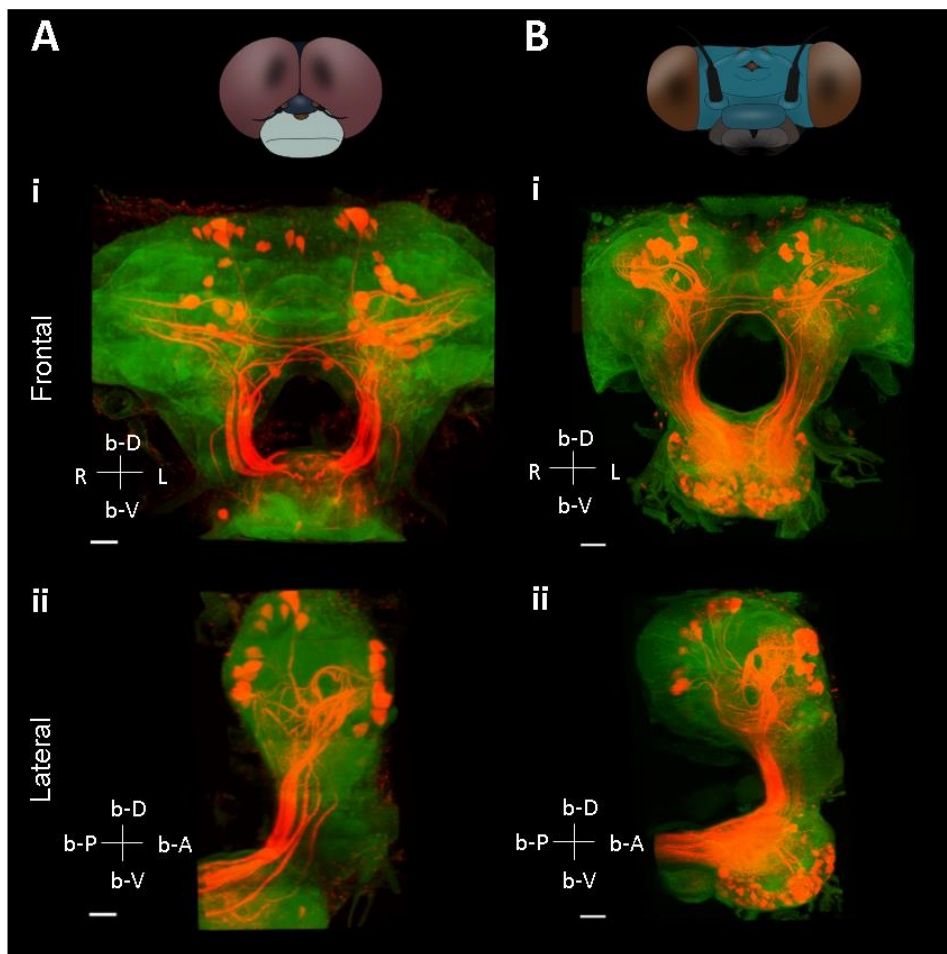


Figure 3.5 (legend right)

**Figure 3.5 (left) TSDNs serving the demoiselle frontal foveae** Comparison between the receptive field maps of TSDNs in dragonflies and demoiselle TSDNs. All dragonfly maps were intracellularly acquired, and are here reproduced from (Gonzalez-Bellido et al., 2013). The damselfly recordings, both extracellular and intracellular, show one recording (for all extracellular recordings see Figure 3.SI2). The direction receptive field (RF) shows the position and direction of the target that elicited the spike. The spike triggered average (STA) displays the relative spiking activity across the receptive field, normalized to maximum number of spikes in that recording in any one screen location (pixel). Polar histograms represent the binned target direction for each spike ( $10^\circ$  bins, black bars) and the resultant vector (red arrow) for the example receptive field. The red dots indicate the resultant vector direction for all neurons recorded. Elevation and azimuth scale are relative to the animal's head axis. The different types of TSDNs are labelled with their names (i.e. MDT1-5, DIT1-3). The symbol \* next to a map notes that it was acquired intracellularly.



**Figure 3.6 Widefield responses of demoiselle TSDNs** (A) Responses of all demoiselle TSDN types in Figure 3.5 and 3.SI2 to widefield moving gratings, compared with responses from a wide-field detecting neuron. (B) (i) Example recording of a demoiselle TSDN under widefield grating stimuli (grey). Directions of grating stimuli indicated by arrows using the same coordinate system in Figure 3.4. Note that TSDNs respond between grey gratings stimulus periods due to an ON-OFF flicker when the stimulus is loaded, however they do not sustain responses during grating movement (grey). (ii) Example widefield neuron responding to the same stimuli.



**Figure 3.7 Descending neuron anatomy in dragonflies and demoiselles (A)** Maximum intensity projections of dragonfly (*Sympetrum vulgatum*) and **(B)** demoiselle (*Calopteryx splendens*) brains. Ventral nerve cords were backfilled with Texas Red (red), staining both ascending and descending neuronal processes along with any associated cell bodies. Neuropile is stained with Lucifer Yellow (green). (i) Frontal view, (ii) lateral view. Scale bars 100µm. Coordinates with respect to body axis (b-). Abbreviations: A, Anterior; P, Posterior; D, Dorsal; V, Ventral; L, Left; R, Right.

**Figure 3.8 (right) Neuroanatomy of intracellularly identified demoiselle TSDNs** TSDN traces of the damselfly neurons whose intracellular maps are shown in Figure 3.5, shown in comparison with the anatomical traces of TSDNs in Aeshnid dragonflies (reproduced with permission from (Frye and Olberg, 1995; Olberg, 1986)). A= anterior, D= dorsal, V = ventral, L= left, R = right.

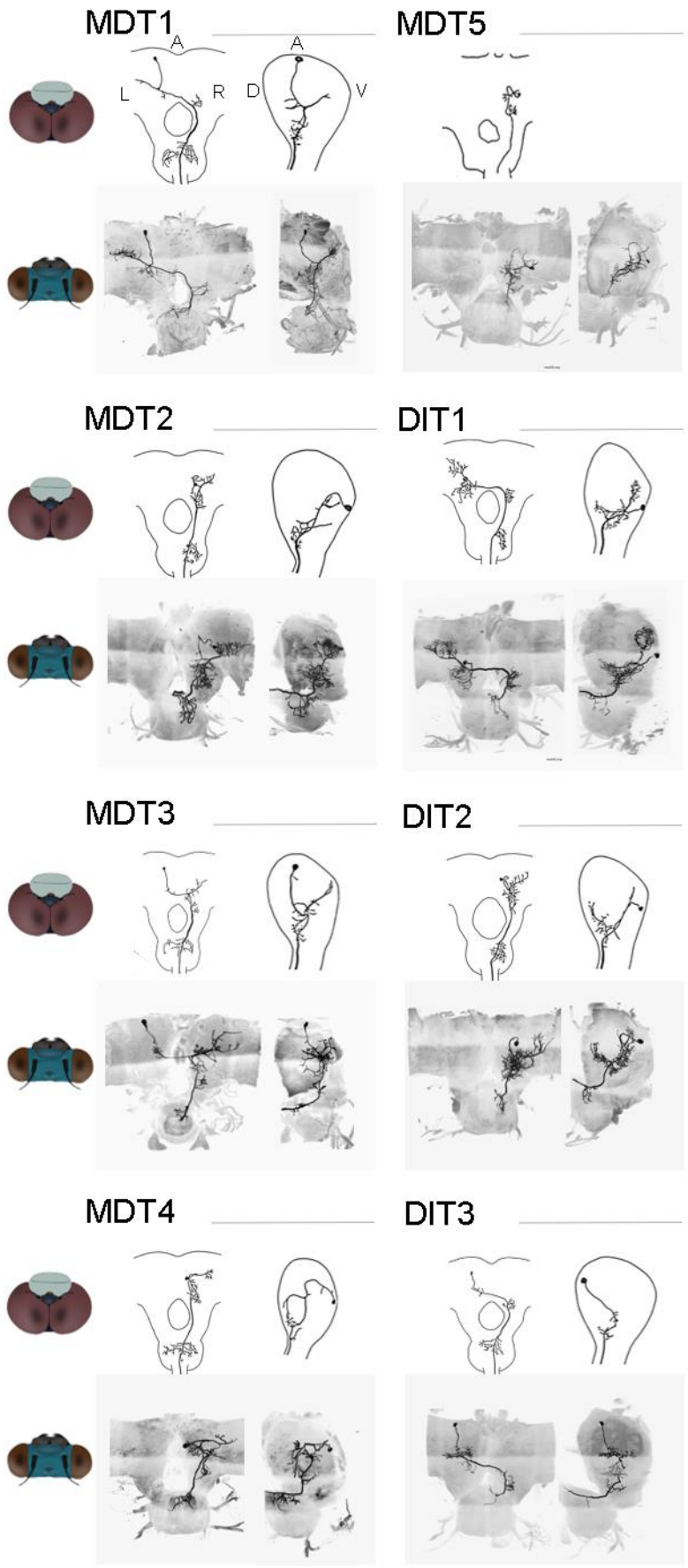
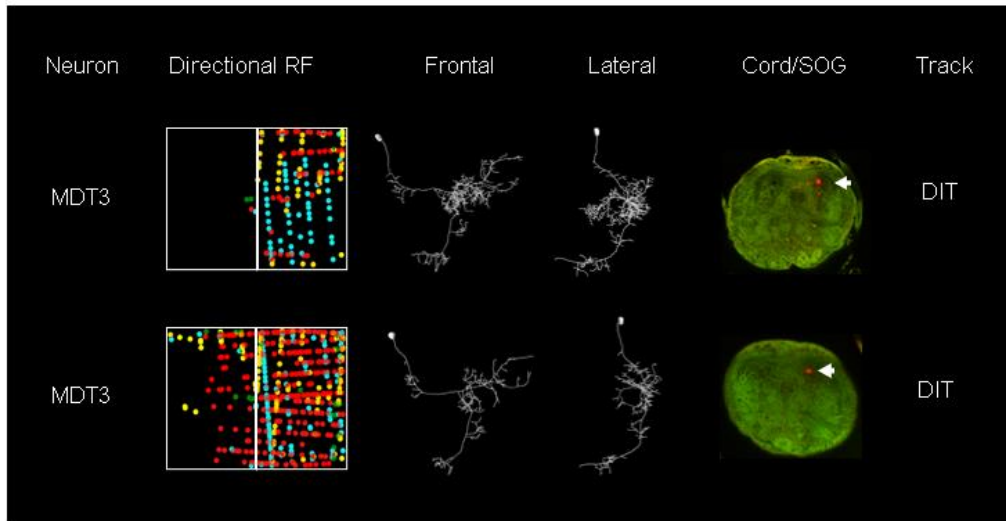
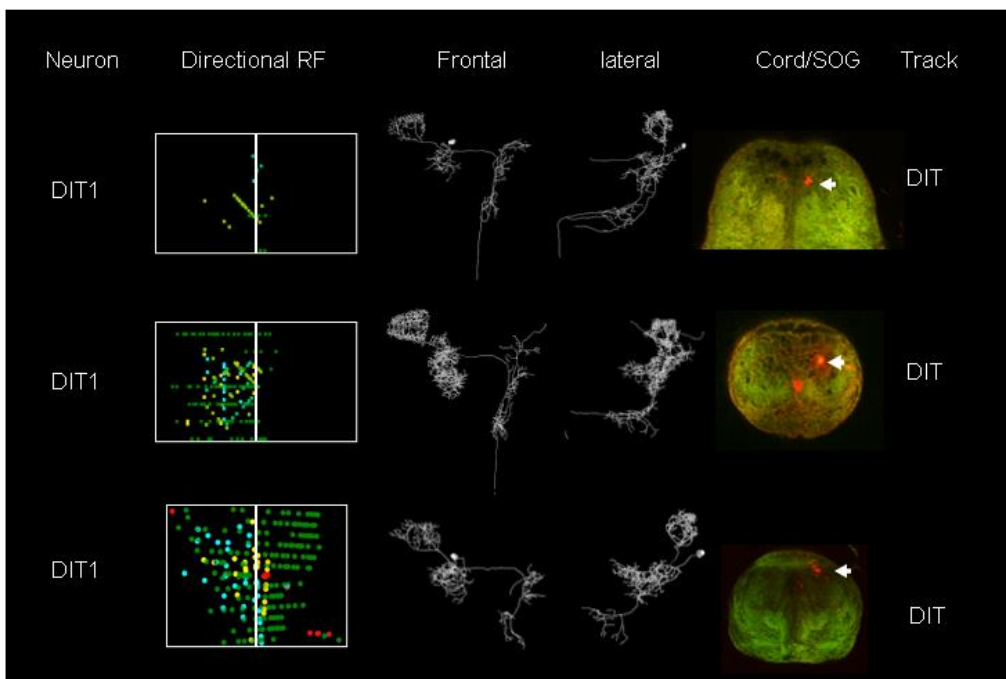


Figure 3.8 (legend left)

A



B



**Figure 3.9 Spike number and degree of binocular overlap, within the same type of TSDNs, shows high variability between damselfly individuals** We used the directional tuning (from electrophysiology) and the neuronal morphology (from dye fills) to identify that we had recorded from (A) MDT3 and (B) DIT1 in two and three animals, respectively. Neurons of the same type exhibit high variability in spike numbers, and in the binocular overlap. Note that MDT3 was so named because it travels through the MDT tract in Aeshnid dragonflies (Olberg, 1986), but it travels though the DIT tract in Libellulids (Gonzalez-Bellido et al., 2013), and in demoiselles (this study). Abbreviations: DIT, Dorsal Intermediate Tract; MDT, Medial Dorsal Tract; GNG, gnathal ganglia.

Whilst demoiselle and dragonfly TSDNs share many characteristics, we also found important differences, notably in the extent of overlap across the visual midline (Figure 3.5). The receptive fields of most dragonfly TSDNs display a sharp vertical boundary at or just over the midline, confining responses to target movement within a single hemifield (Figure 3.5) (Gonzalez-Bellido et al., 2013). Only two dragonfly TSDNs (DIT3 and MDT3), exhibit responses that extend more than 10° into the opposing hemifield, and the responses within only that opposing hemifield are not directionally tuned (Figure 3.5) (Gonzalez-Bellido et al., 2013). In contrast, the receptive fields of demoiselle TSDNs often extend beyond 20° across the visual midline and maintain the directional tuning across both hemifields (Figure 3.5). Next, we investigated how such bilateral receptive fields arise in demoiselle damselflies.

### **3.3.4 Demoiselle TSDNs are binocular, exhibiting binocular-only, ocular-balanced, or ocular-dominant responses**

To investigate how the extension of receptive fields across the visual midline in demoiselle TSDNs relates to inputs from either eye, we recorded TSDN responses under monocular conditions where one eye was occluded with an opaque eye patch (Figure 3.10). Compared to the uncovered control conditions, all TSDNs exhibited a significant drop in spike numbers when either eye was covered (Friedman test for repeated measures with *post hoc* sign test,  $p = 0.00014$ ,  $n = 12$ ; Figure 3.10), demonstrating that demoiselle TSDNs depend upon simultaneous binocular inputs. For all cells recorded, the hemifield ipsilateral to the patched eye had very low activity relative to controls (Figure 3.10A-C, relative response integral  $< 0.5$ ), which is consistent with the patch fully occluding visual input from that side. However, we saw varying responses in the hemifield that corresponded to the unoccluded eye, which we will refer to the “contralateral hemifield” (as it is contralateral to the patch). We categorised these responses into three types.

In Type 1 responses, the contralateral hemifield activity was low regardless of whether the patch was on the right or left (Figure 3.10A), indicating these responses belonged to neurons that were exclusively binocular with visual responses dependent on both eyes contributing in an all (binocular) or none (monocular) fashion (Figure 3.10A,  $n = 3$  cells from 2 animals, Figure 3.SI3). Very few spikes were observed in each monocular condition, and those present were mostly in the non-occluded visual hemifield, suggesting that the contralateral eye was not accidentally occluded (Figure 3.10A). This binocular-only group implies that for these neurons, monocular responses to a moving target do not reach the threshold required to fire the TSDN, but that such threshold is reached by the combination of both monocular responses at or upstream of the TSDN (Figure 3.10A model).

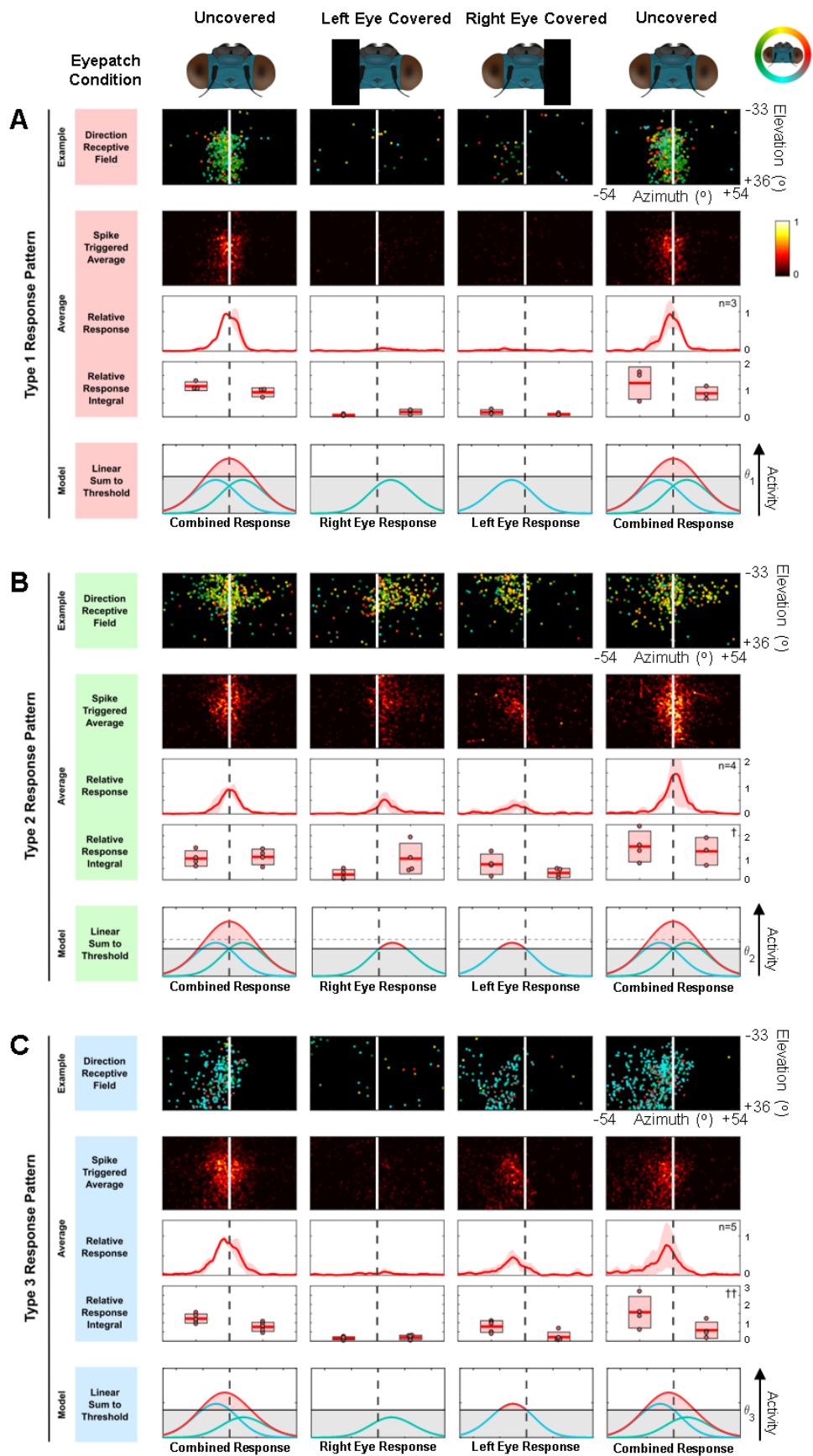


Figure 3.10 (legend right)

**Figure 3.10 (left) Demoiselle TSDNs are binocular, with differing thresholds and input weights.**

TSDNs were mapped under binocular (equivalent to Figure 3.5), and monocular conditions (left and right eye patches), followed by another binocular map to control for habituation and to ensure the cell was still detectable by the electrode. Monocular responses were categorized into three types (Types 1-3, A-C respectively), according to the binocular interaction observed. For each response type: row 1 = representative direction receptive field map from a single cell (example). Row 2 = average spike triggered map from cells falling within the category. Row 3 = relative response densities (STAs projected onto the horizontal axis, mean  $\pm$  std for each cell recording). Row 4 = left vs right hemifield relative response cumulative sum. Row 5 = proposed summation-to-threshold model that could generate the responses. Full data given in Figure 3.SI3.

(A) Type 1: Binocular-only, in which visual responses are dependent on both eyes in an all-or-none fashion. n = 3 cells from 2 animals allocated to this category.

(B) Type 2: Balanced split-monocular, in which receptive fields are bisected along the midline with absent responses from the hemifield ipsilateral to the eyepatch, and reduced responses, but still present, in the contralateral hemifield (arising from non-occluded eye). n = 4 cells from 4 animals allocated to this category. † For 1 cell, the right eye hemifield of this second control had an unusually high relative response. This hemifield was noted as an outlier, possibly caused by electrode or animal movement, and excluded from mean/variance calculation.

(C) Type 3: Ocular dominant, in which occlusion of one eye fully suppresses the entire receptive field. However, occlusion of the adjacent eye bisects the receptive field at the midline with responses found only in the non-occluded hemifield. n= 5 cells from 5 animals allocated to this category. †† One Type 3 cell is missing the uncovered positive control due to deterioration of recording signal (see Figure 3.SI3).

Type 2 responses exhibited moderate, if variable, activity in the contralateral hemifield whether the patch was on the left or right eye. (Figures 3.10 and 3.SI3, n = 4 cells from 4 animals). Hence, in TSDNs with Type 2 responses (Figure 3.10B), the single unoccluded eye that was not patched sufficiently excited the neuron to fire. We speculate that the input weighting from each eye is balanced in these neurons, and by combining the two monocular responses, binocular contributions synergise to increase spike numbers across the entire receptive field (Figure 3.10B model). It is possible that the difference between Type 1 and Type 2 responses are due to different spiking thresholds (i.e. sensitivity) at the time of the experiment (Figure 3.10B, model), a TSDN property that we had previously observed in our intracellular recordings (Figure 3.9).

Type 3 responses were asymmetrical in that we observed contralateral hemifield activity when the patch was on the right, but not when the patch was on the left (Figures 3.10 and 3.SI3, n = 5 cells from 5 animals). Hence, the neurons in this category exhibit ‘left ocular dominance’. This response pattern could arise from a similar summation-to-threshold mechanism as Type 2 responses, but with ocular

weightings that are not balanced, and thus only one visual hemifield can reach threshold under monocular conditions (Figure 3.10C, model). It is possible that the different threshold sensitivities and ocular weightings are in fact invariant properties of individual TSDNs types, but we cannot resolve if this is the case from our extracellular data in this experiment, because some of the TSDN responses have directional tuning responses and receptive field locations similar to each other (but see Figure 3.S13 for putative TSDN ID allocation for the recordings in this experiment).

### **3.3.5 Differences in global light intensity do not underlie the binocular input requirements of TSDNs**

Our results above demonstrate that target tracking at the pre-motor stage in demoiselles depends on binocular input. Do TSDNs require that both eyes perceive a discrete moving target, or is the observed dependence a result of a decrease in global luminance in the patched eye (see for example (Zhou et al., 2013))? To test this possibility, we compared monocular responses resulting from eyepatches made of either an opaque or translucent material (Figure 3.11A,  $n = 3$  cells from 2 animals. Cells 1 and 2 were recorded simultaneously from the same animal). Note that for this experiment a reduced mapping stimulus was used (also chosen for intracellular recordings). This resulted in sparser receptive field maps, with lines of activity arising from the longer, rasterised target trajectories presented across the visual field. This stimulus choice aimed to maximise the number of conditions per recording. The translucent eyepatch functioned to diffuse target contrast details within the visual field, such that no TSDN target responses were observed when both eyes were covered, although overall changes in light level still made the neuron fire, as seen in the preservation of wide-field ON-OFF responses (Figure 3.11A-B). All three types of binocular responses described above were observed again under both opaque and translucent monocular conditions, with no obvious differences in spike firing rates between the two eyepatch materials (Figure 3.11A). This demonstrates that the abolition of demoiselle TSDN spike firing for Type 1 responses and the reduction of spike firing in the contralateral uncovered visual hemifield of Type 2 and 3 responses does not arise from global luminance intensity differences between both eyes. Instead, this lack of response appears to result from an unsatisfied requirement of demoiselle TSDNs for simultaneous stimulation of each eye by a moving target.

### **3.3.6 Demoiselle TSDN receptive fields resulting from reduced binocularity are consistent with binocular summation**

Given that target-tracking responses from both eyes are necessary to drive demoiselle TSDNs effectively, we next investigated whether reducing the level of binocular overlap between the two eyes would result in similarly dramatic changes to the TSDNs receptive fields (Figure 3.12). We speculated that a small decrease in binocular overlap (i.e.  $4^\circ$ ) would not have a significant impact in the ability of the TSDN to summate to threshold, and thus spike numbers would be similar to control. In contrast, a

large drop in binocular overlap (i.e.  $10^\circ$ ), should result in the TSDN failing to reach threshold, and thus lead to a lower number of spikes.

Wedge prisms that deviated the visual scene by either  $4^\circ$  or  $10^\circ$  to the left of the animal were positioned in front of one or both eyes. When placed over only the left eye, the prism decreases binocular overlap compared to uncovered controls (Figure 3.12A). As a control, we placed prisms over both eyes, shifting the entire visual field to the left (Figure 3.12A). As expected, shifting global visual input also shifted the receptive field with the  $4^\circ$  prism (two-sided sign test for matched pairs,  $4^\circ$  deviation:  $p = 0.004$ , Figure 3.12B, blue densities). The receptive field also shifted under  $10^\circ$  prism although it did not reach statistical significance (two-sided sign test for matched pairs,  $10^\circ$  deviation:  $p = 0.07$ ; Figure 3.12B, blue densities). The receptive field densities continue to resemble Gaussian distributions when the prism covers both eyes. Subtracting the uncovered response density from the shifted prism-both response density generates a curve anti-symmetric about the vertical axis, resembling a sinusoid, as expected for two Gaussians of similar width and offset medians (Figure 3.12B, bottom row, blue, B-U).

When we used a prism over the left eye to reduce binocular overlap by  $4^\circ$ , there was no significant reduction in spike density within the receptive field (two-sided sign test for matched pairs,  $p = 1.0$ ,  $n = 9$  cells from 6 animals, Figure 3.12B). This is in contrast to the attenuation observed in monocular occluding experiments (Figure 3.10 and 3.11A), and is consistent with summation of two monocular responses, with the offset monocular response (left eye) still sufficiently overlapping with the other (right eye) to reach threshold when combined. Indeed, under these  $4^\circ$  deviation conditions, the receptive field widens to the left (Figure 3.12B, ellipses) with a higher number of spikes seen in the entirety of the left hemifield (Figure 3.12B, bottom row, compare L-U and B-U). This is as expected from monocular inputs that are moved further apart, albeit still overlapping in their areas of peak sensitivity. In contrast, when a more powerful prism reduced binocular overlap by  $10^\circ$ , the relative response within the receptive field was attenuated significantly (two-sided sign test for matched pairs,  $p = 0.0078$ ,  $n = 8$  cells from 7 animals; Figure 3.12B, compare purple densities and bottom row L-U). This indicates that at this deviation power, the two monocular responses are sufficiently offset such that the summed TSDN response is no longer able to reach threshold, similar to that observed under monocular occluding conditions (Figure 3.10 and 3.11A).

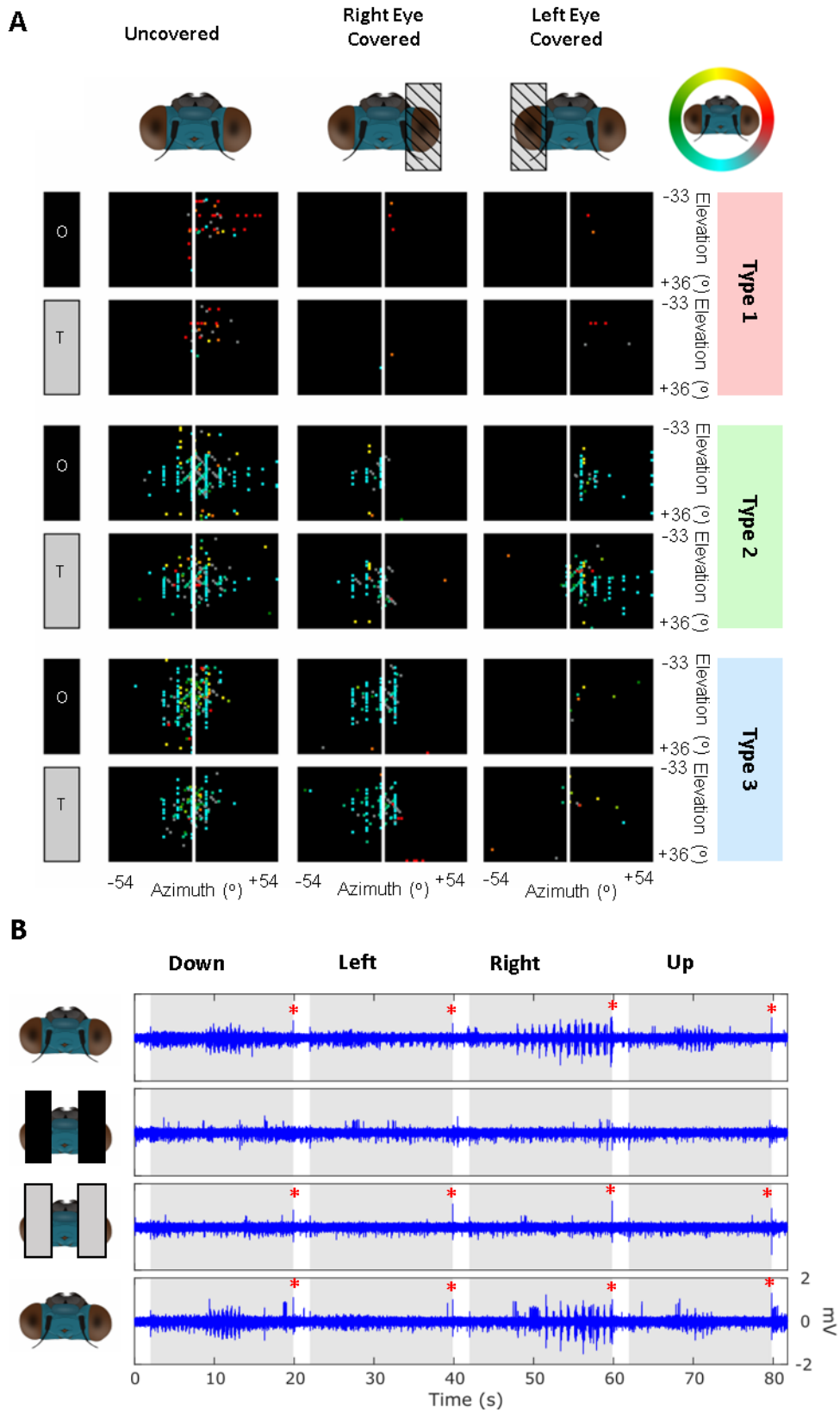


Figure 3.11 (legend right)

**Figure 3.11 (left) Demoiselle TSDN receptive fields under opaque vs translucent eyepatches**

(A) The effect of global intensity on the TSDNs responses was tested by mapping their receptive fields using a brief rasterized stimulus under opaque (as in Figure 3.10) and translucent eye patches (noted with letters O and T). All three types of response categories described in Figure 3.10 were also found in this experiment as indicated. Receptive fields were recorded in series (i.e. binocular uncovered, left/right opaque eyepatch, binocular uncovered, left/right translucent eyepatch, binocular uncovered - the final binocular uncovered condition is excluded for presentation clarity).

(B) Ventral nerve cord responses to small targets scanning across the visual field along four directions under uncovered (top and bottom rows), binocular opaque (second row from top), and binocular translucent eyepatches (third row from top). Responses are abolished when both eyes are covered with either the opaque or translucent eyepatches, indicating that the translucent eyepatches are diffusing the target contrast sufficiently to be undetected by the demoiselle. Under both uncovered and translucent eyepatch conditions there is a transient 'off' response (red asterisk) at the end of each stimulus (grey blocks) which correlates with a step decrease in screen intensity when the stimulus finishes rendering. This transient off response is not present under opaque eyepatch conditions, indicating that opaque eyepatches fully block all luminance, whereas the translucent patch transmits a detectable global luminance.

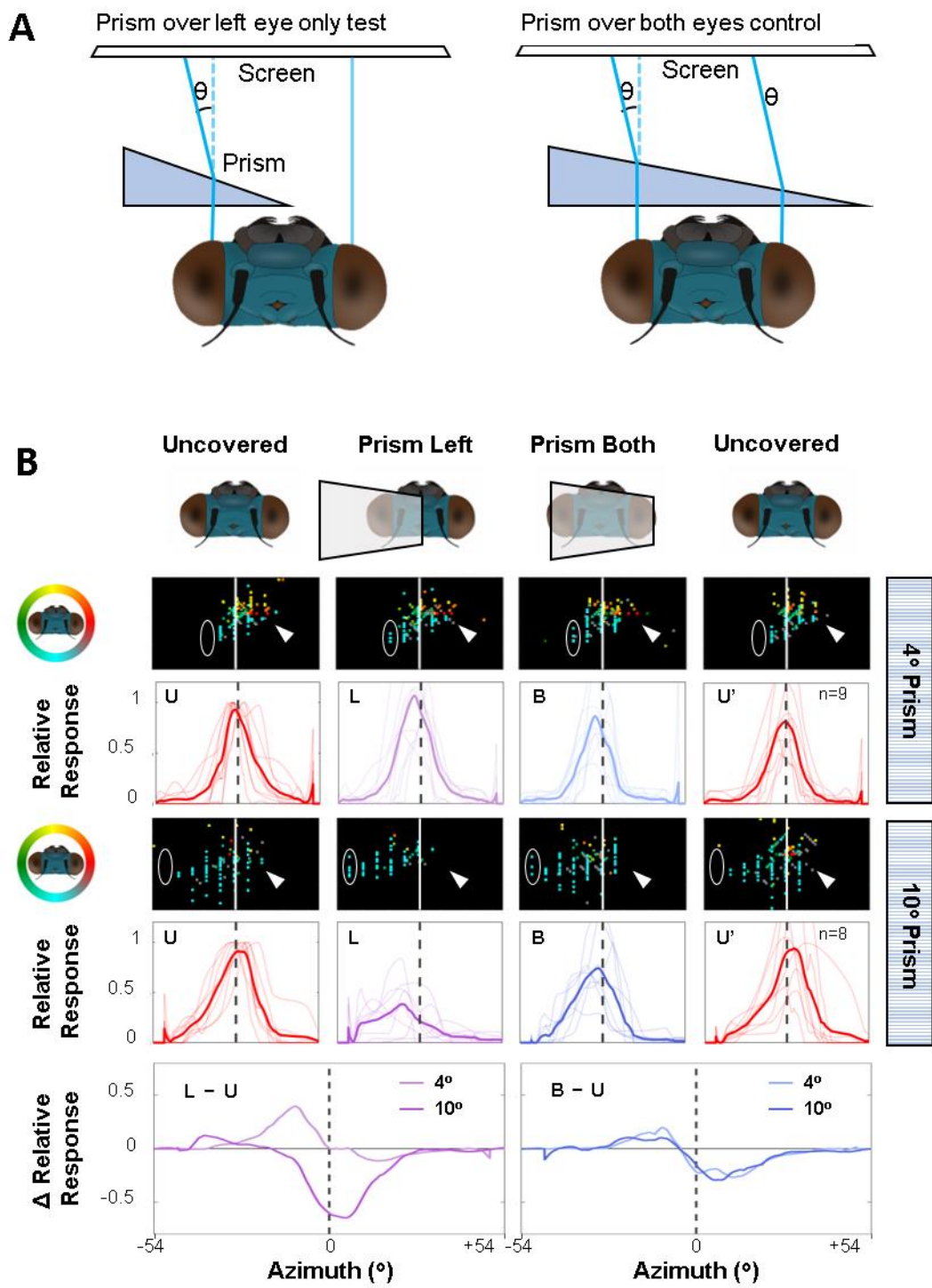


Figure 3.12 (legend right)

### **Figure 3.12 (left) Demoiselle TSDN receptive fields under prisms of varying deviation power**

(A) A wedge prism placed in front of the left eye with the thick end lateral to the animal reduces the binocular overlap between the two eyes by the deviation ( $\theta$ ) induced by the prism. Placing the wedge prism in front of both eyes simply shifts the entire visual field leftwards, and thus acts as a control. (B) 4° and 10° prisms were used to test the TSDN responses under reduced binocular overlap between the two eyes. Reducing binocularity by 4° did not significantly affect spike density (two-sided sign test for matched pairs,  $p = 1.0$ ,  $n = 9$ , blue traces), but a shift of 10° significantly lowered the spike densities compared to uncovered control (two-sided sign test for matched pairs,  $p = 0.0078$ ,  $n = 8$ , see purple traces). No prism, or prism over both eyes served as controls for the effect of the prism. Rows 1 and 3 = three example directional receptive fields at each prism deviation. White arrowheads mark the right-hand boundary of the receptive field. White ellipses indicate the left-hand boundary of the receptive field. Rows 2 and 4 = Relative response densities (STAs projected onto the horizontal axis, mean  $\pm$  individual traces from each recording, 4°  $n=9$  cells from 6 animals, 10°  $n = 8$  cells from 7 animals). Row 5 =  $\Delta$ -Relative response plots calculated by subtracting the first binocular uncovered response density (control) from each condition. U=Uncovered; L=Monocular prism over left eye; B=Binocular Prism; U'=Uncovered control. Full data set for prism experiments in Figure 3.SI4.

## **3.4 Discussion**

### **3.4.1 Eye morphology, hunting strategy, and TSDN homology within Odonata**

Damselflies and dragonflies share a last common ancestor ~270 MYA and have thereafter evolved distinct behavioural and anatomical divergence, most notably in predatory tactic (Corbet, 1999), flight kinematics (Wakeling and Ellington, 1997), and ocular configuration (Corbet, 1999; Grimaldi and Engel, 2005; Horridge, 1978). Dichoptic eyes resembling those of Zygoptera and some Eiprocta are present in fossils of extinct early odonates (Bechly et al., 2001; Grimaldi and Engel, 2005). Our data describing the intermediate ocular separation and elevation of foveae in dichoptic *Gomphoidea* dragonflies between that of damselflies and holoptic dragonflies (Figure 3.1A-B) suggests a dichoptic ancestral morphology.

With regards to body orientation, demoiselles actuate a more frontal angle of attack compared to the dorsal path of Libellulid dragonflies (Figure 3.3 B-C and 3.SI1). Although the high-speed videos in this study do not have the resolution required to quantify the orientation of the head axis relative to the body axis, an offset between these two axes exists in the dragonfly and demoiselle species here investigated (Figure 3.SI1). For example, when *Erythemis simplicicollis* is perched in preparation for hunting, the head is tilted ventrally by ~30° with regards to the body axis (Figure 3.SI1C). Similarly, when ready for hunting, a demoiselle perches with its body axis pitched downward (~12°), and with its head pitched

dorsally by the same amount (Figure 3.SI1D). Therefore, on average, *E. simplicicollis* responds to prey that is  $\sim 63^\circ$  above the dragonfly head axis (Figure 3.SI1C). This is consistent with the high acuity dorsal fovea of this species, which is positioned at  $60^\circ$  elevation [10], and within the preferred hunting range of  $57^\circ$  to  $102^\circ$  in elevation previously reported for common white tail dragonflies (*P. lydia*) [15]. Likewise, we can estimate that, on average, a demoiselle responds when the prey is flying  $\sim 2^\circ$  above its head axis (Figure S1E). This also fits well with the location of the visual fovea published for other damselfly species as directed forward and slightly downward (Horridge, 1978; Walguarnery et al., 2009). Given such estimations, we predict that the differences in the attack (i.e. dorsal-dragonfly and frontal-demoiselle) here reported between the two groups would be even more pronounced if the measurements of the prey elevation were made relative to the head axis instead (i.e. prey location within the visual field of the predator).

Together, the behaviour and the alignment of homologous TSDN receptive fields to the frontal and dorsal aspect of the visual field respectively, suggests that an ancestral target tracking neuronal circuitry was inherited by these sister lineages and co-evolved with divergent ocular anatomy and predatory strategies. In this case, the holoptic morphology and dorsally elevated fovea found among holoptic Anisopterans likely evolved from a gradual shift in ancestral frontal foveae (Figure 3.1). Interestingly, however, holoptic dragonflies also possess a less pronounced frontal fovea (Figure 3.2B) (Horridge, 1978); whether this frontal dragonfly fovea represents a vestigial duplication of the primary dorsal fovea, or an independent convergent fovea arising from need for collision avoidance or other selective pressures is unknown and would be an interesting area for future study.

Despite the distal ancestry between damselflies and dragonflies, TSDN receptive field architecture is remarkably conserved (Figure 3.5). Demoiselle TSDNs are directionally selective, with some demoiselle TSDNs often indistinguishable from those in the dragonfly (Figure 3.5). This was somewhat surprising especially given the dissimilarity in flight kinematics in these sister lineages (Wakeling and Ellington, 1997), and suggests that pre-motor encoding is robust to peripheral idiosyncrasies in flight actuation. It would be interesting to compare circuitry downstream of TSDNs in the thoracic motor centres to investigate whether peripheral circuitry is similarly robust to flight kinematics or whether these circuits are the subject of specialisation (Bidaye et al., 2018).

### **3.4.2 Neuronal encoding of holoptic versus dichoptic visual space**

Holoptic eyes have evolved independently in other insect lineages, and is especially common amongst dipteran males who intercept or pursue fast flying females, including hoverflies, horseflies, and soldierflies (Perry and Desplan, 2016). Functionally, holoptic eyes are believed to aid in tracking small fast moving targets (Perry and Desplan, 2016), but how so was not clear. For example, holoptic eyes are usually associated with a dorsal acute zone where resolution is increased by flattening the ommatidial plane to reduce interommatidial angles (see Chapter 1, section 1.2.1) (Perry and Desplan,

2016); however, this advantage alone is attainable without dorsal fusion of the eyes, as found in robberflies (Wardill et al., 2017) and mantids (Barrós-Pita and Maldonado, 1970).

Our comparative work suggests that in Odonata the reference frame within which a target is encoded differs between holoptic and dichoptic eyes. Because demoiselle TSDNs are directionally tuned, and because their responses are dependent on the summation of input from both eyes, they encode directional information in an absolute egocentric frame of reference i.e. directional information of a target moving towards the midline in the left eye must be combined with the directional information of the target moving away from the midline in the right eye. This is in contrast to the TSDNs of *Aeshnoidea* and *Libellulidea* dragonflies, whose receptive fields possess a sharp midline boundary, which can arise monocularly (Frye and Olberg, 1995; Gonzalez-Bellido et al., 2013; Olberg, 1986) and are likely sharpened by neural processes. For example, the responses of a dragonfly lobula centrifugal neuron drop below baseline when a target enters the contralateral visual hemisphere (Wiederman and O’Carroll, 2013), which could be used via an inter-ocular inhibitory pathway to sharpen the midline boundary in downstream TSDNs. We propose that the sharpening of this midline boundary in dragonfly TSDNs has co-evolved with the holoptic eye, and functions to simplify the pre-motor representation of the visual scene by encoding movement of targets in each eye as two halves of a visual panorama. This encoding explicitly represents target movement with respect to the holoptic midline, and thus aligns the sensory coordinate system to represent lateralised commands for the thoracic motor centres. This design may enhance the efficiency of neuronal processing for rapid and accurate responses in interception strategies that do not require stereoscopic information, as is thought to be the case in *Libellulidea* (Lin and Leonardo, 2017). We would expect other holoptic species to employ a similarly lateralised simplification of premotor target movement representations relative to other closely related dichoptic species and/or conspecifics.

### **3.4.3 Binocular properties of demoiselle TSDNs**

We have shown that the responses of demoiselle TSDNs to small moving targets are highly or entirely dependent on simultaneous binocular stimulation (Figures 3.10 and 3.11). In insects, binocular neurons that assess self-motion through wide field optic flow includes those of the lobula complex (Farrow et al., 2006; Hennig et al., 2011; Krapp et al., 2001), descending neurons (Wertz et al., 2008, 2009b), and motor neurons (Huston et al., 2008). Such binocular wide field neurons respond strongly to monocular stimulation, and binocular integration functions to extend the receptive field across the visual panorama to enhance directional selectivity and match specific modes of self-motion (Farrow et al., 2006; Huston et al., 2008; Krapp et al., 2001; Wertz et al., 2009b). In addition, there are accounts of binocular integration of moving objects in the lobula complex of crabs, mantids, and dragonflies (Rosner et al., 2018; Scarano et al., 2018; Wiederman and O’Carroll, 2013). The dragonfly centrifugal neuron responds to small moving objects with an extended receptive field across the two visual hemispheres,

and is thought to attend to targets moving from one visual hemisphere to the other (Wiederman and O'Carroll, 2013); in this respect the function of binocular integration appears to be to extend the receptive field, similar to binocular optic flow neurons. In crabs and mantids, lobula neurons typically respond to independent monocular stimulation with vertical bars, with responses modulated under coincident binocular stimulation (Rosner et al., 2018; Scarano et al., 2018). In the case of mantids, binocular responses are consistent with a linear summation to threshold mechanism (Rosner et al., 2018). Thus, given that demoiselle TSDNs appear to sum monocular responses to threshold (Figure 3.10), it is possible that mantis and demoiselle object tracking circuits earlier in the visual system may integrate binocular information similarly.

Without anatomical verification for the eye patch experiments, we are currently unable to conclude whether the three types of binocularity patterns recorded in this study pertain to specific TSDN types, so this possibility remains to be investigated. However, we do know that the extent of binocular overlap can change dramatically within a TSDN type across animals (Figure 3.9) and that simultaneously recorded TSDNs in the same animal exhibit different binocularity patterns (Figure 3.11A), evidencing that differences in binocularity are present within an individual and across the population. Such differences could arise from changes in eye dominance (weighing of inputs) and sensitivity (threshold). Changes in eye dominance could result from experience driven plasticity (Klink et al., 2010). Since dragonfly TSDNs remain silent for the first 1-2 days after eclosion (Olberg, unpublished results), input weightings may be fine-tuned during this period. With regards to differences in threshold sensitivity, it is known that the same TSDNs recorded in different individuals of the same dragonfly species exhibit markedly different spiking levels (Gonzalez-Bellido et al., 2013), a finding reproduced here in demoiselles (Figure 3.9). This is likely a combination of recent stimulus history (repeated stimulation quickly results in a reduction of responses due to habituation), and internal state (such as hunger, temperature, or maturity level). Indeed, in the stomatogastric system of crabs and lobsters, the properties of individual neurons forming a circuit varies across animals, but all populations reach an equilibrium that produces a common motor output (Golowasch et al., 1999; Marder and Goaillard, 2006). Whether such heterogeneity in TSDNs responses influences the quality of predatory flights should be investigated further; however, this will first depend on in-depth studies investigating the factors leading to such variation in TSDN responses.

Whilst demoiselle TSDN receptive fields are binocular and receive bilateral input, our monocular (Figures 3.10-3.11A), and prism experiments (Figure 3.12) indicate that the visual midline is nonetheless encoded within the inputs to these neurons. It is not clear from our data how a binocular TSDN threshold becomes positioned at the visual midline to yield the truncated Type 2 and Type 3 monocular receptive fields (Figures 3.10-3.11A). It is possible that interocular inhibition may function to fine tune the positioning of this threshold. Indeed, in the dragonfly lobula, heterolateral inhibitory feedback between centrifugal CSTMD1 neurons results in an abrupt decrease in firing rate as a target

crosses the midline from the ipsilateral into the contralateral visual hemisphere (see Chapter 1, Figure 1.17, section 1.3.3) (Geurten et al., 2007b; Wiederman and O'Carroll, 2013). Analogous circuitry in the demoiselle lobula may function to define a visual midline which could feed into threshold tuning.

In summary, this study presents evidence that target tracking information at the pre-motor level is fused across visual hemispheres in demoiselles. Binocular fusion is known to confer perceptual advantages relevant for a target tracking system such as enhanced visual sensitivity (Campbell and Green, 1965; Elberger, 1989) and decreased reaction times (Blake et al., 1980). However, such binocular fusion necessitates encoding visual motion in a binocular-fused frame of reference. In contrast, the reference frame of holoptic eyes is relative to the midline. This may result in a simpler descending control system that only needs to implement the commands from one eye/neuron, preventing the temporal resolution problems that may arise when integrating equivalent signals from neurons with different sensitivities and latencies. As a trade-off, the holoptic eye is limited in stereoscopic computation of depth compared to a dichoptic morphology. Our data indicates that demoiselle TSDNs are disrupted when their binocular overlap is reduced by more than  $10^\circ$ . It remains to be shown if these binocular neurons respond to disparities and whether a population of disparity tuned cells, which could be used for stereoscopic processing of depth, are present earlier in the demoiselle visual system.

### 3.5 Supplementary Information

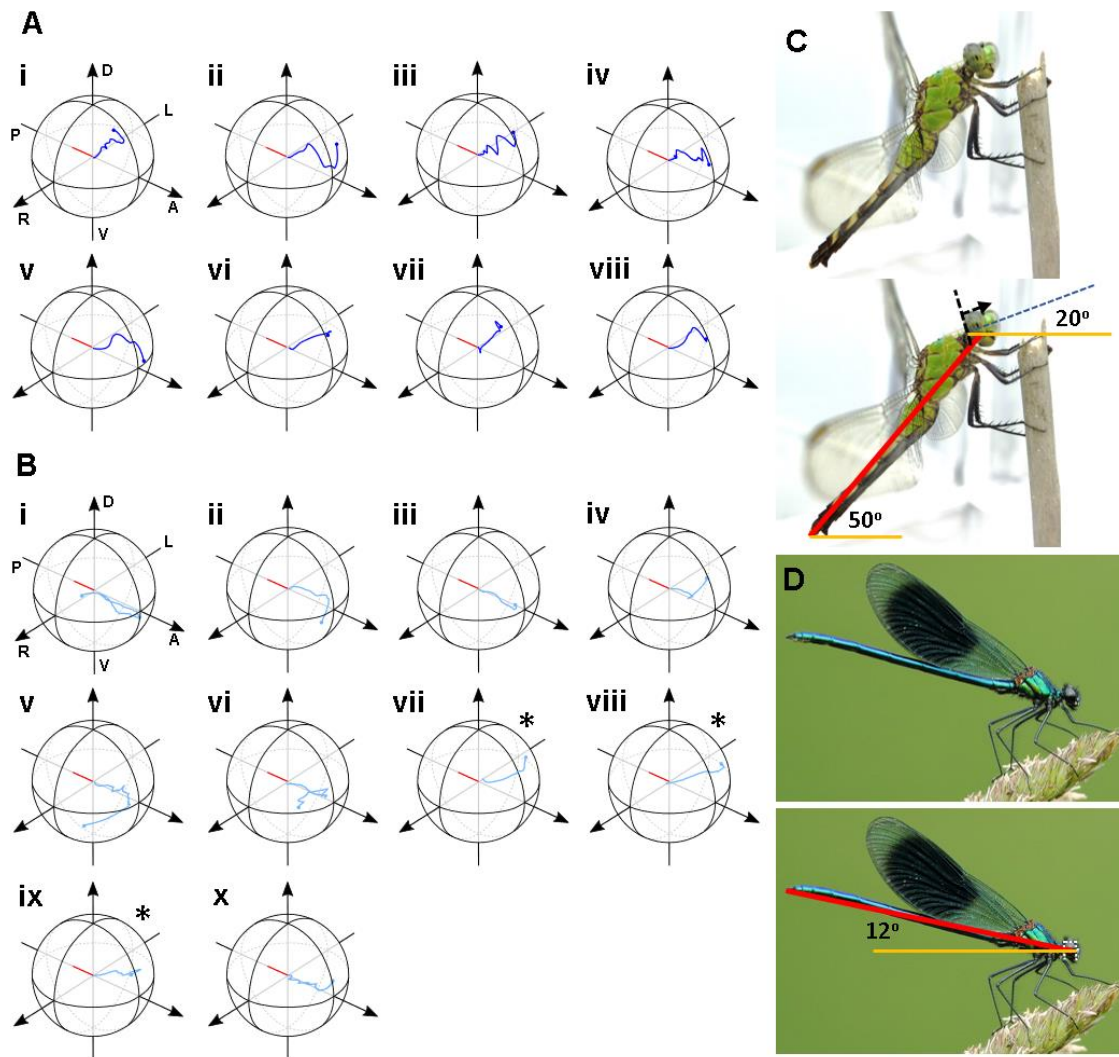


Figure 3.SI1

**Figure 3.SI1 (left) Path of prey through the visual field during predatory flights**

Full dataset of **(A)** dragonfly and **(B)** demoiselle attack trajectories, tracing the path of the artificial prey relative to the body axis. Relating to Figure 3.3. D=Dorsal, V=Ventral, A=Anterior, P=Posterior, L=Left, R=Right. Note that the three demoiselle trajectories marked with an asterisk show a more dorsal attack because the location of the bead was changed slowly around the animal from posterior-dorsal to anterior-ventral. Thus, the results of those trajectories aimed to identify the dorsal limit for the location of a bead that elicits a demoiselle attack. **(C)** Picture of an *Erythemis simplicicollis* dragonfly in hunting position in our arena, and the measurements of the differences in orientation between body and head axis in such conditions. The body axis and head axis are positioned  $50^\circ$  and  $20^\circ$  relative to the horizon, respectively. Thus, the head is tilted ventrally by  $30^\circ$  ( $50^\circ - 20^\circ$ ) relative to the body axis when the animal is perched. **(D)** A picture of *Calopteryx splendens* in the wild (image credit, Dave Soons), and the measurements of the differences in orientation between body and head axis in such conditions. The body axis is tilted downward  $12^\circ$  degrees when perched, with the head axis aligned with the horizon. Thus, the head is tilted dorsally  $12^\circ$  relative to the body axis when the animal is perched.

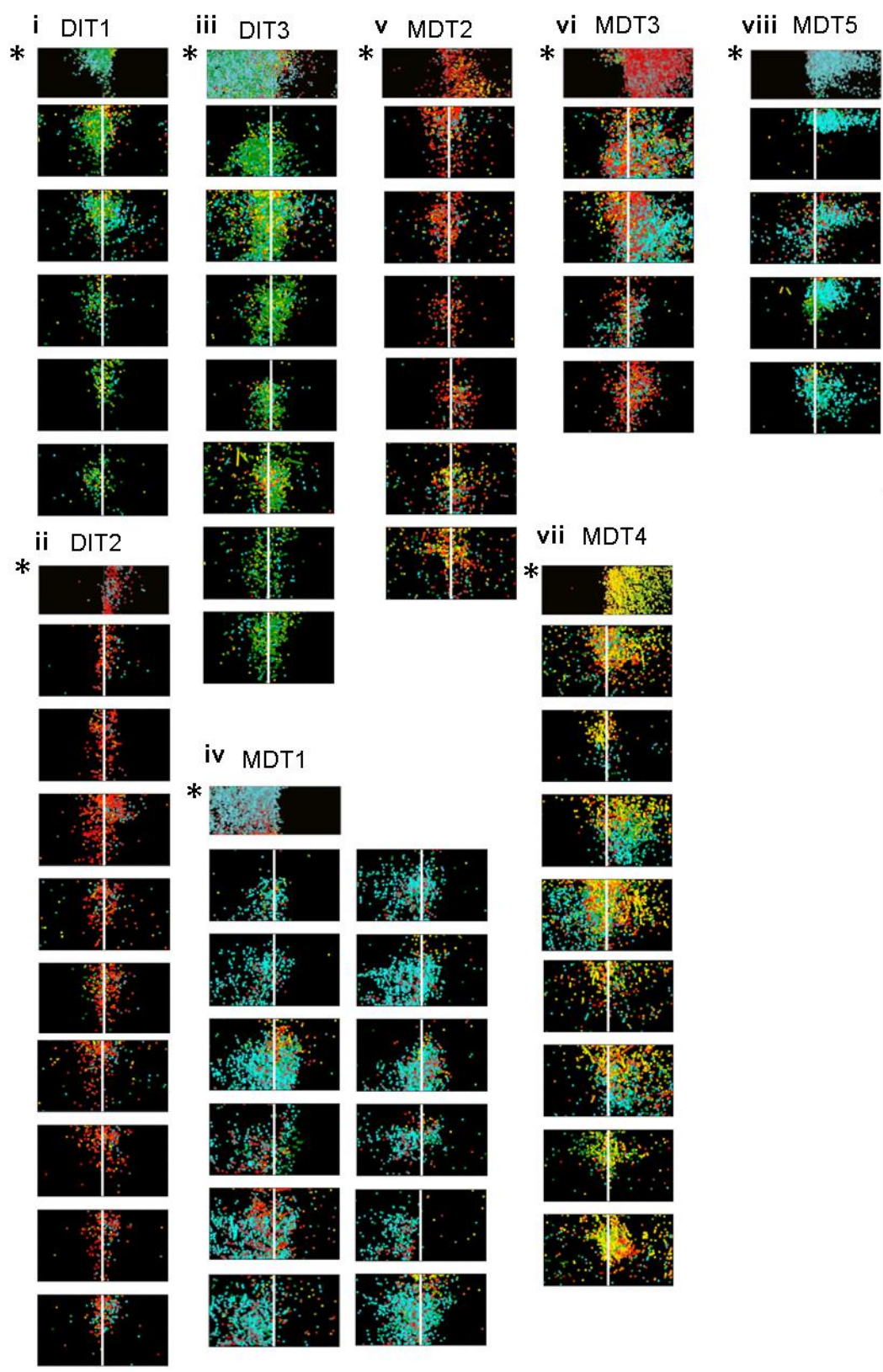
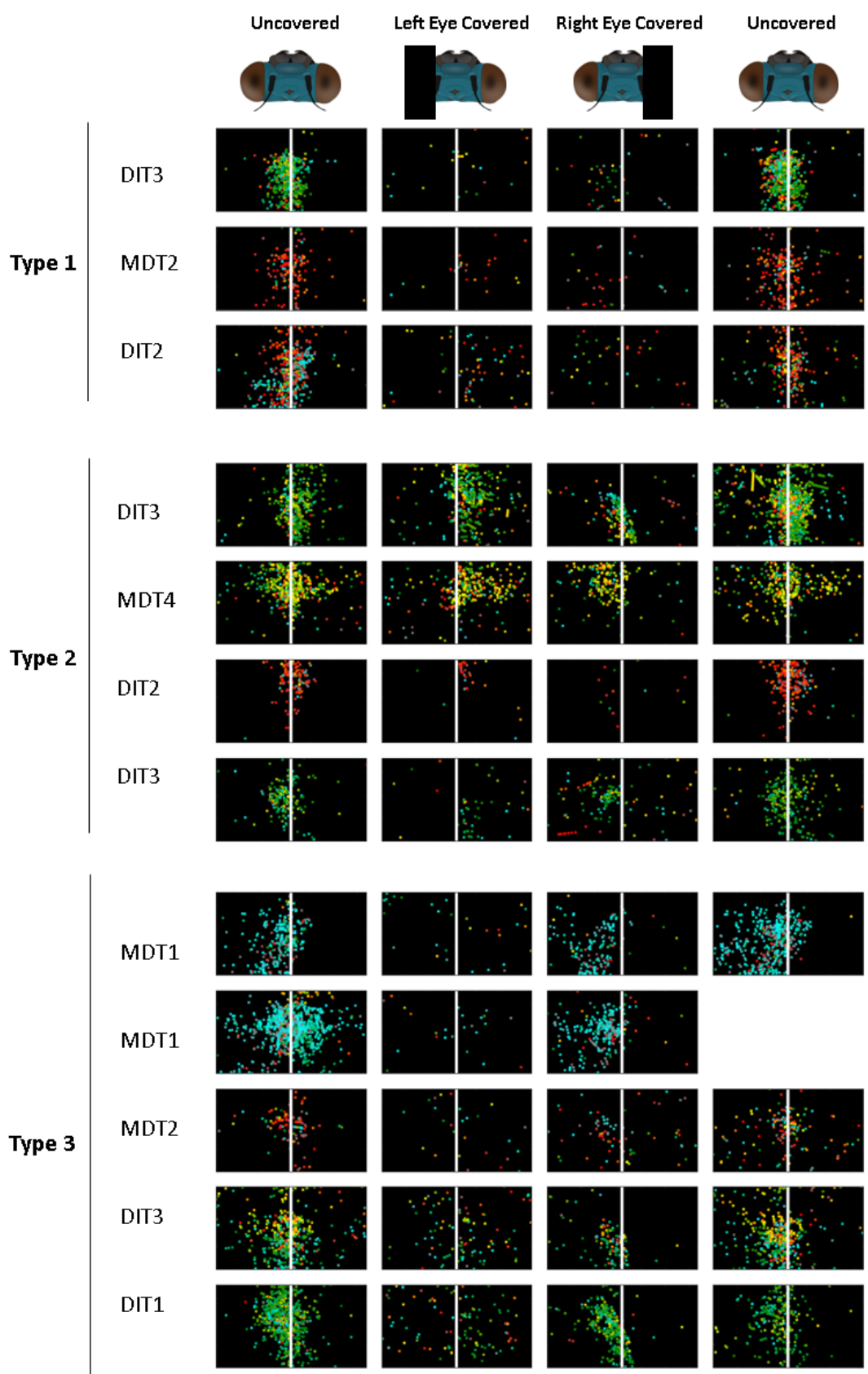


Figure 3.SI2

**Figure 3.SI2 (left)** The receptive field maps of demoiselle TSDNs are allocated qualitatively to TSDNs types known from dragonflies (dragonfly maps marked with an asterisk), according to their directional tuning, as well as size and center position of the receptive field. All recorded demoiselle TSDN receptive fields deemed to have acceptable spike sorting are included. The most difficult assignments were between dragonfly DIT1/DIT3 (i-ii) and DIT2/MDT2 (vi-vii) as the directional tuning of these cells is very similar. For DIT2/DIT3 (i-ii) the distinction was made by the vertical extent of the receptive field, with DIT3 (ii) having a longer vertical extent compared to DIT1 (i) in dragonflies. For DIT2/MDT2 (vi-vii), the distinction was based on the horizontal extend of the receptive fields, with dragonfly MDT2 (vii) having a wider horizontal spread in the receptive field compared to DIT2 (vi). Dragonfly maps reproduced from (Gonzalez-Bellido et al., 2013).



### **Figure 3.SI3**

**Figure 3.SI3 (left)** The original directional maps, and putative TSDNs IDs, resulting from the opaque eye patches used to calculate averages in Figure 3.10. Monocular conditions are with the opaque eyepatch. The spike counts of these receptive fields were each normalized to the maximum pixel spike count in the first binocular uncovered condition. These normalized receptive fields were then averaged to form the data in Figure 3.10. Suggested TSDN cell types are indicated on the left. One Type 3 receptive field is missing the final binocular uncovered positive control.

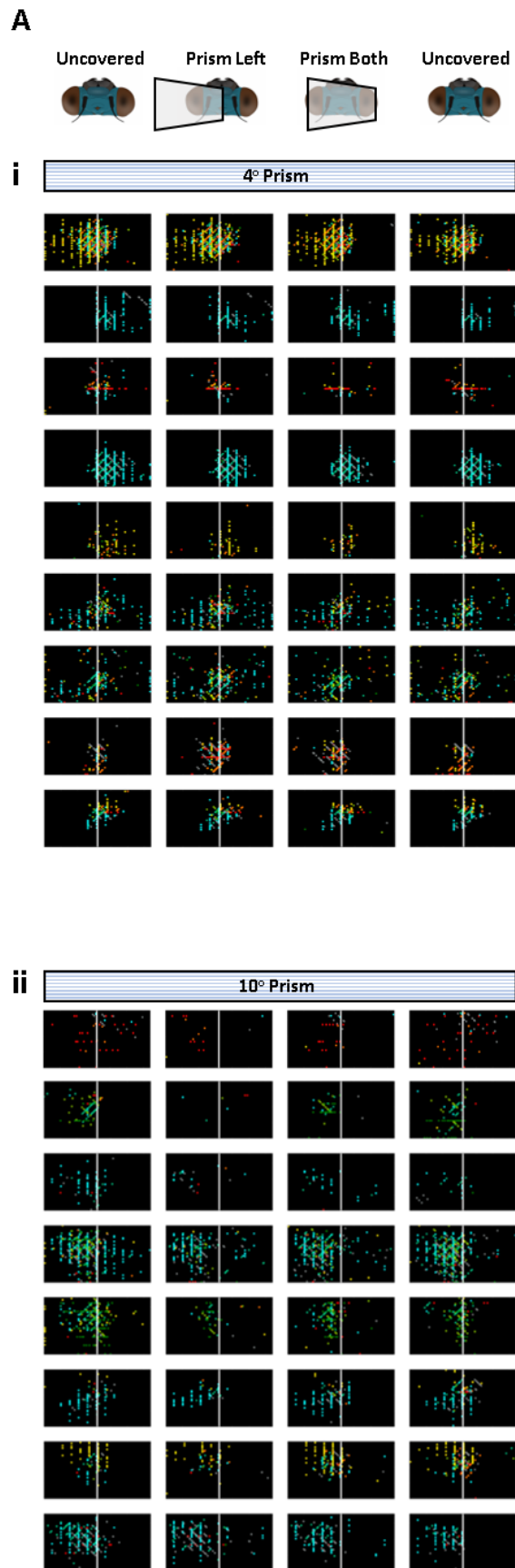


**Figure 3.SI4**

Full data set of prism experiments used in Figure 3.11 (A) 4.2° prism (n=9 cells from 6 animals). (B) 10° prism (n=8 cells from 7 animals).

# Chapter 4

## Target Selective Descending Neurons in convergent predatory dipterans

### 4.0 Acknowledgements and contributions

Embedded ventral nerve cord cross sections in Figure 4.1 were collected by Paloma Gonzalez-Bellido. *Holcocephala* target resolution scan in Figure 4.4 was acquired by Paloma Gonzalez-Bellido and analysed by Jack Supple. All other data was collected and analysed by Jack Supple.

### 4.1 Introduction

Visual detection, tracking, and closed-loop interaction with moving targets is a task faced by many animals. At the core of this undertaking is an information processing challenge to efficiently transform sensory signals into the task-specific activation of muscles. Predatory flying insects present an extreme example, performing complex visually-guided pursuits of small, often fast flying prey over extremely small timescales (Olberg et al., 2007; Wardill et al., 2015, 2017). This behaviour is controlled by a tiny nervous system, further constraining neural circuits for optimal coding efficiency (Gonzalez-Bellido et al., 2016).

In Dragonflies, a population of eight pairs of bilaterally symmetric Target Selective Descending Neurons (TSDNs) relay visual information about small moving objects from the brain to the thoracic motor centres (Gonzalez-Bellido et al., 2013; Olberg, 1986). These neurons encode the movement of small moving objects across the dorsal fovea region of the eye, which is fixated on prey during predatory pursuit (Lin and Leonardo, 2017; Mischianti et al., 2015; Olberg et al., 2007), and are thought to constitute the commands necessary for actuating an interception flight path (Gonzalez-Bellido et al., 2013; Olberg, 1986). Each TSDN type has a characteristic receptive field, with responses spatially confined to a specific portion of the dorsal fovea visual field and tuned to a specific direction of object

motion (Gonzalez-Bellido et al., 2013). Whilst the direction of target motion can be decoded with high accuracy using a population vector decoder of TSDN activity (Gonzalez-Bellido et al., 2013), the spatial and directional tuning specificity of individual TSDN receptive fields do not appear to follow a simple geometric pattern, but rather over-represent some dimensions of motion more than others. It is currently unexplored whether dragonfly TSDNs constitute a generalisable premotor representation or is specifically tailored to dragonfly body plan, flight kinematics, and/or predatory strategy.

Diptera is a large and diverse order of winged insects, with adults of many species highly specialised for tracking and chasing other fast flying insects suited as mates or prey (Collett and Land, 1975; Perry and Desplan, 2016; Wiegmann et al., 2011). Many descending neurons projecting to neck and flight motor centres have been described in dipterans responding to object expansion (i.e. ‘looming’) (Ache et al., 2019; von Reyn et al., 2014) and specific patterns of wide-field optic motion (Namiki et al., 2018; Strausfeld and Bassemir, 1985a; Suver et al., 2016). Few accounts describe dipteran descending neurons responding selectively to moving objects (Gronenberg and Strausfeld, 1990, 1991). However, one male-specific descending neuron (DNDC3-6b) in *Sarcophaga* has is reported to respond to small moving targets within the acute zone of the compound eye, a male-specific adaptation for detecting and tracking females (Gronenberg and Strausfeld, 1990, 1991), indicating a role in premotor control of target pursuit (see Chapter 1, section 1.3.3.2). This neuron has a cell body at the n-ventral anterior aspect of the midbrain close to the anterior optic tubercle (AOTU), and arborizes at both the AOTU and the ventral lateral protocerebrum (see Chapter 1, Figure 1.19) (Gronenberg and Strausfeld, 1991). Whilst this neuron responds to movement in the ipsilateral eye (Gronenberg and Strausfeld, 1990, 1991), little more is known about its receptive field properties, nor whether this neuron functions within a population of target tracking descending neurons, as is the case for Odonate TSDNs (Chapter 3) (Frye and Olberg, 1995; Gonzalez-Bellido et al., 2013; Olberg, 1986).

Several dipteran lineages have independently converged to predatory lifestyles in adulthood, offering a unique opportunity to investigate the evolution of neural circuits specifically involved in controlling predation. In this study we investigate the descending target tracking neural circuitry in two relatively distantly related dipteran species converging to predation, the adult robberfly *Holcocephala fusca* (family *Asilidae*) (Fabian et al., 2018; Wardill et al., 2017), and the adult killerfly *Coenosia attenuata* (also known as hunterflies, family *Muscidae*) (Bautista-Martínez et al., 2017; Gonzalez-Bellido et al., 2011; Wardill et al., 2015). Akin to many dragonflies, *Holcocephala* and *Coenosia* are generalist predators, detecting their prey from a perched position before initiating intercepting flight paths (Fabian et al., 2018; Wardill et al., 2015, 2017). *Holcocephala* position themselves on tall perches within vegetal clearings to contrast prey against the sky (Wardill et al., 2017), whilst *Coenosia* typically hunt amongst foliage under relatively lower light levels (Bautista-Martínez et al., 2017; Wardill et al., 2015). Interception is achieved by maintaining a constant line-of-sight angle between the pursuer and prey whilst closing the distance between them, a navigation principle known as parallel navigation (Brighton

et al., 2017; Fabian et al., 2018). Both *Holcocephala* and *Coenosia* are thought to compute parallel navigation using a proportional navigation algorithm, which rotates the pursuer's heading proportional to the rate of rotation of line-of-sight with the prey (Fabian et al., 2018). However, *Holcocephala* manoeuvre with a higher proportional gain and longer time delay compared with *Coenosia*, reflecting longer and less erratic flight paths in *Holcocephala* (Fabian et al., 2018). Both dipterans possess ocular adaptations to facilitate target detection (Gonzalez-Bellido et al., 2011; Wardill et al., 2017). However, *Holcocephala* are noticeably specialised, with two enlarged dichoptic (i.e. separated) compound eyes with forward facing foveae (see Chapter 1, section 1.2.1, Figure 1.5) (Wardill et al., 2017), which are not found in *Coenosia* nor any other *Muscidae*. Furthermore, *Holcocephala* have highly mobile heads and display saccadic head-flicks followed by a brief tracking period of potential prey before take-off (Wardill et al., 2017), resembling saccades seen in dragonflies (Olberg et al., 2007). Considering these differences, *Holcocephala* and *Coenosia* offer unique systems to investigate whether similar representations to the Odonate TSDN system have independently evolved, or whether novel encoding strategies have emerged, tailored to specific visual ecologies, body plan, and hunting strategy.

## 4.2 Methods and materials

### 4.2.1 Animals and electrophysiology

Robberflies and killerflies were collected and handled as described in the Methods Chapter, section 2.1.2. Briefly, adult *Holcocephala fusca* robberflies were wild-caught between July-August (inclusive) in York, Pennsylvania, USA. Adult *Coenosia attenuata* killerflies were reared from larvae in an established breeding colony in the laboratory in Cambridge, UK. Animals were anaesthetised at  $-20^{\circ}\text{C}$  for 3 minutes, then waxed down to a platform ventral side up, ready for ventral nerve cord dissection (see Methods Chapter, section 2.2.1). The head was positioned with a gentle dorsal tilt such that the region of high acuity on the eye (Gonzalez-Bellido et al., 2011; Wardill et al., 2017) pointed towards the centre of the screen.

Extracellular recordings from 16 female and 3 male robberflies, and 14 female killerflies were performed as described in the Methods Chapter (section 2.4). Since the dipteran cervical connective is fused, electrode penetrations were always directed towards the right-hand side of the connective in order to sample as fully as possible one side of the bilaterally symmetric population of descending neurons. Visual stimuli were presented using a DepthQ 360 projector focused onto a 17.3 x 9.6 cm white screen material (section 2.3.1). Animals were placed at 7 cm, resulting in a subtended screen size of  $102^{\circ} \times 69^{\circ}$ . Visual stimuli consisted of widefield gratings ( $4^{\circ}$  spatial frequency,  $45^{\circ}/\text{sec}$ ) and a series of 3000 small ( $2^{\circ} \times 2^{\circ}$ ) moving targets as described previously (section 2.4.3) (Gonzalez-Bellido et al., 2013).

## 4.2.2 2-photon brain imaging

Female robberflies and female killerflies were prepared for ventral nerve cord backfills as described in Methods Chapter, section 2.5.1. Brains were cleared and imaged in TDE (2,2'-Thiodiethanol) using an Olympus XLSL Plan N 25x /1.00 Glyc MP  $\infty$ /0-0.23/FN18 multiphoton objective (section 2.5.1). Images were acquired at 0.3  $\mu$ m isovoxel resolution. Tiled z-stacks were stitched in Fiji and viewed in Vaa3D (section 2.5.1).

## 4.2.3 Data analysis

Electrophysiology data was analysed in Spike2 (CED) and MATLAB (Mathworks). Latency, direction tuning maps, and STA maps were calculated as described in the Methods Chapter 2, section 2.4.3. STAs were calculated for both stationary targets appearing on the screen, and for moving targets to compare object detection and motion detection responses. Direction tuning maps were calculated only for moving targets.

# 4.3 Results

## 4.3.1 Neuroanatomy and descending neuron organisation

As in all dipterans, robberflies and killerflies possess cephalised central brain ganglia connected via a fused cervical connective to three fused thoracic ganglia which innervate the pro-, meso-, and meta-thoracic segments (Namiki et al., 2018; Yeates et al., 2002) (Figure 4.1C-F). The *Holcocephala* brain is distinctly encephalised relative to the *Coenosia*, measuring ~2.3 mm x 0.93 mm in female *Holcocephala* (n=1, Figure 4.1E) and ~1.3 mm x 0.65 mm in female *Coenosia* (n=1, Figure 4.1F). Whilst the central brain is comparable in size for both *Holcocephala* and *Coenosia* (box, Figure 4.1E-F), the cerebral ganglia of *Holcocephala* is overwhelmingly comprised of two large optic lobes, whilst the optic lobes of *Coenosia* are far less enlarged (Figure 4.1E-F).

Despite the difference in overall size of each nervous system, the cervical connective of both female *Holcocephala* and female *Coenosia* measures ~500 $\mu$ m from the posterior aspect of the suboesophageal ganglion to the anterior aspect of the prothoracic ganglion (Figure 4.1E-F). Cross-sections of the cervical connective reveal numerous large caliber axons passing along the dorsal aspect (Figure 4.1G-H), which in arthropods corresponds to the position of descending pre-motor tracts (Namiki et al., 2018; Smarandache-Wellmann et al., 2016; Strausfeld and Gronenberg, 1990). Such increases in axon diameter suggest specialisation for reduced reaction times and increased information transmission rates (Perge et al., 2012). In *Coenosia*, a pair of axons are noticeably enlarged relative to others, resembling the giant fibres found in other dipterans (Coggshall et al., 1973) (asterisk, Figure 4.1H). In *Holcocephala*, several large calibre neurons are visible, with no conspicuous enlargement of any single pair (Figure 4.1G).

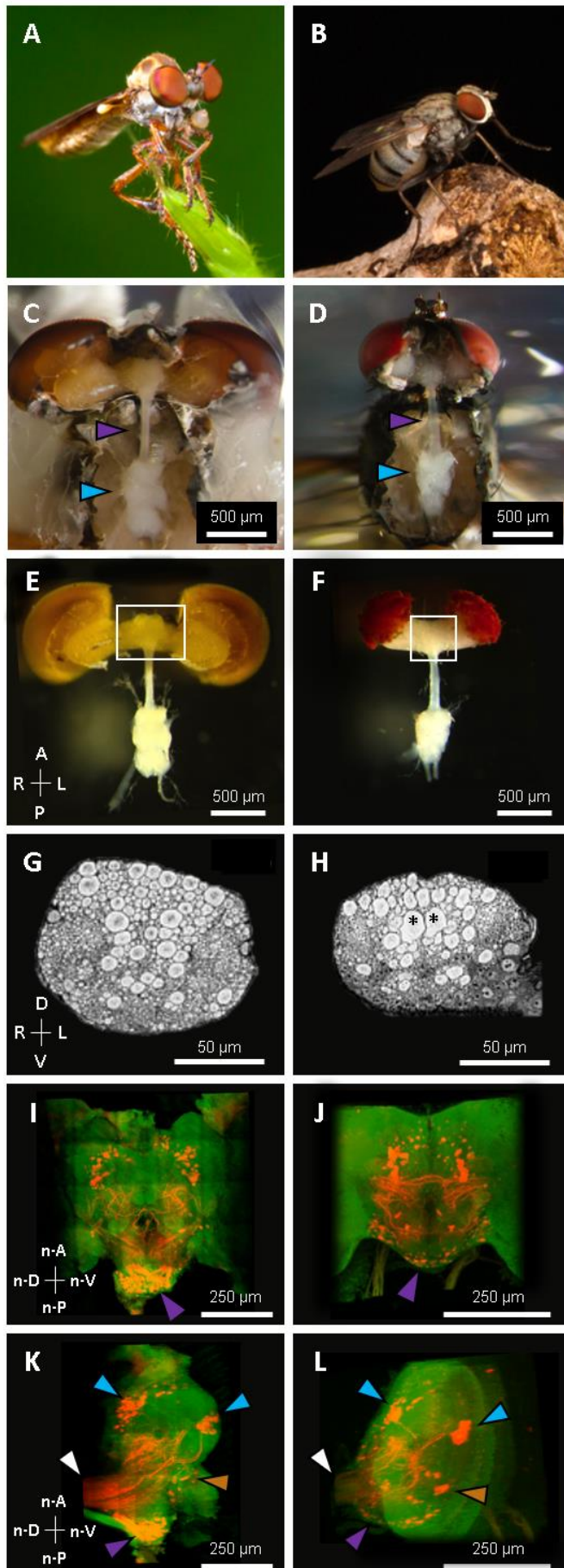


**Figure 4.1 Comparative neuroanatomy of *Holcocephala* and *Coenosia*** (A) Female *Holcocephala fusca* and (B) Female *Coenosia attenuata*. (C-D) Minimal dissection of (C) *Holcocephala* and (D) *Coenosia* revealing the cerebral ganglia, cervical connective (purple arrow), and thoracic ganglia (blue arrow). (E-F) Full dissection of (E) *Holcocephala* and (F) *Coenosia* nervous systems. Central brain indicated by white box. (G-H) Cervical connective cross-sections. Asterisks indicate potential giant fiber homologues in *Coenosia*. (I-J) Frontal and (K-L) lateral maximum intensity projections of ventral nerve cord backfills from a female *Holcocephala* (n=1 animal) and female *Coenosia* (n=1 animal). Brain axes in are given with respect to the neuraxis (n-, neuraxis). Purple arrows indicate gnathal ganglia cell bodies. Blue arrows indicate the two most prominent clusters of cell bodies at the anterior ventral (AOTU cluster) and dorsal surface (SMP cluster). Orange arrows indicate less conspicuous cell body clusters at the posterior ventral surface (AVLP and PNEP clusters). White arrows indicate cervical connective.

To investigate the population of descending neurons passing through the cervical connective, ventral nerve cords were backfilled with dextran dye (Figure 4.1I-L) (Hsu and Bhandawat, 2016; Strausfeld and Gronenberg, 1990). All cell bodies in the cerebral ganglia stained with this technique are by definition descending neurons, whilst neuropil labelling in the brain represent processes of both descending and ascending neurons (Hsu and Bhandawat, 2016). Nonetheless it should be noted that the inputs of descending and ascending neurons may not be confined to the ganglia of developmental origin, although this it thought to be the case for the majority of descending neurons hitherto described (Namiki et al., 2018).

Several clusters of descending neuron cell bodies are present in each species, and match the positions of descending neuron cell bodies previously described in *Drosophila* (Hsu and Bhandawat, 2016; Namiki et al., 2018), *Calliphora* (Strausfeld and Bassemir, 1985a; Strausfeld and Gronenberg, 1990), and *Sarcophaga* (Gronenberg and Strausfeld, 1990, 1991, 1992; Strausfeld and Gronenberg, 1990). Two most prominent clusters of bilaterally symmetric cell bodies are located at the n-ventral and n-dorsal aspect of the midbrain, respectively (blue arrows, Figure 4.1I-L). The n-ventral cluster in each species is located anteriorly, lateral to the vertical lobe of the mushroom body and medial to the anterior optic tubercle (AOTU), matching the so-called AOTU (aka DN<sub>a</sub>) cluster in *Drosophila* and *Sarcophaga* (Gronenberg and Strausfeld, 1992; Hsu and Bhandawat, 2016; Namiki et al., 2018). This is the location of male-specific DNDC3-6b in *Sarcophaga* (Gronenberg and Strausfeld, 1990, 1991). The dorsal cluster likely corresponds to the superior medial protocerebrum (SMP, aka DN<sub>p</sub>) cluster annotated in *Drosophila* (Hsu and Bhandawat, 2016). In *Drosophila* and *Calliphora*, this is the location of giant fibre (Ache et al., 2019; Bacon and Strausfeld, 1986; Milde and Strausfeld, 1990), and DNOVS/DNHS widefield descending neuron cell bodies (Namiki et al., 2018; Strausfeld and Bassemir, 1985a; Suver et al., 2016). As in other species, *Holcocephala* and *Coenosia* n-dorsal cell bodies are relatively disperse along the medial-lateral plane compared to the AOTU clusters (Hsu and Bhandawat, 2016) (Figure 4.1I-J).

Two less prominent clusters are also present at the posterior ventral surface (orange arrows, Figure 4.1I-L). One is medial to the anterior ventrolateral protocerebrum (AVLP) and lateral to the antennal lobe (AL), matching the AVLP (aka DN<sub>d</sub>) cluster in *Drosophila* (Hsu and Bhandawat, 2016; Namiki et al., 2018). The second is ventral to the AL matching the *Drosophila* periesophageal neuropil (PNEP) cluster (aka DN<sub>b</sub>) (Hsu and Bhandawat, 2016; Namiki et al., 2018). Interestingly, there is a much higher density of large descending cell bodies in the gnathal ganglia (GNG) of *Holcocephala* compared with *Coenosia* (purple arrows, Figure 4.1I-L) and *Drosophila* (Hsu and Bhandawat, 2016; Namiki et al., 2018). In *Coenosia* (Figure 4.1J) and *Drosophila* these GNG cell bodies are relatively dispersed medial-laterally along the posterior rind (Hsu and Bhandawat, 2016; Namiki et al., 2018), whereas in *Holcocephala* they are concentrated medially (Figure 4.1I).

Extensive descending neuron arborisation was seen within dorsal neuropils in both *Holcocephala* and *Coenosia*, predominantly within the posterior slope (PS), posterior lateral protocerebrum (PLP), and ventral lateral protocerebrum (VLP) (Figure 4.1I-L). All three regions are known to receive input from lobula visual output neurons that project to a mosaic of optic glomeruli (Aptekar et al., 2015; Mu et al., 2012; Strausfeld and Okamura, 2007; Wu et al., 2016b). In *Holcocephala* there is also a higher density of neuropil staining around the gnathal ganglia more caudally in the midbrain compared with *Coenosia* (Figure 4.1I-L). Both species also have fibers decussating dorsal to the esophagus, albeit more prominently in *Coenosia* than *Holcocephala* (Figure 4.1K-L).

### **4.3.2 Dipteran Target Selective Descending Neurons (dTSDNs) in robberflies and killerflies**

Extracellular electrophysiological recordings from the cervical connective of both *Holcocephala* and *Coenosia* detected several neurons responding vigorously to small moving targets (Figure 4.2). Wide-field moving gratings did not initiate sustained responses, although often responded with a transient response at the onset of grating motion (Figure 4.2 A-Bi). These neurons in both species, termed dTSDNs by analogy with dragonfly TSDNs (Nicholas et al., 2018a; Olberg, 1986), responded both to targets suddenly appearing in the visual field without any directional movement, in addition to targets moving across the visual field (red and green phases, Figure 4.2A-Biii). Interestingly, the timing of spikes in response to objects suddenly appearing in the visual field in *Coenosia* was typically much less variable than in *Holcocephala* (compare red phases, Figure 4.2A-Biii).

Spike latency was longer for *Holcocephala* compared to *Coenosia* for both stationary and moving targets ( $15.9 \pm 2.4$  ms and  $20.5 \pm 2.7$  ms in *Holcocephala*, and  $5.7 \pm 1.9$  ms and  $9.2 \pm 1.8$  ms in *Coenosia*, respectively; Figure 4.3). Latencies in both species were on average shorter for target appearance compared to target movement (difference of 4.6 ms in *Holcocephala* and 3.5 ms in *Coenosia*; Figure 4.3). This difference between target appearance and target movement response latencies could be due to a bias of moving phase spikes towards greater delays if the target initially appeared outside of the dTSDN receptive field and thus needed to move into the receptive field before initiating a spike. However, when only including trajectories that initiated spikes in both stationary and moving phases (indicating that the target must have appeared within the receptive field), the moving phase latency was not affected, with the latency for this condition  $19.9 \pm 2.7$  ms and  $8.8 \pm 1.5$  ms *Holcocephala* and *Coenosia* respectively (union, Figure 4.3).

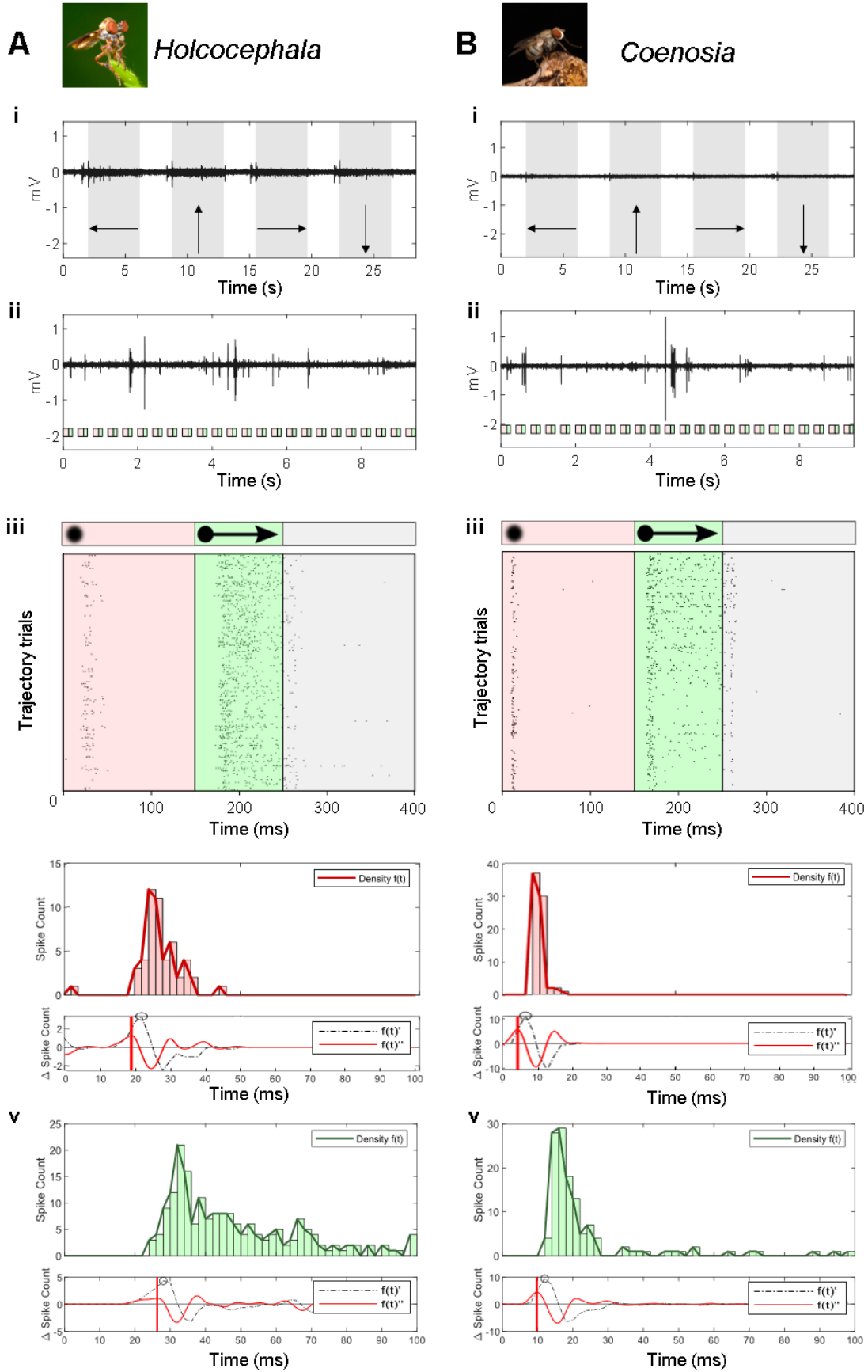
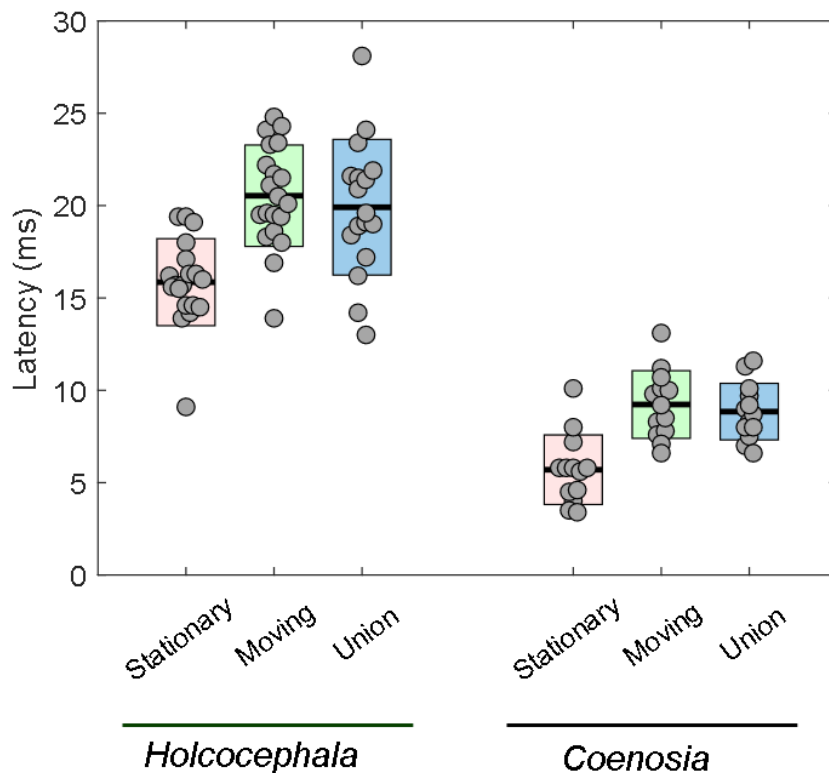


Figure 4.2 (legend right)

**Figure 4.2 (left) Target selectivity in dTSDNs (A) *Holcocephala* and (B) *Coenosia* dTSDNs. (i)** Example response to presentation of wide-field gratings ( $4^\circ$  spatial frequency,  $45^\circ/\text{sec}$ ). Grating durations indicated in gray, direction indicated by arrows. **(ii)** The same neurons in (i) responding to a series of moving targets. Trajectory presentations indicated by blocks. Each trajectory consists of a small target ( $2^\circ \times 2^\circ$ ) appearing stationary at a random location in the visual field for 150 ms (red) before moving in a random direction at fixed speed ( $160^\circ/\text{sec}$ ) for 100 ms (green). A 150 ms delay separates each trajectory. **(iii)** Raster plot of responses to a series of 3000 trajectories. Only those trajectories initiating a spike are included. dTSDN latencies to **(iv)** the appearance of stationary targets (red phase) and **(v)** moving targets (green phase). Top panels in (iv-v) represent the peri-stimulus time histogram (PSTH) for the first spike in each phase of the trajectory. Bottom panels indicate the first (black line) and second derivative (red line) of the respective PSTH. Peak in the first derivative indicated with black circle, peak in the second derivative indicated with vertical red line and taken as the latency of spike onset. Note the absence of spontaneous firing after the initial response to a stationary target.



**Figure 4.3 dTSDN response latency *Holcocephala* (n = 20 spike sorted cells from 13 animals) and *Coenosia* (n = 13 spike sorted cells from 10 animals) response latencies for stationary (red), moving (green) targets, and moving targets associated with a stationary response within the same trajectory (blue). Mean  $\pm$  std.**

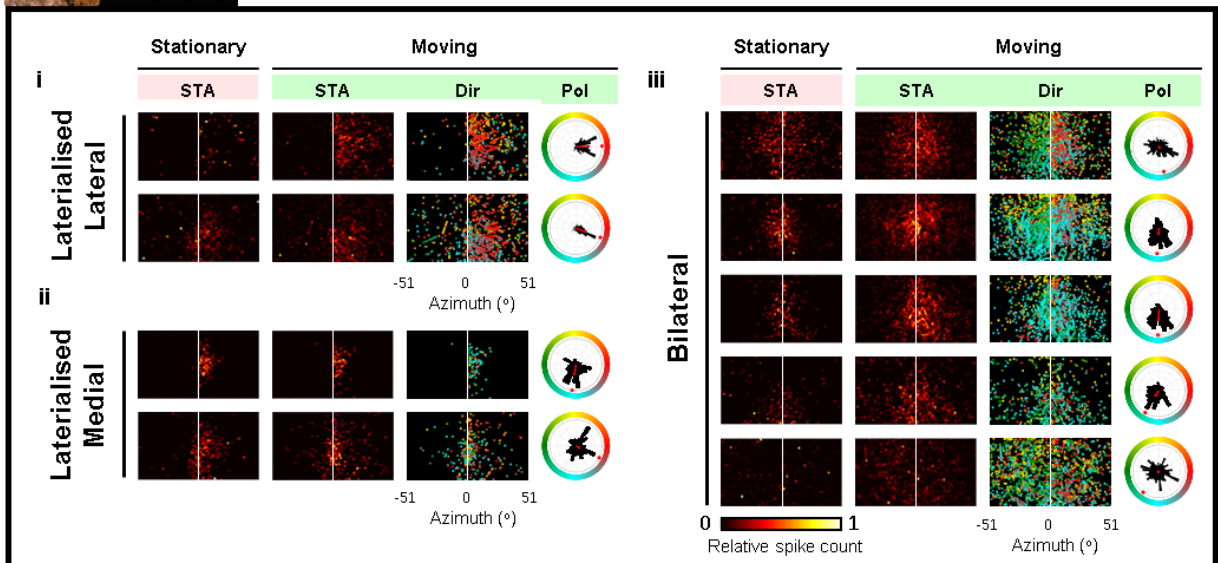
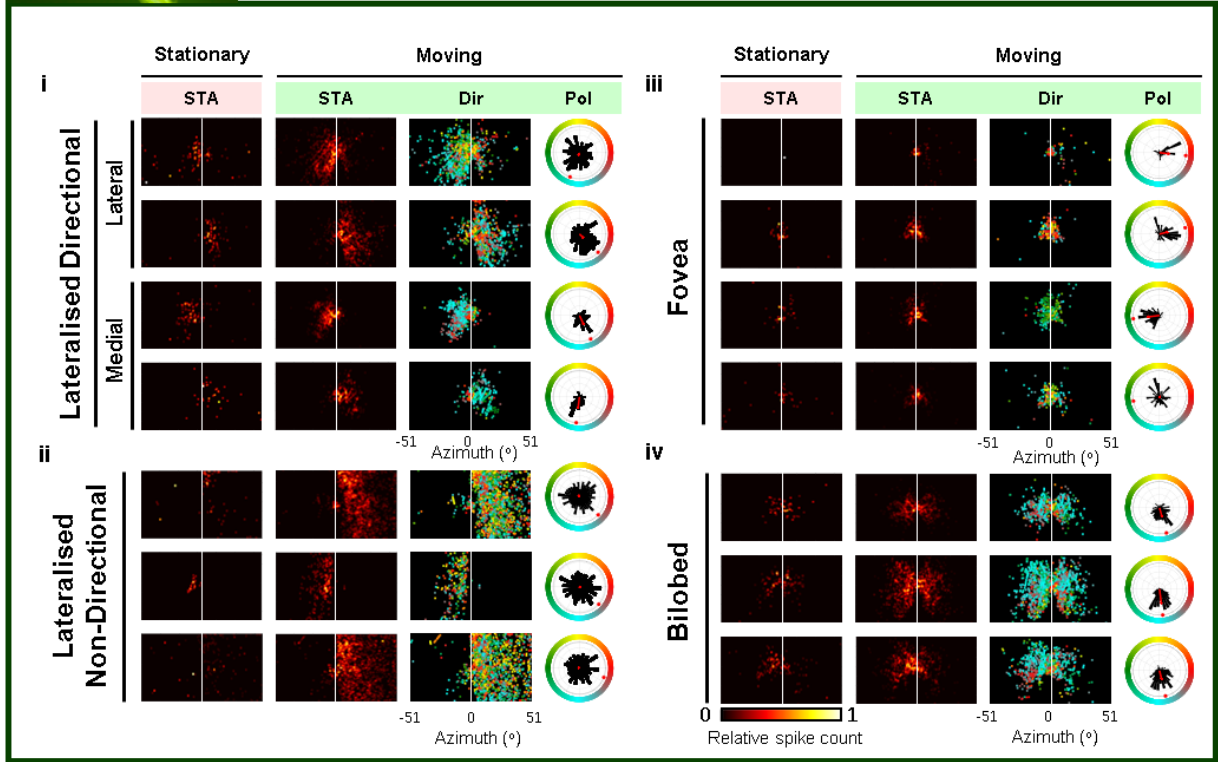
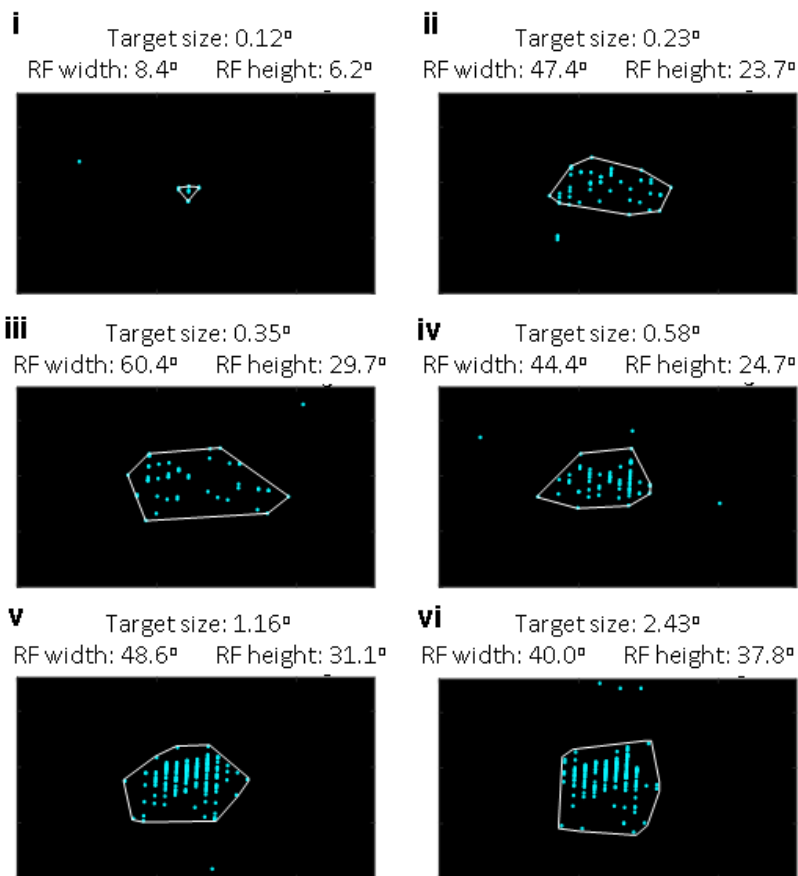


Figure 4.4 (legend right)

**Figure 4.4 (left) dTSDN receptive fields in *Holcocephala* and *Coenosia*** Spike triggered average maps (STA) indicate the relative dTSDN spike count across the visual field (see scale bottom right) for stationary (red) and moving (green) targets. Direction field maps (Dir) indicate the location and direction of motion of moving targets. Target direction color coded as indicated in diagrams. All receptive field plots correspond to  $\pm 54^\circ$  in azimuth (horizontal axis, as indicated on the bottom right receptive field for each group), and  $\pm 34.5^\circ$  in elevation along the vertical axis (scale omitted for presentation clarity). Polar histograms (Pol) represent the distribution of target directions each example dTSDN responded to, with red arrow and red dot indicating resultant vector and circular mean. **(A)** Example *Holcocephala* dTSDNs were clustered into four groups: (i) lateralised directional (LD), of which there are two subtypes, lateral and medial; (ii) lateralised non-directional (LND); (iii) fovea; and (iv) bilobed. **(B)** Example *Coenosia* dTSDNs were clustered into three groups: (i) lateralised lateral (LL); (ii) lateralised medial (LM); and (iii) bilateral.



**Figure 4.5**

***Holcocephala* dTSDN receptive fields are dependent on target size** Targets varying in size from  $0.12^\circ$  (i) to  $2.43^\circ$  (vi) moving downwards (i.e. ventral-dorsal, blue, same scale as Figure 4.4) were scanned across the visual field in a raster pattern. Receptive field areas were estimated with a convex hull (white line). Target size, receptive field (RF) width, and RF height are indicated.

### 4.3.3 *Holcocephala* dTSDN receptive fields

The highest sensitivity in the receptive fields of *Holcocephala* and *Coenosia* dTSDN to both stationary and moving targets is spatially localized towards the center of the visual field (Figure 4.4A-B). Receptive field patterns in both species appear to encode a visual midline, with several cell types lateralised along the visual midline (Figure 4.4A-B). For all *Holcocephala* and *Coenosia* dTSDNs recorded, the receptive fields for stationary object appearance never extended beyond the receptive field for moving targets and responses were often localized closer to the center of the visual field (compare STA maps, Figure 4.4A). Four categories of dTSDN receptive fields were found in *Holcocephala* (Figure 4.4A). Two receptive field types were distinctly lateralized along the visual midline (Figure 4.4Ai-ii), whilst the other two were bilateral (Figure 4.4Aiii-iv).

#### *Lateralised Holcocephala dTSDNs*

The two lateralised dTSDN types were differentiated by the extent of directional selectivity for target movement within their receptive field (Figure 4.4Ai-ii). Neither type was unidirectional in motion selectivity, however one type, termed lateralized directional (LD) dTSDNs (Figure 4.4Ai) tended to have distinct and stereotypic sub-regions of directional selectivity within the receptive field. In contrast, the second type, termed lateralized non-directional (LND), did not have any clear directional selectivity (Figure 4.4Aii). All LD dTSDNs were predominantly responsive to ventral-dorsal motion (downwards, Figure 4.4Ai). Two further subclassifications of LD dTSDNs were distinguished by sub-regional directional selectivity for either lateral from or medial to the visual midline (center of the screen) (Figure 4.4Ai). For example, lateral LD dTSDNs on the left visual hemisphere responded more to targets moving leftward away from the visual midline (green), whilst medial LD dTSDNs on the left visual hemisphere had a stereotypic region of directional selectivity to targets moving rightward towards the visual midline from the dorsal aspect of the receptive field (red). This pattern of regional directional selectivity was mirrored in the corresponding lateral and medial LD dTSDNs in the adjacent hemifield (Figure 4.4Ai).

#### *Bilateral Holcocephala dTSDNs*

Of the bilateral cells, one group of receptive fields was specifically responsive to targets moving within a small central region of the visual field subtending  $\sim 10\text{-}20^\circ$  in diameter (Figure 4.4Aiii). *Holcocephala* are known to chase prey subtending as little as  $0.13^\circ$  on the retina which is enabled by a specialized fovea with a central and telescopic field of view of  $\sim 8^\circ$  (Wardill et al., 2017). Thus, these dTSDNs are likely sampling from this small fovea region and are accordingly termed fovea dTSDNs (Figure 4.4Aiii). Indeed, when presented with targets decreasing in size to  $0.12^\circ$ , the receptive field of dTSDN responses is confined to an  $\sim 8^\circ$  region in the center of the visual field (Figure 4.5); the relatively larger diameter of fovea dTSDN receptive fields in Figure 4.4Aiii is likely due to the larger target sizes ( $2^\circ \times$

2°) used in these receptive field scans (see methods). Fovea dTSDNs were further subdivided into directionally selective and non-directionally selective, with most fovea-type dTSDN receptive fields observed to be directionally selective to either left- or right-wards target motion across the fovea (green or red respectively, Figure 4.4Aiii).

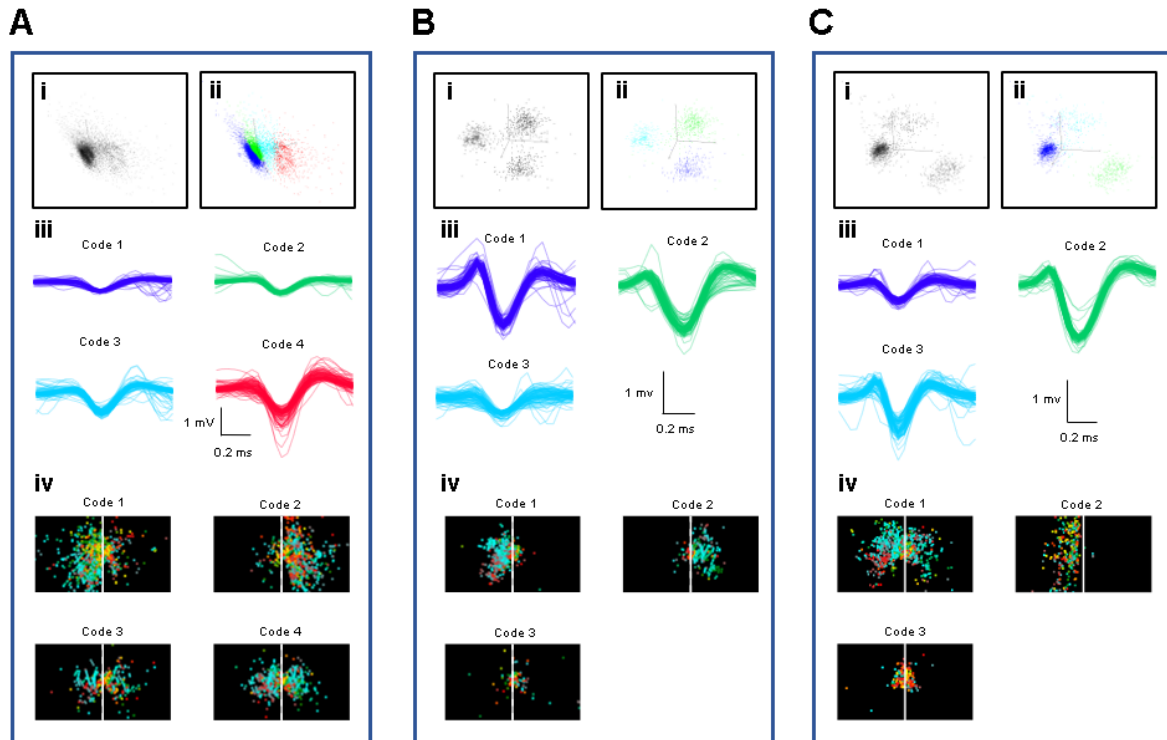


**Figure 4.6 Spike sorting *Holcocephala* dTSDNs** Spike sorting workflow includes manual clustering based on principle component analysis of spike waveforms (i-ii). This method represents each spike waveform as a coordinate with dimensions equal to the number of data points. The resultant dataset is rotated so the dimensions of maximal variation are presented along three orthogonal axes (i-ii). Clustered codes (iii) are displayed based on the clustering in (ii). (iv) Receptive fields for each spike sorted code. Receptive field maps are displayed as in Figure 4.3. (A) Example recording where a bilobed receptive field (codes 3-4) collocates with two lateral lateralised directional receptive fields (codes 1-2). (B) Example spike sorting of two medial lateralised directional dTSDN (codes 1-2) and a fovea dTSDN (code 3). (C) Example spike sorting of a bilobed (code 1), lateralised non-directional (code 2), and fovea dTSDN (code 3).

A second bilateral cell type was frequently observed with two large lobes extending from the midline to ~25° lateral from the midline (Figure 4.4Aiv). These bilobed receptive fields respond primarily to downwards targets (ventral to dorsal), but also feature local regions of directional selectivity in a stereotyped manner with flow-fields directed in towards the fovea. For example, the dorsal apex of the left lobe typically responded to targets moving towards the right (red), whilst the dorsal apex of the right lobe typically responds to targets moving to the left (green, Figure 4.4Aiv). However, this pattern

of directional selectivity is conspicuously similar to the lateral pairs of medial LD dTSDN receptive fields. Bilobed dTSDNs were often recorded in unison with other dTSDN types, and likely result from inseparable spike sorting of these lateral cell types, joining the pairs of lateralised receptive fields into a single unit (Figure 4.6). Bilobed dTSDNs were frequently observed in multiunit recordings along with well separated lateral LD dTSDNs (Figure 4.6A), and bilobed dTSDNs were usually composed of medial type LD dTSDNs, which may suggest that all LD type dTSDNs are located close together within the dorsal tract of the cervical connective, with medial LD dTSDNs closer together than lateral type LD dTSDNs leading to the higher probability of combining medial LD dTSDNs into a single bilobed receptive field.

#### **4.3.4 *Coenosia* dTSDN receptive fields**

Three categories of dTSDN receptive fields were observed in *Coenosia* (Figure 4.4B): two lateralised (Figure 4.4Bi-ii), and the other bilateral (Figure 4.4iii).

##### ***Lateralised Coenosia dTSDNs***

One type of lateralised dTSDN, termed lateralised lateral (LL), was directionally selective to lateral movement away from the midline (Figure 4.4Bi). Two of these cells were recorded and had receptive fields in the right visual hemisphere; as recordings were aimed at the right side of the cervical connective (animal point-of-view) these receptive fields are likely to be ipsilateral in connectivity, receiving input from the right optic lobe and projecting through the right side of the cervical connective. Other lateralised receptive field were observed in *Coenosia* without this lateral directional selectivity: one recording was directionally selective to ventral-dorsal movement along the midline (Figure 4.4Bii, top), whilst the other did not have distinct directional selectivity (Figure 4.4Bii, bottom); these cells are preliminarily termed lateralised medial (LM) dTSDNs.

##### ***Bilateral Coenosia dTSDNs***

Most frequently, *Coenosia* dTSDNs were bilateral with a diffuse region of activity centered on the frontal visual field (Figure 4.4Biii). In most recordings, these bilateral receptive fields tended to be regionally directionally selective. Typically, bilateral receptive fields were split along the visual midline with respect to directional selectivity, with each lobe responding to targets moving away from the midline. For example, the left receptive hemifield responded to targets moving to the left (green, Figure 4.4Biii), and the right receptive hemifield responded to targets moving to the right (red, Figure 4.4Biii). The visual midline of these receptive fields is represented only by this lateralised directional selectivity and not by relative spiking activity and/or lobed hemifield receptive fields as seen in *Holcocephala* (compare STA and direction maps in Figure 4.3Biii). However, this is likely explained by incomplete separation of spike sorted codes, with this pattern of directionality arising from a bilaterally symmetric pair of LL dTSDNs recorded simultaneously. Other bilateral *Coenosia* dTSDNs included receptive

fields directionally selective to ventral-dorsal target movement (downwards, Figure 4.4Biii), in addition to non-directionally selective cells (Figure 4.4Biii, bottom).

## 4.4 Discussion

Robberflies and killerflies are two relatively distant dipteran lineages converging to predation (Wardill et al., 2015, 2017; Wiegmann et al., 2011). *Holcocephala fusca* robberflies and *Coenosia attenuata* killerflies implement similar control algorithms to intercept their prey (Fabian et al., 2018), and possess ocular and neurophysiological adaptations in the peripheral visual system to facilitate target detection (Gonzalez-Bellido et al., 2011; Wardill et al., 2017). Dragonflies (Olberg, 1986), and dipterans specialized for visually-guided conspecific pursuit (Coggshall et al., 1973; Gronenberg and Strausfeld, 1990, 1991, 1992; Milde and Strausfeld, 1990; Strausfeld and Gronenberg, 1990) possess several large caliber neurons in the dorsal motor tracts of the ventral nerve cord. The enlargement of numerous dorsal axons in the cervical connectives of *Holcocephala* and *Coenosia* likely reflects their adaptation to aerial predation (Figure 4.1G-H). In dragonflies, TSDNs constitute a subset of the most enlarged dorsal axons (Olberg, 1986) and respond selectively to small objects moving across the dorsal fovea (Gonzalez-Bellido et al., 2013; Olberg, 1986). In this study we demonstrate that *Holcocephala* and *Coenosia* also feature neurophysiological adaptations for target tracking at the premotor level in the ventral nerve cord (Figure 4.1-4.2). Our data suggest the existence of dipteran TSDNs (dTSDNs) in both *Holcocephala* and *Coenosia* that may represent a specialized target tracking circuitry similar to that in dragonflies (Figure 4.2).

### 4.4.1 dTSDN response latencies

*Holcocephala* pursue their prey over distances up to ~80 cm, compared with ~20 cm for *Coenosia* (Fabian et al., 2018). Consequently, for the same translational motion of the prey, *Coenosia* experience greater rates of rotation in the line-of-sight to the prey compared with *Holcocephala*. *Coenosia* must respond with a relatively shorter delay to prevent the image of the prey escaping the acute zone of the visual field. Indeed, *Holcocephala* perform in-flight compensatory movements in response to prey deviation with a temporal delay of ~28 ms, and *Coenosia* with a temporal delay of ~18 ms (Fabian et al., 2018). This is further reflected in our neurophysiological latency measurements for dTSDNs, at ~20.5 ms in *Holcocephala*, and ~9.2 ms in *Coenosia* (Figure 4.3). Both dTSDN latency measurements are shorter than the respective behavioral latencies for each species, as would be expected for premotor signals controlling compensatory movements. The longer response latency in *Holcocephala* dTSDNs could result either from longer photoreceptor latencies, or longer processing latencies in the optic lobes. Owing to their relatively greater hunting distances, *Holcocephala* detect and initiate predatory flight for targets subtending as little as  $0.13^\circ$  (Wardill et al., 2017). The high visual acuity required to detect such objects results in extremely small rhabdomere acceptance angles ( $\sim 0.28^\circ$ ) (Wardill et al., 2017), which

necessarily results in decreased sensitivity due to a reduction in photopigment area. Whilst *Holcocephala* use the sky as a visual contrast enhancer (Wardill et al., 2017), *Holcocephala* may also compensate for this reduction in sensitivity by increasing photoreceptor integration time relative to *Coenosia*, which may account for the difference in dTSDN latencies measured in this study. However, our dTSDN latency measurements were collected at 23°C under laboratory conditions; whilst *Coenosia* behavioral latencies were measured under similar temperatures, behavioral latencies in *Holcocephala* were acquired under natural conditions in the Pennsylvanian summertime, often reaching upwards of 30°C (Fabian et al., 2018). Photoreceptor latencies are reduced at higher temperatures, with an increase in temperature from 19°C to 34°C resulting in a ~4 ms decrease in photoreceptor latency in blowflies (Tatler et al., 2000). Thus, dTSDN delays in *Holcocephala* under natural conditions are likely to be shorter than measured in this study. However, this is unlikely to account for the ~10 ms difference between *Holcocephala* and *Coenosia* dTSDN latency, suggesting temperature independent mechanisms are likely involved. It is currently unknown whether *Coenosia* behavioral latencies are reduced at higher temperatures. It would be interesting to investigate whether *Coenosia* dTSDN responses are shorter at higher temperatures, or whether the processing latencies measured in this study represent a limit to the temporal processing within this neural circuitry.

Latencies in both species were on average shorter for target appearance compared to target movement (difference of 4.6 ms in *Holcocephala* and 3.5 ms in *Coenosia*; Figure 4.3). This longer latency for moving compared with stationary objects potentially represents upstream visual processing delays due to the spatiotemporal cross-correlation of luminance changes in elementary motion detectors (EMDs) within the receptive field (see Chapter 1, section 1.3.1) (Borst and Helmstaedter, 2015). In *Drosophila*, the temporal delay between medulla interneurons thought to implement the EMD is estimated at ~18 ms (Behnia et al., 2014). This is much longer than the difference in latency for stationary and moving targets in *Holcocephala* and *Coenosia*. Whether this represents a specialization for shorter EMD temporal delays in these predators remains to be investigated.

#### **4.4.2 dTSDNs receptive fields**

Challenges in extracellular spike sorting of individual units is likely reflected by the large number of bilateral receptive fields measured in this study (Figure 4.6). It is likely that the bilobed receptive fields of *Holcocephala* and the bilateral receptive fields of *Coenosia* are composite recordings of multiple neurons, resulting in the diffuse receptive field structures across the visual field (Figures 4.4 and 4.6). Future studies should aim to identify these neurons with intracellular recordings to ensure single cell isolation.

TSDN receptive fields in odonates are spatially confined to specific subsets of the dorsal fovea visual field, and directionally selective to specific directions of target motion (see Chapter 3) (Frye and Olberg, 1995; Gonzalez-Bellido et al., 2013; Olberg, 1986). Interestingly, several *Holcocephala* and *Coenosia*

dTSDN receptive field types are similarly localized to specific parts of the visual field and directionally tuned (Figure 4.4), suggesting the general strategy of separating visual features into discrete parallel channels is also present in these dipterans. Of note are *Holcocephala* fovea (Figure 4.4Aiii) and *Coenosia* lateralised lateral dTSDNs (Figure 4.4Bi), both of which include receptive fields directionally tuned to targets moving laterally in the visual field. This directional tuning is comparable to numerous dragonfly TSDN types encoding movement away from the visual midline (DIT1, DIT2, MDT2, MDT3) (Gonzalez-Bellido et al., 2013; Olberg, 1986), leaving them suitably configured to control compensatory yaw and/or roll movements during flight. The only other dTSDN in this study resembling an odonate TSDN is one bilateral *Coenosia* dTSDN (middle row, Figure 4.4Biii) which is directionally selective to ventral-dorsal movement across a broad region of the visual field predominantly in the right hemifield. This neuron is comparable to MDT1 in dragonflies and damselflies (Chapter 3) (Gonzalez-Bellido et al., 2013; Olberg, 1986).

Odonate TSDNs, *Holcocephala* fovea dTSDNs, and *Coenosia* lateralised lateral dTSDNs may represent the directionally selective descending neurons within the Land and Collett model (Chapter 1, section 1.4.1) Laterally directionally tuned cells (i.e. dragonfly DIT1, DIT2, MDT2, MDT3; *Holcocephala* fovea dTSDNs; *Coenosia* lateralised lateral dTSDNs) may actuate corrective yaw movements, and ventral-medially tuned cells (i.e. dragonfly MDT1, MDT5; *Coenosia* bilateral dTSDN) actuating corrective pitch and/or thrust corrections.

Without intracellularly identified anatomical information for *Holcocephala* and *Coenosia* dTSDNs, the present study is unable to conclude whether these neurons derive from the same progenitor cells to those of odonate TSDNs. Odonate TSDNs arise from three distinct clusters of cell bodies in the n-dorsal, n-anterior, and n-ventral aspect of the midbrain (Chapter 3) (Frye and Olberg, 1995; Olberg, 1986). The majority of odonate TSDNs (DIT1, DIT2, MDT2, MDT4, MDT5) arise from the n-ventral cluster (Chapter 3) (Frye and Olberg, 1995; Olberg, 1986). This likely corresponds to the AOTU clusters previously annotated in *Drosophila* (Hsu and Bhandawat, 2016; Namiki et al., 2018), crickets (Staudacher, 1998), cockroaches (Okada et al., 2003), and again here in *Holcocephala* and *Coenosia* (Figure 4.11-L). If *Holcocephala* and *Coenosia* dTSDNs are homologous to odonate TSDNs as descending premotor controllers for pursuit, these directional dTSDNs would be expected to arise from the AOTU cell body cluster. Interestingly, the only previously described dipteran descending neuron responding specifically to small targets (DNDC3-6b) arises from the AOTU cluster in *Sarcophaga* (Gronenberg and Strausfeld, 1990, 1991). Future studies should aim to characterize the anatomy of dTSDNs as this will aid in determining their developmental origin.

### 4.4.3 Diversity of dipteran TSDNs

Other dTSDN receptive fields do not share similar encoding representations to any dragonfly TSDN. *Holcocephala* dTSDNs in particular appear to implement a relatively complex representation of target

movement, with some receptive fields characterized by localized flow-fields either medial or lateral from the fovea (lateralised directional, Figure 4.3Ai), or broad receptive fields responding to target movement without directional specificity anywhere within a visual hemisphere (lateralised non-directional, Figure 4.3Aii).

#### ***Holcocephala lateralised directional dTSDNs***

The non-linear directional tuning of *Holcocephala* lateralised directional dTSDNs is of interest, as this is in contrast to the many variations of orthogonal cosine vector coding found so ubiquitously across sensory neuron populations (Butts and Goldman, 2006; Gonzalez-Bellido et al., 2013; van Hemmen and Schwartz, 2008; Todorov, 2002). Several wide-field optic-flow neurons involved in flight stabilisation reflexes are found to respond selectively to specific, kinematically relevant modes of motion most likely to be experienced during flight, rather than along idealised cardinal axes (see Chapter 1, section 1.3.2) (Farrow et al., 2006; Huston et al., 2008; Krapp et al., 1998, 2001; Wertz et al., 2008, 2009a). This ‘matched filter’ encoding scheme aligns sensory and motor axes to optimise sensorimotor transformation (Huston et al., 2008). Interestingly, robberflies, which are long-bodied and thus passively stabilised in pitch, but not in roll, during flight are found to under-represent vertical modes of motion in the lobula plate tangential cells associated with pitch rotation (Buschbeck and Strausfeld, 1996). It may be the case that lateralised directional dTSDNs in *Holcocephala* may explicitly convolve directional tuning with a function representing a specific and relevant mode of retinal slip. Indeed, the non-uniform receptive field flow patterns in lateralised directional dTSDNs lead either inwards or outwards from the fovea in a manner consistent with target slip following roll perturbations (Figure 4.3Ai). These lateralised directional neurons may thus feed into the hypothesised Land and Collett circuitry (Collett and Land, 1975; Gronenberg and Strausfeld, 1991; Land and Collett, 1974), albeit tailored specifically to robberfly flight kinematics.

#### ***Holcocephala lateralised non-directional dTSDNs***

The existence of sharply lateralised non-directional dTSDNs in *Holcocephala* may have interesting implications for the initiation of pursuit. *Holcocephala* perform saccadic head-flicks to potential prey prior to take-off (Wardill et al., 2017). This saccade presumably requires neurons to detect prey in the periphery of the visual field to initiate rotatory head movements that position the prey onto the fovea. Neck motor neurons arise from both the central brain and prothoracic ganglion (Milde et al., 1987), and are the target of descending neuron terminals prior to or following the cervical connective (Gronenberg and Strausfeld, 1990; Strausfeld and Gronenberg, 1990). Lateralised non-directional dTSDNs are well-placed to accomplish this as they have relatively expansive receptive fields relative to other *Holcocephala* dTSDNs (Figure 4.3Aii). These neurons may function to initiate a fast, simple head movement that brings peripheral objects into the receptive fields of other dTSDNs which then take-over target tracking. This may explain the strict lateralisation and indiscriminate direction tuning of these

dTSDNs according to the following algorithm: (1) if an object is detected moving anywhere in the receptive visual hemifield, (2) initiate a simple yaw head-flick towards that hemifield; (3) as the object approaches towards the central visual field, lateralised directional dTSDNs coordinate fine head movements that fixate the target on the fovea, where (4) it is stabilised by fovea dTSDNs. However, to avoid over-compensation, the gain of the initial yaw head-flick should be proportional to the distance of the target from the midline. This would predict that the response lateralised non-directional dTSDNs increases with distance from the visual midline; however, this does not seem to be the case (Figure 4.3Aii). It could nonetheless be the case that the visual angles subtended by receptive fields of lateralised directional dTSDNs represent the range of azimuthal prey location to which *Holcocephala* foveate: this should be explored with behavioural analysis of the range of receptive angles for foveation.

In summary, this study presents evidence of a specialised target tracking descending neuron system in two predatory dipterans. These neurons are specialised for decreased visuomotor transduction latencies and encode target motion across parallel channels with distinct receptive fields. The structure of these receptive fields differs between species; however, whether and how these receptive fields are matched to the behavioural ecology of each species remains speculative.



# Chapter 5

## Integration of small- and wide-field visual features in Target Selective Descending Neurons of both predatory and nonpredatory dipterans

### 5.1 Acknowledgements and contributions

This chapter is based on a collaborative study with Dr Karin Nordström's group at Flinder's University, Australia. Most of this work has been published in the *Journal of Neuroscience* (Nicholas et al., 2018a). All *Holcocephala fusca* visual stimuli were designed and generated by Jack Supple. *Holcocephala fusca* data was collected and analysed by Jack Supple. All *E. tenax* hoverfly data was collected and analysed by Dr Nordström's group at Flinder's University, Australia.

### 5.2 Introduction

Target detection and tracking serve important biological functions for animals to efficiently avoid predators, find prey, or identify conspecifics. Targets often need to be detected and tracked against wide-field optic flow resulting from self-motion, which is a computationally difficult task (Held et al., 2016; Yang et al., 2012), especially in conditions where both local luminance and relative contrast may change rapidly (Ma et al., 2015; Mohamed et al., 2014). Nonetheless, many insects appear to have solved this challenge efficiently, as evidenced by their high-speed pursuits of targets, despite a small brain and relatively low resolution vision (Land, 1997).

The optic lobes possess neurons sensitive to target movement with visual receptive fields that often collocate with the fovea of the compound eye (Barnett et al., 2007; Strausfeld, 1980), such as small target motion detector (STMD) neurons (Nordström et al., 2006; O'Carroll, 1993). STMDs are thought to project directly or indirectly to target selective descending neurons (TSDNs) (Barnett et al., 2007; Frye and Olberg, 1995; Gonzalez-Bellido et al., 2013; Olberg, 1981b, 1986) whose receptive fields also collocate with the optical fovea (Gonzalez-Bellido et al., 2013).

In the lobula, some hoverfly and dragonfly STMDs show remarkably robust responses to targets moving in visual clutter (Nordström and O'Carroll, 2009; Nordström et al., 2006). The STMD response to target motion is unaffected by the addition of background motion with the same velocity (i.e., syn-directional motion, without relative velocity differences) (Nordström et al., 2006; Wiederman and O'Carroll, 2013). To date, it is unclear how target selective neurons further along the sensorimotor pathway such as TSDNs respond to targets moving in clutter. In dragonflies, TSDNs project to the thoracic ganglion (Gonzalez-Bellido et al., 2013) and presumably transmit information utilised by motor circuits to coordinate intercepting flights. Thus, it would be instructive to understand how these neurons operate under cluttered conditions. One early description of a dragonfly TSDN indicates that subthreshold membrane potential has an inverse relationship between target and background movement when presented separately, and inhibition of TSDN action potentials when presented concurrently (see Chapter 1, section 1.4.2, Figure 1.23) (Olberg, 1986). The relevance of this response pattern for the control of target interception remains unknown. In addition to TSDNs, there are many other visual descending neurons described in flying insects that also project to thoracic motor centres, but respond exclusively to wide-field patterns of background motion (Namiki et al., 2018; Suver et al., 2016; Wertz et al., 2009b, 2009a). Whether and how these neurons interact with TSDNs, either in the central brain or thoracic ganglion, has not been investigated.

In this study we report dipteran target selective descending neurons (dTSDNs), with similar response properties to dragonfly TSDNs, in the predatory robberfly *Holcocephala fusca* and the nonpredatory hoverfly *Eristalis tenax* which pursue conspecifics. We found that, dTSDNs in either species did not respond to targets moving across background clutter unless the background moved in the opposite direction, moved slowly, or was highly un-naturalistic. In *Eristalis tenax* the responses of descending neurons selective to wide-field optic flow were found to be inversely correlated to dTSDNs, suggesting that dTSDNs may receive inhibitory input from presynaptic neurons located within this wide-field pathway. As these two dipteran species pursue targets for different purposes, and are evolutionarily distant (Wiegmann et al., 2011), the similarities in dTSDN responses suggests that the interaction of wide-field and small-field motion underlies a general mechanism for target tracking and coordinating target-guided flight.

## 5.3 Methods and Materials

### 5.3.1 Animals and electrophysiology

Thirty-eight male *Eristalis tenax* hoverflies were reared from eggs laid by wild-caught hoverflies and housed as described previously (Nicholas et al., 2018b). Sixteen female and three male adult *Holcocephala fusca* robberflies were wild caught in York, Pennsylvania and recorded from on the day of capture. Before recording, the animal was immobilized ventral side up and a small hole was cut at the anteroventral thoracic surface to expose the ventral nerve cord (see Methods Chapter Section 2.2.1).

For *Eristalis* extracellular recordings, a sharp polyimide-insulated tungsten electrode (0.1 M $\Omega$ ; MicroProbes) was inserted into the nerve cord, with mechanical support given to the cord by a small wire hook. The animal was grounded via a silver wire inserted into the ventral cavity, which also served as the recording reference. To prevent the drying up of the exposed ventral cavity, a small amount of a petroleum jelly and mineral oil mix (1:1 ratio) was applied. Extracellular signals were amplified at 1000 $\times$  gain and filtered through a 10–3000 Hz bandwidth filter on a DAM50 differential amplifier (World Precision Instruments), filtered through a HumBug (Quest Scientific), digitized via a PowerLab 4/30 (ADInstruments), and acquired at 10 kHz with LabChart 7 Pro Software (ADInstruments).

*Holcocephala* extracellular recordings were acquired using sharp glass-insulated tungsten electrodes as described in Methods Chapter, section 2.2.1 and 2.4.1.

### 5.3.2 Visual stimuli

For *Eristalis* experiments, visual stimuli were displayed on an LCD screen (Asus) with a spatial resolution of 2560  $\times$  1440 pixels running at 165 Hz, using the Psychophysics toolbox in Matlab (MathWorks 2017). *Eristalis* males were placed at 7 cm from the screen, giving a projected screen size of 154 $^{\circ}$   $\times$  137 $^{\circ}$ . For *Holcocephala* experiments, visual stimuli were presented as described in section 2.3. *Holcocephala* were placed 7 cm from the screen, giving a projected screen size of 102 $^{\circ}$   $\times$  70 $^{\circ}$ .

For all dTSDN experiments, we first mapped the receptive field (Gonzalez-Bellido et al., 2013; Nordström et al., 2006) and confirmed that the neuron selectively produced spikes in response to small targets and not to wide-field optic flow. For all target–background experiments, the targets moved either horizontally (*Eristalis*) or vertically (*Holcocephala*) across the centre of the receptive field of each neuron. Only data from neurons showing both a robust and consistent response to the target moving over a grey background throughout the recording were included in this study. For size-tuning experiments in *Eristalis*, a black target with a fixed horizontal width (3 $^{\circ}$ ) was moved across a white background at an average velocity of 180 $^{\circ}$ /s (since flat screens were used, the projected angular velocity varied between their central and peripheral parts). The vertical extent of the target was varied from 0.2 $^{\circ}$

to bars that covered  $137^\circ$ . For size-tuning experiments in *Holcocephala*, a black square target appeared in a random location anywhere on the screen, remained stationary for 150 ms, and then moved in a random direction for 100 ms, in a total of 2400 random trajectories. The size of the target was varied randomly between  $1^\circ$  and  $22^\circ$ .

For target–background experiments in both *Eristalis* and *Holcocephala*, we used an artificially generated naturalistic background pattern with a slope constant ( $\alpha$ ) of the amplitude spectrum and rms contrast close to those of natural scenes (Dyakova and Nordström, 2017). To generate this background pattern, we used the fact that the spatial statistics of an image can be quantified by constructing a fast Fourier transform and plotting the rotationally averaged amplitude as a function of spatial frequency (Figure 5.1) (Tolhurst et al., 2007). Displayed in a log-log graph, the amplitude is then inversely proportional to the spatial frequency raised to the power  $\alpha$  (Dyakova and Nordström, 2017). In natural scenes, the  $\alpha$  is close to 1.1 (Dyakova and Nordström, 2017; Tolhurst et al., 2007). In *Eristalis*, the target ( $3^\circ \times 3^\circ$ ) moved horizontally across the screen at an average velocity of  $180^\circ/\text{s}$ . In *Holcocephala*, the target ( $2^\circ \times 2^\circ$ ) moved vertically across the screen at an average velocity of  $160^\circ/\text{s}$ . Unless otherwise indicated, the target and the background moved at the same velocity.

In *Eristalis*, optic flow-sensitive neurons were defined based on their receptive field properties and response to a high-contrast sinusoidal grating moving in eight different directions (wavelength of  $7^\circ$  drifting at 5 Hz; Figure 5.2Biv), using blowfly data as a comparison (Wertz et al., 2009b, 2009a). The same artificially generated naturalistic background pattern was used as in the target–background experiments described above, but without the target. The pattern moved horizontally across the screen, unless otherwise indicated.

### 5.3.3 Data analysis

Spike sorting of *Eristalis* extracellular data (Figure 5.2A-B) was performed using LabChart 7 Pro with the Spike Histogram Add-On (ADInstruments), which uses the action potential amplitude and width to identify responses from individual neurons (Figure 5.2Ai, Bi, insets). *Holcocephala* extracellular data (Figure 5.2C) were sorted in Spike2 (Cambridge Electronic Design), which uses principal component analysis on the waveform shape to identify single units (see Chapter 2). Inter-spike intervals (Figure 5.2Aii, Bii) from the resulting spike sequences were quantified to validate single unit sorting. All further data analysis was performed in MATLAB.

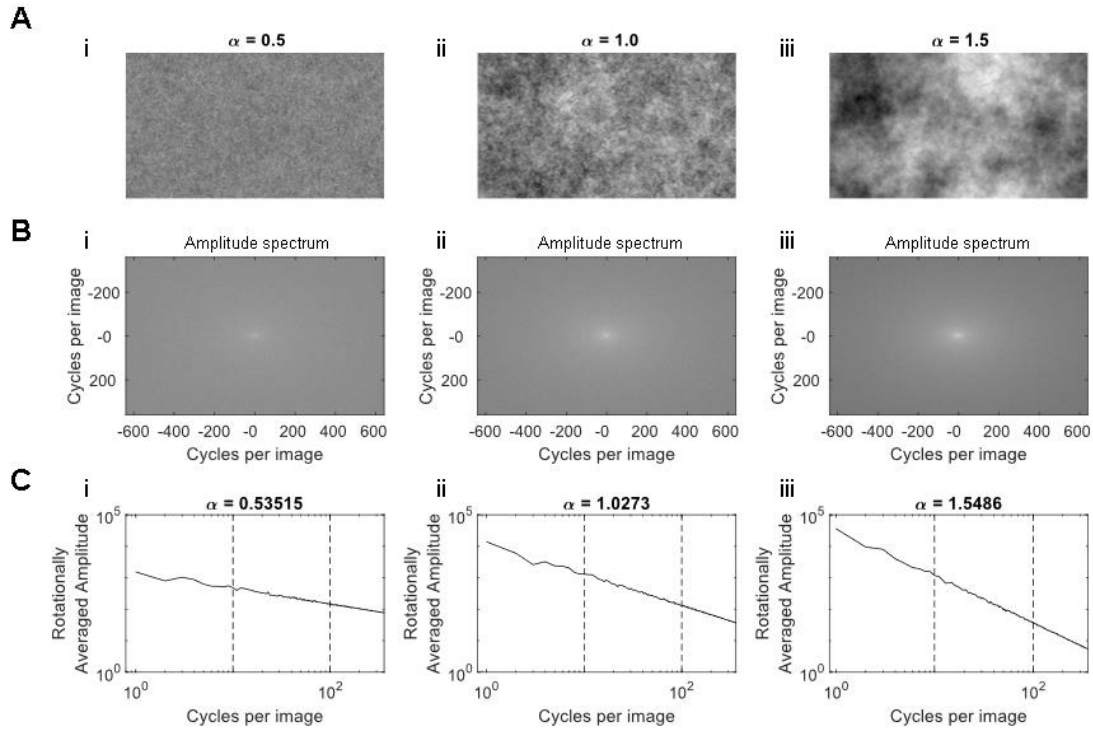


**Figure 5.1 Fourier transforms and image spatial frequencies (A)** Three example greyscale images with differing spatial frequency profiles generated from amplitude spectra with slope constants 0.5, 1.0, and 1.5. Each image is 720 x 1280 pixels. **(B)** Amplitude spectra of each image generated by the 2D fast-Fourier transform. Amplitudes are presented as logarithms. Spatial frequencies are presented as cycles per image, with one cycle per two pixels. Thus, the highest (Nyquist) spatial frequency in each dimension equals half the number of pixels image (i.e. 360 x 640 cycles for these 720 x 1280 pixel images). **(C)** Rotationally averaged amplitude spectra as a function of spatial frequency for each image. These spectra represent the average amplitude per spatial frequency and are generated by averaging amplitudes along radii starting from the center of the 2D amplitude spectra in (B). When presented on log-log axes, the slope constant ( $\alpha$ ) of these curves are usually extracted from a limited range of spatial frequencies (dashed lines) (Dyakova and Nordström, 2017; Dyakova et al., 2015) and characterize the spatial frequency profile of the image according to the equation:

$$A(f) = \frac{1}{f^\alpha}$$

Where A is the rotationally averaged amplitude and f the spatial frequency. Natural images typically have  $\alpha =$  close to 1.1 (Dyakova and Nordström, 2017; Tolhurst et al., 2007).

For all experiments in *Eristalis* TSDNs, the mean spike frequency was quantified over the time that the target traversed the receptive field of each neuron (Figure 5.2Aiii, bar under data). For optic flow-sensitive neurons, mean spike frequency was quantified for the entire stimulus duration (Figure 5.2Biii, bar under data). All experiments were repeated 6–18 times in each animal, with the precise target location varied slightly between trials to avoid habituation. Data from repetitions within a neuron were

averaged with error representing variation across neurons. For *Holcocephala* target–background experiments, each condition consisted of three repetitions of the stimuli. Target-induced responses were separated from any background-induced responses by subtracting any activity under background-only motion from the response to target-only motion (Figure 5.2Ciii, bar under data). For size-tuning curves, *Holcocephala* and *Eristalis* responses were normalized to the maximum response of each neuron. Statistical analysis was performed in GraphPad Prism (version 7.0d, GraphPad Software), after ensuring that the data were normally distributed, with details of the test and significance given in each figure legend.  $p$  values  $<0.05$  were used to refute the null hypothesis.

## 5.4 Results

### 5.4.1 Descending Neuron identification in hoverflies and robberflies

Extracellular recordings were performed in the ventral nerve cord of *Holcocephala fusca* robberflies and *Eristalis tenax* hoverflies (Figure 5.2, top row), with individual neurons identified based on the spike waveform shape (including amplitude and width of each action potential; Figure 5.2, insets, top row). Descending visual neurons were defined as dTSDNs by their peak response to small objects subtending a few degrees of the visual field, with no response to elongated bars (*Eristalis* data; Figure 5.2Ai-iv), to larger objects (*Holcocephala* data, Figure 5.2Ci-iv), or wide-field stimuli (*Eristalis* data; Figure 5.2Biv). The selective response of dTSDNs to the motion of small targets (Figure 5.2) is similar to the small target selectivity of previously described STMDs found in the lobula of *Eristalis* hoverflies (Chapter 1, Section 1.3, Figure 1.15) (Nordström et al., 2006). These results (Figure 5.2A,C) are in accordance with the previously proposed notion that TSDNs may be downstream of the lobula STMD neurons (Barnett et al., 2007; Nordström and O’Carroll, 2009). However, whether STMDs and TSDNs are directly or indirectly connected in the protocerebrum remains to be clarified.

In *Eristalis*, a second group of wide-field sensitive descending visual neurons responded selectively to sinusoidal gratings in a direction-selective manner (Figure 5.2B). Two types of wide field-sensitive neurons were found to respond preferentially to either motion up and to the right across the visual field of the animal (Figure 5.2Biv, 225°, light purple) or to motion down across the visual field (Figure 5.2Biv, 90°, dark purple), respectively. The direction tuning (Figure 5.2Biv) follows the typical sinusoidal shape seen in similar descending neurons previously described in blowflies and *Drosophila*, which receive direct input from optic flow-tuned lobula plate tangential cells (LPTCs) (Suver et al., 2016; Wertz et al., 2009b).

### **5.4.2 Dipteran TSDNs do not respond to targets moving in the same direction as background clutter**

In the *Eristalis lobula*, some STMDs respond robustly to targets moving in visual clutter, even when there are no velocity differences between target and background (Nordström et al., 2006). To investigate whether this property is also present at the dTSDN level, we presented *Eristalis* and *Holcocephala* with a small, high-contrast target ( $3^\circ \times 3^\circ$  and  $2^\circ \times 2^\circ$ , respectively) moving across a background pattern. The background was artificially generated to have naturalistic spatial statistics and rms contrast (Dyakova and Nordström, 2017). The target was presented moving horizontally (*Eristalis*) or vertically (*Holcocephala*) across the screen, with the background pattern moving in the same direction. As controls, we recorded the response to the target moving over a mean luminance background (Figure 5.3A-C open symbols) or over a stationary cluttered background (Figure 5.3A-C, grey symbols).

A consistent trend was observed in both species as follows: the presence of background movement substantially reduced the dTSDN responses (Figure 5.3A-C). This effect became significantly different from stationary backgrounds when the background moved at velocities  $>10^\circ/\text{s}$  (Figure 5.3B, green data). When the target and the background moved at the same velocity (Figure 5.3A-C, grey arrow), the response to the motion of the target had completely disappeared in both species (Figure 5.3A-C, *Eristalis* = green, *Holcocephala* = red). The dTSDN responses were also absent when the background moved two or three times faster than the target (Figure 5.3A-C, data points to the right of grey arrow) or at half the velocity in *Eristalis* (Figure 5.3B, green data point to the left of the grey arrow). It thus seems as though dTSDNs are unresponsive to targets presented against syn-directional background motion, with or without relative velocity differences.

In contrast, *Eristalis* wide-field neurons increased with the velocity of the background pattern (Figure 5.3D). Thus, across the same range of background velocities, as the response of the *Eristalis* wide-field neurons to background velocity increased (Figure 5.3D), the response of the dTSDNs to targets moving over backgrounds with different velocities decreased (Figure 5.3B).

### **5.4.3 Dipteran TSDNs respond stronger to target motion when the background moves in the opposite direction**

Next, we tested the effect of varying the relative direction of target and background motion. We presented the target and background moving at the same speed (Figure 5.3B, grey arrow), but tested a variety of background directions (Figure 5.3C, closed symbols). For comparison, we recorded the

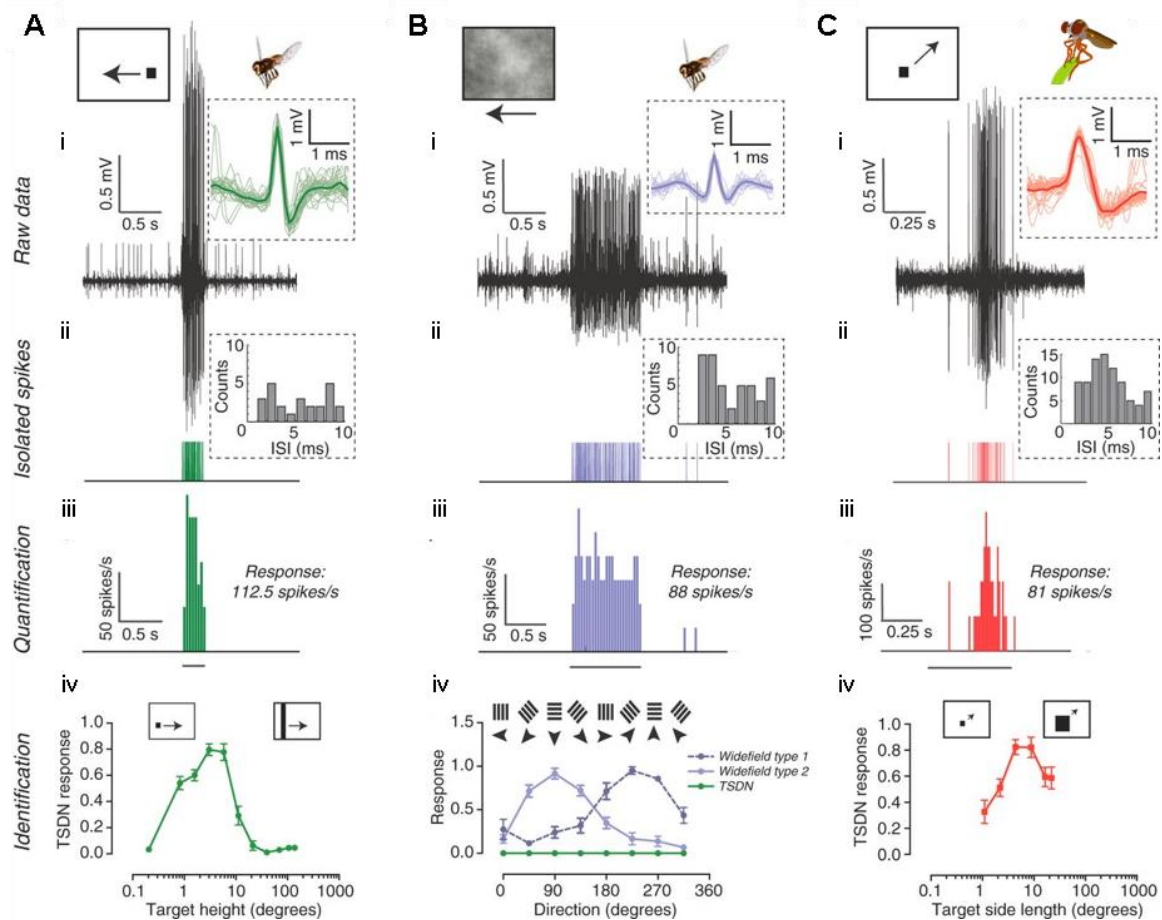


**Figure 5.2 dTSDNs in *Eristalis* and *Holcocephala*** (A) (i) Example *Eristalis* dTSDN response during stimulation with a small target drifting horizontally across the receptive field (stimulus duration indicated by bar below the axis of iii). Inset shows the mean (thick line) and individual (thin lines) waveforms of 30 action potentials isolated from this example. (ii) The resulting spike train as a function of time. The inset graph shows the inter-spike intervals (ISIs). (iii) Histogram of spike rate within 40 ms bins and mean response during target motion across the dTSDN receptive field (stimulus duration indicated by bar under data). (iv) Responses to different target heights, where the target width was fixed at 3°. When the bar subtended >10° of the visual field, the dTSDN response was strongly suppressed. The data are normalized to the maximum response of each neuron.  $N = 27$  neurons. (B) (i) Example *Eristalis* wide-field neuron responding to a background pattern moving horizontally. Inset shows the mean (thick) and individual (thin lines) waveforms of 30 action potentials. (ii) The resulting spike train as a function of time and the ISI (inset). (iii) The spike rate in 40 ms bins and the mean response during the peristimulus duration (bar under data). (iv) The response to high-contrast sinusoidal gratings moving in eight different directions (wavelength at 7°, 5 Hz) of dTSDNs (green,  $N = 27$  neurons) and two different types of wide field-sensitive neurons, here referred to as type 1 (dark purple,  $N = 8$  neurons) and type 2 (light purple,  $N = 14$  neurons) (C) (i) Example *Holcocephala* dTSDN response and the waveform (inset). (ii) The resulting spike train and ISI. (iii) The spike rate within 10 ms bins and the mean response for the stimulus duration (bar under data). (iv) Responses to square targets of varying size (side length indicated on  $x$ -axis). The target appeared (continued right)

(continued) at a random position on the screen, remained stationary for 150 ms, and then moved in a random direction for 100 ms.  $N = 12$  neurons from 9 animals. The data are normalized to the maximum response of each neuron. In all panels, the data are displayed as the mean  $\pm$  SEM.

response to targets moving over a uniform mean luminance background (Figure 5.3C, open symbols). We found that the response to target motion depended on the direction of background motion (Figure 5.3C). dTSDN responses were completely suppressed when the target and the background moved in the same direction (i.e.,  $0^\circ$  relative direction difference; Figure 5.3C). However, the dTSDN response to the motion of the target increased along a sinusoid function when the background moved in the opposite direction to the target (i.e.,  $180^\circ$  relative direction difference; Figure 5.3C). Nonetheless, even when the background moved in the opposite direction to the target, the response was significantly lowered to 46% in *Eristalis*, and 24% in *Holcocephala* compared with the control condition (no background; Figure 5.3C).

In contrast, *Eristalis* wide field-sensitive neurons increased firing rate as a cosine function of background motion direction with respect to the preferred direction. Thus, as seen with background velocity, the response of the *Eristalis* TSDNs to targets moving over backgrounds in different directions (Figure 5.3C) was inversely related to the response of the wide-field neurons to different directions of background motion (Figure 5.3E).

#### **5.4.4 Local mechanisms do not explain dTSDN response suppression from background motion**

In some STMDs in the *Eristalis* brain, a moving target is detected against background motion even in the absence of relative movement (Nordström et al., 2006), but this ability seems to be absent in dTSDNs (Figure 5.3). This fact, in combination with the inverse relationship between dTSDN and wide-field descending neurons to moving backgrounds (Figure 5.3), suggests that the response to target motion may be actively suppressed by the wide-field system. Suppression appears to be weaker at low velocities (Figure 5.3B) and when the background moves in a different direction to the target (Figure 5.3D).

One possible alternative explanation is that the response suppression is caused by a reduced local relative contrast at the target edge when the target moves over the naturalistic background, compared with when it moves over a uniform mean luminance background. To investigate this possibility a grey mean luminance patch over the background was centred around the trajectory of the target. The patch ensured that the local contrast surrounding the trajectory of the target was equal to the control grey mean luminance no background condition (Figure 5.3B-C, open symbols). For this experiment, the target and the background moved at the same velocity. A small cover did

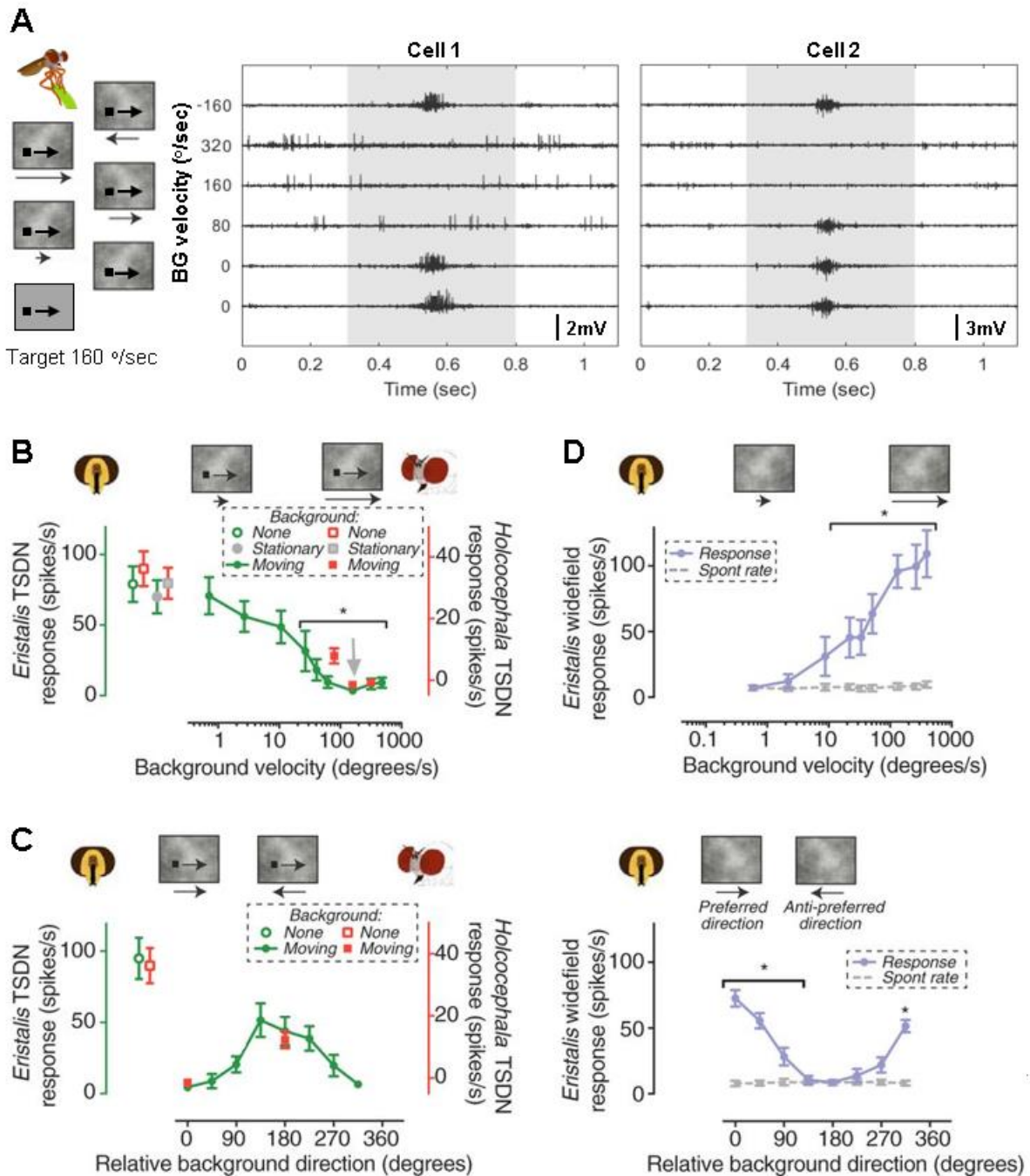


**Figure 5.3 Syn-directional background pattern motion strongly suppresses the dTSDN response to target motion** (A) Example responses of two *Holcocephala* dTSDNs to targets moving against different wide-field motion conditions. Target movement indicated by grey block on trace. Naturalistic background patterns, when present, were moving for entire duration plotted (i.e. white and grey sections). Background velocities indicated on y-axis and with schematics. Arrow length indicates relative target and background speeds (B) Average dTSDN responses to targets moving against backgrounds moving in the same direction as the target at different speeds as in (A). The green data show the response of *Eristalis* TSDNs ( $N = 8$  neurons from individual animals), and the red data the response of *Holcocephala* TSDNs ( $N = 38$  neurons from 19 animals).  $*p < 0.05$ , one-way ANOVA. (C) Average dTSDN responses to targets moving against backgrounds moving at the (continued right)

(continued) same speed in different directions as the target as in (A). The green data show the response of *Eristalis* TSDNs ( $N = 5$  neurons from individual animals), and the red data the response of *Holcocephala* TSDNs ( $N = 38$  neurons from 19 animals). (D) The response of *Eristalis* wide field-sensitive neurons to the naturalistic background pattern moving at different velocities ( $N = 8$  neurons from individual animals). Significant differences are indicated, corresponding to two-way ANOVA followed by Sidak's multiple-comparisons test comparing wide-field responses to spontaneous firing rate. (E) The response of *Eristalis* wide field-sensitive neurons to the naturalistic background pattern moving in different directions ( $N = 8$  neurons from individual animals). Significant differences are indicated, corresponding to two-way ANOVA followed by Sidak's multiple-comparisons test comparing wide-field responses to spontaneous firing rate. In all panels, the data are displayed as the mean  $\pm$  SEM.

not increase the *Eristalis* dTSDN response (the smallest cover was three times higher than the target; Figure 5.4A, closed symbols). It was not until most of the background texture was covered ( $127^\circ$  height, 77% of the total area) that the dTSDN response to target motion increased significantly, but even then, it was significantly lower than under control conditions (Figure 5.4A). This was surprising because in all these cases the local contrast was the same as in the control condition (Figure 5.4A, open symbol). In contrast, the response of *Eristalis* wide-field neurons decreased linearly with the height of a similarly positioned grey mean luminance strip of varying heights (Figure 5.4B).

To further explore the influence of local background motion on dTSDN responses, the uniform and naturalistic background areas were inverted: i.e. the strip surrounding the target now contained the original background pattern, and the screen outside of the patch had uniform luminance (i.e., no pattern). *Eristalis* dTSDN responses to target motion decreased as the height of the patch with the moving background pattern increased (Figure 5.4C). This was in contrast to *Eristalis* wide field-sensitive neurons, where responses increased with the height of the background pattern (Figure 5.4D). Together, these experiments (Figure 5.4) suggest that local contrast differences between the target and the background are not responsible for dTSDNs response attenuation when the target and background move in the same direction. Rather, the reduction in dTSDN target responses depends on wide-field motion across the visual field.

#### **5.4.5 dTSDN response suppression is strongest when the background is most naturalistic**

The background pattern used in our experiments was artificially generated to have natural image statistics with respect to its contrast and amplitude spectrum (Dyakova and Nordström, 2017). Natural images have amplitude spectra slope constants of nearly 1 (Tolhurst et al., 2007), to which

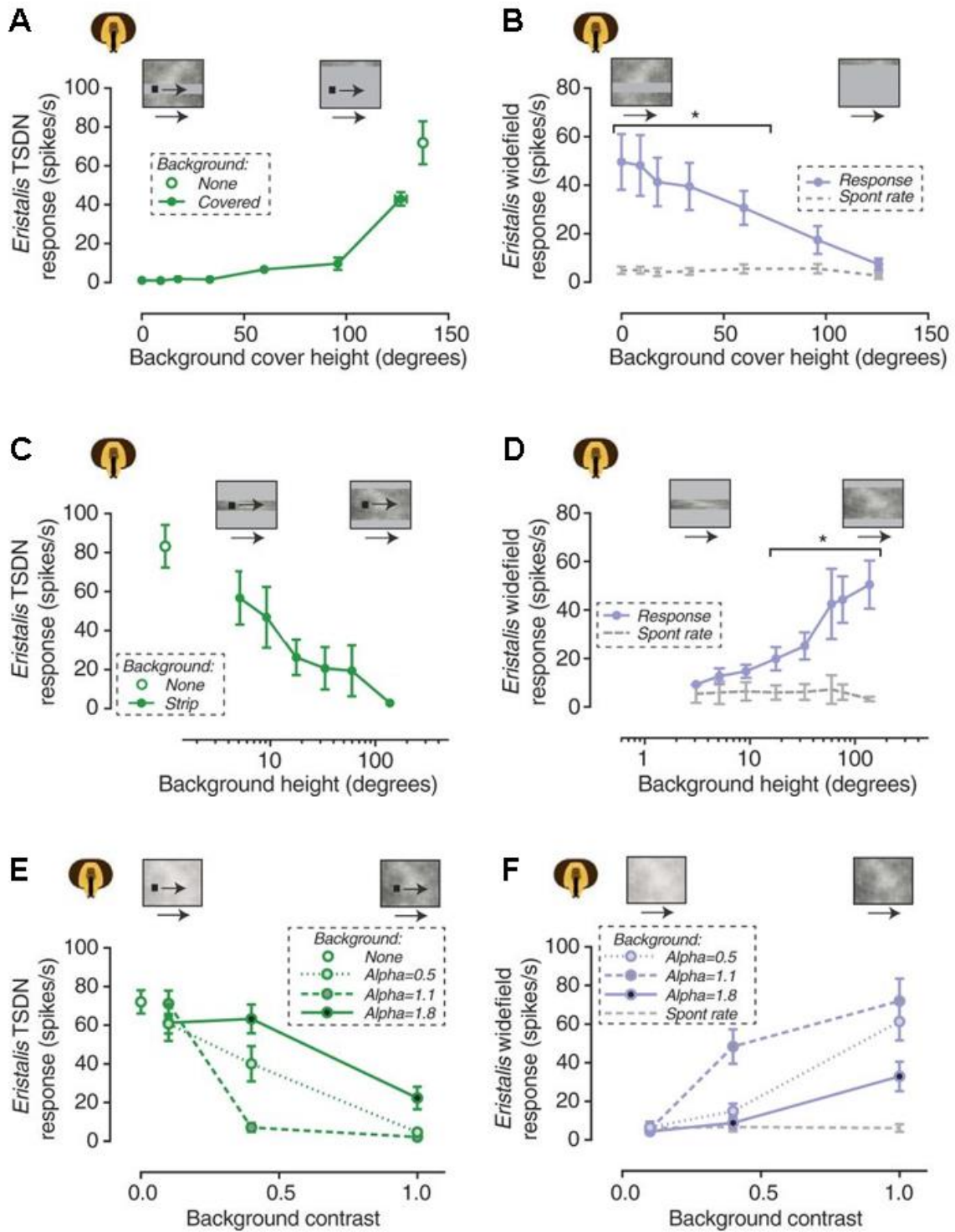


**Figure 5.4** dTSDN response suppression is not explained by local mechanisms and is strongest when the background is most naturalistic (A) The *Eristalis* dTSDN response to a small target moving across a background pattern, both moving at the same velocity. The background pattern was covered by a stationary mean luminance strip of different heights, centred on the trajectory of the target. (B) The response of *Eristalis* wide field-sensitive neurons to the background pattern, covered by a stationary mean luminance strip of different heights,  $N = 7$  neurons in individual (continued right)

(continued) animals. Significant differences are indicated, corresponding to two-way ANOVA followed by Sidak's multiple-comparisons test comparing wide-field responses to spontaneous firing rate. (C) The *Eristalis* dTSDN response to a small target moving across a background pattern, at the same velocity. The vertical extent of the background pattern was varied, and centered on the trajectory of the target. (D) The response of *Eristalis* wide field-sensitive neurons to different background pattern heights.  $N = 11$  neurons in individual animals. Significant differences are indicated, corresponding to two-way ANOVA followed by Sidak's multiple-comparisons test comparing wide-field responses to spontaneous firing rate. (E) The *Eristalis* dTSDN response to a small target moving across a background pattern, at the same velocity. We varied the contrast of the background pattern ( $x$ -axis) and the slope constant of its amplitude spectrum ( $\alpha$ , as color coded). Two-way ANOVA indicates a significant effect of  $\alpha$  ( $p = 0.0046$ ) and contrast ( $p < 0.0001$ ), and a significant interaction between contrast and  $\alpha$  ( $p = 0.0002$ ).  $N = 5$  neurons in individual animals. (F) The response of *Eristalis* wide field-sensitive neurons to background patterns with varied contrast ( $x$ -axis) and a slope constant of its amplitude spectrum ( $\alpha$ , as color coded). A two-way ANOVA showed a significant effect of  $\alpha$  ( $p < 0.0001$ ) and contrast ( $p < 0.0001$ ), and a significant interaction between contrast and  $\alpha$  ( $p < 0.0001$ ).  $N = 7$ . In all panels, the data are displayed as the mean  $\pm$  SEM.

both peripheral and central sensory neurons are tuned (Dyakova et al., 2015; van Hateren, 1992; Song and Juusola, 2014). To investigate the influence of background statistics on dTSDN responses, the relative contrast of the pattern and the amplitude spectrum slope constant were varied (see Figure 5.1). The target and the background moved at the same velocity (i.e., there was no relative motion between the two). *Eristalis* dTSDN responses to target motion were higher when the contrast of the background was lower (Figure 5.4E). In addition, when the background had medium contrast (0.4), the most naturalistic pattern ( $\alpha$ , 1.1), resulted in a near absence of dTSDN responses (Figure 5.4E, dashed line, grey symbol). This was surprising because with the same contrast level, the  $\alpha$  of 1.8 gave responses similar to those for controls, and an  $\alpha$  of 0.5 reached at least half of the control responses. This finding is of importance because it suggests that the suppression of dTSDN responses, shown in this study, is strongest when the target is presented against more naturalistic backgrounds.

In contrast, *Eristalis* wide-field neuron responses to the same background pattern variations increased with contrast (Figure 5.4F). Furthermore, at medium background contrast (0.4) the strongest response was generated by the most naturalistic background pattern (Figure 5.4F, dashed line, grey symbol,  $\alpha$  of 1.1). Thus, dTSDN and wide-field descending neuron responses were inversely correlated to variation of background contrast and amplitude spectrum, further suggesting a role of wide-field neurons in suppressing the dTSDN response to target motion.

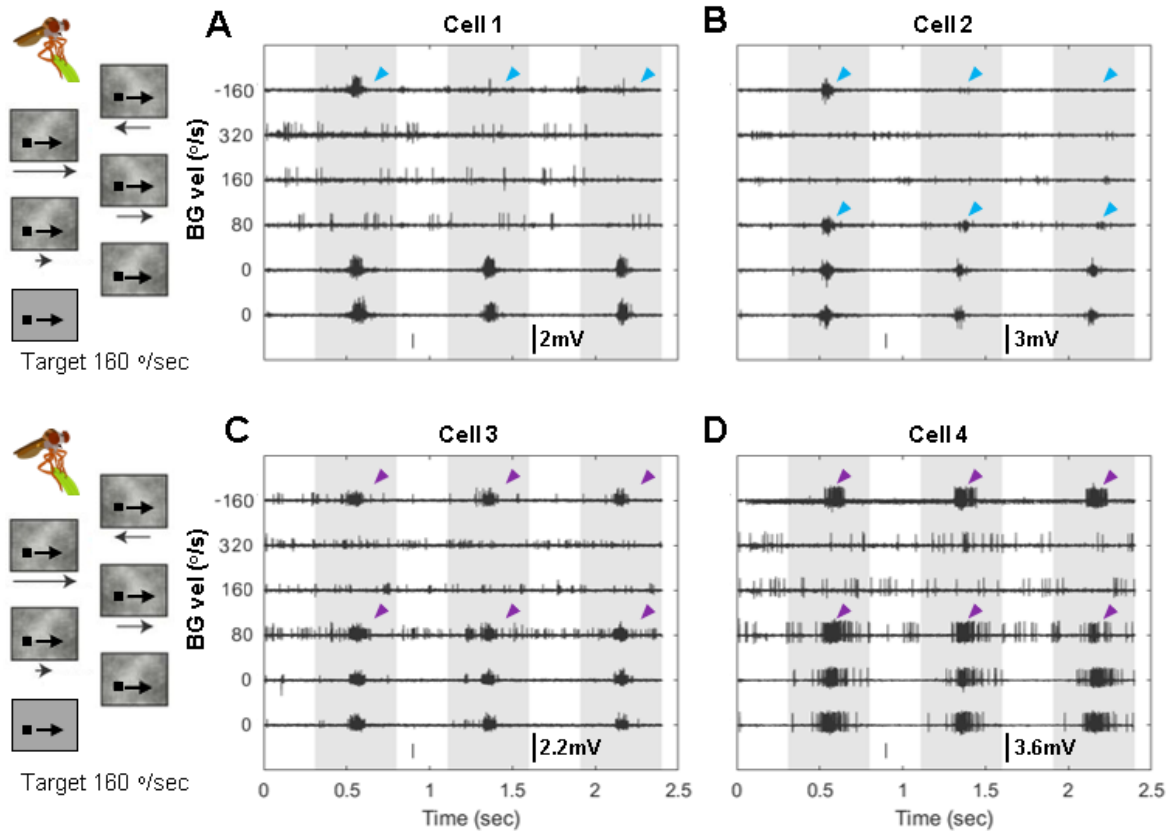


**Figure 5.5 dTSDN habituation is facilitated by background movement.** Example responses of four *Holcocephala* dTSDNs. Stimulus design is the same as in Figure 5.4A, however each condition consists of three presentations of the target moving along the same part of the screen sequentially for each condition (grey blocks on trace). Background patterns, when present, were moving for entire duration plotted (i.e. white and grey sections). (A-B) Two dTSDNs exhibiting fast habituation of responses to sequential targets under moving background conditions (blue arrows). (C-D) Two dTSDNs with absent or less distinct habituation under target movement with background movement conditions (purple arrows).

### 5.4.6 dTSDN habituation is facilitated by wide-field motion

Dragonfly TSDNs are known to exhibit short and long-term reduction in responses, i.e. habituation, following repeated presentations of a moving target (Adelman et al., 2003; Frye and Olberg, 1995; Gonzalez-Bellido et al., 2013; Olberg, 2010; Olberg and Pinter, 1990). Thus far, our dTSDN data describes the responses of dTSDNs to single presentations of target trajectories in each experimental condition (Figure 5.2-5.4). When presented with three sequential presentations of the target under each condition of background motion, *Holcocephala* dTSDNs were often observed to habituate faster under conditions with concurrent background movement compared with uniform mean luminance or stationary background control conditions (Figure 5.5 A-B, blue arrows). This effect was only observed in background motion conditions that were less effective at suppressing dTSDN responses (i.e. opposite

direction and half-speed syn-directional motion, Figure 5.2B-C), as dTSDN responses were completely absent in more suppressive background conditions (Figure 5.5). Not all cells exhibited the same level of suppression, with many cells responding robustly to sequential targets under background motion conditions (Figure 5.5C-D; purple arrows) which may represent the high variability of habituation across animals due to state dependent mechanisms (Bacon et al., 1995; Gray, 2005; Krasne and Teshiba, 1995). Nonetheless, this habituating effect may indicate a summation of intrinsic (i.e. habituating) and extrinsic (i.e. wide-field mediated) inhibitory mechanisms within dTSDNs, which is consistent with the hypothesis that wide field-sensitive neurons feed on to and suppress the dTSDN responses to target motion.

## 5.5 Discussion

### 5.5.1 TSDNs in predatory and non-predatory dipterans

In hoverflies and many other nonpredatory flies, target tracking is primarily used for conspecific identification or territorial interactions (Wellington and Fitzpatrick, 1981). Robberflies additionally track targets for predation, with the male *Holcocephala* searching for stationary perched mates (Fabian et al., 2018; Wardill et al., 2017). In this study we have shown that *Eristalis* and *Holcocephala* have target selective descending neurons (Figure 5.2), each with comparable moving object size tuning to STMDs in the dragonfly and hoverfly lobula (Nordström et al., 2006; O'Carroll, 1993) and to TSDNs in the dragonfly ventral nerve cord (Gonzalez-Bellido et al., 2013; Olberg, 1986).

Dragonfly TSDNs descend from the brain, projecting to the gnathal and all three thoracic ganglia, where they are presumed to connect and coordinate motor neurons innervating neck, leg, and wing musculature (Gonzalez-Bellido et al., 2013; Olberg, 1986). Dipteran TSDNs may similarly provide input to the motor neurons involved in target-pursuit behaviours, for example, by aligning the head (and thus the fovea) to the image of the target, and/or by rapidly changing flight course as is necessary during high-speed target pursuits (Collett and Land, 1975, 1978; Wardill et al., 2015, 2017). Despite the marked ecological differences between *Eristalis* and *Holcocephala*, the size tuning (Figure 5.2Aiv,Civ) and responses to targets in clutter (Figure 5.3B-C) were remarkably similar, suggesting that this descending neural circuitry may be robust to differences in visual ecology and/or flight kinematics in these different species.

### 5.5.2 Integration of small- and wide-field visual features in dTSDNs

A subset of STMDs in the hoverfly and dragonfly lobula complex respond robustly to the motion of small targets against a cluttered background, even without relative velocity differences (Chapter 1, section 1.3.3.1, Figure 1.16A) (Nordström et al., 2006; Wiederman and O'Carroll, 2011). It was therefore surprising to find that the dTSDN responses (i.e., descending neurons presumed to be

downstream targets of STMDs) (Nordström and O'Carroll, 2009) were so strongly influenced by background motion (Figure 5.3A-C). The target size, as well as the angular velocities of the target and the background were within the range of those experienced during target pursuits in *Eristalis* (Collett and Land, 1978) and *Holcocephala* (Wardill et al., 2017). Furthermore, background inhibition was observed in both *Eristalis* and *Holcocephala*, whose responses were recorded at different times, by different teams, and with different instrumentation, thus this finding is likely not a species- or experimental-specific oddity. Our results also follow a similar qualitative pattern to the subthreshold responses of dragonfly TSDNs to targets on moving backgrounds (Olberg, 1986) (Figure 5.1).

We found that in the presence of a moving background dTSDNs responded to the target only when the background velocity was low (Figure 5.3B) or had un-naturalistic spatial characteristics (Figure 5.4E). This corresponded to conditions in which background motion did not drive optic flow-sensitive neurons strongly (Figures 5.3C,5.4F). Since suppression from the wide-field system was also observed when the target moved over a moving background partially covered by a patch of uniform luminosity (figure 5.4A), it is unlikely that local contrast mechanisms preventing target detection underpin our finding. Rather, the relationship between the responses of dTSDNs and the neurons tuned to wide-field optic flow suggests that activation of the wide-field pathway results in inhibition of the target-tracking pathway (Figures 5.3-5.4). Presently, it is unclear where such inhibition arises. Whilst some STMDs respond to moving targets irrespective of background motion, other STMD responses are also repressed by background motion (Chapter 1, section 1.3.3.1, Figure 1.16B) (Barnett et al., 2007; Nordström et al., 2006). It could be the case that dTSDNs receive input from this optic flow sensitive subset of STMDs. Alternatively, dTSDNs may receive input from those STMDs insensitive to wide-field motion (Barnett et al., 2007; Nordström et al., 2006), with inhibition of target responses arising at the level of the dTSDNs. Inhibition could be implemented directly by LPTCs, which project to the posterior slope, a major site of descending neuron dendritic arborisation (Namiki et al., 2018; Suver et al., 2016), and also a site targeted by STMDs (Barnett et al., 2007). Indeed, TSDN input dendrites branch in this area in both dragonflies and damselflies (Chapter 3) (Frye and Olberg, 1995; Olberg, 1986). Interestingly, male-specific target-detecting MLG neurons in *Sarcophaga* flesh flies arborize in close proximity to lobula plate HS cell terminals in the posterior slope (see Chapter 1, section 1.4.2, Figure 1.23A) (Gronenberg and Strausfeld, 1991). MLG neurons are presynaptic to DNDC3-6b, the only previously described descending neuron responsive to moving targets in dipterans (Gronenberg and Strausfeld, 1990, 1991).

### **5.5.3 Function of background suppression in premotor target tracking**

Irrespective of anatomical origin, the suppression of target tracking responses by wide-field motion (Figure 5.3B) and the sinusoidal dependence on the relative direction of background and target motion

(Figure 5.3C) raises interesting algorithmic implications for implementation of pursuit (Figure 6). At early stages of visual processing in the optic lobes, motion is encoded within a retinal frame of reference by correlating ON and OFF luminance changes between adjacent ommatidia (see Chapter 1, section 1.3) (Borst and Helmstaedter, 2015; Taylor and Krapp, 2007). Consequently, from the reference frame of the retina, it is not explicitly encoded whether wide- or small-field motion across the compound eye results from motion of external objects or from self-motion.

In the case of wide-field motion, LPTCs operate within an optomotor reflex pathway that stabilises the animal following unexpected self-motion, arising either as a consequence of external perturbation or internal motor error (Bishop and Keehn, 1967; Geiger and Nässel, 1981; Haikala et al., 2013; Heisenberg et al., 1978). During voluntary turns, LPTC responses are suppressed by a motor-related efference copy of opposite sign to the expected turn to temporarily inhibit this reflex (Chapter 1, section 1.4.2) (Kim et al., 2015). Thus, implicit in lobula circuitry is an assumption that wide-field motion correlates with self-motion, and so in the absence of an efference copy should be directed to activate stabilisation reflexes. Importantly, LPTCs remain sensitive to any additional optic flow beyond that predicted by the efference copy during a voluntary manoeuvre.

In the case of target tracking, STMD excitation could result either from externally generated motion of the target relative to the pursuer, or from self-motion. Subtracting wide-field motion (as detected by LPTCs) from small-field target motion (as detected by STMDs) results in a signal of target motion *relative* to any self-motion (Figures 6 and 7). Combining this relative target motion with an optomotor stabilisation response will result in a turning command of appropriate magnitude to fixate the target (Figures 6 and 7). If relative motion were not calculated, then the target motion signal will contain the additional component arising from self-motion, which when added to the optomotor stabilisation response would result in over-compensation of the resultant turn.

This model predicts that optomotor reflexes remain sensitive throughout pursuit, and that both TSDN and widefield descending pathways are activated to generate corrective movements (Figure 6). This is consistent with behavioural experiments, in which chasing hoverflies placed in a rotating drum are found to have both an optomotor and target tracking component to their flight paths (Collett, 1980). However, optomotor turning responses were measured to have a significantly longer delay of ~60 ms compared to ~20 ms for target induced turns (Collett, 1980). At first it is not clear why the relatively slower optomotor pathway would be incorporated into the target tracking circuitry. However, it may be the case that the target tracking pathway implemented by TSDNs is reserved for faster, more erratic movements of the target, delegating the relatively slower self-motion components to the optomotor pathway. In this regime, TSDNs are reserved exclusively to correct for high frequency motion of the target. Similarly, it should be noted that the present model (Figure 6) yields qualitatively the same output as one in which the optomotor response is entirely inhibited (Figure 7).

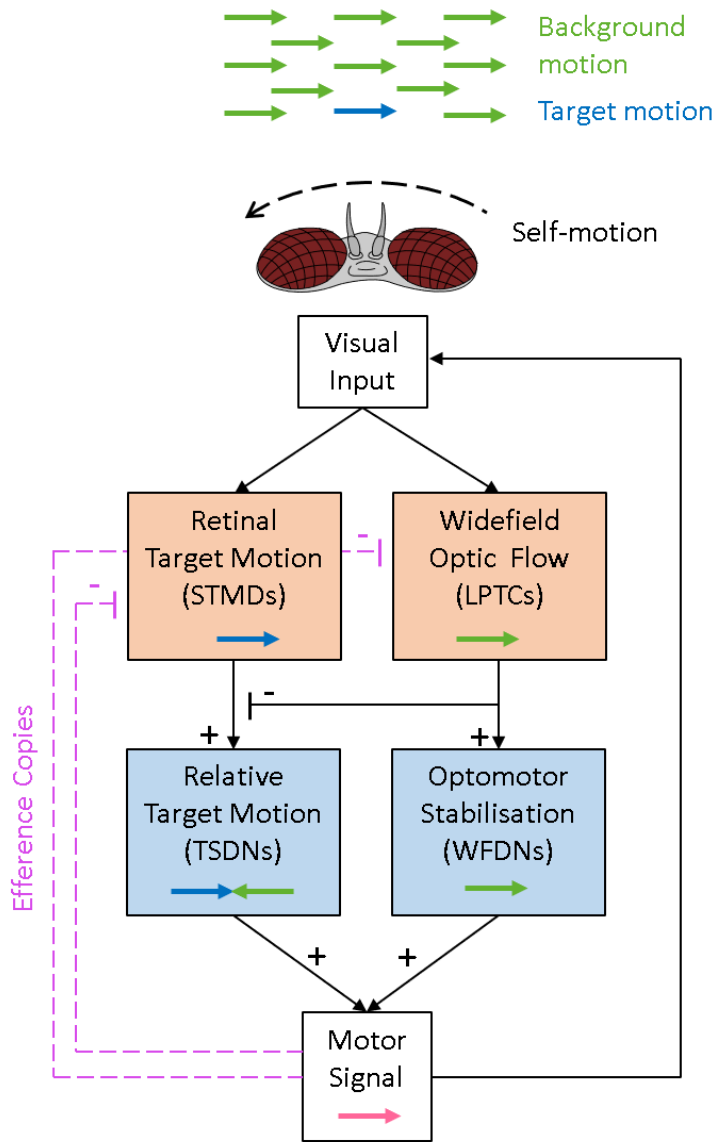


**Figure 5.6 Model for the integration of small- and wide-field descending channels during pursuit** Self-motion results in motion of the target (blue) and background image (green) across the retina. Arrow lengths represent the relative speed. In the optic lobes (shaded orange) target motion is encoded by STMDs, and wide-field optic flow by LPTCs. Motion vectors (arrows) are encoded in a retinal frame of reference. Target motion information is relayed to TSDNs, and wide-field motion information is sent to wide-field descending neurons (WFDNs) in the central brain (shaded blue) that descend to motor centres. Subtraction of the wide-field motion vector from the target motion vector results in relative target motion in an inertial frame of reference. WFDNs control canonical optomotor stabilization reflexes to correct for unexpected self-motion. In addition, TSDNs control corrective manoeuvres to correct for any deviation of the target not due to self-motion. Together these

two pathways initiate a turning movement of appropriate magnitude (pink) to fixate the target (see figure 5.7). Efference copies (magenta) are sent to the target tracking and wide-field motion detection circuits (STMDs and LPTCs) such that these detectors only sense unexpected self-motion, arise either from external perturbation or errors in the motor system.

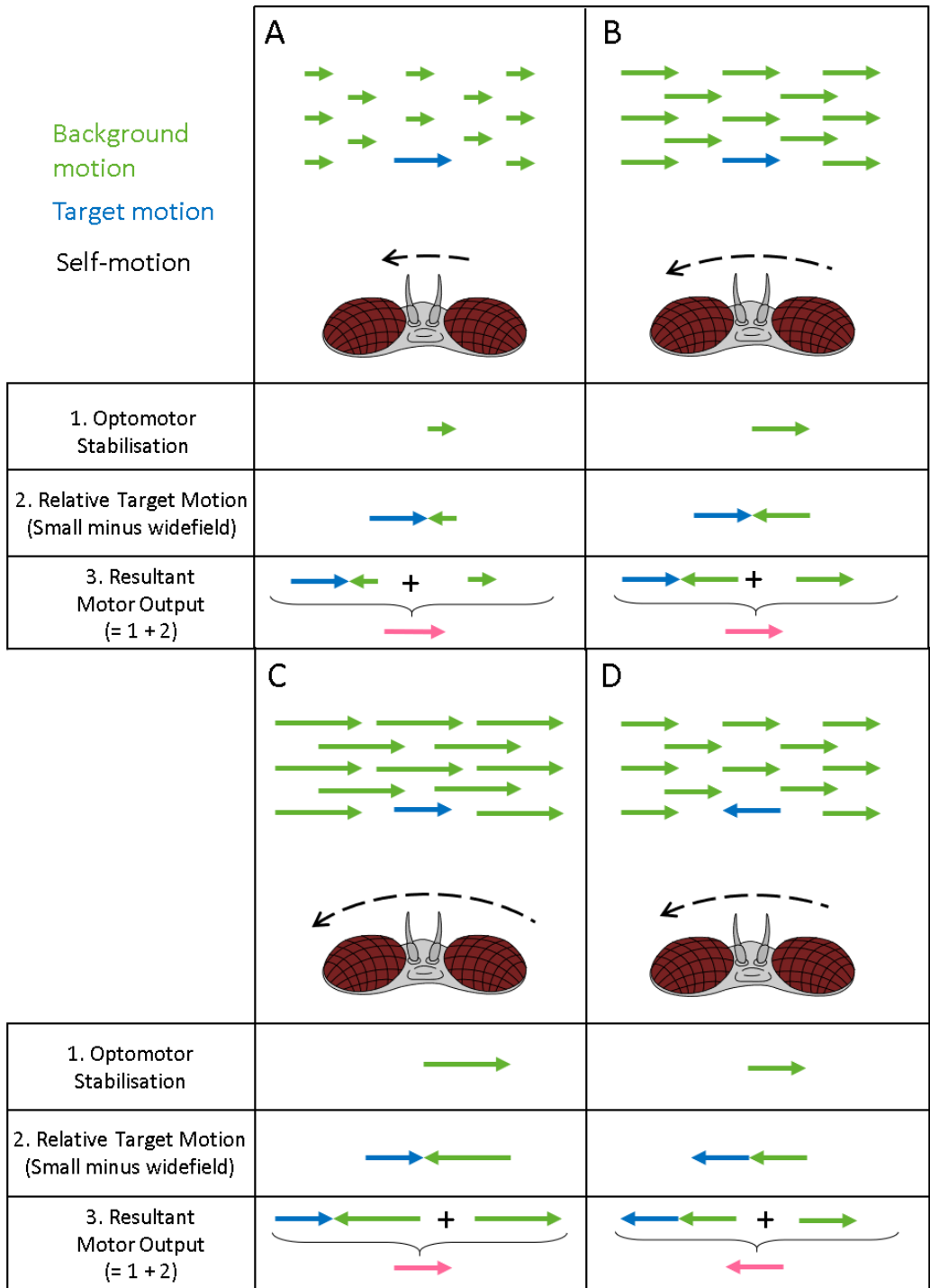


**Figure 5.7 Output properties of the proposed controller** Background motion in green, target motion in blue, self-motion in black. Arrow length indicates relative speed. In each case, the optomotor response magnitude (1) is subtracted from the target tracking pathway to calculate relative target motion (2). This relative motion magnitude is then added to the optomotor stabilization magnitude, resulting in an appropriate turning magnitude (pink, 3). This enables the optomotor stabilization pathway to remain active throughout pursuit.

Why remove the self-motion component from the target tracking system, rather than fully suppress the wide-field optomotor system? Again, this algorithmic implementation may represent a specialisation in which the target tracking system is exclusively reserved to detect and react to relative target motion, which likely require higher temporal frequency responses compared with optomotor stabilisation. It could furthermore be the case that the wide-field detection system is generally more reliable for detecting self-motion as this system integrates across larger regions of visual space compared with the target tracking system (Taylor and Krapp, 2007), and uses specialised matched filter receptive fields tuned to detect the components of self-motion (see Chapter 1, section 1.3.2) (Krapp and Hengstenberg, 1996; Taylor and Krapp, 2007).

One initial prediction of this model is that TSDN responses should be inhibited when presented with background motion of equal speed and direction to the target, regardless of absolute speed. In this study only a single target speed was investigated; thus, future experiments should measure the background suppression effect for a range of target speeds. Furthermore, our experiments were performed on immobilised animals. The widefield system is known to adjust its gain and frequency tuning upon active motion of the animal, or upon application of the insect norepinephrine analog, octopamine (Longden and Krapp, 2010; Suver et al., 2012). It is currently unknown whether TSDN response properties are altered by locomotive state, however the present model suggests that the descending target tracking system would need to match its relative gain to the optomotor system to maintain the resultant representation of relative target motion. It would be instructive to measure TSDN responses either when the animal is free to move (e.g. in tethered flight (Suver et al., 2012), or when able to walk on a treadmill (Longden et al., 2014)), or alongside octopamine agonists (Longden and Krapp, 2010; Suver et al., 2012). The model presented in Figure 5.6 also predicts that an efference copy of the motor signal is sent both to the wide-field and target tracking system. The efference copy continuously updates the system to only detect target and widefield motion arising from unexpected rather than volitional self-motion. Efference copies have been demonstrated to adjust LPTC responses (Chapter 1, Section 1.4.2, Figure 1.22), however their integration into target tracking circuitry remains to be verified.

In summary, our data presents evidence that the dTSDN target tracking response is repressed by relative background motion. This effect suggests a model for the computation of target pursuit in which dTSDNs encode the relative motion of the target, which is then combined with an optomotor pathway to adjust flight path in an inertial frame of reference. Future experiments should (1) investigate the anatomical origin of wide-field inhibition in dTSDNs, and (2) address predictions of this target tracking model, such as the dependence of background suppression on target speed, and whether TSDNs exhibit state-dependent activity changes comparable to those within the wide-field motion processing pathway.

# Chapter 6

## General Discussion

This thesis presents a comparative investigation into the descending neuronal circuitry underlying target tracking among flying insects. Target selective descending neurons (TSDNs) are found throughout Odonata (Chapter 3) and Diptera (Chapters 4-5), suggesting a common design principle in which separate descending channels encode target motion alongside widefield motion. Furthermore, in each species individual TSDNs have distinctive receptive fields selectively tuned to specific aspects of target motion, such as the direction of motion and/or location within the visual field.

Chapter 3 investigated TSDN representations in damselflies. Damselflies and dragonflies share a last common ancestor ~270 Million Years Ago (MYA), and have subsequently diverged in behaviour, anatomy, and flight kinematics. Damselflies have distinctly separated dichoptic eyes with frontal facing foveae (Chapter 3, Figures 3.1-3.3), which matches their predatory strategy of attacking their prey head on (Chapter 3, Figure 3.3). This contrasts with most dragonflies, which pursue their prey from below and fixate the image of the target upon a holoptic dorsal fovea (Chapter 3, Figure 3.3). In dragonflies, a small population of TSDNs have been studied for nearly 40 years (Adelman et al., 2003; Frye and Olberg, 1995; Gonzalez-Bellido et al., 2013; Horridge et al., 1990; Olberg, 1978, 1981a, 1986; Olberg and Pinter, 1990). Dragonfly TSDNs encode target motion across the dorsal fovea using a distributed representation in which individual TSDN encode specific directions of motion within different but overlapping regions of the visual field (Chapter 1, Figure 1.20). In damselflies, a similar population of cells samples the frontal fovea, with individual TSDN receptive fields that are remarkably similar to those in dragonflies (Chapter 3, Figures 3.4-3.5). The anatomical similarity in dendritic structure and cell body locations between damselflies and dragonflies (Chapter 3, Figure 3.8), along with their evolutionary history as divergent predators, strongly suggests that these neurons are homologous as target tracking descending neurons involved in prey capture. Interestingly however, damselfly TSDNs

sample extensively across the visual midline, unlike dragonfly TSDNs (Chapter 3, Figure 3.5). All damselfly TSDNs receive binocular input, albeit with different monocular weightings (Chapter 3, Figures 3.10-3.12). Whilst it is not clear whether TSDNs of the same type always have the same binocular weighting in different individuals, TSDNs with different binocular weightings were recorded within the same animal (Chapter 3, Figure 3.11), suggesting a heterogenous encoding of binocularity across the damselfly TSDN population.

Chapter 4 investigated TSDN representations in two dipteran predators, the robberfly *Holcocephala fusca*, and the killerfly *Coenosia attenuata*. Each species has TSDNs responding to target appearance and movement with extremely short latencies (Chapter 4, Figures 4.2-4.3). dTSDN latencies in *Coenosia* were ~10 ms shorter than in *Holcocephala* (Chapter 4, Figure 4.3), correlating with behavioural latencies for flight course correction to target movement, which is ~18 ms in *Coenosia*, and ~28 ms in *Holcocephala* (Fabian et al., 2018). Furthermore, dTSDN responses to target appearance were ~3.5 ms and ~4.6 ms faster than moving target responses in *Coenosia* and *Holcocephala*, respectively (Chapter 4, Figure 4.3). This additional delay for moving targets may correspond to the time required for spatiotemporal cross-correlation within elementary motion detectors (EMDs) in earlier stages of visual processing (see Chapter 1, Section 1.3.1). In this case, *Coenosia* computes elementary motion ~1 ms faster than *Holcocephala*. The remaining ~9 ms difference in TSDN latency between these two species likely represents differences in synaptic transmission rates within the optic lobes, and between lobula visual projection neurons and the dTSDNs. It would be interesting to measure dTSDN and lobula interneuron latency at higher temperatures more closely matching those that would be experienced under natural conditions to see whether the latency differences measured in this study are reflected across all operating conditions. It may be the case that *Holcocephala* is more temperature dependent than *Coenosia*, and latencies may converge to similar timings at a higher temperature.

The receptive field organisation in *Holcocephala* and *Coenosia* are markedly different given the identical experimental conditions (Chapter 4, Figure 4.4). Limitations in extracellular spike sorting leave individual receptive field structures tentative, with the bilobed *Holcocephala* receptive fields and the bilateral *Coenosia* receptive fields likely resulting from contamination by multiple neuronal units (Chapter 4, Figure 4.6). Nonetheless, there is clear lateralisation around the midline in several dTSDNs in both species, in addition to non-random directional selectivity as seen in Odonate TSDNs. *Holcocephala* fovea dTSDNs and *Coenosia* lateralised lateral dTSDNs are directionally selective to motion along the visual azimuth (Chapter 4, Figure 4.4). This is reminiscent of Odonate TSDNs which overrepresent lateral target motion compared with other directions (Chapter 3, Figure 3.5). Interestingly in *Holcocephala*, highly lateralised non-directional dTSDNs are directionally indiscriminate but highly responsive to target motion (Chapter 4, Figure 4.4), suggesting a novel encoding strategy focused on the detection of motion in any direction within a visual hemifield. This contrasts with all previously described TSDNs in odonates.

Chapter 5 investigated the relationship between descending channels for target tracking and self-motion. One early description of dragonfly TSDNs found that the subthreshold membrane potential has an inverse relationship for target and background movement, with backgrounds moving along the preferred direction for target motion resulting in hyperpolarisation of the TSDN (Olberg, 1986). In *Holcocephala* and *Eristalis*, a similar relationship was observed in which dTSDN target responses were attenuated when presented against cluttered backgrounds moving in the preferred direction of target motion (Chapter 5, Figure 5.3). This effect was dependent on both the speed of the clutter, with faster background motion resulting in stronger inhibition of the target response (Chapter 5, Figure 5.3B), and the direction of background motion, with opposite target and background motion resulting in less inhibition of the dTSDN response (Chapter 5, Figure 5.3C). In contrast, wide-field sensitive descending neurons increased their firing rates with increasing speed of background motion (Chapter 5, Figure 5.3D) and were directionally sensitive to a preferred direction of background motion (Chapter 5, Figure 5.3E). The functional implications of these results are speculative, however a model for the integration of inner-loop stabilisation reflexes and outer-loop goal directed behaviours predicts several TSDN response properties that can be tested experimentally (see section 6.1.3 below).

The following sections review the role of TSDNs within the neuronal circuitry underlying target chasing, along with open questions and suggestions for future experimentation.

## **7.1 TSDN implementation of the Land and Collet circuitry**

Visually-guided target tracking and chasing requires the transformation of the motion of a target across the retina into changes in the rotational and/or translational velocity of the pursuer (Boeddeker and Egelhaaf, 2005; Land, 1992; Land and Collett, 1974). Following observations of conspecific pursuit among houseflies, Land and Collett proposed a minimal circuitry sufficient to guide pursuit comprised of two pairs of bilaterally symmetric frontal velocity sensors and a lattice of peripheral positional sensors feeding onto descending neurons to control the rotational velocity of the pursuer (Figure 6.1; see also Chapter 1, Section 1.4.1) (Land and Collett, 1974). A pair of descending neurons are directionally selective and represent the magnitude of contralateral yaw torque in response to lateral target movement (Figure 6.1). For example, a right-hand-side descending neuron (red) receives input from ipsi- and contra-lateral tangential cells, each responding selectively to rightward motion of a target (Figure 6.1). Additionally, ipsilateral

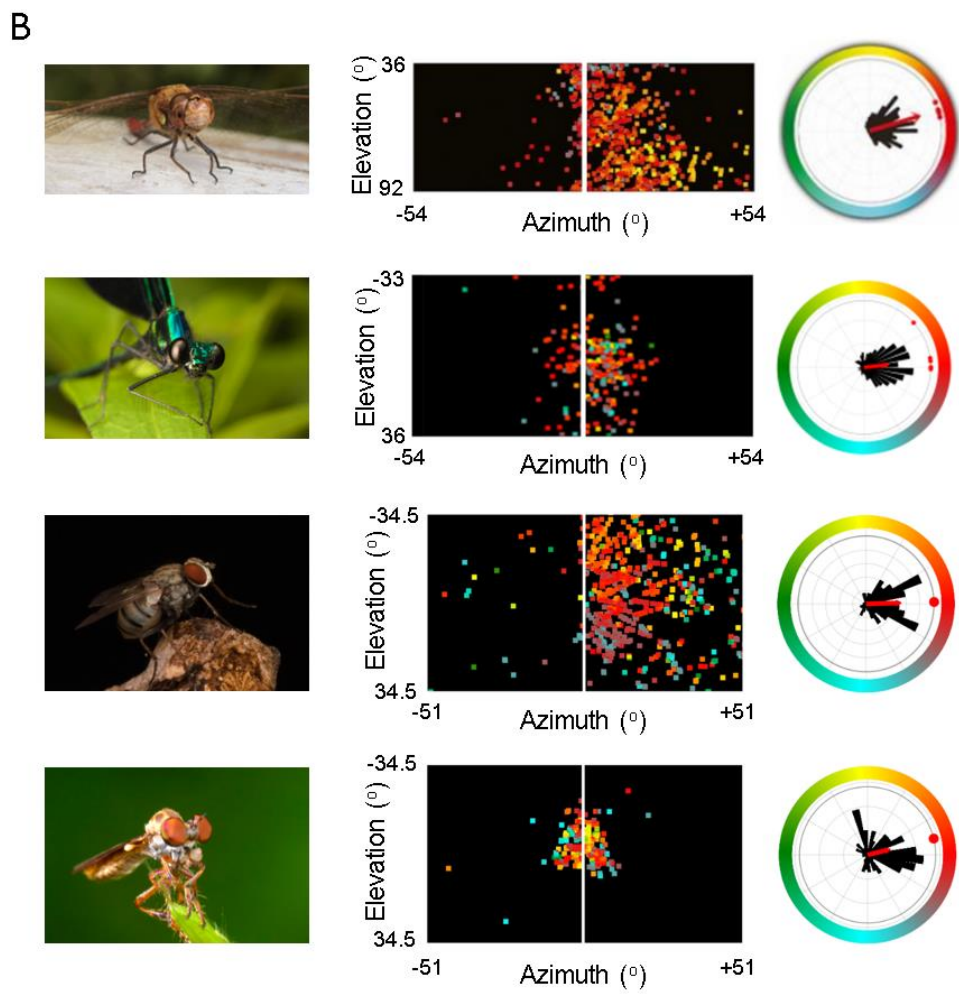
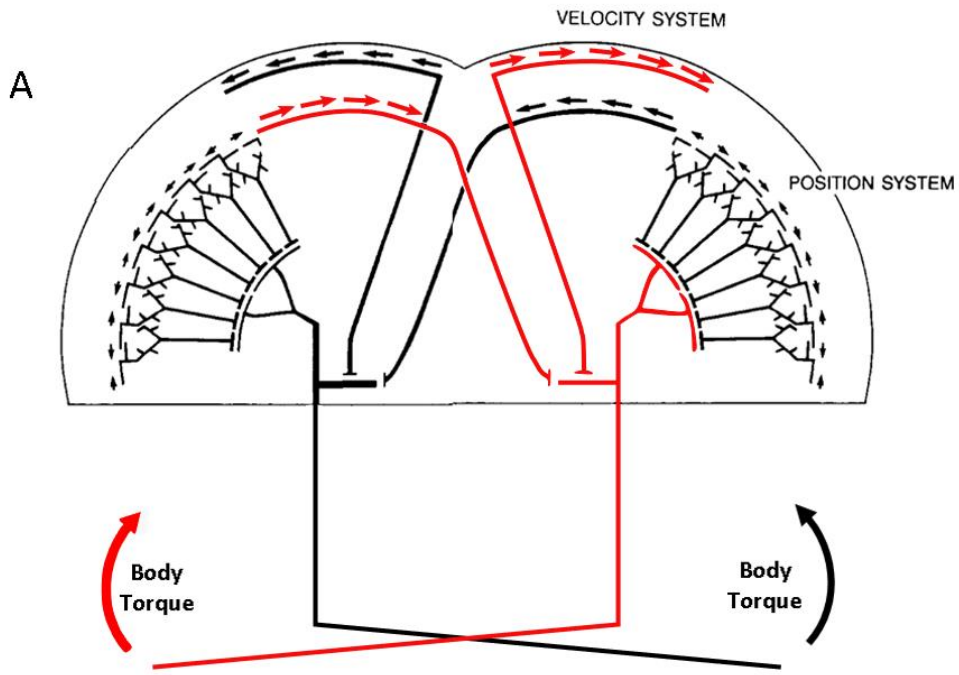


Figure 6.1 (legend right)

**Figure 6.1 (left) TSDN implementation of the Land and Collett minimal target tracking circuitry (A)**

Schematic of the minimal target tracking circuitry described by Land and Collett (Land and Collett, 1974) and elaborated by Strausfeld based on anatomical and physiological data (Strausfeld, 1991). Adapted from (Strausfeld, 1991). Two bilaterally symmetric tangential cell types in the lobula (**a**, **b**) receive input from the frontal visual field of each eye and respond to opposite velocities of target motion (arrows). These neurons respond to either medial-to-lateral (**a**) or lateral-to-medial movement (**b**) in each eye. Subsets of these neurons are predicted to project to descending neurons (**d**) that control body torque. Ipsilateral medial-to-lateral input from (a) and contralateral lateral-to-medial input from (b) result in descending neurons responding to targets moving towards the side of each neuron. These descending neurons input to contralateral steering motors to generate a compensatory body torque in the direction of target movement. Land and Collett also suggested the presence of a separate positional detection system (**c**) to account for very high gain turns to peripheral targets in hoverflies (Land and Collett, 1974). These neurons provide ipsilateral input to the same descending neurons, with increased gain the more lateral the target is from the midline. (**B**) TSDNs responding to lateral target motion in dragonflies (top row, from Chapter 3), damselflies (second row, from Chapter 3), killerflies (third row, from Chapter 4), and robberflies (bottom row, from Chapter 4). Polar plots indicate the directional selectivity of each neuron, with red corresponding to rightward motion corresponding to the pathway highlighted in red in (A). These neurons may represent the directionally selective descending neurons controlling yaw torque as predicted by Land and Collett.

columnar cells responding to target position with increased weighting towards the periphery would facilitate additional responses to targets further from the midline. Such descending neurons project to the contralateral right-hand-side wing motor to generate net rightward torque (Figure 1.21).

TSDNs are obvious candidates for the Land and Collett descending channels. Indeed, TSDNs selective for lateral target movement are found in all species in this study for which receptive fields were analysed (Figure 6.1). As a population, dragonfly and damselfly TSDNs over-sample lateral target motion with respect to the midline compared to other directions of target movement, suggesting lateral corrective movements form an important aspect of the descending controller. However, there is currently little evidence for the position-sensitive input to TSDNs. TSDNs respond to both target appearance and motion, although responses to target appearance are confined to the visual midline, rather than increasing in gain towards the visual periphery as predicted by the Land and Collett model. However, one class of descending neurons in *Holcocephala* are indifferent to the direction of motion and may represent a positional detector (lateralised non-directional, Chapter 4, Figure 4.4A). It would be interesting to investigate whether these neurons represent a specific TSDN adaptation in *Holcocephala*. Prior to flight, *Holcocephala* initiate saccadic head flicks to align the frontal fovea towards the prey (Fabian et al., 2018; Wardill et al., 2017). Non-directional dTSDNs in *Holcocephala* may function to initiate this head flick, signalling only the presence of a moving object within one or the other hemifield. However, dragonflies also perform head flick saccades prior to the initiation of flight, but do not possess

non-directional TSDNs. Whether a *Holcocephala* non-directional system represents a simplified head flick algorithm relative to that in dragonflies would be an interesting area for further exploration.

The Land and Collett model accounts only for the generation of yaw torque. However, half of the odonate TSDN population (MDT1, MDT4, MDT5, DIT3), and the majority of receptive fields recorded in *Holcocephala* and *Coenosia*, roughly encode target motion along the anterior-posterior visual field axis. Whilst it may be the case that these neurons are important for controlling pitch or thrust adjustments, the function of these neurons for target tracking is unknown and remains entirely speculative. However, the ubiquity of TSDNs encoding motion along this axis implies a fundamental role within the controller for target chasing for which the Land and Collett model does not consider. Ultimately, this can only be confirmed by recording from these neurons during flight. This approach is experimentally challenging due to the need for simultaneous neurophysiological and wing beat motion recordings, in addition to requiring information about wing beat motion along multiple axes rather than the laboratory standard left-right amplitude difference (See Chapter 1, section 1.4.2, Figure 1.22B). However, advances in image-based wing beat measurements (Suver et al., 2016) may make these experiments more accessible.

## 7.2 The role of TSDN binocularity

The Land and Collett model predicts descending neurons that receive directional input from both visual hemispheres (Land and Collett, 1974). However, this appears only to be the case in binocular *Calopteryx* (Chapter 3) and *Holcocephala* fovea dTSDNs (Chapter 4), as the receptive fields of these neurons overlap the visual midline. In dragonflies (Gonzalez-Bellido et al., 2013) and *Coenosia* (Chapter 4), directionally selective TSDN receptive fields are lateralised at the visual midline. From an algorithmic level there is no obvious reason why dragonfly and *Coenosia* TSDN do not respond to targets moving in towards the midline from the contralateral hemifield: this configuration would pre-emptively manoeuvre the pursuer to correct for a target about to pass the midline. One possible explanation for TSDN lateralisation could involve the stability of the system. Owing to the fast velocities involved, descending premotor systems have short latencies (Chapter 4) and likely have a high gain in controlling flight musculature, thus it may be the case that pre-emptive rotations to a fast target moving in towards the midline would result in turning over-compensation. Indeed, dragonflies (Mischianti et al., 2015; Olberg et al., 2007) and *Coenosia* (Fabian et al., 2018; Wardill et al., 2015) tend to perform faster aerial interceptions compared with *Calopteryx* and *Holcocephala* (Fabian et al., 2018; Wardill et al., 2017), which may explain the sharpening of the receptive field lateralisation in the latter two species, and potentially also the evolution of holoptic ocular arrangements in many flying insects specialised for target tracking (Perry and Desplan, 2016).

The algorithmic implications for damselfly TSDN binocularity remain speculative (Chapter 3). Monocular and prism experiments demonstrate that damselfly TSDNs require simultaneous target motion in both eyes. However, it is unknown to what extent target motion must correspond in each eye. For example, must the targets be of similar sizes in each eye? Must they be travelling at the same speed, or in the same direction? Do individual TSDNs respond across broad or narrow range of target disparity? The experiments in Chapter 3 were limited by only testing only two values for target disparity using 4° and 10° prisms. Furthermore, target disparity was only tested relative to one eye, corresponding to a lateral displacement of the target. It would be interesting to measure individual TSDN responses to ranges of target disparity 3D stimulation protocol, either using physical beads moving in three dimensions, or stereoscopic digital projection protocols to vary the target image in each eye independently (Nityananda et al., 2016). It may be the case that different subsets of TSDNs are sensitive to different ranges of target disparity between the two eyes. This would imply that different TSDNs are active at different distances from the target which may have implications for the control of close-range manoeuvres such as grasping.

### **7.3 Inner- and outer-loop control**

Motor control is broadly comprised of two functional divisions: inner-loop stabilization reflexes, and outer-loop goal-directed behaviours (Chapter 1, Figure 1.22) (Krapp and Wicklein, 2008). Stabilization reflexes function to maintain postural equilibrium in response to external perturbation, and are continuously implemented by an inner-loop control system (Krapp and Wicklein, 2008). The Land and Collett model does not account for any interaction between the outer-loop target tracking system with inner-loop stabilisation reflexes (Figure 6.1). However, Chapter 5 presents evidence that wide-field optic flow is integrated with target motion in dTSDNs, finding an inverse correlation between dTSDN and widefield descending neuron activity under similar background motion conditions. This response pattern in dTSDNs matches that of a previous description dragonfly TSDNs (Olberg, 1986), suggesting common mechanisms in dipteran and dragonfly TSDNs.

Integration of wide-field optic flow with target motion in TSDNs suggests a control architecture in which target motion across the retina is decomposed into a component due to self-motion, and an external component corresponding movement of the target within an inertial frame of reference relative to the pursuer (Figure 6.2; Chapter 5, Figures 5.6 and 5.7). Flight course correction for self-motion is implemented by the canonical optomotor pathway throughout pursuit, whilst correction for target motion within an inertial frame of reference is implemented by the TSDN pathway

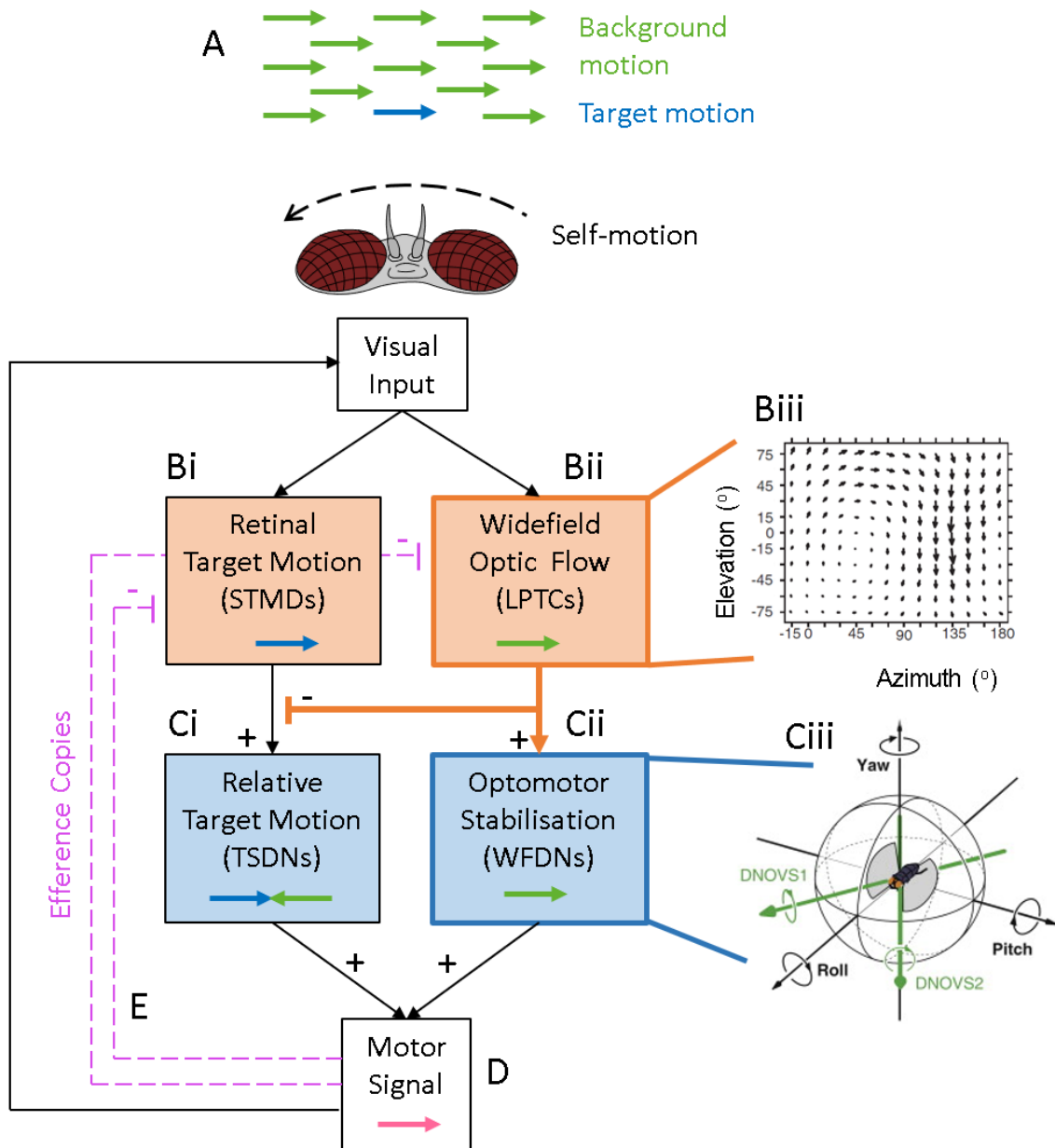


**Figure 6.2 Relationship of TSDNs to matched filter representations in the optomotor pathway** An

elaborated model for the integration of wide-field and target motion in TSDNs, in the context of matched filters for self-motion. (A) Self-motion results in motion of the target (blue) and background image (green) across the retina. Arrow lengths represent the relative speed. (B) In the optic lobes (shaded orange), target motion is encoded by STMDs (i), and wide-field optic flow by LPTCs (ii). Motion vectors (arrows) are encoded in a retinal frame of reference. (iii) LPTCs detect the components of self-motion using receptive fields tuned to specific modes of motion (known as matched filtering in the biological literature, inset depicts a receptive field tuned to rotation by VS8; see Chapter 1, Section 1.3.2.1, Figure 1.12). (C) In the central brain (shaded blue), target motion information detected by STMDs is relayed to TSDNs (i), and wide-field motion information is sent to wide-field descending neurons (ii, WFDNs) that descend to motor centres. Subtraction of the wide-field motion vector from the target motion vector results in relative target motion in an inertial frame of reference. WFDNs control canonical optomotor (*continued right*)

(continued) stabilization reflexes to correct for unexpected self-motion. TSDNs represent target motion that did not arise from self-motion. (iii) Matched filter representations are maintained at the level of wide-field descending neurons. For example, DNOVS1-2 respond selectively to rotation axes offset  $\pm 30^\circ$  in azimuth relative to the body axis (see Chapter 1, Section 1.3.2.2, Figure 1.13). It may be the case that inhibitory input to TSDNs follows a similar receptive field pattern corresponding to matched filter for a specific mode of motion. If so, the spatial pattern of inhibitory input to TSDNs may provide insight into the TSDN actuation axes. **(D)** When the TSDN representation of relative target motion is combined with the WFDN response, a corrective movement of appropriate amplitude is sent to the motor centres to fixate the target (pink vector). If the wide-field signal was not subtracted from the original target motion signal, the system would over-compensate the turning response. **(E)** Efference copies (magenta) representing the intended movement is fed back to target and wide-field motion detectors to offset the system to only respond to unintended motion.

(Figure 6.2). By subtracting an estimate of self-motion from the target tracking signal in TSDNs, only target movement relative to the pursuer is transmitted by the target tracking pathway. This may function to prevent over-compensation in the turning response which would otherwise result from addition of the target and optomotor pathways. This model is consistent with behavioural observations of male hoverflies chasing females within a rotating drum, in which the optomotor system was found to remain active throughout pursuit (Collett, 1980), and makes several predictions about dTSDN physiology that can be tested experimentally.

Foremost, the model in Figure 6.2 predicts that TSDNs encode relative target motion. Therefore, TSDNs should be fully inhibited by wide-field optic flow motion travelling at the same velocity as the moving target, regardless of the magnitude of that velocity. This can directly be tested by repeating the experiments in Chapter 5 for a range of target speeds.

Secondly, the wide-field motion processing pathway detects optic flow using ‘matched filters’ tuned to specific components of self-motion (Chapter 1, Section 1.3.2) (Krapp and Hengstenberg, 1996; Taylor and Krapp, 2007). For example, VS cells in the dipteran lobula plate have receptive fields sensitive to rotational optic flow fields with axes of rotation distributed approximately along the eye equator (Chapter 1, Section 1.3.2.1, Figure 1.12). Similarly, wide-field sensitive descending neurons have receptive fields matched to specific axes of rotational optic flow fields, with DNOVS1-2 sensitive to combinations of pitch and roll rotation (Chapter 1, Section 1.3.2.2, Figure 1.13). Given the present model in which the wide-field system inhibits the target tracking system (Figure 6.1), and given the fundamental role for matched filter receptive fields throughout the optomotor system (Taylor and Krapp, 2007), it may be the case that the inhibitory input received by TSDNs aligns with a matched filter for specific modes of self-motion. This could be directly investigated by measuring subthreshold TSDN membrane fluctuations in response to local wide-field motion (Figure 6.3), following a similar

experimental protocol used to measure LPTC receptive fields (Krapp and Hengstenberg, 1996). Should it be the case that inhibitory input to TSDNs follows similar matched filter receptive fields to LPTCs, this may reveal axes of flight course correction that are ultimately actuated by individual TSDNs. For example, if a given TSDN receives inhibitory input maximal for image motion corresponding to clockwise roll of the animal, this would indicate that the TSDN actuates corrective movements along this axis. These experiments will be important for validating the control architecture presented in Figure 6.2 and would further our knowledge of TSDNs in the context of flight course correction. It could be the case that TSDN inhibition does not follow such a matched filter pattern. This would imply that the inhibitory background effect either arises from complex combinations of LPTCs, or from alternative pathways in the lobula complex that remain to be described.

Lastly, a fundamental component of the inner- outer-loop controller is the role of efference copies (Chapter 1, Section 1.4.2, Figure 1.22). Volitional movement results in optic flow across the retina, which in the absence of an efference copy activate inner-loop stabilisation reflexes which will actuate corrective movements in the opposite direction to that intended. Evidence for efference copies has been described in LPTCs in *Drosophila*, in which spontaneous turns during flight are accompanied by either inhibitory or excitatory input to LPTCs to cancel optic flow reafference (Chapter 1, Section 1.4.2, Figure 1.22B). The model in Chapter 5 and Figure 6.2 represents a controller sensitive to *unexpected* motion of the target, arising either due to unexpected self-motion, or external motion of the target within an inertial reference frame. For the system to be sensitive to unexpected motion, an efference copy should be sent to both target tracking circuitry and in addition to LPTCs to cancel reafferent detection of target and background motion, respectively. Evidence for this will be experimentally challenging, requiring intracellular recordings from target tracking neurons in free flight when the animal is free to make volitional movements. However, it could be the case that free-flight saccades may result in subthreshold membrane potential changes similar to those observed by Kim et al. in LPTCs (Kim et al., 2015). It would be interesting to investigate whether such a signal is sent to the target tracking system under all conditions, or only when a target is actively attended to.

## **7.4 Drawbacks and limitations to functional interpretations**

The model presented in Figure 6.2 is relatively simplistic, describing lobula complex circuitry as representing image motion in a retinal frame of reference, and descending circuitry representing motion in an inertial frame of reference. This is certainly an over-simplification. Different subsets of target sensitive neurons in the lobula complex are differentially sensitive to background motion (Barnett et al., 2007). In hoverflies, subsets of STMDs are inhibited by concurrent background motion (Chapter 1, Section 1.3.3.1, Figure 1.16) (Barnett et al., 2007), and lobula columnar neurons sensitive to moving

objects in *Drosophila* exhibit a similar heterogeneity in the repressive effect of background motion (Chapter 1, Section 1.3.3.1, Figure 1.18) (Keleş et al., 2020; Staedele et al., 2020). It will be necessary to determine the presynaptic partners of TSDNs, and to measure their dependence on background motion to verify the model in Figure 6.2. Furthermore, in *Drosophila*, the inhibitory effect of concurrent background motion in object detecting lobula columnar neurons appears to be influenced by internal state, with disinhibition of target responses occurring under application of an octopamine agonist (Chapter 1, Section 1.3.3.1, Figure 1.16B-C) (Staedele et al., 2020). Octopamine is an insect analog of norepinephrine and a neuromodulator correlate for in-flight internal state (Cheng and Frye, 2020; Suver et al., 2012). All experiments in this thesis were performed on restrained, dissected animals. It is unknown to what extent TSDN receptive fields, latencies, and wide-field integration properties are influenced by internal state. It would be interesting to measure TSDN receptive fields in animals free to move. Experimentally tractable preparations include recordings under octopamine agonist application, or in tethered animals able to fly or walk. Whilst TSDNs are presumably involved in flight course correction, it could be the case that freedom to walk may adjust gains and frequency tuning of target tracking circuitry as is found in LPTCs (Longden et al., 2014). Indeed, the model in Chapter 5 and Figure 6.2 implies that target tracking circuitry matches internal state dependent changes in wide-field motion processing circuitry in order to maintain the representation of relative movement in TSDNs.

## 7.5 TSDN evolution

The preceding work illustrates the ubiquity of premotor descending neurons encoding object movement among fast flying insects specialised for tracking and chasing targets. Pterygota, the winged insects, represent a monophyletic lineage arising ~410 MYA and are comprised of three extant groups: Odonoptera (containing Odonata), Ephemeroptera (common name: mayflies), and Neoptera (including Diptera) (Grimaldi and Engel, 2005). The phylogeny of pterygota is contentious (Hovmoller et al., 2002), although recent evidence supports Odonoptera as basal to Ephemeroptera and Neoptera (Rutschmann et al., 2017). Odonoptera is comprised of three orders, of which Odonata contains the only surviving members, the damselflies and dragonflies. The similarity of damselfly and dragonfly TSDN receptive fields (Chapter 3) suggests this descending circuitry is homologous and highly conserved since divergence from the last common ancestor of these sister lineages ~270 MYA. Basal to Odonata are Geroptera and Protodonata, the latter of which, known as griffenflies, diverged from Odonata ~ 350 MYA. Whilst little is known about Geroptera, fossilised griffenflies are notable for their extraordinary size, reaching wingspans up to 70 cm, and possession of large toothed mandibles and spiny legs, which are indicative of predation. This implies a requirement for descending neurons to facilitate prey capture reaching at least ~350 MYA.

Of the remaining pterygota, Neoptera is unique for its extreme diversification relative to Odonatoptera and Ephemeroptera (Grimaldi and Engel, 2005; Wiegmann et al., 2011). Neoptera includes the vast majority of insects, including orthoptera (crickets), hemiptera (true bugs), hymenoptera (bees and ants), coleoptera (beetles), lepidoptera (butterflies and moths), and diptera (true flies). The directional selectivity of several dTSDN receptive field types in two dipteran predators, the robberfly *Holcocephala fusca* and the killerfly *Coenosia attenuata* (chapter 4) suggests a physiologically similar system to dragonfly TSDNs within Diptera. The similarity of hoverfly and robberfly dTSDN integration of small- and wide-field stimuli (Chapter 4) to that previously described in dragonfly TSDNs (Olberg, 1986) further suggests the physiological analogy of these neurons as a descending controller for small-object interception (Gonzalez-Bellido et al., 2013; Olberg, 1986).

In the absence of single neuron anatomical data, the present work is insufficient to determine whether the apparent functional analogy of dragonfly and dipteran TSDNs results from orthologous populations of neurons. The majority of dragonfly TSDNs arise from cell bodies positioned at the n-ventral surface of the central brain (Chapter 3) (Olberg, 1986). Both *Holcocephala* and *Coenosia* possess clusters of conspicuously enlarged descending neuron cell bodies in corresponding locations (Chapter 4). This cluster has previously been annotated in other neopterans including *Drosophila* (Hsu and Bhandawat, 2016; Namiki et al., 2018), crickets (Staudacher, 1998), and cockroaches (Okada et al., 2003), whilst other studies document visually responsive descending neurons with cell bodies at this location (Gronenberg and Strausfeld, 1991). Should future work discover that both dTSDNs and TSDNs arise from this ventral cell body cluster, this may suggest that an ancient and homologous descending neuron population coordinates object tracking across pterygota. This would imply this basal population of descending neurons also controls visually guided object tracking among species less-specialised for target tracking and pursuit, opening a fascinating avenue to investigate how selective pressures recruit and reshape existing circuitry.

In contrast with Neoptera, extant Ephemeroptera comprise little over 3,200 species (Barber-James et al., 2007) and are identifiable by their uniformity in body plan, life-cycle, and mating behaviour (Grimaldi and Engel, 2005). Interestingly, males across Ephemeroptera display intricate target tracking behaviour of female conspecifics throughout their brief adulthood. Imago males of several families of mayfly are renowned for their enlarged turbanate dorsal eyes specialised for tracking females from below (Horridge and McLean, 1978). These turbate eyes, in addition to the behavioural specialisation of tracking targets from below, thus appear to be functionally analogous, but evolutionarily convergent to the dragonfly dorsal fovea. Experiments investigating whether mayflies possess TSDNs similar to those described in damselflies (Chapter 3) and dragonflies (Frye and Olberg, 1995; Gonzalez-Bellido et al., 2013; Olberg, 1986) would provide a unique insight into the descending circuitry present in the last common ancestor of all flying insects.

## 7.6 Summary

The work in this thesis illustrates the ubiquity of target selective descending neurons (TSDNs) among flying insects. Whilst there are many similarities in the receptive field organisation of TSDNs in different species, such as directional selectivity for target motion, TSDNs appear to reflect upstream differences in ocular morphology, suggesting flexibility for the representations encoded among TSDNs. TSDNs are present in both predatory and non-predatory insects indicating that similar neuronal hardware is implemented in both chasing displays and interception. In contrast to previous interpretations, TSDNs appear to function within a control architecture that integrates optomotor stabilisation pathways with target tracking circuitry with the possibility that TSDNs encode target motion in an inertial frame of reference. However, interpretation of TSDN function, both within this thesis and throughout the published literature, is severely limited by an absence of data from freely behaving animals. It will be crucial to measure TSDN properties in actively moving animals to move forward our understanding of these neurons in the context of target pursuit.

# Bibliography

Ache, J.M., Polsky, J., Alghailani, S., Parekh, R., Breads, P., Peek, M.Y., Bock, D.D., von Reyn, C.R., and Card, G.M. (2019). Neural Basis for Looming Size and Velocity Encoding in the *Drosophila* Giant Fiber Escape Pathway. *Curr. Biol.* 29, 1073-1081.e4.

Adelman, T.L., Bialek, W., and Olberg, R.M. (2003). The Information Content of Receptive Fields. *Neuron* 40, 823–833.

Agi, E., Langen, M., Altschuler, S.J., Wu, L.F., Zimmermann, T., and Hiesinger, P.R. (2014). The evolution and development of neural superposition. *J. Neurogenet.* 28, 216–232.

Aptekar, J.W., Kele, M.F., Lu, P.M., Zolotova, N.M., and Frye, M.A. (2015). Neurons Forming Optic Glomeruli Compute Figure-Ground Discriminations in *Drosophila*. *J. Neurosci.* 35, 7587–7599.

Arendt, J., and Reznick, D. (2008). Convergence and parallelism reconsidered: what have we learned about the genetics of adaptation? *Trends Ecol. Evol.* 23, 26–32.

Arenz, A., Drews, M.S., Richter, F.G., Ammer, G., and Borst, A. (2017). The Temporal Tuning of the *Drosophila* Motion Detectors Is Determined by the Dynamics of Their Input Elements. *Curr. Biol.* 27, 929–944.

Bacon, J.P., and Strausfeld, N.J. (1986). The dipteran “Giant fibre” pathway: neurons and signals. *J. Comp. Physiol. A* 158, 529–548.

Bacon, J.P., Thompson, K.S., and Stern, M. (1995). Identified octopaminergic neurons provide an arousal mechanism in the locust brain. *J. Neurophysiol.* 74, 2739–2743.

Barber-James, H.M., Gattolliat, J.-L., Sartori, M., and Hubbard, M.D. (2007). Global diversity of mayflies (Ephemeroptera, Insecta) in freshwater. In *Freshwater Animal Diversity Assessment*, (Dordrecht: Springer Netherlands), pp. 339–350.

Barendregt, M., Harvey, B.M., Rokers, B., and Dumoulin, S.O. (2015). Transformation from a retinal to a cyclopean representation in human visual cortex. *Curr. Biol.* 25, 1982–1987.

Barnett, P.D., Nordström, K., and O’Carroll, D.C. (2007). Retinotopic Organization of Small-Field-Target-Detecting Neurons in the Insect Visual System. *Curr. Biol.* 17, 569–578.

Barrós-Pita, J.C., and Maldonado, H. (1970). A fovea in the praying mantis eye. *Z. Vgl. Physiol.* 67, 79–92.

Bautista-Martínez, N., Illescas-Riquelme, C.P., and García-Ávila, C. de J. (2017). First Report of “Hunter-Fly” *Coenosia attenuata* (Diptera: Muscidae) in Mexico. *Florida Entomol.* 100, 174–175.

- Bechly, G., Brauckmann, C., Zessin, W., and Groning, E. (2001). New results concerning the morphology of the most ancient dragonflies (Insecta: Odonatoptera) from the Namurian of Hagen-Vorhalle (Germany). *J. Zool. Syst. Evol. Res.* *39*, 209–226.
- Behnia, R., Clark, D.A., Carter, A.G., Clandinin, T.R., and Desplan, C. (2014). Processing properties of on and off pathways for *Drosophila* motion detection. *Nature* *512*, 427–430.
- Berens, P. (2009). CircStat : A MATLAB Toolbox for Circular Statistics. *J. Stat. Softw.* *31*, 1–21.
- Berry, R.P., Warrant, E.J., and Stange, G. (2007a). Form vision in the insect dorsal ocelli: An anatomical and optical analysis of the Locust Ocelli. *Vision Res.* *47*, 1382–1393.
- Berry, R.P., Stange, G., and Warrant, E.J. (2007b). Form vision in the insect dorsal ocelli: An anatomical and optical analysis of the dragonfly median ocellus. *Vision Res.* *47*, 1394–1409.
- Bidaye, S.S., Bockemühl, T., and Büschges, A. (2018). Six-legged walking in insects: how CPGs, peripheral feedback, and descending signals generate coordinated and adaptive motor rhythms. *J. Neurophysiol.* *119*, 459–475.
- Bishop, L.G., and Keehn, D.G. (1967). Neural correlates of the optomotor responses in the fly. *Kybernetik* *3*, 288–295.
- Blake, R., Martens, W., and Di Gianfilippo, A. (1980). Reaction time as a measure of binocular interaction in human vision. *Invest. Ophthalmol. Vis. Sci.* *19*, 930–941.
- Boeddeker, N., and Egelhaaf, M. (2005). A single control system for smooth and saccade-like pursuit in blowflies. *J. Exp. Biol.* *208*, 1563–1572.
- Boeddeker, N., Kern, R., and Egelhaaf, M. (2003). Chasing a dummy target: smooth pursuit and velocity control in male blowflies. *Proc. R. Soc. London. Ser. B Biol. Sci.* *270*, 393–399.
- Boergens, K.M., Kapfer, C., Helmstaedter, M., Denk, W., and Borst, A. (2018). Full reconstruction of large lobula plate tangential cells in *Drosophila* from a 3D EM dataset. *PLoS One* *13*, e0207828.
- Bolzon, D.M., Nordström, K., and O’Carroll, D.C. (2009). Local and large-range inhibition in feature detection. *J. Neurosci.* *29*, 14143–14150.
- Bomphrey, R.J., Nakata, T., Henningsson, P., and Lin, H.-T. (2016). Flight of the dragonflies and damselflies. *Philos. Trans. R. Soc. B Biol. Sci.* *371*, 20150389.
- Borst, A., and Egelhaaf, M. (1989). Principles of visual motion detection. *Trends Neurosci.* *12*, 297–306.
- Borst, A., and Haag, J. (2002). Neural networks in the cockpit of the fly. *J. Comp. Physiol. A Neuroethol. Sensory, Neural, Behav. Physiol.* *188*, 419–437.

- Borst, A., and Helmstaedter, M. (2015). Common circuit design in fly and mammalian motion vision. *Nat. Neurosci.* *18*, 1067–1076.
- Borst, A., Haag, J., and Reiff, D.F. (2010). Fly Motion Vision. *Annu. Rev. Neurosci.* *33*, 49–70.
- Boyan, G., Reichert, H., and Hirth, F. (2003). Commissure formation in the embryonic insect brain. *Arthropod Struct. Dev.* *32*, 61–77.
- Brighton, C.H., Thomas, A.L.R., and Taylor, G.K. (2017). Terminal attack trajectories of peregrine falcons are described by the proportional navigation guidance law of missiles. *Proc. Natl. Acad. Sci. U. S. A.* *114*, 13495–13500.
- Buschbeck, E.K., and Strausfeld, N.J. (1996). Visual motion-detection circuits in flies: small-field retinotopic elements responding to motion are evolutionarily conserved across taxa. *J. Neurosci.* *16*, 4563–4578.
- Buschbeck, E.K., and Strausfeld, N.J. (1997). The relevance of neural architecture to visual performance: Phylogenetic conservation and variation in dipteran visual systems. *J. Comp. Neurol.* *383*, 282–304.
- Butler, A.B., and Hodos, W. (2005). Evolution and Variation. In *Comparative Vertebrate Neuroanatomy*, (Hoboken, NJ, USA: John Wiley & Sons, Inc.), pp. 1–17.
- Butler, A.B., and Saidel, W.M. (2000). Defining sameness: historical, biological, and generative homology. *BioEssays* *22*, 846–853.
- Butts, D.A., and Goldman, M.S. (2006). Tuning Curves, Neuronal Variability, and Sensory Coding. *PLoS Biol.* *4*, e92.
- Bybee, S., Córdoba-Aguilar, A., Duryea, M.C., Futahashi, R., Hansson, B., Lorenzo-Carballea, M.O., Schilder, R., Stoks, R., Suvorov, A., Svensson, E.I., et al. (2016). Odonata (dragonflies and damselflies) as a bridge between ecology and evolutionary genomics. *Front. Zool.* *13*, 46.
- Campbell, F.W., and Green, D.G. (1965). Monocular versus Binocular Visual Acuity. *Nature* *208*, 191–192.
- Cheng, K.Y., and Frye, M.A. (2020). Neuromodulation of insect motion vision. *J. Comp. Physiol. A Neuroethol. Sensory, Neural, Behav. Physiol.* *206*, 125–137.
- Cogshall, J.C., Boschek, C.B., and Buchner, S.M. (1973). Preliminary Investigations on a Pair of Giant Fibers in the Central Nervous System of Dipteran Flies. *Zeitschrift Fur Naturforsch. - Sect. C J. Biosci.* *28*, 783-784b.
- Collett, T.S. (1980). Angular tracking and the optomotor response an analysis of visual reflex

interaction in a hoverfly. *J. Comp. Physiol. A* *140*, 145–158.

Collett, T.S., and Land, M.F. (1975). Visual control of flight behaviour in the hoverfly *Syrirta pipiens* L. *J. Comp. Physiol. A* *99*, 1–66.

Collett, T.S., and Land, M.F. (1978). How hoverflies compute interception courses. *J. Comp. Physiol. A* *125*, 191–204.

Corbet, P.S. (1999). *Dragonflies: Behaviour and Ecology of Odonata* (Cornell University Press).

Crapse, T.B., and Sommer, M.A. (2008). Corollary discharge across the animal kingdom. *Nat. Rev. Neurosci.* *9*, 587–600.

DeVoe, R.D., Kaiser, W., Ohm, J., and Stone, L.S. (1982). Horizontal movement detectors of honeybees: Directionally-selective visual neurons in the lobula and brain. *J. Comp. Physiol. A* *147*, 155–170.

Duchâteau, G., Florkin, M., and Leclercq, J. (1953). Concentrations des bases fixes et types de composition de la base totale de l'hémolymphe des insectes. *Arch. Physiol. Biochem.* *61*, 518–549.

Dunbier, J.R., Wiederman, S.D., Shoemaker, P.A., and O'Carroll, D.C. (2012). Facilitation of dragonfly target-detecting neurons by slow moving features on continuous paths. *Front. Neural Circuits* *6*, 1–29.

Dyakova, O., and Nordström, K. (2017). Image statistics and their processing in insect vision. *Curr. Opin. Insect Sci.* *24*, 7–14.

Dyakova, O., Lee, Y.-J., Longden, K.D., Kiselev, V.G., and Nordström, K. (2015). A higher order visual neuron tuned to the spatial amplitude spectra of natural scenes. *Nat. Commun.* *6*, 8522.

Elberger, A.J. (1989). Binocularity and single cell acuity are related in striate cortex of corpus callosum sectioned and normal cats. *Exp. Brain Res.* *77*, 213–216.

Evans, B.J.E., O'Carroll, D.C., Fabian, J.M., and Wiederman, S.D. (2019). Differential Tuning to Visual Motion Allows Robust Encoding of Optic Flow in the Dragonfly. *J. Neurosci.* *39*, 8051–8063.

Fabian, J.M., Jundi, B. el, Wiederman, S.D., O'Carroll, D.C., El Jundi, B., Wiederman, S.D., and O'carroll, D.C. (2020). The complex optic lobe of dragonflies. *BioRxiv* 2020.05.10.087437.

Fabian, S.T., Sumner, M.E., Wardill, T.J., Rossoni, S., and Gonzalez-Bellido, P.T. (2018). Interception by two predatory fly species is explained by a proportional navigation feedback controller. *J. R. Soc. Interface* *15*, 20180466.

Farrow, K., Haag, J., and Borst, A. (2006). Nonlinear, binocular interactions underlying flow field selectivity of a motion-sensitive neuron. *Nat. Neurosci.* *9*, 1312–1320.

- Franz, M.O., and Krapp, H.G. (2000). Wide-field, motion-sensitive neurons and matched filters for optic flow fields. *Biol. Cybern.* 83, 185–197.
- Frye, M.A., and Olberg, R.M. (1995). Visual receptive field properties of feature detecting neurons in the dragonfly. *J. Comp. Physiol. A* 177, 569–576.
- Geiger, G., and Nässel, D.R. (1981). Visual orientation behaviour of flies after selective laser beam ablation of interneurons. *Nature* 293, 398–399.
- Gengs, C., Leung, H.T., Skingsley, D.R., Iovchev, M.I., Yin, Z., Semenov, E.P., Burg, M.G., Hardie, R.C., and Pak, W.L. (2002). The target of *Drosophila* photoreceptor synaptic transmission is a histamine-gated chloride channel encoded by *ort* (*hclA*). *J. Biol. Chem.* 277, 42113–42120.
- Geurten, B.R.H., Nordström, K., Sprayberry, J.D.H., Bolzon, D.M., and O’Carroll, D.C. (2007a). Neural mechanisms underlying target detection in a dragonfly centrifugal neuron. *J. Exp. Biol.* 210, 3277–3284.
- Geurten, B.R.H., Nordström, K., Sprayberry, J.D.H., Bolzon, D.M., and O’Carroll, D.C. (2007b). Neural mechanisms underlying target detection in a dragonfly centrifugal neuron. *J. Exp. Biol.* 210, 3277–3284.
- Gilbert, C., and Strausfeld, N.J. (1991). The functional organization of male-specific visual neurons in flies. *J. Comp. Physiol. A* 169, 395–411.
- Gilbert, C., and Strausfeld, N.J. (1992). Small-field neurons associated with oculomotor and optomotor control in muscoid flies: Functional organization. *J. Comp. Neurol.* 316, 72–86.
- Golowasch, J., Casey, M., Abbott, L.F., and Marder, E. (1999). Network Stability from Activity-Dependent Regulation of Neuronal Conductances. *Neural Comput.* 11, 1079–1096.
- Gonzalez-Bellido, P.T., and Wardill, T.J. (2012). Labeling and Confocal Imaging of Neurons in Thick Invertebrate Tissue Samples. *Cold Spring Harb. Protoc.* 2012, pdb.prot069625-pdb.prot069625.
- Gonzalez-Bellido, P.T., Wardill, T.J., and Juusola, M. (2011). Compound eyes and retinal information processing in miniature dipteran species match their specific ecological demands. *Proc. Natl. Acad. Sci. U. S. A.* 108, 4224–4229.
- Gonzalez-Bellido, P.T., Peng, H., Yang, J., Georgopoulos, A.P., and Olberg, R.M. (2013). Eight pairs of descending visual neurons in the dragonfly give wing motor centers accurate population vector of prey direction. *Proc. Natl. Acad. Sci.* 110, 696–701.
- Gonzalez-Bellido, P.T., Fabian, S.T., and Nordström, K. (2016). Target detection in insects: optical, neural and behavioral optimizations. *Curr. Opin. Neurobiol.* 41, 122–128.

- Goodman, L.J., Fletcher, W.A., Guy, R.G., Mobbs, P.G., and Pomfrett, C.D.J. (1987). Motion Sensitive Descending Interneurons, Ocellar LD Neurons and Neck Motoneurons in the Bee: A Neural Substrate for Visual Course Control in *Apis mellifera*. In *Neurobiology and Behavior of Honeybees*, (Springer Berlin Heidelberg), pp. 158–171.
- Gray, J.R. (2005). Habituated visual neurons in locusts remain sensitive to novel looming objects. *J. Exp. Biol.* *208*, 2515–2532.
- Greiner, B. (2006). Adaptations for Nocturnal Vision in Insect Apposition Eyes. *Int. Rev. Cytol.* *250*, 1–46.
- Grimaldi, D.A., and Engel, M.S. (2005). *Evolution of the insects* (Cambridge University Press).
- Griss, C., and Rowell, C.H.F. (1986). Three descending interneurons reporting deviation from course in the locust - I. Anatomy. *J. Comp. Physiol. A Sensory, Neural, Behav. Physiol.* *158*, 765–774.
- Gronenberg, W., and Strausfeld, N.J. (1990). Descending neurons supplying the neck and flight motor of Diptera: Physiological and anatomical characteristics. *J. Comp. Neurol.* *302*, 973–991.
- Gronenberg, W., and Strausfeld, N.J. (1991). Descending pathways connecting the male-specific visual system of flies to the neck and flight motor. *J. Comp. Physiol. A* *169*, 413–426.
- Gronenberg, W., and Strausfeld, N.J. (1992). Premotor descending neurons responding selectively to local visual stimuli in flies. *J. Comp. Neurol.* *316*, 87–103.
- Gronenberg, W., Milde, J.J., and Strausfeld, N.J. (1995). Oculomotor control in calliphorid flies: Organization of descending neurons to neck motor neurons responding to visual stimuli. *J. Comp. Neurol.* *361*, 267–284.
- Haag, J., and Borst, A. (2001). Recurrent network interactions underlying flow-field selectivity of visual interneurons. *J. Neurosci.* *21*, 5685–5692.
- Haag, J., and Borst, A. (2004). Neural mechanism underlying complex receptive field properties of motion-sensitive interneurons. *Nat. Neurosci.* *7*, 628–634.
- Haag, J., and Borst, A. (2008). Electrical coupling of lobula plate tangential cells to a heterolateral motion-sensitive neuron in the fly. *J. Neurosci.* *28*, 14435–14442.
- Haag, J., Wertz, A., and Borst, A. (2007). Integration of Lobula Plate Output Signals by DNOVS1, an Identified Premotor Descending Neuron. *J. Neurosci.* *27*, 1992–2000.
- Haikala, V., Joesch, M., Borst, A., and Mauss, A.S. (2013). Optogenetic control of fly optomotor responses. *J. Neurosci.* *33*, 13927–13934.
- Hardcastle, B.J., and Krapp, H.G. (2016). Evolution of Biological Image Stabilization. *Curr. Biol.* *26*,

R1010–R1021.

Hardie, R.C. (1985). *Functional Organization of the Fly Retina*. (Springer, Berlin, Heidelberg), pp. 1–79.

Hardie, R.C. (2012). Polarization vision: *Drosophila* enters the arena. *Curr. Biol.* 22, R12–R14.

Hardie, R.C., and Juusola, M. (2015). Phototransduction in *Drosophila*. *Curr. Opin. Neurobiol.* 34, 37–45.

van Hateren, J.H. (1992). Real and optimal neural images in early vision. *Nature* 360, 68–70.

Hausen, K. (1982a). Motion sensitive interneurons in the optomotor system of the fly. *Biol. Cybern.* 45, 143–156.

Hausen, K. (1982b). Motion sensitive interneurons in the optomotor system of the fly - II. The horizontal cells: Receptive field organization and response characteristics. *Biol. Cybern.* 46, 67–79.

Hausen, K. (1984). The Lobula-Complex of the Fly: Structure, Function and Significance in Visual Behaviour. In *Photoreception and Vision in Invertebrates*, (Springer US), pp. 523–559.

Heinrich, R. (2002). Impact of descending brain neurons on the control of stridulation, walking, and flight in orthoptera. *Microsc. Res. Tech.* 56, 292–301.

Heisenberg, M., Wonneberger, R., and Wolf, R. (1978). Optomotor-blindH31-a *Drosophila* mutant of the lobula plate giant neurons. *J. Comp. Physiol. A* 124, 287–296.

Held, D., Thrun, S., and Savarese, S. (2016). Learning to Track at 100 FPS with Deep Regression Networks. (Springer, Cham), pp. 749–765.

van Hemmen, J.L., and Schwartz, A.B. (2008). Population vector code: a geometric universal as actuator. *Biol. Cybern.* 98, 509–518.

Hengstenberg, R. (1993). Multisensory control in insect oculomotor systems. *Rev. Oculomot. Res.* 5, 285–298.

Hengstenberg, R., Hausen, K., and Hengstenberg, B. (1982). The number and structure of giant vertical cells (VS) in the lobula plate of the blowfly *Calliphora erythrocephala*. *J. Comp. Physiol. A* 149, 163–177.

Hennig, P., Kern, R., and Egelhaaf, M. (2011). Binocular Integration of Visual Information: A Model Study on Naturalistic Optic Flow Processing. *Front. Neural Circuits* 5, 4.

Horridge, G.A. (1977a). Insects which turn and look. *Endeavour* 1, 7–17.

Horridge, G.A. (1977b). The Compound Eye of Insects. 237, 108–121.

- HorrIDGE, G.A. (1978). The separation of visual axes in apposition compound eyes. *Philos. Trans. R. Soc. Lond. B. Biol. Sci.* 285, 1–59.
- HorrIDGE, G.A., and McLean, M. (1978). The dorsal eye of the mayfly *Atalophlebia* (Ephemeroptera). *Proc. R. Soc. London. Ser. B. Biol. Sci.* 200, 137–150.
- HorrIDGE, G.A., Wang, X., and Zhang, S.W. (1990). Colour inputs to motion and object vision in an insect. *Philos. Trans. R. Soc. London. Ser. B Biol. Sci.* 329, 257–263.
- Horstmann, W., Egelhaaf, M., and Warzecha, A.-K. (2000). Synaptic interactions increase optic flow specificity. *Eur. J. Neurosci.* 12, 2157–2165.
- Hovmoller, R., Pape, T., and Kallersjo, M. (2002). The Palaeoptera Problem: Basal Pterygote Phylogeny Inferred from 18S and 28S rDNA Sequences. *Cladistics* 18, 313–323.
- Hsu, C.T., and Bhandawat, V. (2016). Organization of descending neurons in *Drosophila melanogaster*. *Sci. Rep.* 6, 20259.
- Huston, S.J., Krapp, H.G., Egelhaaf, M., Lindemann, J., and Egelhaaf, M. (2008). Visuomotor Transformation in the Fly Gaze Stabilization System. *PLoS Biol.* 6, e173.
- Ibbotson, M.R. (1991a). Wide-field motion-sensitive neurons tuned to horizontal movement in the honeybee, *Apis mellifera*. *J. Comp. Physiol. A* 168, 91–102.
- Ibbotson, M.R. (1991b). A motion-sensitive visual descending neurone in *Apis mellifera* monitoring translatory optic flow-fields in the horizontal plane. *J. Exp. Biol.* 157, 573–577.
- Ibbotson, M.R., and Goodman, L.J. (1990). Response characteristics of four wide-field motion-sensitive descending interneurons in *Apis mellifera*. *J. Exp. Biol.* 148, 255–279.
- Ibbotson, M.R., Hung, Y.S., Meffin, H., Boeddeker, N., and Srinivasan, M. V. (2017). Neural basis of forward flight control and landing in honeybees. *Sci. Rep.* 7.
- Ichikawa, T. (1994). Motion-sensitive cells: Putative larval neurones incorporated into the optic lobe of the adult swallowtail butterfly. *J. Exp. Biol.* 195, 361–380.
- IngleY, S.J., Bybee, S.M., Tennessen, K.J., Whiting, M.F., and Branham, M.A. (2012). Life on the fly: Phylogenetics and evolution of the helicopter damselflies (Odonata, Pseudostigmatidae). *Zool. Scr.* 41, 637–650.
- Ito, K., Shinomiya, K., Ito, M., Armstrong, J.D., Boyan, G., Hartenstein, V., Harzsch, S., Heisenberg, M., Homberg, U., Jenett, A., et al. (2014). A Systematic Nomenclature for the Insect Brain. *Neuron* 81, 755–765.
- Kanzaki, R., Soo, K., Seki, Y., and Wada, S. (2003). Projections to Higher Olfactory Centers from

Subdivisions of the Antennal Lobe Macroglomerular Complex of the Male Silkworm. *Chem. Senses* 28, 113–130.

Keeley, B.L. (2000). Neuroethology and the Philosophy of Cognitive Science. *Philos. Sci.* 67.

Keleş, M., and Frye, M.A. (2017a). Visual behavior: The eyes have it. *Elife* 6.

Keleş, M.F., and Frye, M.A. (2017b). Object-Detecting Neurons in *Drosophila*. *Curr. Biol.* 27, 680–687.

Keleş, M.F., Hardcastle, B.J., Städele, C., Xiao, Q., and Frye, M.A. (2020). Inhibitory Interactions and Columnar Inputs to an Object Motion Detector in *Drosophila*. *Cell Rep.* 30, 2115-2124.e5.

Kern, R. (1998). Visual position stabilization in the hummingbird hawk moth, *Macroglossum stellatarum* L. II. Electrophysiological analysis of neurons sensitive to wide-field image motion. *J. Comp. Physiol. - A Sensory, Neural, Behav. Physiol.* 182, 239–249.

Kien, J. (1974). Sensory integration in the locust optomotor system-II: Direction selective neurons in the circumoesophageal connectives and the optic lobe. *Vision Res.* 14, 1255–1268.

Kim, A.J., Fitzgerald, J.K., and Maimon, G. (2015). Cellular evidence for efference copy in *Drosophila* visuomotor processing. *Nat. Neurosci.* 18, 1247–1255.

Klink, P.C., Brascamp, J.W., Blake, R., and van Wezel, R.J.A. (2010). Experience-driven plasticity in binocular vision. *Curr. Biol.* 20, 1464–1469.

Krapp, H.G. (2010). Sensorimotor Transformation: From Visual Responses to Motor Commands. *Curr. Biol.* 20, R236–R239.

Krapp, H.G. (2014). Flies, optic flow and multisensory stabilization reflexes. In *Flow Sensing in Air and Water: Behavioral, Neural and Engineering Principles of Operation*, (Springer Berlin Heidelberg), pp. 215–243.

Krapp, H.G. (2015). How a fly escapes the reflex trap. *Nat. Neurosci.* 18, 1192–1194.

Krapp, H.G., and Hengstenberg, R. (1996). Estimation of self-motion by optic flow processing in single visual interneurons. *Nature* 384, 463–466.

Krapp, H.G., and Wicklein, M. (2008). Central Processing of Visual Information in Insects. In *The Senses: A Comprehensive Reference*, (Elsevier Inc.), pp. 131–203.

Krapp, H.G., Hengstenberg, B., and Hengstenberg, R. (1998). Dendritic Structure and Receptive-Field Organization of Optic Flow Processing Interneurons in the Fly. *J. Neurophysiol.* 79, 1902–1917.

Krapp, H.G., Hengstenberg, R., and Egelhaaf, M. (2001). Binocular contributions to optic flow

- processing in the fly visual system. *J. Neurophysiol.* 85, 724–734.
- Krasne, F.B., and Teshiba, T.M. (1995). Habituation of an invertebrate escape reflex due to modulation by higher centers rather than local events. *Proc. Natl. Acad. Sci. U. S. A.* 92, 3362–3366.
- Labhart, T., and Nilsson, D.E. (1995). The dorsal eye of the dragonfly *Sympetrum*: specializations for prey detection against the blue sky. *J. Comp. Physiol. A* 176, 437–453.
- Lancer, B.H., Evans, B.J.E., Fabian, J.M., O’Carroll, D.C., and Wiederman, S.D. (2019). A Target-Detecting Visual Neuron in the Dragonfly Locks on to Selectively Attended Targets. *J. Neurosci.* 39, 8497–8509.
- Land, M.F. (1989). Variations in the Structure and Design of Compound Eyes. In *Facets of Vision*, (Springer Berlin Heidelberg), pp. 90–111.
- Land, M.F. (1992). Visual tracking and pursuit: Humans and arthropods compared. *J. Insect Physiol.* 38, 939–951.
- Land, M.F. (1993). Chasing and pursuit in the dolichopodid fly *Poecilobothrus nobilitatus*. *J. Comp. Physiol. A* 173, 605–613.
- Land, M.F. (1997). Visual acuity in insects. *Annu. Rev. Entomol. Vol. 42* 42, 147–177.
- Land, M.F., and Collett, T.S. (1974). Chasing behaviour of houseflies (*Fannia canicularis*) - A description and analysis. *J. Comp. Physiol.* 89, 331–357.
- Land, M.F., and Eckert, H. (1985). Maps of the acute zones of fly eyes. *J. Comp. Physiol. A* 156, 525–538.
- Land, M.F., and Nilsson, D.-E. (2007). *Animal Eyes* (Oxford University Press).
- Laughlin, S., and McGinness, S. (1978). The structures of dorsal and ventral regions of a dragonfly retina. *Cell Tissue Res.* 188, 427–447.
- Lin, H.T., and Leonardo, A. (2017). Heuristic Rules Underlying Dragonfly Prey Selection and Interception. *Curr. Biol.* 27, 1124–1137.
- Longden, K.D., and Krapp, H.G. (2010). Octopaminergic modulation of temporal frequency coding in an identified optic flow-processing interneuron. *Front. Syst. Neurosci.* 4.
- Longden, K.D., Muzzu, T., Cook, D.J., Schultz, S.R., and Krapp, H.G. (2014). Nutritional state modulates the neural processing of visual motion. *Curr. Biol.* 24, 890–895.
- Lythgoe, J.N. (1979). *Ecology of Vision* (Oxford University Press).
- Ma, C., Huang, J.-B., Yang, X., and Yang, M.-H. (2015). Hierarchical Convolutional Features for

Visual Tracking. In 2015 IEEE International Conference on Computer Vision (ICCV), (IEEE), pp. 3074–3082.

Mahato, S., Nie, J., Plachetzki, D.C., and Zelhof, A.C. (2018). A mosaic of independent innovations involving eyes shut are critical for the evolutionary transition from fused to open rhabdoms. *Dev. Biol.* 443, 188–202.

Maisak, M.S., Haag, J., Ammer, G., Serbe, E., Meier, M., Leonhardt, A., Schilling, T., Bahl, A., Rubin, G.M., Nern, A., et al. (2013). A directional tuning map of *Drosophila* elementary motion detectors. *Nature* 500, 212–216.

Marder, E., and Goaillard, J.-M. (2006). Variability, compensation and homeostasis in neuron and network function. *Nat. Rev. Neurosci.* 7, 563–574.

Meyer, E.P., and Labhart, T. (1993). Morphological specializations of dorsal rim ommatidia in the compound eye of dragonflies and damselflies (Odonata). *Cell Tissue Res.* 272, 17–22.

Milde, J.J., and Strausfeld, N.J. (1990). Cluster organization and response characteristics of the giant fiber pathway of the blowfly *Calliphora erythrocephala*. *J. Comp. Neurol.* 294, 59–75.

Milde, J.J., Seyan, H.S., and Strausfeld, N.J. (1987). The neck motor system of the fly *Calliphora erythrocephala*. *J. Comp. Physiol. A* 160, 225–238.

Mischiati, M., Lin, H.-T., Herold, P., Imler, E., Olberg, R., and Leonardo, A. (2015). Internal models direct dragonfly interception steering. *Nature* 517, 333–338.

Mohamed, M.A., Boddeker, C., and Mertsching, B. (2014). Real-time moving objects tracking for mobile-robots using motion information. In 2014 IEEE International Symposium on Safety, Security, and Rescue Robotics (2014), (IEEE), pp. 1–6.

Morimoto, M.M., Nern, A., Zhao, A., Rogers, E.M., Wong, A.M., Isaacson, M.D., Bock, D.D., Rubin, G.M., and Reiser, M.B. (2020). Connectivity establishes spatial readout of visual looming in a glomerulus lacking retinotopy. *BioRxiv* 2020.04.19.036947.

Mu, L., Ito, K., Bacon, J.P., and Strausfeld, N.J. (2012). Optic glomeruli and their inputs in *Drosophila* share an organizational ground pattern with the antennal lobes. *J. Neurosci.* 32, 6061–6071.

Namiki, S., Dickinson, M.H., Wong, A.M., Korff, W., and Card, G.M. (2018). The functional organization of descending sensory-motor pathways in *Drosophila*. *Elife* 7.

Nel, A., Prokop, J., Pecharová, M., Engel, M.S., and Garrouste, R. (2018). Palaeozoic giant dragonflies were hawkler predators. *Sci. Rep.* 8, 12141.

Nicholas, S., Supple, J., Leibbrandt, R., Gonzalez-Bellido, P.T., and Nordström, K. (2018a). Integration

of Small- and Wide-Field Visual Features in Target-Selective Descending Neurons of both Predatory and Nonpredatory Dipterans. *J. Neurosci.* 38, 10725–10733.

Nicholas, S., Thyselius, M., Holden, M., and Nordström, K. (2018b). Rearing and Long-Term Maintenance of *Eristalis tenax* Hoverflies for Research Studies. *J. Vis. Exp.* e57711.

Nicholas, S., Leibbrandt, R., and Nordström, K. (2020). Visual motion sensitivity in descending neurons in the hoverfly. *J. Comp. Physiol. A Neuroethol. Sensory, Neural, Behav. Physiol.* 206, 149–163.

Nityananda, V., and Read, J.C.A. (2017). Stereopsis in animals: evolution, function and mechanisms. *J. Exp. Biol.* 220, 2502–2512.

Nityananda, V., Tarawneh, G., Rosner, R., Nicolas, J., Crichton, S., and Read, J. (2016). Insect stereopsis demonstrated using a 3D insect cinema. *Sci. Rep.* 6, 18718.

Niven, J.E., Graham, C.M., and Burrows, M. (2008). Diversity and Evolution of the Insect Ventral Nerve Cord. *Annu. Rev. Entomol.* 53, 253–271.

Nordström, K. (2012). Neural specializations for small target detection in insects. *Curr. Opin. Neurobiol.* 22, 272–278.

Nordström, K., and O’Carroll, D.C. (2006). Small object detection neurons in female hoverflies. *Proceedings. Biol. Sci.* 273, 1211–1216.

Nordström, K., and O’Carroll, D.C. (2009). Feature detection and the hypercomplex property in insects. *Trends Neurosci.* 32, 383–391.

Nordström, K., Barnett, P.D., and O’Carroll, D.C. (2006). Insect detection of small targets moving in visual clutter. *PLoS Biol.* 4, 0378–0386.

Nordström, K., Bolzon, D.M., and O’Carroll, D.C. (2011). Spatial facilitation by a high-performance dragonfly target-detecting neuron. *Biol. Lett.* 7, 588–592.

O’Carroll, D. (1993). Feature-detecting neurons in dragonflies. *Nature* 362, 541–543.

O’Carroll, D.C., Bidwell, N.J., Laughlin, S.B., and Warrant, E.J. (1996). Insect motion detectors matched to visual ecology. *Nature* 382, 63–66.

O’Carroll, D.C., Laughlin, S.B., Bidwell, N.J., and Harris, R.A. (1997). Spatio-temporal properties of motion detectors matched to low image velocities in hovering insects. *Vision Res.* 37, 3427–3439.

Okada, R., Sakura, M., and Mizunami, M. (2003). Distribution of dendrites of descending neurons and its implications for the basic organization of the cockroach brain. *J. Comp. Neurol.* 458, 158–174.

- Olberg, R.C. (1978). Visual and multimodal interneurons in dragonflies. PhD Thesis, Univ. Washingt.
- Olberg, R.M. (1981a). Object- and self-movement detectors in the ventral nerve cord of the dragonfly. *J. Comp. Physiol. A* *141*, 327–334.
- Olberg, R.M. (1981b). Parallel Encoding of Direction of Wind, Head, Abdomen, and Visual Pattern Movement by Single Interneurons in the Dragonfly. *J Comp Physiol J. Comp. Physiol.* *142*, 27–41.
- Olberg, R.M. (1983). Identified interneurons steer flight in the dragonfly. *Soc. Neurosci. Abstr.* *9*,326.
- Olberg, R.M. (1986). Identified target-selective visual interneurons descending from the dragonfly brain. *J. Comp. Physiol. A* *159*, 827–840.
- Olberg, R.M. (2010). Insect Optic Glomeruli: Exploration of a Universal Circuit for Sensorimotor Processing.
- Olberg, R.M. (2012). Visual control of prey-capture flight in dragonflies. *Curr. Opin. Neurobiol.* *22*, 267–271.
- Olberg, R., and Pinter, R. (1990). The effect of mean luminance on the size selectivity of identified target interneurons in the dragonfly. *J. Comp. Physiol. A* *166*, 851–856.
- Olberg, R.M., and Willis, M.A. (1990). Pheromone-modulated optomotor response in male gypsy moths, *Lymantria dispar* L.: Directionally selective visual interneurons in the ventral nerve cord. *J. Comp. Physiol. A* *167*, 707–714.
- Olberg, R.M., Worthington, A.H., and Venator, K.R. (2000). Prey pursuit and interception in dragonflies. *J. Comp. Physiol. - A Sensory, Neural, Behav. Physiol.* *186*, 155–162.
- Olberg, R.M., Seaman, R.C., Coats, M.I., and Henry, A.F. (2007). Eye movements and target fixation during dragonfly prey-interception flights. *J. Comp. Physiol. A Neuroethol. Sensory, Neural, Behav. Physiol.* *193*, 685–693.
- Osorio, D. (2007). Spam and the evolution of the fly's eye. *BioEssays* *29*, 111–115.
- Parsons, M.M., Krapp, H.G., and Laughlin, S.B. (2010). Sensor Fusion in Identified Visual Interneurons. *Curr. Biol.* *20*, 624–628.
- Peek, M.Y., and Card, G.M. (2016). Comparative approaches to escape. *Curr. Opin. Neurobiol.* *41*, 167–173.
- Peng, H., Ruan, Z., Long, F., Simpson, J.H., and Myers, E.W. (2010). V3D enables real-time 3D visualization and quantitative analysis of large-scale biological image data sets. *Nat. Biotechnol.* *28*, 348–353.

- Perge, J.A., Niven, J.E., Mugnaini, E., Balasubramanian, V., and Sterling, P. (2012). Why Do Axons Differ in Caliber? *J. Neurosci.* 32.
- Perry, M.W., and Desplan, C. (2016). Love spots. *Curr. Biol.* 26, R484–R485.
- Preibisch, S., Saalfeld, S., and Tomancak, P. (2009). Globally optimal stitching of tiled 3D microscopic image acquisitions. *Bioinformatics* 25, 1463–1465.
- Rajashekhar, K.P., and Shamprasad, V.R. (2004). Golgi analysis of tangential neurons in the lobula plate of *Drosophila melanogaster*. *J. Biosci.* 29, 93–104.
- Rebora, M., Dell’Otto, A., Rybak, J., Piersanti, S., Gaino, E., and Hansson, B.S. (2013). The antennal lobe of *Libellula depressa* (Odonata, Libellulidae). *Zoology* 116, 205–214.
- Rey, H.G., Pedreira, C., and Quiñero, R. (2015). Past, present and future of spike sorting techniques. *Brain Res. Bull.* 119, 106–117.
- von Reyn, C.R., Breads, P., Peek, M.Y., Zheng, G.Z., Williamson, W.R., Yee, A.L., Leonardo, A., and Card, G.M. (2014). A spike-timing mechanism for action selection. *Nat. Neurosci.* 17, 962–970.
- von Reyn, C.R., Nern, A., Williamson, W.R., Breads, P., Wu, M., Namiki, S., and Card, G.M. (2017). Feature Integration Drives Probabilistic Behavior in the *Drosophila* Escape Response. *Neuron* 94, 1190–1204.e6.
- Rind, C.F. (1990). Identification of directionally selective motion-detecting neurones in the locust lobula and their synaptic connections with an identified descending neurone. *J. Exp. Biol.* 149, 21–43.
- Rosner, R., Hadeln, J. von, Tarawneh, G., and Read, J. (2018). The neuronal basis of insect stereopsis. *BioRxiv* 395939.
- Rosner, R., von Hadeln, J., Tarawneh, G., and Read, J.C.A. (2019). A neuronal correlate of insect stereopsis. *Nat. Commun.* 10, 2845.
- Rowell, C.H.F., and Reichert, H. (1986). Three descending interneurons reporting deviation from course in the locust - II. Physiology. *J. Comp. Physiol. A Sensory, Neural, Behav. Physiol.* 158, 775–794.
- Rüppell, G. (1999). Prey capture flight of *Calopteryx haemorrhoidalis* (Vander Linden) (Zygoptera: Calopterygidae). *Int. J. Odonatol.* 2, 123–131.
- Rutschmann, S., Chen, P., Zhou, C., and Monaghan, M.T. (2017). Mitochondrial genomes infer phylogenetic relationships among the oldest extant winged insects (Palaeoptera). *BioRxiv* 164459.
- Scarano, F., Sztarker, J., Medan, V., Berón de Astrada, M., and Tomsic, D. (2018). Binocular neuronal processing of object motion in an arthropod. *J. Neurosci.* 38, 6933–6948.

- Schindelin, J., Arganda-Carreras, I., Frise, E., Kaynig, V., Longair, M., Pietzsch, T., Preibisch, S., Rueden, C., Saalfeld, S., Schmid, B., et al. (2012). Fiji: an open-source platform for biological-image analysis. *Nat. Methods* 9, 676–682.
- Schnaitmann, C., Haikala, V., Abraham, E., Oberhauser, V., Thestrup, T., Griesbeck, O., and Reiff, D.F. (2018). Color Processing in the Early Visual System of *Drosophila*. *Cell* 172, 318–330.e18.
- Schnaitmann, C., Pagni, M., and Reiff, D.F. (2020). Color vision in insects: insights from *Drosophila*. *J. Comp. Physiol. A Neuroethol. Sensory, Neural, Behav. Physiol.* 206, 183–198.
- Seifert, P., and Smola, U. (1990). Adaptive structural changes indicate an evolutionary progression towards the open rhabdom in diptera. *J. Evol. Biol.* 3, 225–242.
- Shinomiya, K., Karuppudurai, T., Lin, T.Y., Lu, Z., Lee, C.H., and Meinertzhagen, I.A. (2014). Candidate neural substrates for off-edge motion detection in *drosophila*. *Curr. Biol.* 24, 1062–1070.
- Shinomiya, K., Huang, G., Lu, Z., Parag, T., Xu, C.S., Aniceto, R., Ansari, N., Cheatham, N., Lauchie, S., Neace, E., et al. (2019). Comparisons between the ON- and OFF-edge motion pathways in the *Drosophila* brain. *Elife* 8.
- Singarajah, K. V. (1988). Spectral sensitivity of motion-sensitive units of the butterfly ventral nerve cord. *J. Insect Physiol.* 34, 1005–1012.
- Smarandache-Wellmann, C.R., Arendt, D., Nübler-Jung, K., Burrows, M., Büschges, A., Wolf, H., Büschges, A., Scholz, H., Manira, A. El, Elson, R.C., et al. (2016). Arthropod neurons and nervous system. *Curr. Biol.* 26, R960–R965.
- Song, Z., and Juusola, M. (2014). Refractory Sampling Links Efficiency and Costs of Sensory Encoding to Stimulus Statistics. *J. Neurosci.* 34, 7216–7237.
- Sorokina, V.S. (2014). On the taxonomy of the Genus *Coenosia* Meigen, 1826 (Diptera, Muscidae) in the Russian Fauna, with a Description of *Coenosia tschernovi* sp. n. *Entomol. Rev.* 94, 630–638.
- Staedele, C., Keles, M., Mongeau, J.-M., and Frye, M.A. (2020). Fly Feature Detectors Show Contrast Invariance, Omni-Directionality, Velocity Constancy, and Octopaminergic Loss of Background Motion Suppression. *SSRN Electron. J.*
- Stange, G., Stowe, S., Chahl, J.S., and Massaro, A. (2002). Anisotropic imaging in the dragonfly median ocellus: A matched filter for horizon detection. *J. Comp. Physiol. A Neuroethol. Sensory, Neural, Behav. Physiol.* 188, 455–467.
- Staudacher, E. (1998). Distribution and morphology of descending brain neurons in the cricket *Gryllus bimaculatus*. *Cell Tissue Res.* 294, 187–202.

- Sterling, P., and Laughlin, S. (2015). *Principles of neural design* (The MIT Press).
- Strausfeld, N.J. (1980). Male and female visual neurones in dipterous insects. *Nature* 283, 381–383.
- Strausfeld, N.J. (1984). Functional Neuroanatomy of the Blowfly's Visual System. In *Photoreception and Vision in Invertebrates*, (Boston, MA: Springer US), pp. 483–522.
- Strausfeld, N.J. (1991). Structural organization of male-specific visual neurons in calliphorid optic lobes. *J. Comp. Physiol. A* 169, 379–393.
- Strausfeld, N.J. (2005). The evolution of crustacean and insect optic lobes and the origins of chiasmata. *34*, 235–256.
- Strausfeld, N.J. (2009a). Brain and Optic Lobes. In *Encyclopedia of Insects*, (Elsevier Inc.), pp. 121–130.
- Strausfeld, N.J. (2009b). Brain organization and the origin of insects: an assessment. *Proc. R. Soc. B Biol. Sci.* 276, 1929–1937.
- Strausfeld, N.J., and Bassemir, U.K. (1985a). Lobula plate and ocellar interneurons converge onto a cluster of descending neurons leading to neck and leg motor neuropil in *Calliphora erythrocephala*. *Cell Tissue Res.* 240, 617–640.
- Strausfeld, N.J., and Bassemir, U.K. (1985b). The organization of giant horizontal-motion-sensitive neurons and their synaptic relationships in the lateral deutocerebrum of *Calliphora erythrocephala* and *Musca domestica*. *Cell Tissue Res.* 242, 531–550.
- Strausfeld, N.J., and Gilbert, C. (1992). Small-field neurons associated with oculomotor control in muscoid flies: Cellular organization in the lobula plate. *J. Comp. Neurol.* 316, 56–71.
- Strausfeld, N.J., and Gronenberg, W. (1990). Descending neurons supplying the neck and flight motor of diptera: Organization and neuroanatomical relationships with visual pathways. *J. Comp. Neurol.* 302, 954–972.
- Strausfeld, N.J., and Okamura, J.-Y. (2007). Visual system of calliphorid flies: Organization of optic glomeruli and their lobula complex efferents. *J. Comp. Neurol.* 500, 166–188.
- Strausfeld, N.J., and Seyan, H.S. (1985). Convergence of visual, haltere, and prosternai inputs at neck motor neurons of *Calliphora erythrocephala*. *Cell Tissue Res.* 240, 601–615.
- Strausfeld, N.J., Seyan, H.S., and Milde, J.J. (1987). The neck motor system of the fly *Calliphora erythrocephala* - I. Muscles and motor neurons. *J. Comp. Physiol. A* 160, 205–224.
- Supple, J.A., Pinto-Benito, D., Khoo, C., Wardill, T.J., Fabian, S.T., Liu, M., Pusdekar, S., Galeano, D., Pan, J., Jiang, S., et al. (2020). Binocular Encoding in the Damselfly Pre-motor Target Tracking

System. *Curr. Biol.* *30*, 645-656.e4.

Suver, M.P., Mamiya, A., and Dickinson, M.H. (2012). Octopamine neurons mediate flight-induced modulation of visual processing in *Drosophila*. *Curr. Biol.* *22*, 2294–2302.

Suver, M.P., Huda, A., Iwasaki, N., Safarik, S., and Dickinson, M.H. (2016). An array of descending visual interneurons encoding self-motion in *Drosophila*. *J. Neurosci.* *36*, 11768–11780.

Takemura, S. ya, Nern, A., Chklovskii, D.B., Scheffer, L.K., Rubin, G.M., and Meinertzhagen, I.A. (2017). The comprehensive connectome of a neural substrate for ‘ON’ motion detection in *Drosophila*. *Elife* *6*.

Takemura, S.Y., Bharioke, A., Lu, Z., Nern, A., Vitaladevuni, S., Rivlin, P.K., Katz, W.T., Olbris, D.J., Plaza, S.M., Winston, P., et al. (2013). A visual motion detection circuit suggested by *Drosophila* connectomics. *Nature* *500*, 175–181.

Tatler, B., O’Carroll, D.C., and Laughlin, S.B. (2000). Temperature and the temporal resolving power of fly photoreceptors. *J. Comp. Physiol. - A Sensory, Neural, Behav. Physiol.* *186*, 399–407.

Taylor, G.K., and Krapp, H.G. (2007). Sensory Systems and Flight Stability: What do Insects Measure and Why? *Adv. In Insect Phys.* *34*, 231–316.

Todorov, E. (2002). Cosine Tuning Minimizes Motor Errors. *Neural Comput.* *14*, 1233–1260.

Tolhurst, D.J., Tadmor, Y., and Chao, T. (2007). Amplitude spectra of natural images. *Ophthalmic Physiol. Opt.* *12*, 229–232.

Wakeling, J., and Ellington, C. (1997). Dragonfly flight. II. Velocities, accelerations and kinematics of flapping flight. *J. Exp. Biol.* *200*.

Walguarnery, J.W., Schröder, R., and Butler, M.A. (2009). Visual Target Detection in Damselflies. AFOSR Grant Rep. *611102*.

Wang, S., Borst, A., Zaslavsky, N., Tishby, N., and Segev, I. (2017). Efficient encoding of motion is mediated by gap junctions in the fly visual system. *PLOS Comput. Biol.* *13*, e1005846.

Wardill, T.J., List, O., Li, X., Dongre, S., McCulloch, M., Ting, C.Y., O’Kane, C.J., Tang, S., Lee, C.H., Hardie, R.C., et al. (2012). Multiple spectral inputs improve motion discrimination in the *Drosophila* visual system. *Science* (80-. ). *336*, 925–931.

Wardill, T.J., Knowles, K., Barlow, L., Tapia, G., Nordström, K., Olberg, R.M., and Gonzalez-Bellido, P.T. (2015). The Killer Fly Hunger Games: Target Size and Speed Predict Decision to Pursuit. *Brain. Behav. Evol.* *86*, 28–37.

Wardill, T.J., Fabian, S.T., Pettigrew, A.C., Stavenga, D.G., Nordström, K., and Gonzalez-Bellido, P.T.

- (2017). A Novel Interception Strategy in a Miniature Robber Fly with Extreme Visual Acuity. *Curr. Biol.* 27, 854–859.
- Warrant, E.J. (2017). The remarkable visual capacities of nocturnal insects: vision at the limits with small eyes and tiny brains. *Philos. Trans. R. Soc. B Biol. Sci.* 372, 20160063.
- Wehrhahn, C., Poggio, T., and Bühlhoff, H. (1982). Tracking and chasing in houseflies (*Musca*) - An analysis of 3-D flight trajectories. *Biol. Cybern.* 45, 123–130.
- Wellington, W.G., and Fitzpatrick, S.M. (1981). Territoriality in the drone fly, *Eristalis tenax* (diptera: Syrphidae). *Can. Entomol.* 113, 695–704.
- Wernet, M.F., Perry, M.W., and Desplan, C. (2015). The evolutionary diversity of insect retinal mosaics: Common design principles and emerging molecular logic. *Trends Genet.* 31, 316–328.
- Wertz, A., Borst, A., and Haag, J. (2008). Nonlinear integration of binocular optic flow by DNOVS2, a descending neuron of the fly. *J. Neurosci.* 28, 3131–3140.
- Wertz, A., Gaub, B., Plett, J., Haag, J., and Borst, A. (2009a). Robust Coding of Ego-Motion in Descending Neurons of the Fly. *J. Neurosci.* 29, 14993–15000.
- Wertz, A., Haag, J., and Borst, A. (2009b). Local and global motion preferences in descending neurons of the fly. *J. Comp. Physiol. A* 195.
- Wicklein, M., and Varjú, D. (1999). Visual system of the european hummingbird hawkmoth *Macroglossum stellatarum* (sphingidae, lepidoptera): Motion-sensitive interneurons of the lobula plate. *J. Comp. Neurol.* 408, 272–282.
- Wiederman, S.D., and O’Carroll, D.C. (2011). Discrimination of Features in Natural Scenes by a Dragonfly Neuron. *J. Neurosci.* 31, 7141–7144.
- Wiederman, S.D., and O’Carroll, D.C. (2013). Selective attention in an insect visual neuron. *Curr. Biol.* 23, 156–161.
- Wiederman, S.D., Fabian, J.M., Dunbier, J.R., and O’Carroll, D.C. (2017). A predictive focus of gain modulation encodes target trajectories in insect vision. *Elife* 6.
- Wiegmann, B.M., Trautwein, M.D., Winkler, I.S., Barr, N.B., Kim, J.-W., Lambkin, C., Bertone, M.A., Cassel, B.K., Bayless, K.M., Heimberg, A.M., et al. (2011). Episodic radiations in the fly tree of life. *Proc. Natl. Acad. Sci. U. S. A.* 108, 5690–5695.
- Wijngaard, W. (2010). Accuracy of insect position control as revealed by hovering male *Eristalis nemorum*.
- Wolpert, D.M., Ghahramani, Z., and Jordan, M.I. (1995). An internal model for sensorimotor

integration. *Science* 269, 1880–1882.

Wu, M., Nern, A., Ryan Williamson, W., Morimoto, M.M., Reiser, M.B., Card, G.M., and Rubin, G.M. (2016a). Visual projection neurons in the *Drosophila* lobula link feature detection to distinct behavioral programs. *Elife* 5.

Wu, M., Nern, A., Williamson, W.R., Morimoto, M.M., Reiser, M.B., Card, G.M., and Rubin, G.M. (2016b). Visual projection neurons in the *Drosophila* lobula link feature detection to distinct behavioral programs. *Elife* 5, e21022.

Yamaguchi, S., Wolf, R., Desplan, C., and Heisenberg, M. (2008). Motion vision is independent of color in *Drosophila*. *Proc. Natl. Acad. Sci. U. S. A.* 105, 4910–4915.

Yamawaki, Y., and Toh, Y. (2009). A descending contralateral directionally selective movement detector in the praying mantis *Tenodera aridifolia*. *J. Comp. Physiol. A. Neuroethol. Sens. Neural. Behav. Physiol.* 195, 1131–1139.

Yang, J.-B., Shi, M., and Yi, Q.-M. (2012). A New Method for Motion Target Detection by Background Subtraction and Update. *Phys. Procedia* 33, 1768–1775.

Yeates, D.K., Merritt, D.J., and Baker, C.H. (2002). The adult ventral nerve cord as a phylogenetic character in brachyceran Diptera. *Org. Divers. Evol.* 2, 89–96.

Zhou, J., Clavagnier, S., and Hess, R.F. (2013). Short-term monocular deprivation strengthens the patched eye's contribution to binocular combination. *J. Vis.* 13, 12–12.